New Materials for Oxygen Reduction Electrodes

Johansson, Tobias Peter

Publication date:
2012

Document Version
Publisher's PDF, also known as Version of record

New Materials for Oxygen Reduction Electrodes

Tobias Peter Johansson

Ph.D. Thesis, February 2012

Supervisor: Ib Chorkendorff

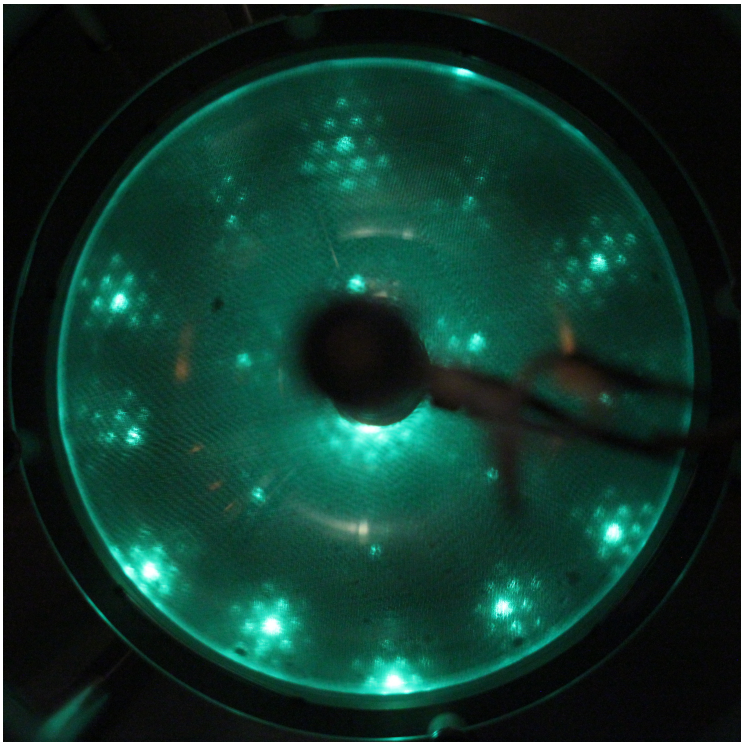

Center for Individual Nanoparticle Functionality
Technical University of Denmark

To Elias,
-the best result during my Ph.D.
Papy

Front page picture: LEED pattern of Y/Pt(111) annealed to 1348 K.

Contents

Preface

The work presented in this thesis has been carried out at the Technical University of Denmark (DTU), Department of Physics, at the Center for Individual Nanoparticle Functionality (CINF) with Professor Ib Chorkendorff as supervisor and Professor Jane Hvolbæk Nielsen as co-supervisor. CINF is funded by the Danish National Research Foundation which is greatly acknowledged for its support to this project. My Ph.D. has been funded by the HyCycle centre which is financed by the Danish Council for Strategic Research.

I would like to thank my supervisor Ib Chorkendorff for his support and motivation throughout the project. I would also like to thank Assistant Professor Ifan Stephens for countless discussions and ideas. I am grateful for your support.

During the beginning of my Ph.D. I had the pleasure to work closely together with Dr. Aliaksandr Bandarenka who I thank for good collaboration. I enjoyed working together with Angela den Dunnen (who made a 4 months internship with me in 2010) and my successor at Yggdrasil, Elisabeth Ulrikkeholm, who I worked together with at the end of my Ph.D.

I am most grateful to all my colleagues at the Center for Individual Nanoparticle Functionality and the Center for Atomic Scale Materials Design, in particular my coauthors, Jeff Greeley, Heine Hansen, Thomas Jaramillo, Jan Rossmeisl, Jens Nørskov, Jakob Schiøtz, David McCarthy, Anders Nierhoff, Christian Strebel, Patricia Hernandez-Fernandez, Lone Bech, Paolo Malacrida, Francisco Perez-Alonso, Federico Calle-Vallejo, Vladimir Tripkovic, Rasmus Frydendal, Brian Knudsen, Anders Jepsen and Ulrik Andersen.

I have really enjoyed working at CINF and I would like to express my appriciation of the open and informal working environment existing there.

Last but not least I would like to thank my family for their support. In particular a thanks should go to my parents, Torben and Elisabeth Johansson, my girlfriend

Elisabetta Fiordaliso and my son Elias Johansson, to whom I dedicate this thesis.

Tobias Peter Johansson
Kongens Lyngby, February 2012

Abstract

This thesis is concerned with the discovery, characterisation and testing of new catalysts for the oxygen reduction reaction (ORR). A theroretical screening study was performed, in close collaboration with the theory group at the Center for Atomic-scale Materials Design (CAMD), searching for catalysts which were both active and stable. The screening study identified Pt_3Y and Pt_3Sc as interesting candidates for the ORR.

The activity of the ORR on sputter cleaned bulk polycrystalline electrodes of Pt_3Y and Pt_3Sc was probed in an electrochemical cell using a rotating disk electrode setup. Pt_3Y and Pt_3Sc showed an enhancement in ORR activity by a factor of 1.5–1.8 and 6–10, respectively, in the range 0.9–0.87 V.

Ultra high vacuum (UHV) annealing of bulk polycrystalline samples of Pt_3Y, Pt_5Y and Pt_3La did not result in a Pt overlayer formation. For the bulk polycrystalline Pt_3Sc sample, on the other hand, a Pt overlayer was formed upon annealing in UHV. The reactivity of the Pt overlayer was tested by temperature programmed desorption (TPD) of CO, which yielded a lower desorption temperature compared to Pt(111). The ORR activity of the annealed Pt_3Sc sample was found to be on the same order as the sputter cleaned Pt_3Sc.

The deposition of Y on a Pt(111) crystal was then investigated. It was found that when annealing the crystal above 800 K a Pt overlayer was formed on top of a Pt_xY structure. Low energy electron diffraction (LEED) was used to probe the ordering of the surface and the LEED patterns indicated a 1.88×1.88 R30° structure compared to Pt(111). CO TPD measurements showed a distinct peak at 295 K and a general weaker bonding of CO (on the order of 120 K) compared to Pt(111). The ORR activity of the annealed Y/Pt(111) was measured to be comparable to that of sputter cleaned bulk polycrystalline Pt_3Y. The angle resolved x-ray photoelectron spectroscopy (ARXPS) depth profile after the electrochemical measurements

showed the formation of a thick Pt overlayer.
Finally, the possible changes in the surface morphology of Pt nanoparticles by annealing in high pressures of CO was correlated with measurements done on a sputtered Pt(111) crystal. For the Pt(111), crystal high pressures of CO was seen to enhance the annealing of the defect sites, whereas for nanoparticles a slight roughening was observed.

Dansk resumé

Denne afhandling omhandler opdagelse, karakterisering og afprøvning af nye katalysatorer til oxygen reduktion reaktionen (ORR). En teoretisk screening undersøgelse blev udført, i tæt samarbejde med teorigruppen ved Center for Atomar-skala Materiale Design (CAMD). Der blev undersøgt katalysatorer der både er aktive og stabile for ORR reaktionen. Pt_3Y og Pt_3Sc blev identificeret som interessante kandidater. ORR aktiviteten af sputter rengjorte polykrystallinske prøver af Pt_3Y og Pt_3Sc blev målt i en elektrokemisk celle, ved brug af en roterende disk elektrode. Pt_3Y og Pt_3Sc viste en forøgelse i ORR aktiviteten med en faktor på hhv. 1,5–1,8 og 6–10, i spændingsområdet 0.9–0.87 V.
Opvarmning af polykrystallinske prøver af Pt_3Y, Pt_5Y og Pt_3La i ultra højt vakuum (UHV) resulterede ikke i dannelsen af et Pt overlag. Det gjorde tilgengæld opvarmning af polykrystallinsk Pt_3Sc i UHV. Reaktiviteten af Pt overlaget blev testet ved brug af temperatur programmeret desorption (TPD) af CO. Dette gav en lavere desorptionstemperatur i forhold til Pt(111). ORR aktiviteten af den UHV opvarmede Pt_3Sc prøve var omtrent den samme som for sputter rengjort Pt_3Sc.
Deponering af Y på Pt(111) blev også undersøgt. Opvarmning af krystallen til 800 K resulterede i dannelsen af et Pt overlag oven på en Pt_xY struktur. Lav energi elektron diffraktion (LEED) blev brugt til at undersøge ordningen af overfladen og LEED mønstrene viste en 1.88×1.88 R30° struktur i forhold til Pt(111). CO TPD målinger viste en skarp top ved 295 K og en generel lavere binding af CO (ca. 120 K) i forhold til Pt(111). ORR aktiviteten af den opvarmede Y/Pt(111) krystal blev målt til at være sammenlignelig med den for polykrystallinsk Pt_3Y. Vinkel opløst røntgenspektroskopi (ARXPS) efter de elektrokemiske målinger viste at et tykt Pt overlag var dannet.
Mulige ændringer i overfladestrukturen af Pt nanopartikler og en sputter rengjort Pt(111) krystal blev undersøgt under højt tryk af CO. For Pt(111) krystallen resul-

terede det høje tryk af CO i en udjævning af defekter i krystallen hvorimod for Pt nanopartikler resulterede det høje tryk af CO i flere defekter.

List of abbreviations

AES	Auger Electron Spectroscopy
ARXPS	Angle Resolved X-ray Photoelectron Spectroscopy
CE	Counter Electrode
DFT	Density Functional Theory
FCC	Face Centered Cubic
HOR	Hydrogen Oxidation Reaction
HPC	High Pressure Cell
HSA	HemiSpherical Analyser
IR	InfraRed
ISS	Ion Scattering Spectroscopy
LEED	Low Energy Electron Diffraction
ML	MonoLayers
MTOE	Mega Tonne of Oil Equivalent
NHE	Normal Hydrogen Electrode
ORR	Oxygen Reduction Reaction
PEMFC	Polymer Electrolyte Membrane Fuel Cell
PM-IRRAS	Polarisation Modulation InfraRed Reflection Absorption Spectroscopy
QCM	Quartz Crystal Microbalance
QMS	Quadropole Mass Spectrometer

RDE	Rotating Disk Electrode
RE	Reference Electrode
RHE	Reversible Hydrogen Electrode
RPM	Revolutions Per Minute
STM	Scanning Tunneling Microscopy
SXS	Surface X-ray Scattering
TEM	Transmission Electron Microscopy
TPD	Temperature Programmed Desorption
UHV	Ultra High Vacuum
WE	Working Electrode
XPS	X-ray Photoelectron Spectroscopy
XRD	X-Ray Diffraction

Chapter 1

Introduction

One of the biggest challenges that modern society is facing is the energy problem. Figure 1.1 shows the primary energy world consumption in the years from 1965 to 2010. In 2010 the percentage of the total energy originating from fossil fuels was 87 %. In the not too distant future fossil fuels will run out and it is therefore necessary to find a sustainable solution.

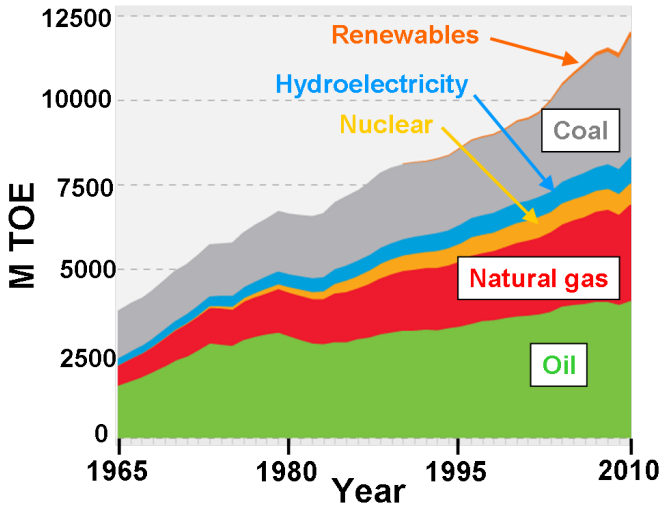

Figure 1.1: The primary energy world consumption in Mega Tonne of Oil Equivalent (MTOE). In 2010 the relative percentages were: renewable: 1.3 %, coal: 29.6 %, hydro: 6.5 %, nuclear: 5.2 %, natural gas: 23.8 %, oil: 33.6 %. Figure adapted from [1].

Renewable energy sources, such as wind and solar energy are attractive alternatives to fossil fuels. However, if one has to rely largely from energy originating from renewable energy sources, the problem of storing energy must be adressed, since solar energy is produced when the sun is shining and wind energy when the wind is blowing. In the words of Nathan Lewis, "He who cannot store, shall not have power after four!" [2].

A specific area where storing is essential is in the transportation sector. If one has to replace the use of hydrocarbon fuels in todays automotives a new way of storing energy is required. There are different possiblities to store energy (for a review on different possibilities of energy storage see e.g. [3]), but the one related to the work in this thesis is the possibility to store energy in the chemical bonds of hydrogen.

Hydrogen is an attractive energy carrier due to its large amount of energy per unit weight (142 MJ/kg) compared to hydrocarbon fuel (47 MJ/kg) [4]. Hydrogen gas, however, has a low density and under standard conditions 1 kg of H_2 occupies a volume of 12 m^3 [4]. Storing hydrogen in pressurised tanks is one way of solving this problem, but it leads to an increase in the gravimetric density due to the weight of the pressurised tank. Figure 1.2 compares the weight and volumes for energy storage systems of diesel, compressed hydrogen at 700 bar and lithium ion batteries. The numbers are based on a vehicle range of 500 km.

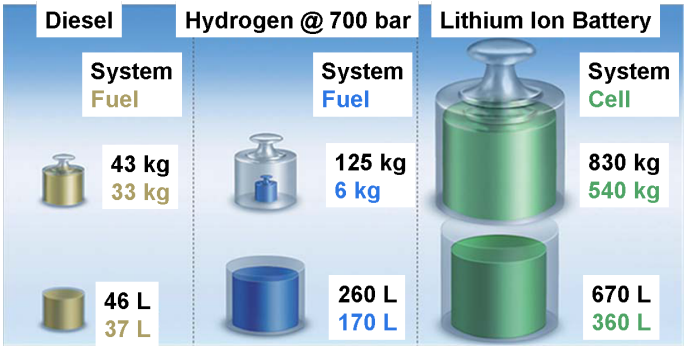

Figure 1.2: Energy storage system weight and volumes for various energy carriers. The comparison is based on a vehicle range of 500 km and assumes a fuel cell with 50 % effeciency. Figure adapted from [5].

In order to convert the chemical energy stored in hydrogen into electrical energy a fuel cell can be used. The thermodynamic attainable efficiencies for a fuel cell is close to 100 %, however, practical efficiensies are around 40-60 % due to different

losses which will be adressed in the following section.

1.1 Low temperature fuel cell

The Polymer Electrolyte Membrane Fuel Cell (PEMFC) is an attractive source of power. It uses hydrogen and oxygen and produces water and electricity. For a broad overview on fuel cells see e.g. the chapter by Gastieger and Garche in [6].
Given that hydrogen can be produced and stored in a renewable manner the PEMFC can be considered as a renewable energy source. Figure 1.3 shows a sketch of a PEMFC.

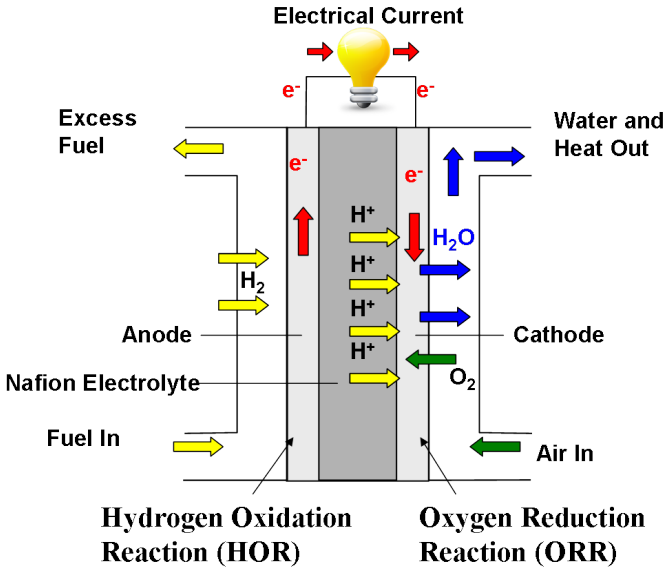

Figure 1.3: Sketch of a PEMFC. Figure adapted from [7].

Hydrogen comes in at the anode side where it is oxidised to electrons and protons. This reaction is called the Hydrogen Oxidation Reaction (HOR) . The protons are then led through a proton conducting membrane, typically made of nafion, and the electrons are forced to move through an external circuit. At the cathode of the PEMFC the protons and electrons react with oxygen to give water. This reaction is called the Oxygen Reduction Reaction (ORR). Catalysts are required for both the

HOR and the ORR. The overall reaction in a PEMFC is:

$$2H_2 + O_2 \longrightarrow 2H_2O \tag{1.1}$$

The thermodynamic potential for this reaction is 1.169 V at 80 °C. If no losses were present the overall cell potential of a PEMFC would be equal to the thermodynamic potential. However, losses are present in a fuel cell due to the ohmic resistances, mass transport and poor kinetics of each of the half reactions. The overall cell potential can therefore be written as follows [6, 8]:

$$U_{\text{cell}} = U_{\text{rev}} - j \cdot R_{\text{ohmic}} - \eta_{\text{HOR}} - \eta_{\text{ORR}} - \eta_{\text{tx}} \tag{1.2}$$

where U_{rev} is the reversible thermodynamic cell potential, j is the current density, R_{ohmic} is the in situ measured ohmic resistance, η_{HOR} is the H_2 oxidation reaction overpotential, η_{ORR} is the O_2 reduction reaction overpotential and η_{tx} includes all mass transport-induced potential losses.

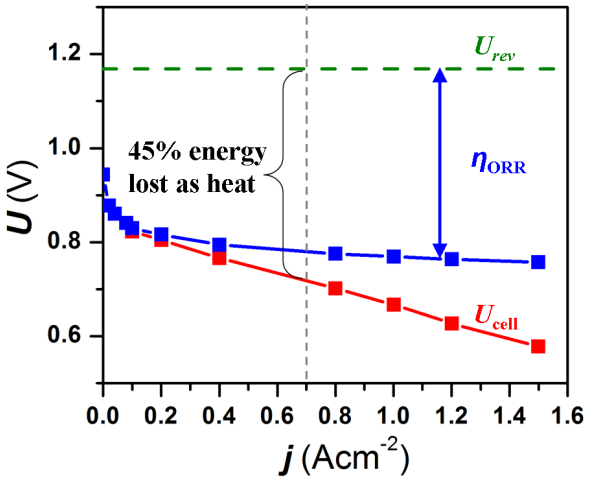

Figure 1.4: The potential (U) and current density (j) relationship for a state of the art PEMFC using Pt/carbon as catalyst. The main loss in a PEMFC is due to the slow kinetics of the ORR. Figure adapted from [8].

Figure 1.4 shows the efficiency of a "state of the art" PEMFC. The green dotted line represents the reversible potential of the reaction and the red graph is the actual potential of the cell. At a current density of 0.7 A/cm^2 45 % of the chemical

energy is seen to be lost as heat, even when using state of the art platinum catalysts. The blue graph in Figure 1.4 represents the cell potential after correcting for both ohmic losses, mass transport losses and losses due to the kinetics of the HOR. The distance between the blue graph and the reversible potential (green dotted line) therefore represents the losses in the PEMFC due to the slow kinetics of the ORR. Figure 1.4 clearly shows that the sluggish kinetics of the ORR constitute the main contribution to the loss in a PEMFC [8, 9].

A more active catalyst for the ORR, giving a higher current density at a given potential, is therefore needed. Gasteiger et al. suggested that a 4-10 fold improvement in ORR activity over pure Pt is required to enable the commercialisation of PEMFC's in automotives [10]. Pt is a scarce and expensive metal and therefore the ideal catalyst would be made from more abundant materials and experience a higher activity than Pt. The acidic and oxidising conditions in a PEMFC, however, greatly limits the choise of catalyst material which can be deployed. In fact at potentials greater than 0.9 V only Pt, Au and Ir are thermodynamically stable in their bulk metallic form and even Pt corrodes at potentials $\sim$1 V [11–13]. Most research efforts are therefore focused on improving the activity of Pt. This can e.g. be done by forming a Pt overlayer structure on a core of Pt alloyed with less noble transition metals. The underlying Pt alloy modifies the electronic structure of the Pt overlayer giving it a higher ORR activity. Although thermodynamically most Pt alloys are unstable under the conditions of the ORR, dissolution of the less noble metal is kinetically hindered by the Pt overlayer.

Pt_xNi, Pt_xCo and Pt_xFe have all been shown to be good catalysts for the ORR in PEMFC [14], however, there are reports suggesting that they are not stable on a long term under operating conditions of the PEMFC [15].

1.2 The Oxygen Reduction Reaction

In order to better understand the improvement in activity of Pt alloys over pure Pt it is useful to consider the ORR in more detail.

The overall oxygen reduction reaction is:

$$O_2 + 4H^+ + 4e^- \longrightarrow 2H_2O \tag{1.3}$$

This is a challenging reaction to catalyse because the catalyst must be stable under the extremely corrosive conditions at a fuel cell cathode. Furthermore the catalyst must be chemically active enough to activate O_2 and noble enough to release the oxygen from the surface in the form of H_2O [16, 17].
Figure 1.5 shows the calculated ORR activity for different materials as a function of their oxygen binding energy. The data is seen to fall on a so called "volcano curve" where on the left side of the volcano oxygen is bound too strongly and on the right side of the volcano oxygen is bound too weakly. The optimum of the vulcano curve is seen to be close to platinum.

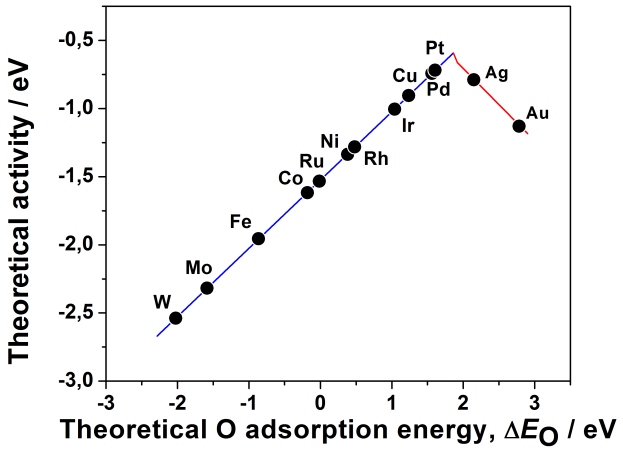

Figure 1.5: The ORR activity as a function of the oxygen binding energy for different metals. All data points are calculated values. Figure adapted from [18].

The reaction mechanism has been studied and speculated on for several decades and it still remains controversial [19, 20]. This is, at least partly, due to the fact that it is challenging to experimentally elucidate the reaction mechanism since the intermediates cannot easily be probed in-situ. Theoretical modelling of the ORR is also complex, but it turns out that the overall trends can be found by linking to gas phase heterogeneous catalysis [21]. By considering the adsorption energies of the different intermediates in the ORR, it is possible to calculate the overall free energy pathway for the ORR as a function of potential. The following reaction meachanism

is considered [17]:

$$O_2(g) + H^+ + e^- + * \longrightarrow HOO^* \tag{1.4}$$

$$HOO^* + H^+ + e^- + * \longrightarrow O^* + H_2O(l) \tag{1.5}$$

$$O^* + H^+ + e^- + * \longrightarrow HO^* \tag{1.6}$$

$$HO^* + H^+ + e^- + * \longrightarrow * + H_2O(l) \tag{1.7}$$

where $*$ indicates a catalytically active site on the surface and X^* indicates X adsorbed. As an alternative to the first reduction step, the dissociation of molecular oxygen ($O_2(g) \leftrightarrow 2O^*$) could be considered. However, it was shown by Karlberg et al. that the dissociative mechanism is less important for Pt in the potential range interesting for this study [18].

Clearly the oxygen reduction reaction is a complex reaction involving both O^*, HO^* and HOO^* as intermediate species. For a material to be an efficient catalyst for the oxygen reduction reaction it needs to bind all of these intermediates optimally. Figure 1.6 shows the free energy (ΔG) diagram for the ORR at 0.9 V on Pt(111). When relating the ORR activity to the free energy diagram it is assumed that any additional barriers scale with the size of the potential determining step. This assumption has been confirmed by detailed studies of the ORR mechanism on Pt(111) by both Neurock and coworkers and Tripkovic et al. which included the effect of reaction barriers [22, 23].

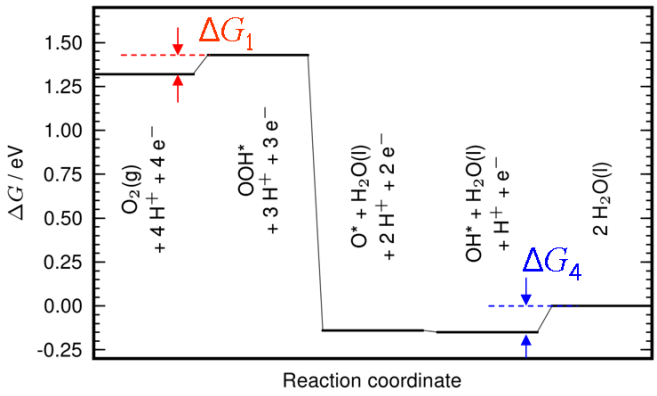

Figure 1.6: Free energy diagram for the ORR steps from eq. (1.4)-(1.7) at 0.9 V on Pt(111). ΔG_1 and ΔG_4 indicates the only steps which are uphill namely the formation of HOO^* and the removal of HO^*. Figure adapted from [17].

There are two candidates for the potential determining step. One is the formation of HOO* eq. (1.4) and the other is the removal of HO* eq. (1.7) [17]. In order to improve the activity of the ORR, a material is needed which binds HOO* species stronger and HO* species weaker. However, it turns out that it is not possible to vary the binding energies of HOO* and HO* independently since the O*, HO* and HOO* binding energies are linearly related on metal surfaces [24]. The binding energy of both HO* and HOO* is roughly half the binding energy of O*. This is can be understood intuitively, since HO* and HOO* are bound with a single bond to the surface whereas O* is double bonded. The best catalyst is therefore the one for which the two uphill steps in Figure 1.6, ΔG_1 and ΔG_4, are equal. At 0.9 V this corresponds to binding HO* and HOO* around 0.1 eV weaker (or O* 0.2 eV weaker).

1.3 Bulk Pt bimetallic alloys

In recent years, bulk polycrystalline platinum bimetallic alloys, Pt_3M (M=Ni, Co, Fe, Ti, V), have been shown to exhibit an increased ORR activity over platinum [25–27]. The solute metal is typically not stable in the surface upon immersion in the acidic electrolyte and the catalysts therefore consists of platinum overlayers on top of platinum alloys. In general two different platinum overlayer structures are considered. When the surface of the bulk polycrystalline platinum alloy is prepared by clean sputtering followed by immersion into acidic electrolyte a so called "platinum skeleton" structure is obtained [14]. The Pt skeleton structure is the result of the dissolution of the solute metal surface atoms into the electrolyte solution. Following the sputtering the surface is most likely rough, however, there is evidence that the Pt overlayer forms ordered (111) facets upon exposure to the electrolyte [28]. Another way of preparing the Pt overlayer is by clean sputtering the crystal followed by annealing in ultra high vacuum. For Pt_3M alloys (M=Ni, Co, Fe, Ti, V) annealed in ultra high vacuum the formation of a smooth Pt overlayer is seen [14]. Figure 1.7 shows a sketch of the platinum skeleton and platinum skin surfaces. The platinum skeleton surfaces are less defined, but are reported to have 100 % platinum in the first layer and a minimum of 75 % platinum from the second layer and down [14]. In the case of UHV annealing the platinum overlayer is formed by Pt diffusion to the surface. Stamenkovic et al. [14] reports that the platinum overlayer

formation occurs by platinum atoms from the second layer exchanging place with the solute atoms in the surface layer leading to a structure with 100 % platinum in the first layer, 50 % platinum in the second layer and (roughly) 75 % platinum in the following layers.

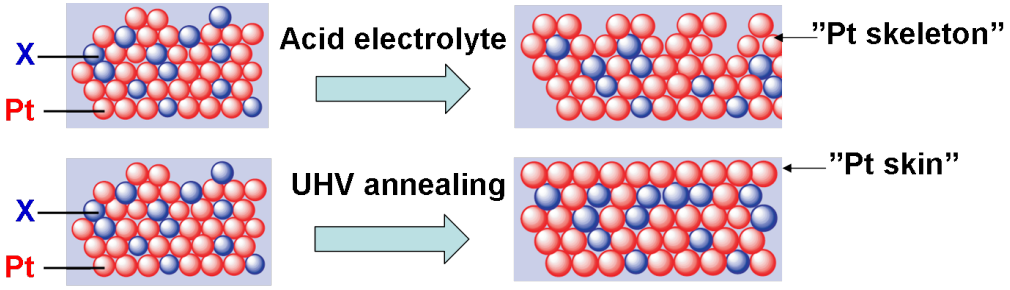

Figure 1.7: Sketch of the platinum skeleton and skin surfaces. Figure adapted from [14].

For $Pt_3Ti(111)$ there are different reports on the termination of the alloy after vacuum annealing. Ross and coworkers [29] suggest that $Pt_3Ti(111)$ is bulk terminated, whereas Duan et al. [30] and Chen et al. [31] suggest the formation of a Pt overlayer upon annealing in vacuum. Chen et al. [31] proposed that Pt atoms segregating to the surface of $Pt_3Ti(111)$ come from the bulk, resulting in a structure consisting of a platinum overlayer and bulk composition, i.e. 75 % Pt, from the second layer and down. They suggest that platinum segregation is enhanced by a slight non-stoichiometry (Pt excess) in the bulk of the crystal. It should also be noted that there is a discrepancy between studies of polycrystalline Pt_3Co, Pt-Co thin films and $Pt_3Co(111)$. Stamenkovic et al. [25] finds that a Pt overlayer is formed on polycrystalline Pt_3Co upon annealing to 1000 K whereas Axnanda et al. finds that Co is still present at the surface of Pt:Co thin films after annealing to 1000 K and also at the surface of $Pt_3Co(111)$ after annealing to 800 K [32].
Figure 1.8 shows the measured kinetic current density as reported in the literature for different alloy electrocatalysts with Pt skins plotted as a function of the calculated oxygen adsorption energy, ΔE_O. All data are shown relative to platinum in order to remove many of the systematic variations in conditions of the different experiments. UHV annealed samples of Pt_3M alloys (M=Ni, Co, Fe) show a high activity for the oxygen reduction reaction. Clean sputtered samples of Pt_3M alloys (M=Ni, Co, Fe) (not shown here) have an activity which is around 75 % lower than

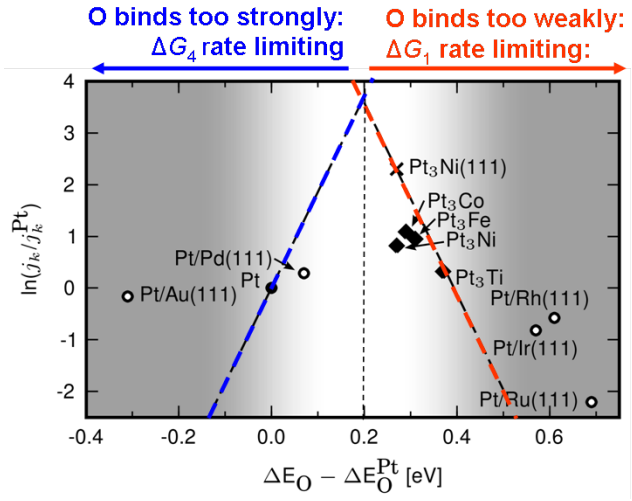

Figure 1.8: Measured kinetic current density as reported in the literature for different alloy electrocatalysts with Pt skins plotted as a function of the calculated oxygen adsorption energy, ΔE_O. The sources of the experimental data are marked by: circles [33] (Pt monolayers supported on single-crystal metal electrodes), diamonds [27] (polycrystalline alloys annealed in UHV before immersion in the electrochemical cell) and cross [26] (bulk $Pt_3Ni(111)$ alloy annealed in UHV before immersion). The dashed lines are the theoretical predictions from [17, 21]. Figure adapted from [16].

the annealed samples, but still higher than polycrystalline Pt [14]. Figure 1.8 also shows the activity of Pt monolayers supported on single-crystal metal electrodes of Au, Pd, Rh, Ir and Ru as obtained by of Adzic and coworkers [33].

It is seen that UHV annealed $Pt_3Ni(111)$ experiences an exceptionally high ORR activity. The surface of UHV annealed $Pt_3Ni(111)$ consists of pure Pt which is counterbalanced by having 50 % Ni in the second layer, so that the concentration profile oscillates around the bulk value (as for bulk polycrystalline Pt_3Ni). The stability of the surface as well as the near-surface composition of the alloy after transfer from UHV into the electrochemical environment was probed in situ by Surface X-ray Scattering (SXS). Both the surface structure as well as the segregation profile of the $Pt_3Ni(111)$ were found to be completely stable in the potential range from 0.05-1.0 V vs. the Reversible Hydrogen Electrode (RHE) in 0.1 M $HClO_4$ [26].

On platinum overlayer structures the binding of HO*, HOO* and O*, is influenced by two different effects, namely the ligand effect and the strain effect [34–37]. The ligand effect originates in the modification of the electronic structure of platinum by neighboring atoms with a different atomic number. In order for the ligand effect

to play a role the solute atoms need to be close to the surface. Already if the solute atoms are in the fourth atomic layer the ligand effect is negligable [36, 38].
The strain effect, on the other hand, appears when the bulk of the Pt alloy has a different lattice parameter than pure Pt. The surface Pt layer will then tend to take on the same lattice parameter as the bulk Pt alloy, thereby changing the interatomic Pt-Pt distances. Compressive lattice strain causes a downshift in the d-band centre leading to a weakening in the binding of adsorbed intermediates to the Pt surface atoms. Tensile lattice strain will cause the opposite effect [35, 39]. It is challenging to separate the ligand effect from the strain effect in single Pt overlayers on bulk Pt bimetallic alloys. For the bulk polycrystalline samples of e.g. Pt_3Ni and Pt_3Co the Pt overlayer is strained because their bulk lattice parameter is different from that of Pt. However, as mentioned above the UHV annealed Pt_3Ni and Pt_3Co samples, which have an enrichment of the solute atom in the second layer, i.e. Pt skin surfaces, have a higher activity than the clean sputtered and leached samples, i.e. Pt skeleton samples. This suggests that also the ligand effect is important for the activity of these catalysts.
Recently two independent investigations, both on Pt-Cu systems, reported the separation of ligand and strain effects. In our own study the effect of subsurface alloying on the ORR activity of Pt(111) was investigated [40]. Cu was underpotentially deposited on a Pt(111) crystal and the Cu/Pt(111) near surface alloy was formed by annealing. Depending on the amount of deposited Cu, the HO^* binding energy was observed to shift. The observed shift in HO^* binding correlated with the increased ORR activity of the crystal in accordance with the volcano plot from Figure 1.8. Since the bulk of the crystal was composed of Pt there was no bulk lattice strain and the observed shifts in HO^* binding was largely due to the ligand effect.
Strasser et al. performed a comprehensive study of the strain effects for both dealloyed Pt_xCu nanoparticles and for Pt overlayers on Cu(111) [39]. Using ex situ characterisation the dealloyed Pt_xCu nanoparticles were seen to form a $\sim$1 nm thick Pt overlayer. The strain in the Pt shell of three samples with different stoichiometry of Pt and Cu was correlated with the measured ORR activity and the DFT calculated ORR activity. Experiments on Pt overlayers on Cu(111) showed a downshift in the d-band centre resulting in a continuous change of the oxygen 2p and platinum 5d antibonding states from above to below the Fermi level as additional compressive strain was applied. This result is consistent with the d-band model and explains the weaker binding of HO^* to the Pt overlayer on dealloyed Pt_xCu nanoparticles.

1.4 Nanoparticles as ORR catalysts

In commercial PEMFC's the catalyst used for the oxygen reduction reaction is typically platinum nanoparticles on a high surface area carbon support, although nanostructured thin films also are a possibility [41, 42]. The smaller the size of the particle, the higher the ratio of surface atoms to non surface atoms. Since the ORR happens at the surface, the smaller the size of the catalyst particles the better utilisation of Pt. However, not all Pt surface sites are equally active for the ORR. It is widely believed that the terrace sites, in particular the (111) facets, are the active sites for the ORR on Pt nanoparticles [40, 43, 44]. Therefore an optimal size of the Pt nanoparticles exists, which maximises the number of active sites per mass (the mass activity). Recent DFT calculations by Tritsaris et al. [45] showed that the optimal size is around 3 nm in diameter, which is in excellent agreement with measurements by Gasteiger et al. [8].
ORR activity measurements on nanoparticles are typically carried out using the "thin-film" method [8, 46]. This allows for easier and more reproducible testing compared to using a PEMFC and the measured ORR activities are found to be remarkably close to those measured in a PEMFC. For Pt bimetallic alloys such as Pt_3Ni and Pt_3Co in nanoparticulate form the surface specific activity is also seen to be lower than for the corresponding bulk polycrystalline samples [47]. However, when compared to pure Pt nanoparticles, the Pt bimetallic nanoparticles still show an increase in specific activity on the order of 2-4. The formation of Pt skin surfaces have also been investigated for nanoparticles. Mayrhofer et al. [48] found that Pt shell structures can be formed on nanoparticles of Pt_3Co either by heating the particles to 473 K in ambient pressure of CO or by potential cycling of Pt_3Co nanoparticles in CO saturated alkaline electrolyte for 60 min. (so-called CO annealing [49]). The reason for Pt segregating to the surface is that the adsorption enthalpy of CO is higher on Pt than on Co [50]. It is worth mentioning that for the Cu-Pt (bulk Pt(111) crystal) near surface alloy, however, Andersson et al. [51] found that annealing in high pressures of CO causes surface segregation of the less reactive alloy component. This was found to be due to a radically stronger Pt-CO bond when both Pt and Cu are present in the surface.
When considering nanoparticles of Pt bimetallic alloys a relevant question is if these alloys are stable under reactive conditions relevant for fuel cell applications. This was adressed by Mayrhofer et al. [15] who measured the stability of both leached

and unleached Pt_3Co nanoparticles supported on carbon. They found that continuous surface segregation of the solute metal can occur for Pt bimetallic catalysts under reactive conditions. Particularly when the potential was cycled in typical fuel cell cathode application ranges, Co atoms were seen to segregate to the surface of the Pt_3Co nanoparticles. Mayrhofer et al. [15] therefore stressed that in order to meet the durability requirements for PEM fuel cells, specific attention must be made to strategies for stabilisation of the catalyst structure. In the following section some of the possible factors determining the stability of Pt_xM nanoparticles will be discussed.

1.5 Stability of Pt_xM nanoparticles

Friebel et al. [52] recently studied the stability, under ORR conditions, of Pt islands deposited on Au(111) and Rh(111). They found that anodic Pt dissolution is promoted on a Au(111) substrate and inhibited on Rh(111). They ascribed this effect to the difference in relative surface energy of Au and Rh to that of Pt. Au has a significantly lower surface energy than Pt, which leads to Pt dissolution, whereas Rh has a higher surface energy than Pt leading to an increased stability of Pt [53]. Nanoparticles of Pt-Rh are therefore expected to provide good long-term stability under ORR conditions, however, their catalytic activity is not optimal.
Menninger and Chen suggested that another effect influencing the stability of Pt_xM nanoparticles is the binding energy of the solute metal to O_2 [54–56]. The effect of O_2 was investigated on Pt-Co-Pt and Pt-Ni-Pt bimetallic samples under UHV conditions by dosing of oxygen and subsequent heating. They found that the surface 3d–Pt–Pt configuration is preferred in O_2. From an Arrhenius analysis of the temperature dependence, the activation barrier from Pt-Ni-Pt to Ni-Pt-Pt was estimated to be 17 kcal/mol attributed to the Pt(111) areas and 27 kcal/mol attributed to the Pt(100). The estimated time to achieve the segregation of approximately half of the subsurface Ni layer at 80 °C (the typical operating temperature of a PEMFC) was 2200 s for the Pt(111) facet and 10^{12} s for the Pt(100) facet. It should, however, be emphasised that the stated segregation times are estimated from a fit of data aquired in UHV and may therefore differ from the situation in an actual PEMFC.
A process that might increase the segregation of the solute metal from the subsurface layer to the surface layer is the formation of subsurface oxide by the direct

interactions between adsorbed O* or HO* and the subsurface metal. On the other hand Markovic and coworkers have proposed that the decreased coverage of O* and HO* on the Pt overlayer on $Pt_3Ni(111)$ could make it less susceptible to subsurface oxide formation than on Pt(111) [57]. Another parameter influencing the stability is the annealing temperature. Makharia et al. investigated the effect of annealing temperature on the stability of the catalyst tested in a PEMFC [58]. They found that the stability of the catalyst increased with increasing annealing temperature. Upon annealing at 1173 K nanoparticles of Pt and Pt-Co showed the same degree of stability.
Finally the degree of alloying [59] and the alloying energy [60] may also be factors which influence the stability.

1.6 Controlling the surface morphology of Pt

The surface morphology is important for the activity of catalysts [61, 62]. This was also discussed earlier in the case of ORR on Pt nanoparticles, which is believed to mainly happen on the (111) facet. Different effects influence the surface morphology, e.g. annealing temperature and gas environment. In the following the effect of high pressures of CO is considered.
Tao et al. [63, 64] have shown the reconstructive effects of high pressure CO on Pt crystals, where Pt atoms are seen to rearrange in order to accomodate a higher CO coverage. The high pressure reconstruction was observed on the Pt(557) and Pt(332) surfaces, where the originally flat (111) terraces break up into nanometer-sized clusters. They also observed it for low pressure doses on the metastable hex-Pt(100) surface.
Kibler et al. on the other hand have shown that colling down a freshly annealed Pt(111) crystal in a CO atmosphere reduces the amount of defect sites on the crystal [65].
The binding energy of CO to platinum depends on the surface structure. CO has been shown to bind preferentially on the under coordinated sites, e.g. steps and kinks [66, 67]. Figure 1.9 shows the CO chemisorption energy as a function of the d-band center for different Pt surfaces. When moving from the most densely packed to the most open surface site, both the CO chemisorption energy and the d-band center are seen to vary by 1 eV.

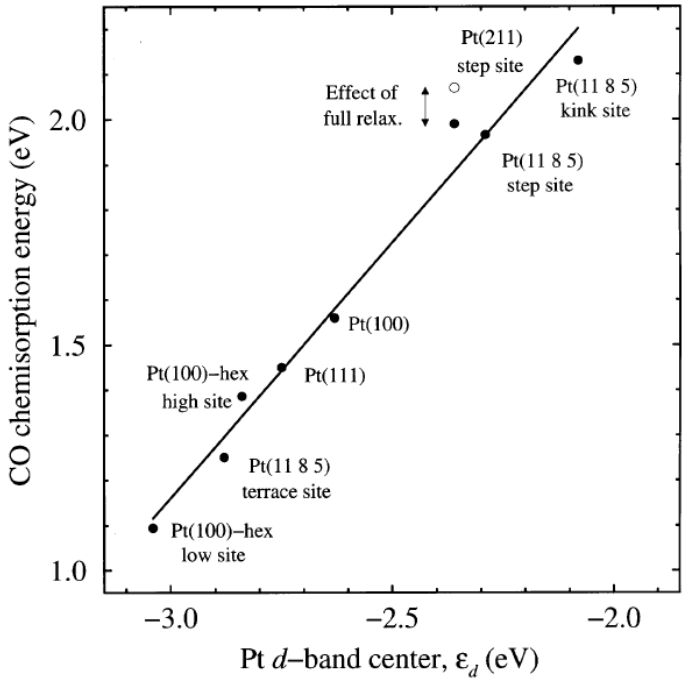

Figure 1.9: Calculated CO binding energy as a function of the d band center for different adsorption sites. Both the CO chemisorption energy and the d-band center are seen to be highly dependent on the coordination of the Pt site. Figure reprinted from [67].

Defect sites can be introduced in a Pt(111) crystal by sputtering. Figure 1.10 shows Scanning Tunneling Microscopy (STM) images aquired by Michely & Comsa [68] illustrating the surface morphology of Pt(111) for different sputter temperatures. Sputtering at 625 K results in a surface rich in defect sites. Upon annealing to 735 K the defect sites anneal out and the same surface structure as for sputtering at 735 K is obtained. This would suggest that the highest temperature to which the crystal has been exposed, regardless of whether this has been during or after sputtering, determines the surface morphology.

1.7 Deposition of rare earth metals on Pt(111)

No reports in literature have been found on the ORR activity of Pt alloyed with rare earth metals. There are, however, surface science studies on the deposition of La, Ce and Tm on Pt(111) [69–75].

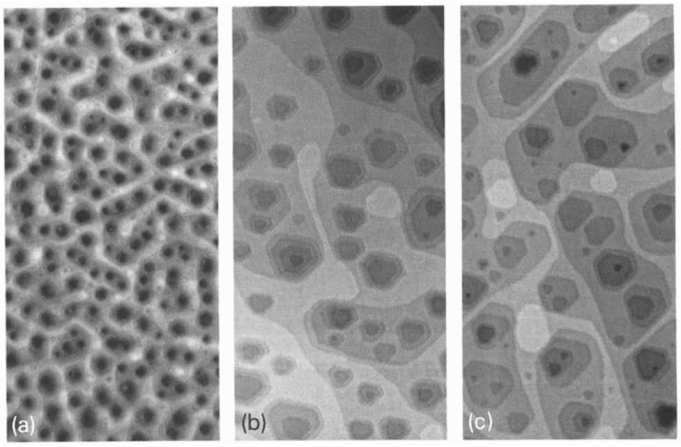

Figure 1.10: STM topographs of 1650 Å x 3300 Å size after removal of 5 monolayers by a) sputtering at 625 K; b) sputtering at 625 K and post-sputtering annealing for 2 minutes at 735 K; c) sputtering at 735 K. Figure reprinted from [68].

Tang et al. used X-ray Photoelectron Spectroscopy (XPS) and Low Energy Electron Diffraction (LEED) to study the growth of thin Ce films on Pt(111) [69]. They found that after heat treatment to 770 K, ordered Ce-Pt compounds were formed. Depending on the initial Ce coverage they observed the following structures, with respect to Pt(111), using LEED: 1.96×1.96, 1.94×1.94 with small satellites around the main spots and 1.96×1.96 R30°.

Baddeley et al. [70] also investigated the deposition of Ce on Pt(111). Using both STM and LEED, they found that annealing Ce overlayers of different thicknesses on Pt(111) to 1000 K leads to the appearance of five different ordered surface alloy structures similar to those observed by Tang et al. [69]. All of these structures were found to be based on the growth of crystalline Pt_5Ce, which is a hexagonal layer structure consisting of alternating layers of Pt_2Ce and so called Kagomé nets of Pt atoms. The Kagomé net is formed from corner sharing hexagons of close-packed Pt atoms with a missing atom in the center of each set of six Pt atoms. Raaen and coworkers [71] found a downshift of 120 K in desorption temperature of CO for the Pt terminated Ce-Pt(111) compared to Pt(111). They argue that this is most likely due to a change in the d-band originating from the hybridisation between Ce and Pt states, resulting in a weakening of the resonant interaction between the CO 5σ and Pt 5d states.

Raaen and coworkers also studied the deposition of La and Tm on Pt(111). For both

systems they observed the formation of an ordered surface alloy with Pt(111) upon annealing to 900 K. They also performed Temperature Programmed Desorption (TPD) experiments of CO in order to probe the reactivity of the surfaces. For both systems a significant decrease in the CO desorption temperature compared to Pt(111) was seen, with distinct peaks at around 200 K and 290 K for La/Pt(111) and 320 K for Tm/Pt(111) [72–74].

1.8 Outline

The outline of this thesis is as follows. Chapter 2 contains a description of the experimental setup and the techniques applied during the project. Chapter 3 deals with the surface morphology of Pt and in particular answers the question of what happens to sputtered Pt(111) when annealing in high pressures of CO? The results from Pt(111) are also related to similar experiments, performed in our group, on size selected Pt nanoparticles. In Chapter 4 results from a DFT screening study on active and stable catalysts for the ORR is presented. The best candidates are tested in an elecrochemical cell and the ORR activity is reported. At the end of Chapter 4 work performed in parallel with this project is presented, since it is highly relevant for the results presented in the later chapters. In Chapter 5 UHV studies of bulk polycrystalline Pt bimetallic alloys are presented along with ORR activity measurements. Chapter 6 deals with the deposition of Y on a Pt(111) crystal under UHV conditions. The structure, activity and stability of the annealed Y/Pt(111) crystal are all points addressed in this chapter. Finally, an overall conclusion and outlook is given in Chapter 7.
Papers and manuscripts written during the project period may be found at the end of this thesis after the bibliography.

Chapter 2

The experimental setup

2.1 Ultra High Vacuum chamber

The main instrument used during this study is an Ultra High Vacuum (UHV) chamber named "Yggdrasil" (in Norse mythology it is a giant ash tree, also called World Tree). Figure 2.1 shows a photograph and a schematic drawing of Yggdrasil.

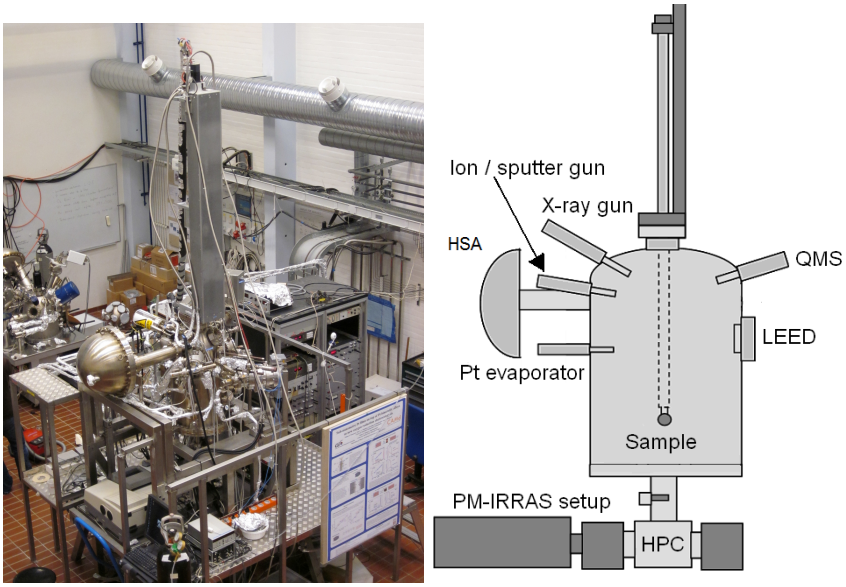

Figure 2.1: Photograph (left) and schematic overview (right) of the UHV chamber. Sketch adapted from [76].

The base pressure of the main chamber is $1 \cdot 10^{-10}$ torr. A High Pressure Cell (HPC) is attached to the main chamber and can be isolated from it by a lock which utilises a Cu gasket. It is thereby possible to have pressures up to several bars in the HPC while maintaining UHV conditions in the main chamber. The sample is transferred between the main chamber and the HPC by means of a vertical manipulator which is controlled by a PC using Labview based software. The manipulator enables the sample to be moved in x, y and z directions as well as rotated around its center axis. The main chamber is equipped with several standard surface science techniques which are presented in the next sections. Pumping of the chamber is done by two turbopumps with capacities of 240 l/s and 500 l/s. The small turbopump is also used for differential pumping of the Quadrupole Mass Spectrometer (QMS) and the ion gun. Two ion pumps, with a pumping capacity of 25 l/s each, are used for differential pumping of the rotational platform for the manipulator and for the X-ray gun.

The HPC and flanges mounted on it are made of Arne steel in order to prevent formation of nickel carbonyls when dosing high pressures of CO. When the sample is in the HPC position, Polarization Modulation InfraRed Reflection Absorption Spectroscopy (PM-IRRAS) measurements can be performed. In order for the IR beam to be transmitted, the windows of the HPC are made of ZnSe, limiting the pressure in the HPC to 5 bar. A sniffer line connecting the HPC to the QMS allows for changes in the gas phase concentration during high pressure experiments to be followed.

All samples used have a diameter of 5 mm and a thickness of 3 mm and were supplied by MaTecK, GmbH, Germany. The samples all have 2 holes which go all the way through the sample (for mounting purposes) and a third hole (for the thermocouple) which goes half way through. The sample is mounted by hanging it in a hairpin shaped 0.38 mm diameter tungsten wire which is then mounted onto the feed-throughs on the manipulator end. The thermocouple (type K2) is placed in the third hole in the sample and held in place by several pieces of 0.125 mm diameter tungsten wire. The sample may be heated resistively up to 1500 K by sending current through the tungsten wire from which it hangs. Cooling of the sample is achieved by pumping pressurised air or liquid nitrogen into the hollow manipulator. Using pressurised air the sample can be cooled down to $\sim$300 K whereas liquid nitrogen cools the sample down to $\sim$90 K. When using liquid nitrogen cooling it is not possible to isolate the sample in the HPC, due to thermal expansion of the

manipulator arm. A photograph of the sample is seen on Figure 2.2.

Figure 2.2: Photograph of a Pt(111) sample while heating. Note that this sample is 11 mm in diameter in whereas all samples studied in this thesis are 5 mm in diameter. Photograph taken by Nana Schumacher.

The gas inlet system is pumped with a small 240 l/s turbo pump, which at high pressures can be bypassed to a roughening pump. Capacitance baratrons, with ranges up to 10 mbar, 1000 mbar, and 30 bar, provide an accurate reading of the pressure close to the inlet line on the HPC. The gases used are N55 purity O_2 and N60 purity CO, Ar, He and H_2. The CO is first led over an active carbon filter in order to obtain higher purity before use, and then through a cooling trap immerged in liquid nitrogen for removal of nickel carbonyls.

2.1.1 X-ray Photoelectron Spectroscopy

In X-ray induced Photoelectron Spectroscopy a photon of energy $h\nu$ is incident on the sample. It penetrates the surface and is then absorbed by an electron with a binding energy E_{bin} below the vacuum level. This electron will then emerge from the sample with a characteristic kinetic energy. The process is known as the photoelectric effect and illustrated in figure 2.3. By measuring the distribution of energies of the emitted electrons the energy distribution of electron states in the sample can be measured [78]. The measured kinetic energy of the electron is:

$$E_{\text{kin}} = h\nu - E_{\text{bin}} - \phi_{\text{analyser}} \tag{2.1}$$

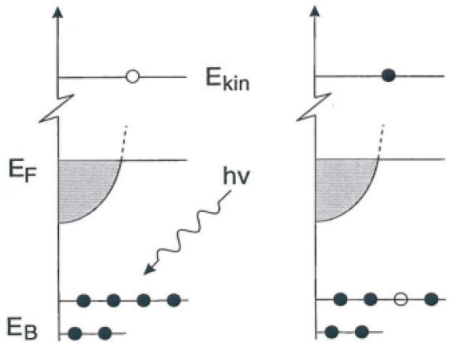

Figure 2.3: Sketch of the photoelectric effect. E_{B}=E_{bin} and E_{F} is the Fermi energy. Figure reprinted from [77].

where ϕ_{analyser} is the work function of the analyser.
The X-ray source on the chamber is a dual anode source with the lines Mg K_α($h\nu$ = 1253.6 eV) and Al K_α ($h\nu$ = 1486.3 eV). Unless indicated otherwise the XPS spectra reported in this thesis are taken using the Al K_α anode. The generated X-rays have a large penetration depth and will therefore excite electrons deep in the sample. The excited electrons will have a kinetic energy ranging from a few eV's and up to $h\nu$. Figure 2.4 shows the mean free path of electrons as a function of their energy. The figure shows that electrons in the energy range 5-1500 eV have mean free paths in the range 0.5-2 nm. This means that only electrons from the surface region of the sample will escape, making XPS a surface sensitive technique.

2.1.1.1 Angle resolved XPS

At a given angle θ between the normal to the sample and the detector, the electrons from a depth a have to travel a distance $a/\cos(\theta)$. This angle dependence can be included as a correction to the mean free path of the electrons $\lambda'_{\mathrm{xk}} = \lambda_{\mathrm{xk}} \cos(\theta)$. By varying the angle θ between the normal to the sample and the detector, it is possible to vary the effective mean free path and thereby to tune the surface sensitivity of the XPS measurement [80]. This is the principle used in the Angle Resolved XPS (ARXPS) apparatus, where it is possible to make a non destructive depth profile of the sample by automatically varying the angle θ and using software to convert the acquired spectra at different angles into a depth profile of the sample.

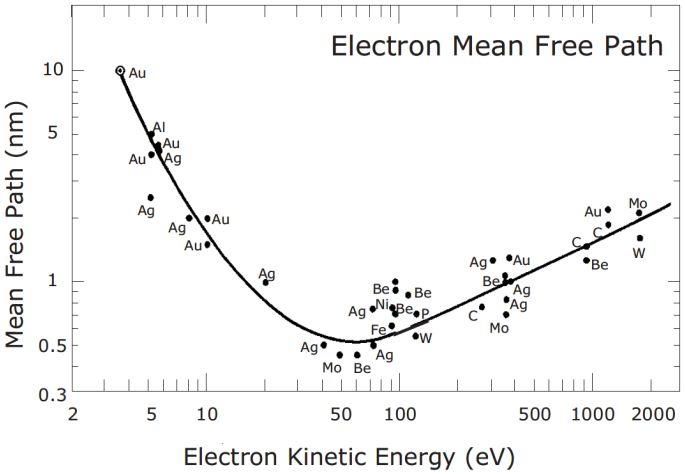

Figure 2.4: Plot of the electron mean free path. Figure adapted from [4] (originally from [79]).

2.1.1.2 Quantitative XPS

The intensity of the peak from level k travelling through material x can be written as [77]:

$$I_{\mathrm{xk}} = S_{\mathrm{xk}} N_{\mathrm{x}} F_{h\nu} \tag{2.2}$$

where S_{xk} is the sensitivity factor, N_{x} is the density and $F_{h\nu}$ is the intensity of photons. Sensitivity factors can be obtained by using the exact same settings while probing different pure materials. In literature relative sensitivity factors can be found, where normally the C1s signal has been set to 1 and all other sensitivity factors are scaled to this.
Using eq. (2.2) it is possible to calculate the composition of a homogeneous compound as [77]:

$$\frac{N_{\mathrm{x}}}{N} = \frac{\frac{I_{\mathrm{xk}}}{S_{\mathrm{xk}}}}{\sum_{i=1}^{n} \frac{I_{\mathrm{xk}}}{S_{\mathrm{xk}}}} \tag{2.3}$$

If the compound, however, is not homogeneous, information of the structure is needed in order to make quantifications. The intensity contribution from a layer in

the depth z of thickness dz is given by:

$$dI_{\mathrm{xk}} = \frac{I^{\infty}_{\mathrm{xk}}}{\lambda'_{\mathrm{xk}}} \exp\left(-\frac{z}{\lambda'_{\mathrm{xk}}}\right) \mathrm{d}z \tag{2.4}$$

where I^{∞}_{xk} is the level k intensity from an infinitely thick layer of material x and $\lambda'_{\mathrm{xk}} = \lambda_{\mathrm{xk}} \cos(\theta)$ is the effective mean free path (including the angle contribution). If the structure for example consists of an overlayer of A of thickness a on top of an alloy of $\mathrm{A}_{1-x}\mathrm{B}_x$, the measured peak intensities, I_{A} and I_{B} can be related in the following way [81]:

$$\begin{aligned} \frac{\frac{I_{\mathrm{A}}}{S_{\mathrm{A}}}}{\frac{I_{\mathrm{B}}}{S_{\mathrm{B}}}} &= \frac{\int_0^a \frac{1}{\lambda'_{\mathrm{A,k}}} \exp\left(-\frac{z}{\lambda'_{\mathrm{A,k}}}\right) \mathrm{d}z + \int_a^{\infty} (1-x) \frac{1}{\lambda'_{\mathrm{AB,k}}} \exp\left(-\frac{z}{\lambda'_{\mathrm{AB,k}}}\right) \mathrm{d}z}{\int_a^{\infty} x \frac{1}{\lambda'_{\mathrm{AB,l}}} \exp\left(-\frac{z}{\lambda'_{\mathrm{AB,l}}}\right) \mathrm{d}z} \Rightarrow \\ \frac{\frac{I_{\mathrm{A}}}{S_{\mathrm{A}}}}{\frac{I_{\mathrm{B}}}{S_{\mathrm{B}}}} &= \frac{1 - \exp\left(-\frac{a}{\lambda'_{\mathrm{A,k}}}\right) + (1-x)\exp\left(-\frac{a}{\lambda'_{\mathrm{AB,k}}}\right)}{x \exp\left(-\frac{a}{\lambda'_{\mathrm{AB,l}}}\right)} \end{aligned} \tag{2.5}$$

where $\lambda'_{\mathrm{AB,k}}$ is the effective mean free path of level k in layer $\mathrm{A}_{1-x}\mathrm{B}_x$. By solving the above equation it is possible to find x and thereby obtain the ratio of A to B in the subsurface alloy.

2.1.2 Ion Scattering Spectroscopy

In Ion Scattering Spectroscopy (ISS) (also known as Low Energy Ion Scattering, LEIS) monoenergetic low energy ions, typically He^+ with a primary energy of E_0=1-2 kV are incident on the sample and the energy distribution of the scattered primary ions is measured. The major scattering contribution results from elastic scattering and the trajectories of the ions can be described by one or more single collisions. The process can in fact be modelled as a "billiard ball game", where the equations for conservation of momentum and energy are [82]:

$$M_i \vec{v}_0 = M_i \vec{v}_1 + M_s \vec{v}_s \tag{2.6}$$

$$\frac{1}{2} M_i v_0^2 = \frac{1}{2} M_i v_1^2 + \frac{1}{2} M_s v_s^2 \tag{2.7}$$

where v_0 and v_1 are the initial and final velocities of the probe ion, and v_s is the velocity of the target atom. M_i is the mass of the ion and M_s is the mass of the surface atom. By combining the above equations it is possible to derive the following relation (valid for $M_s > M_i$) between the energy of the scattered ion (E_1) and the mass of the surface atom M_s [77]:

$$\frac{E_1}{E_0} = \left(\frac{\sqrt{M_s^2 - M_i^2 \sin^2(\theta)} + M_i \cos(\theta)}{M_s + M_i} \right)^2 \tag{2.8}$$

where E_0 is the energy of the incoming probe ion and θ is the angle between the incoming probe ions (the ion gun) and the scattered ions (the detector).

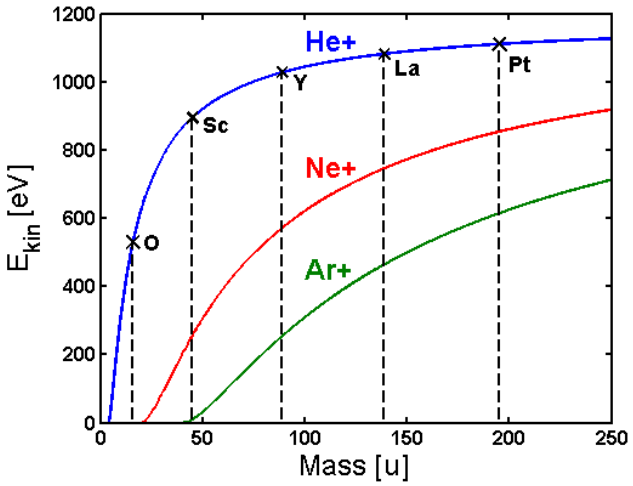

Figure 2.5: Plot of the ISS formula using He^+ ions (blue), Ne^+ ions (red) and Ar^+ ions (green). $E_0 = 1185$ eV and $\theta = 125°$.

Figure 2.5 shows a plot of eq. (2.8) for the parameters used at the setup and using either He^+ ions (blue), Ne^+ ions (red) or Ar^+ ions (green). Using light ions and small gas doses sputtering damage to the sample surface can be kept low. However, Figure 2.5 shows that for increasing atomic number, it gets more challenging to distinguish between elements of similar mass when probing with He^+ ions. This can be solved by using heavier probe ions like Ne^+ or Ar^+, which will, however, increase surface damage. Unless stated otherwise all ISS spectra in this thesis are made using He^+ ions at a pressure of $3 \cdot 10^{-9}$ torr and a primary energy of $E_0 = 1185$ eV. There is a high neutralisation probability ($> 99\%$) for the low energy noble gas ions

hitting the surface. This makes the ISS method particularly surface sensitive since basically all ions which penetrate into the surface or undergoe multiple scattering will be neutralised.
Quantitative analysis of the ISS spectrum is difficult due to the sensitivity factors being very dependent on the settings used. It can, however, be done by comparing the ISS signals of the elements in the sample of interest with those of reference samples [83–85].

2.1.3 Temperature Programmed Desorption

Temperature Programmed Desorption (TPD) also known as Temperature Desorption Spectroscopy (TDS) is a very simple and useful technique. A probe molecule is adsorbed on the surface of the sample. The sniffer line of a quadropole mass spectrometer is placed as close as possible to the sample without touching it and the temperature is then ramped in a linear manner. The measured intensities of preselected mass fragments are then recorded as a function of time, which can later be correlated to the sample temperature:

$$T(t) = T_0 + \beta \cdot t \tag{2.9}$$

where T_0 is the start temperature, t is the time and β is the heating ramp (typically 1-5 K/s). Unless stated otherwise all TPD's in this thesis are made with a temperature ramp of 2 K/s. By analysing the shape of the desorption peak and the temperature of maximum desorption it is possible to gain information about binding energies and desorption kinetics. The area of the peak in a TPD is proportional to the surface coverage.
Assuming an infinite pumping capacity, readsorption can be neglected and the desorption rate can be written as [4]:

$$r = -\frac{\mathrm{d}\theta}{\mathrm{d}t} = \nu(\theta)\theta^n \exp\left(-\frac{E_{\mathrm{des}}(\theta)}{RT}\right) \tag{2.10}$$

where R is the gas constant. If the pre exponential factor, ν, and the desorption energy, E_{des}, are assumed to be independent of the coverage, θ, the following relation

is valid for first order desorption ($n = 1$):

$$E_{\mathrm{des}} = k_B T_{\mathrm{max}} \ln\left(\frac{k_B {T_{\mathrm{max}}}^2 \nu}{E_{\mathrm{des}} \beta}\right) \tag{2.11}$$

where T_{max} is the maximum temperature of the peak and k_B is the Boltzmann constant. A typical value for ν is $10^{13}\mathrm{s}^{-1}$. Usually the desorption energy and the pre exponential factor are, however, dependent on the coverage which makes the interpretation of the TPD spectra non trivial [4].
The TPD spectra presented in this thesis are mainly CO TPD spectra recorded after the surface has been saturated with CO by dosing at $p = 2.0 \cdot 10^{-7}$ torr for 8 min. When possible liquid nitrogen is used to cool the crystal in order to start the TPD from as low temperature as possible. Typically the temperature range used for the TPD's is 90-700 K.

2.1.4 Low Energy Electron Diffraction

In Low Energy Electron Diffraction (LEED), a monochromatic beam of low energy electrons, typically $E_p < 200$ eV, is directed onto the sample, which is positioned in the center of four concentric hemispherical grids. Figure 2.6 shows a schematic drawing of the LEED setup.

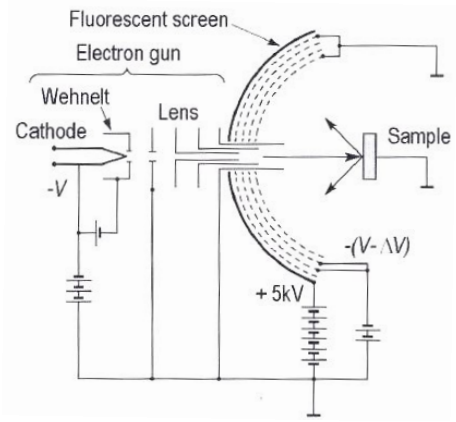

Figure 2.6: Schematic drawing of the LEED setup. Figure reprinted from [86].

The inner grid is set at ground potential whereas the two middle grids are set at a potential slightly below E_p in order to reject most of the inelastically scattered

electrons. The elastically scattered electrons on the other hand continue and are accelerated by a potential difference of 2-5 kV between the last grid and a flourescent screen upon which the diffraction pattern of the backscattered electrons can be observed. In order to generate a back-scattered electron diffraction pattern the sample must be a single crystal with a well-ordered surface structure.
From the de Broglie relation we have that the wavelength of the electrons is given by [86]:

$$\lambda = \frac{h}{p}, \quad p = \sqrt{2m_e E_p} \quad \Rightarrow \lambda(\text{Å}) = \sqrt{\frac{150.4}{E_p(\text{eV})}} \tag{2.12}$$

where p is the momentum of the electron, h is Planck's constant and m_e is the mass of the electron. Eq. (2.12) shows that for energies, E_p in the range 20-200 eV the wavelength is on the order of lattice distances and the scattered electrons will therefore undergo constructive and destructive interference leading to a reciprocal pattern on the fluorescent screen.
Further information along with software to interpret LEED spectra can be found in [87–89].

2.1.5 Evaporation of metals

During the project Pt, Sc and Y evaporators were constructed. Thermal evaporation of the metals was performed by sending current through a W wire onto which Pt, Y, or Sc is attached. The power dissipated in the evaporator is given by $P = RI^2 = \frac{U^2}{R}$. Because the resistance of the wire increases upon heating it is important to control the voltage applied in order for the dissipated power not to "run loose".
In Chapter 5 the deposition rate was calibrated using ISS and XPS, whereas in Chapter 6 a Quartz Crystal Microbalance (QCM) was used to calibrate the deposition rate. The change in vibration frequency of the QCM is related to the change in mass of the quartz crystal [90]. By taking into account the densities and acoustic impedances for each metal the deposition rate can be calibrated.

2.2 Electrochemical cell

The electrochemical measurements were done using the three electrode configuration sketched in Figure 2.7. The reference electrode is a half cell with a known reduction potential. A potential is set between the working electrode and the reference electrode and the current flowing from the working electrode to the counter electrode is measured.

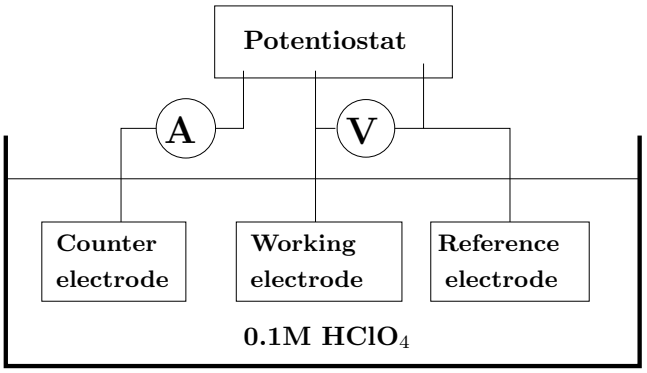

Figure 2.7: Sketch of the three electrode setup. The current is measured on the counter electrode and the potential is measured between the reference and working electrode.

The electrochemical experiments were done in the rotating disk electrode assembly seen in Figure 2.8. It consists of an electrochemical cell made of pyrex glass with various glass joints. The counter electrode was a Pt wire and the reference was a Hg/Hg_2SO_4 electrode. Both were separated from the working electrode compartment using ceramic frits. The working electrode was placed in a teflon holder and mounted in a rotator. Before each measurement the cell was cleaned in hot nitric acid (10 wt. %) and then rinsed and sonicated several times in ultrapure water. The electrolyte, 0.1 M $HClO_4$ (Aldrich, TraceSELECT® Ultra) was prepared from ultrapure water. The electrode was always immersed into the cell under potential control at 0.05 V into a N_2 (N5, Air Products) saturated electrolyte.
The rotation is used in order to correct for diffusion limitations. By measuring the total current and the diffusion limited current, the kinetic current can be obtained using the following relation [46]:

$$\frac{1}{j_{\text{total}}} = \frac{1}{j_{\text{diffusion}}} + \frac{1}{j_{\text{kinetic}}} \tag{2.13}$$

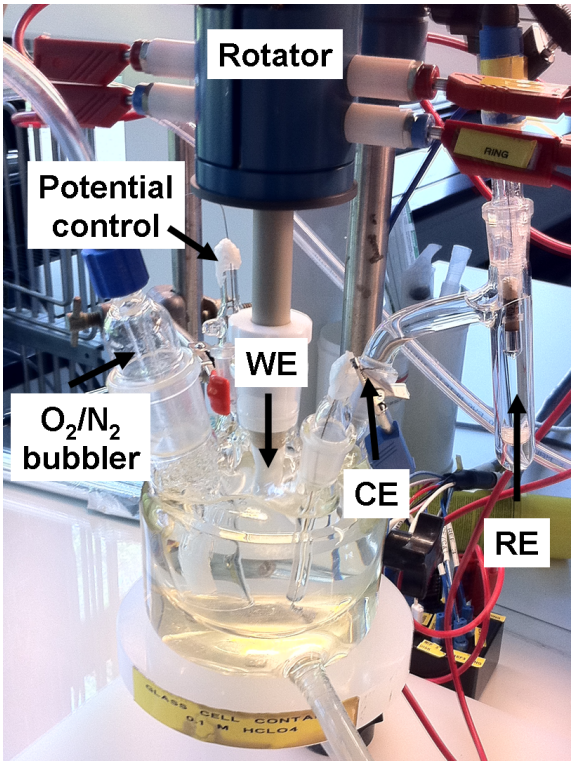

Figure 2.8: Picture of the rotating disk electrode (RDE) setup used. Indicated are the working electrode (WE), the Hg/Hg_2SO_4 reference electrode (RE), the counter electrode (CE). The electrochemical cell is immersed in a water bath which enables temperature control.

For modern PEMFCs the efficient delivery of reactive gases have been optimised and electrochemical kinetics are therefore the primary cause of inefficiency [8]. The oxygen reduction activity is often represented using the so called Tafel plot, which is the logarithm of the kinetic current density plotted against the potential.

Chapter 3

Platinum

In catalysis the activity of a nanoparticle is typically highly coordinated with the surface morphology. In the introduction to this thesis it was discussed that the ORR mainly happens on the (111) facets of Pt nanoparticles (see section 1.4). The CO and methanol electro-oxidation on the other hand shows a significant enhancement in the intrinsic activity with the amount of surface steps [91].
The aim of this chapter is to investigate what happens to sputtered Pt(111) when annealing in high pressures of CO. In particular, does the high CO pressure cause the defect sites to anneal out as seen by Kibler et al. [65] or do they roughen as seen by Tao et al. [63, 64]?
The results are important in order to understand how the surface morphology of Pt can be controlled. This is further investigated by relating the results from Pt(111) to similar experiments, performed in our group, on size selected Pt nanoparticles.

3.1 Annealed Pt(111)

The crystal is a 5 mm diameter 99.99 % purity Pt(111) crystal supplied by Mateck GmbH, Germany. The crystal was cleaned by cycles of Ar sputtering at room temperature, annealing to 1273 K and sputtering at 1273 K. The cleanliness of the crystal was then checked with LEED, XPS and ISS. Figure 3.1 shows a photograph of the LEED pattern of the crystal. A hexagonal pattern is seen corresponding to the (111) direction. Detailed XPS spectra of Pt4f, C1s, O1s, Ni2p, Cu2p are obtained and

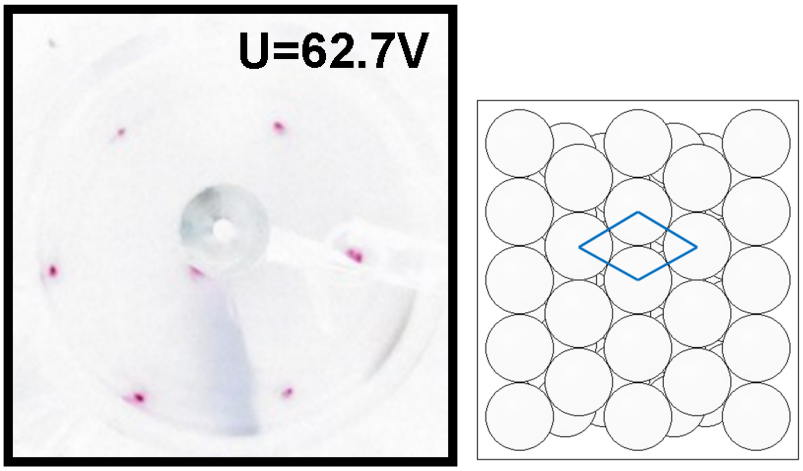

Figure 3.1: Left: photograph of the LEED pattern of annealed Pt(111) taken at T= 523 K. The hexagonal pattern seen corresponds to the hexagonal structure of Pt(111) sketched on the right.

only Pt is seen confirming the cleanliness of the crystal [92]. Figure 3.2 shows the ISS spectrum of the Pt(111) sample after a HPC CO experiment. The sample was kept at 550 K during ISS to prevent CO from adsorbing on the surface. The ISS spectrum shows only one peak, which is located at around 1120 eV, corresponding to Pt (see Figure 2.5). When dosing CO at high pressures it is important to take care that the CO is cleaned from nickel carbonyls since small amounts of these could have a dramatic effect on the catalytic properties of the studied catalyst [93]. In no case was any evidence of Ni from nickel carbonyls seen, either by ISS or XPS.
The surface of the crystal was saturated with CO by background dosing, p=$2.0 \cdot 10^{-7}$torr for 500 s (corresponding to a dose of 100 L[1]), while cooling the crystal from 1273 K to 90 K using liquid nitrogen. Figure 3.3 shows the resulting CO TPD spectrum. At the beginning of the TPD the temperature ramp is not linear. The small feature in the start of the TPD spectrum might therefore be due to initialisation effects, e.g. CO from the W wire holding and heating the sample. The peak at around 400 K corresponds to Pt(111), whereas the feature at around 520 K is attributed to Pt defect sites (see Figure 3.5). There is an exponential decaying background of CO in the chamber (due to the background CO dosing). The CO TPD is corrected for this by fitting an exponential decaying function (black graph in Figure 3.3) and subtracting it.

[1]One langmuir (L) corresponds to an exposure of 10^{-6} torr during one second

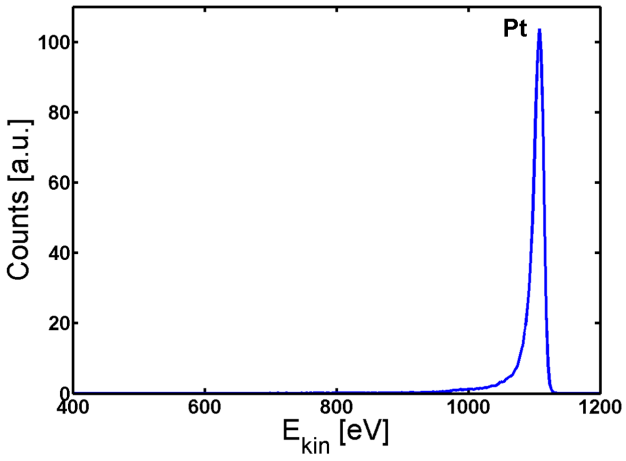

Figure 3.2: ISS spectrum of Pt(111) after a HPC CO experiment, T=550 K. Only a peak corresponding to Pt is seen, indicating a clean surface with no trace of nickel carbonyls.

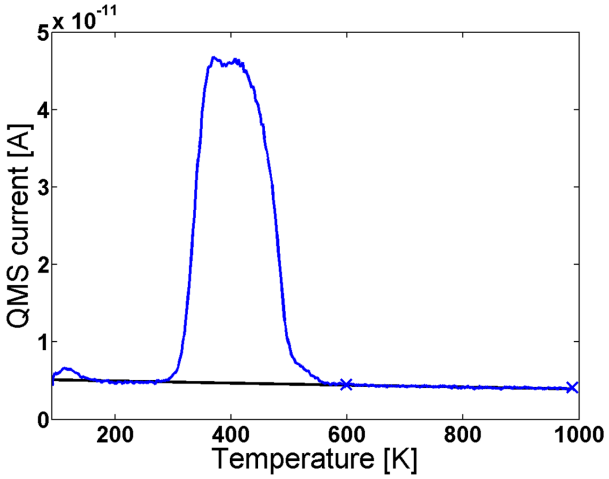

Figure 3.3: CO TPD of annealed Pt(111). The black graph is an exponential fit (between the two blue crosses) to the background.

Figure 3.4 shows the background corrected CO TPD spectrum of annealed Pt(111). The amount of CO desorbed from defects on the crystal is calculated by fitting an exponential decaying function (red graph) to the decaying part of the Pt(111) peak. The difference (black graph) between the CO TPD and the fitted exponential function is attributed to CO desorbed from defect sites on the Pt(111). For the Pt(111) crystal tested for this thesis the amount of CO desorbing from defect sites is found

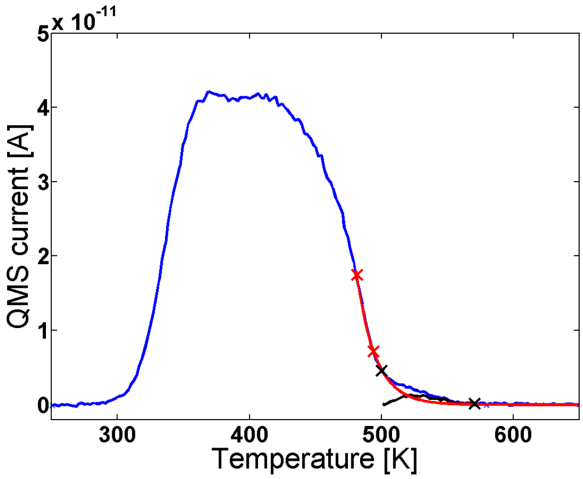

Figure 3.4: Blue graph: background corrected CO TPD of Pt(111). Red graph: fitted exponential decaying function between the two red crosses. Black graph: difference between the fit and the CO TPD (attributed to CO desorbed from defect sites).

to be less than 1 %. It should already now be mentioned that this number is not necessarily equal to the amount of defect sites on the crystal. The reason is that the capacity of undercoordinated Pt atoms to bind CO is not well established. For terrace and step sites the saturation coverage of CO is approximately 0.5 monolayer (ML) [94, 95]. Kink sites, however, can potentially adsorb as many as three CO molecules for each Pt atom [96].

Having established the background correction and the quantification of defects the CO TPD is compared to litterature. Figure 3.5 shows the CO TPD from Figure 3.4 compared to those of Pt(211) and Pt(533) obtained by Yates and coworkers [97]. All three spectra were corrected for the CO background and thereafter normalised to the same maximum signal for comparison purposes.

Yates and coworkers ascribed the peak at 400 K to CO desorption from the Pt(111) terrace of the crystal and the peak at around 510 K to CO desorption from undercoordinated sites. Quantification of the amount of CO desorbed from steps on the two different crystals gives approximately 35 % and 26 % compared to the total amount of CO desorbed from the surface of the Pt(211) and Pt(533) crystal, respectively. Pt(211) has a higher step density than Pt(533) due to the shorter terrace sites of Pt(211) compared to Pt(533). This is seen in the CO TPD spectra as a smaller high temperature peak for Pt(533). As mentioned earlier the amount of desorbed

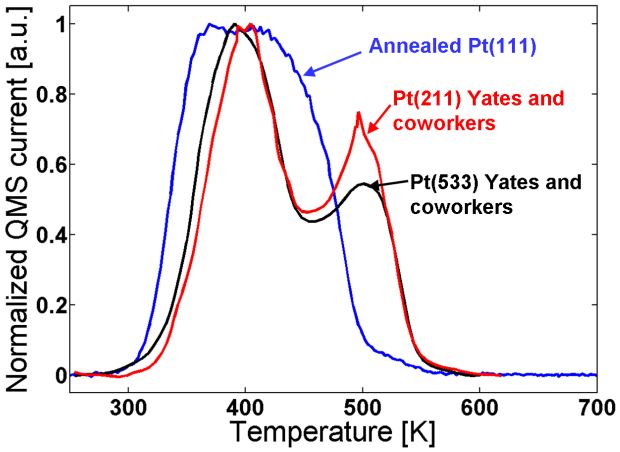

Figure 3.5: CO TPD of Pt(111) (blue graph, heating rate 2 K/s) compared to CO TPD spectra of Pt(211) (red graph, heating rate 1.3 K/s) and Pt(533) (black graph, heating rate 1.4 K/s), both from Yates and coworkers [97]. All spectra are corrected for the background and normalised to the same maximum height.

CO from defect sites on our annealed Pt(111) crystal is found to be less than 1 %.

3.2 Sputtered Pt(111)

The effect of sputtering is now investigated. Figure 3.6 shows a background corrected CO TPD spectrum of the Pt(111) crystal after sputtering at 573 K.
The amount CO desorbing from defect sites on the sputtered surface is calculated by fitting an exponential decay function (red graph) between the red crosses and evaluating the difference (black graph) between the TPD spectrum and the decay function. The area of CO desorbing from defect sites is divided by the total area resulting in 10 % CO desorbed from defect sites on the Pt(111) sample sputtered at a temperature of 573 K.
The effect of the sputtering temperature is now addressed. Figure 3.7 shows the CO TPD spectra obtained for annealed Pt(111) (blue graph) and for Pt(111) sputtered at 88 K (black graph), 373 K (red graph), 573 K (green graph) and 673 K (pink graph).
Sputtering the sample at 873 K (not shown here) resulted in the same spectrum as the annealed Pt(111) (blue graph), meaning that the created defect sites anneal

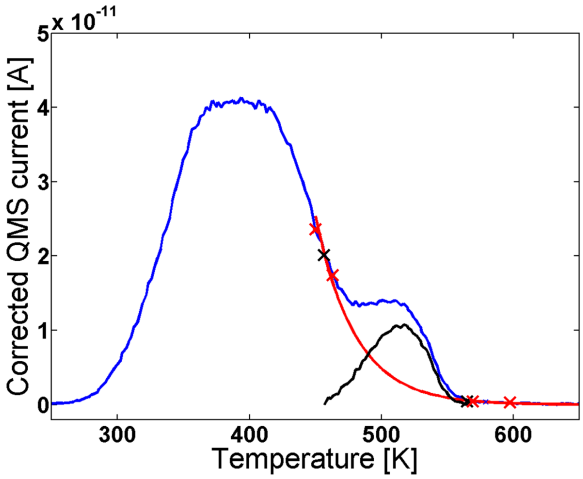

Figure 3.6: CO TPD of Pt(111) sputtered at 573 K. An exponential decay function (red graph) is fitted between the red crosses. The difference between the TPD spectrum and the decay function is attributed to CO desorbed from defect sites (black graph).

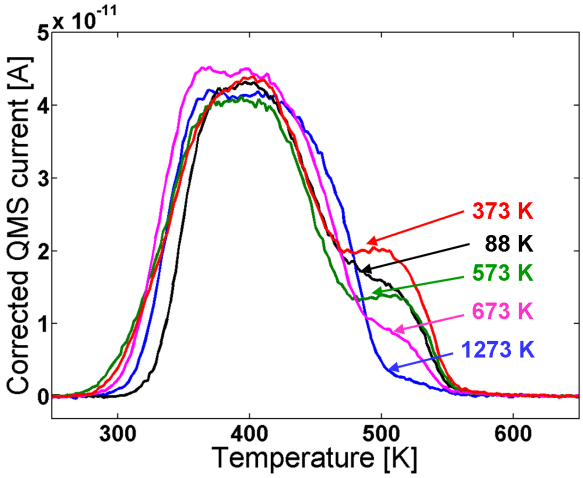

Figure 3.7: CO TPD of Pt(111) sputtered at different temperatures indicated in the figure.

out at high temperatures. When sputtering the crystal for 20 minutes instead of 10 minutes at 88 K the same CO TPD spectrum was obtained (not shown here), meaning that no more defect sites are are created by sputtering twice as long at 88 K. Sputtering at 273 K for 10 minutes (also not shown here) resulted in the same spectrum as the spectrum shown for 88 K (black graph), meaning that no more

defect sites are created by sputtering at temperatures below 273 K.
Figure 3.7 shows that sputtering at different temperatures influences both the starting temperature of CO desorption (left side of the peak) and the amount of CO desorbed from defect sites. Table 3.1 lists the amount of CO desorbed from defect sites relative to the total amount of desorbed CO from the Pt(111) crystal sputtered at different temperatures.

Sample	CO desorbed from defect sites
Sputtered at 88 K	$\sim$ 11 %
Sputtered at 373 K	$\sim$ 14 %
Sputtered at 573 K	$\sim$ 10 %
Sputtered at 673 K	$\sim$ 4 %
Annealed (at 1273 K)	$<$ 1 %

Table 3.1: Relative amount of CO desorbed from defect sites of the Pt(111) crystal sputtered at different temperatures.

Considering the sputtering temperatures from 373 K and up to 1273 K a clear trend is seen that the higher the sputtering temperature the lower the amount of CO desorbed from defect sites. By increasing the temperature the mobility of the atoms is increased and therefore the undercoordinated atoms will order in the stable Pt(111) direction. The sample sputtered at 88 K surprisingly shows a slightly smaller amount of CO desorbed from defect sites than the sample sputtered at 373 K. At present this effect is not understood and other techniques, such as scanning tunneling microscopy, is required to provide additional information on this peculiarity.
Figure 3.8 shows the CO TPD of the Pt(111) sample sputtered at 373 K. The CO TPD is stopped at T=700 K, CO is dosed again and the subsequent TPD (red graph) in Figure 3.8 is obtained.
It is seen that the subsequent CO TPD is very similar to that of annealed Pt(111), meaning that the defect sites anneal out after annealing the sputtered sample to 700 K. This is consistent with the result obtained by Michely and Comsa [68] using STM (as discussed in the introduction).

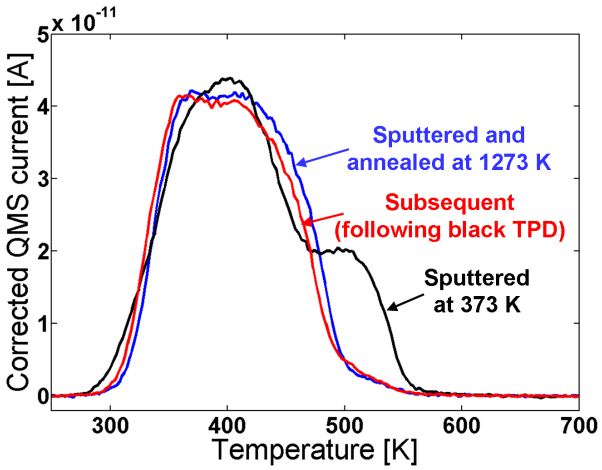

Figure 3.8: CO TPD of Pt(111) sputtered at 373 K (black graph), the subsequent CO TPD without any sputtering (red graph) and the annealed Pt(111) (blue graph).

3.3 Annealing in high pressures of CO

Having established the characteristics of the CO TPD for both annealed Pt(111) and Pt(111) sputtered at different temperatures it is now possible to investigate the effect of annealing in high pressures of CO. It should be emphasised that after each experiment involving high pressures of CO, the sample is checked for nickel carbonyls by both ISS (see Figure 3.2) and XPS. In no case was any trace nickel carbonyls found.

The red graph in Figure 3.9 shows the CO TPD of a Pt(111) sample sputtered at 373 K and exposed to 11 mbar of CO for 10 min at 373 K. For comparison the blue graph in Figure 3.9 shows the CO TPD of a sample sputtered at 373 K and kept at 373 K for 10 min under UHV conditions. It is seen that the two graphs are very similar and only a slight effect of the CO annealing is observed.

Figure 3.10 shows the same experiment as in Figure 3.9, but this time sputtering and annealing was performed at 573 K and the high pressure experiment done both at 2 and 11 mbar CO. From Figure 3.10 it is seen that for 2 mbar and 11 mbar exposures to CO at 573 K the amount of CO desorbing from the defect sites is similar and lower than for the sample kept under UHV conditions for 10 min. This shows that exposure to high pressures (2-11 mbar) of CO at 573 K decreases the amount of defect sites on the sputtered Pt(111). The observation that defect sites anneal out in the presence of high pressures of CO is in agreement with observations

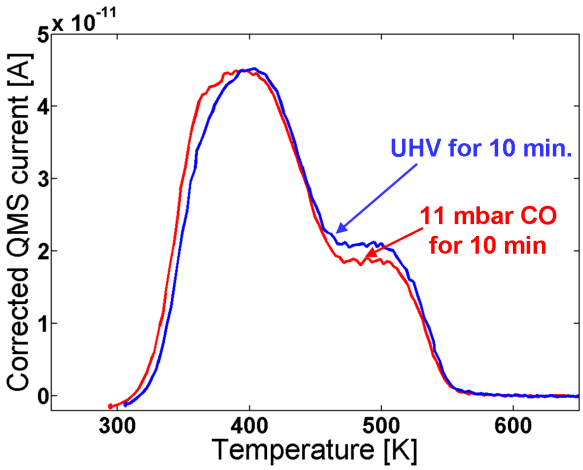

Figure 3.9: CO TPD spectra of Pt(111) sputtered at 373 K after waiting 10 min. in UHV at 373 K (blue graph) and after dosing 11 mbar CO at 373 K for 10 min. (red graph).

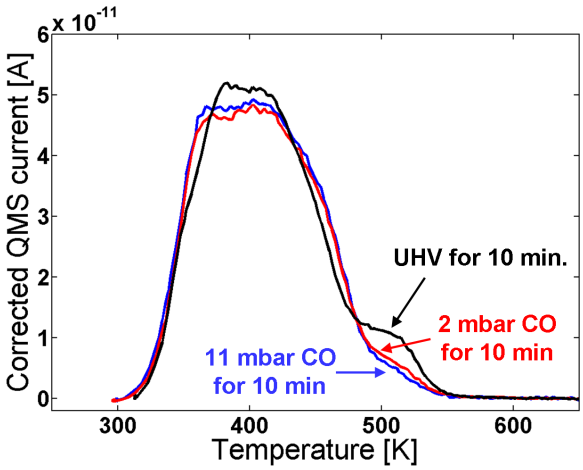

Figure 3.10: CO TPD of Pt(111) sputtered at 573 K. Black graph: after waiting 10 min. at 573 K in $2.0 \cdot 10^{-7}$ torr CO. Blue graph: after dosing 11 mbar CO at 573 K for 10 min. Red graph: after dosing 2 mbar CO at 573 K for 10 min.

by Kibler et al. discussed in the introduction [65].

3.4 Comparison to nanoparticles

The CO TPD's of sputtered Pt(111) are now compared with similar measurements performed on Pt nanoparticles at a different UHV setup at CINF. Mass-selected nanoparticles were deposited from an inert gas aggregation source (Mantis Deposition Ltd.), described in detail elsewhere [98–100]. The nanoparticles are soft landed (i.e. they have a kinetic energy of < 0.1 eV/atom) on a costum made SiO_2/Si(111) substrate.

Figure 3.11 shows the CO TPD spectra of "as deposited" nanoparticles. The TPD's resemble that of the 373 K sputtered Pt(111) from Figure 3.7 showing both a low temperature feature corresponding to Pt(111) terrace sites and a high temperature feature corresponding to defect sites. It is also seen that the feature corresponding to CO desorption from defect sites increases with decreasing size of the nanoparticles, indicating a higher concentration of defect sites on the smaller nanoparticles. As mentioned earlier it is not possible to deduce an absolute number of defect sites from the CO TPD, however, the temperature dependence of the CO desorption is seen to be closely linked to the coordination of the exposed Pt atoms, and can therefore be used as a probe of surface structure.

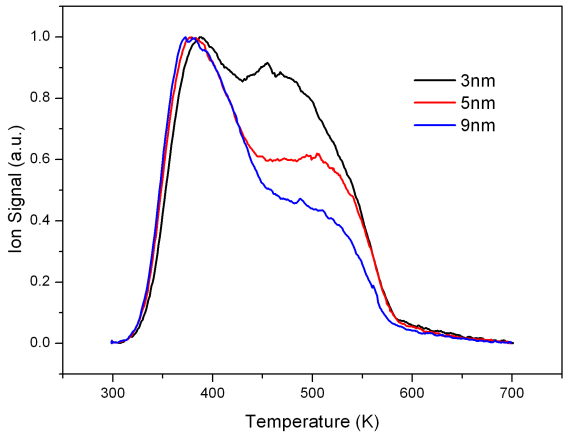

Figure 3.11: CO TPD of "as deposited" platinum nanoparticles of sizes 3, 5 and 9 nm. The feature corresponding to CO desorption from defect sites increases with decreasing size of the nanoparticles. The temperature ramp was 1 K/s. Measurements performed by David McCarthy, Anders Nierhoff and Christian Strebel.

The "as deposited" particles are expected to have a rough surface structure due to the growth conditions being far from equilibrium. Prior to HPC experiments, two

successive CO dosing and TPD cycles were perfomed in order for the particles to attain a near equilibrium configuration. Figure 3.12 shows the CO TPD spectra of pre annealed Pt nanoparticles (solid black lines) together with the TPD spectra obtained after annealing the samples at 573 K in 5 mbar CO (dashed red lines). The CO TPD of the 9 nm sample shows virtually no change before and after the high pressure CO experiment whereas the 3 and 5 nm samples both show an increase in CO desorbing from defect sites. The increase in CO desorption from defect sites shows that the 3 and 5 nm particles roughen upon annealing in high pressures of CO.

ISS measurements (not shown here) after 5 mbar CO exposure shows only three peaks corresponding to Si, O and Pt. The Si and O peaks are due to the SiO_2 support. No nickel peak is seen.

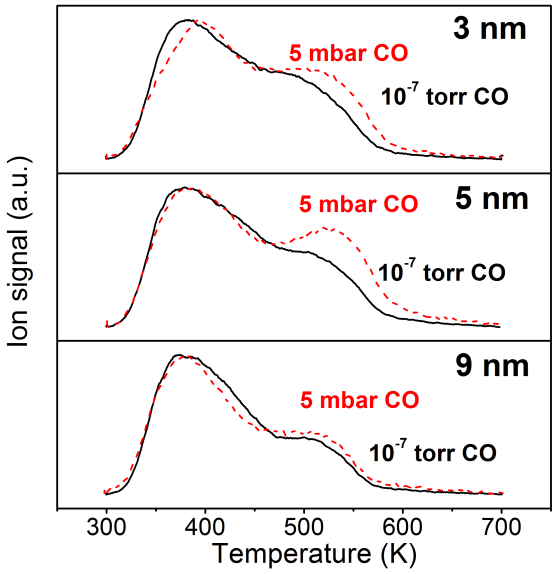

Figure 3.12: CO TPD of pre annealed Pt nanoparticles (solid black lines) and after annealing the samples at 573 K in 5 mbar CO (dashed red lines). The temperature ramp was 1 K/s. Measurements performed by David McCarthy, Anders Nierhoff and Christian Strebel.

3.5 Discussion and conclusion

The annealing out of the defect sites on the Pt(111) crystal under high CO pressures can be understood in terms of the greater binding energies of CO molecules to the undercoordinated Pt atoms at the sputter induced defects. The strong binding between CO and the undercoordinated site causes a weakening in the binding of the undercoordinated Pt atom to its neighbouring Pt atoms. It is presumably this weakening in the intermetallic bonds which allows the undercoordinated Pt-CO species to diffuse away from the step edges at a lower temperature than pure Pt atoms.

Horch et al. [101] have shown a similar effect for hydrogen on Pt(110). They found that when hydrogen adsorbs on Pt, there is a lower barrier for the diffusion of Pt than in the absence of hydrogen. It is not possible to conclude from the TPD results whether the annealing of defect sites at high pressures of CO is actually preceded by a roughening of the step edges to accommodate more CO (as seen by Tao et al. on Pt(557) and Pt(332) using STM [63]). However, since the CO TPD feature attributed to defect sites does not change shape or size significantly, it is suspected that roughening does not occur in this system.

For the nanoparticles on the other hand Figure 3.12 shows that little additional CO is adsorbed on the surface due to the higher pressure. If both annealing and roughening processes happen on the nanoparticles, the observed change in the CO desorption feature will depend on which of these processes is dominant.

For the nanoparticles an issue regarding the interpretation of TPD spectra is that the surface terminations of the particles is actually not well known. Transmission Electron Microscopy (TEM) images acquired from the nanoparticles show that they do not take a perfect Wulff shape even though the trend in surface energies suggests that there is a driving force for the low index facets to be present at the surface. When comparing the CO TPD of the single crystal to those of the nanoparticles it seems reasonable to assign the low temperature feature of the CO TPD from the nanoparticle to CO desorption from the (111) facets. The high temperature feature, however, is more challenging to interpret, since it most likely has contributions from both edges and vertices of the particles, as well as (001) facets.

In summary, the investigations on the effect of CO on Pt(111) and Pt nanoparticles showed that it is possible to correlate the surface roughness with the high temperature peak in the CO TPD. For the Pt(111) crystal high pressures of CO was

seen to enhance the annealing of the defect sites whereas for nanoparticles a slight roughening was observed. In principle, the effects described here, of CO annealing on Pt(111) and on Pt nanoparticles, could be used to tune the catalyst morphology and thereby optimise the catalytic performance.

Chapter 4

Alloys of Pt and early transition metals

If PEMFC's are to become economically viable, new materials are needed as catalyst for the ORR. In the introduction it was discussed that alloying Pt with late transition metals, such as Ni, Co, Fe and Cu increases its ORR activity. In this chapter a new set of Pt alloys is introduced with promising properties for the ORR. The results of this chapter have been published in reference [16] which is included at the end of the thesis. Section 4.3 describes work carried out by Ifan Stephens, Alexander Bondarenko, Lone Bech, Anders Nierhoff, Christian Strebel, David McCarthy and Patricia Hernandez-Fernandez in parallel to the work described in this thesis.

4.1 DFT screening study

In Section 1.2 it was shown that the optimal catalyst for the ORR should bind oxygen around 0.2 eV weaker than pure Pt. It was also discussed that Pt_3M alloys (M=Ni, Co, Fe) exhibit a higher activity for the ORR, but in the nanoparticulate form their degredation is due to dealloying. With this in mind a DFT screening study was performed looking at ORR catalysts of the form Pt_3X or Pd_3X. Two criteria were set up for the screening study. The first was that they should form Pt

or Pd overlayers with an OH binding energy in the range 0.2 eV ± 0.4 eV weaker than Pt. The second was that they should be as stable as possible. The calculated heat of formation of the bulk alloys, ΔE_{alloy} = E(alloy) – E(constituents), is taken as a measure of the stability of the alloy. Figure 4.1 shows the calculated oxygen adsorption energy on Pt overlayers, ΔE_O, relative to that on Pt, as a function of the calculated heat of formation of the bulk alloys. The calculation is performed for 25% of the solute metal in the second layer (circles). For some alloys also the case of 50% concentration of the solute metal in the second layer is included (squares in Figure 4.1). As mentioned in the introduction, this solute metal enriched layer is known to be formed upon vacuum annealing of the Pt_3M alloys (M=Ni, Co, Fe).

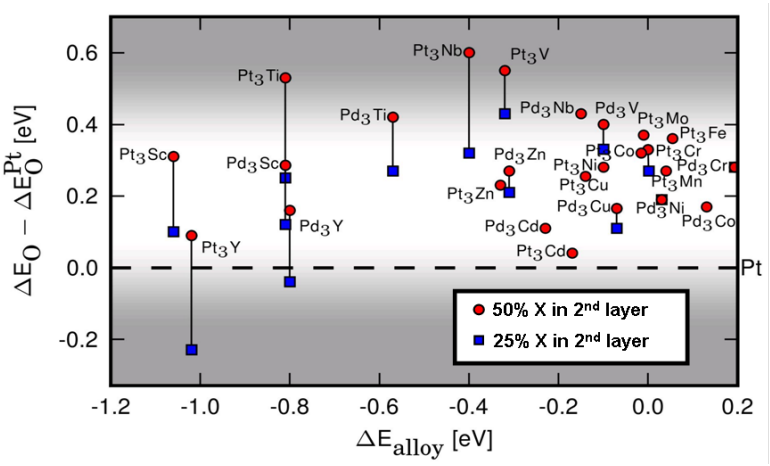

Figure 4.1: The output from the DFT screening study. The binding energy of oxygen relative to that of Pt is plotted as a function of the alloying energy. Figure reprinted from [16].

The systems with 50 % of the solute metal in the second layer only have surface Pt/Pd atoms with M neighbours underneath, whereas systems with only 25 % of the solute metal in the second layer have two different types of Pt/Pd atoms in the overlayer layer. One has a solute metal, M, as neighbour in the second layer and one is coordinated purely to Pt neighbours in the second layer. In principle both these sites contribute to the activity, but in particular for the Pt_3Y system, the Pt surface atoms coordinated purely to Pt neighbours in the second layer will bind oxygen too strongly and will therefore be blocked. It is therefore only the less reactive Pt sites with Y neighbours in the second layer which will be active. These active sites are approximately equivalent to the active surface sites on the Pt_3Y system with 50 %

of the solute metal in the second layer and in the following only this site will be considered as the active site for Pt_3Y.

Figure 4.1 shows that the screening predicts the already known Pt_3M alloys (M=Ni, Co, Fe, Ti) as being very active catalysts for the ORR. However, it is also seen the value of their heat of formation, ΔE_{alloy}, is close to zero, indicating that they are not very stable. Figure 4.1 also shows that, of the alloys with ΔE_O values in the optimal range, Pt_3Y and Pt_3Sc stand out as the most stable. They are in fact, the most stable of all the face-centered cubic (fcc) alloys in a database that consists of more than 60,000 compounds [60].

The high stability of these alloys can be explained in terms of the filling degree of the d-band. Y and Sc are both early transition metals and have one d electron, whereas Pt is a late transition metal and has nine d electrons. When combining the two the metal-metal d-bonds are therefore approximately half filled corresponding to the bonding states being filled and the antibonding states being empty [102]. Although the heat of formation is very negative for these alloys it is worth mentioning that they are still (as most other Pt bimetallic alloys) thermodynamically unstable under the reaction conditions of a cathode in a PEMFC. For Pt_3Y for instance, the alloying energy stabilises each Y atom by 4 eV, however, the standard reduction potential for Y to Y^{3+} is -2.372 V per electron vs. the normal hydrogen electrode (NHE) [13]. Considering an operating potential of 1 V there will be a driving force for the dissolution of each Y atom given by: 3 electrons · (1-(-2.4))V - 4 eV = 6.2 eV. Nonetheless, the high heat of formation of these alloys is expected to significantly increase the barrier for diffusion of solute atoms to the surface with respect to alloys of Pt with late transition metals, such as Pt_xNi, Pt_xCo or Pt_xCu.

4.2 Measured ORR activity of Pt_3Sc and Pt_3Y

Bulk polycrystalline samples of Pt_3Y and Pt_3Sc were supplied by Mateck GmbH, Germany. The samples are 5 mm in diameter (0.196 cm^2 geometric surface area) and 3 mm thick. The bulk composition of each electrode was verified using X-Ray Diffraction (XRD). Figure 4.2 shows the XRD measurements of Pt, Pt_3Y and Pt_3Sc. All electrodes are seen to be composed of face centered cubic (fcc) unit cells. The lattice parameters of Pt, Pt_3Y and Pt_3Sc were determined to be 3.9237 Å, 4.074 Å and 3.9593 Å respectively. These data are in close agreement (±0.005 Å) with

crystallographic data from the literature [103, 104]. Relative to Pt, this corresponds to a lateral tensile strain in the closely packed plane of 3.8 % for Pt_3Y and 0.9 % for Pt_3Sc.

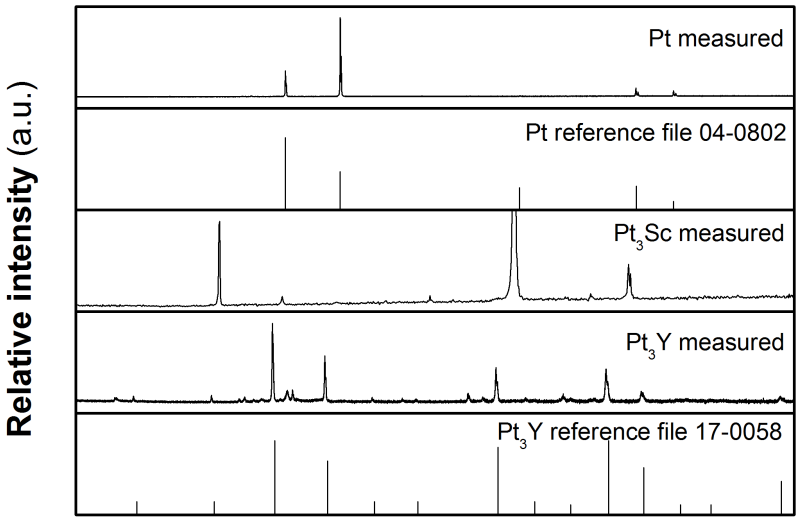

Figure 4.2: X-ray diffraction measurements of Pt, Pt_3Y and Pt_3Sc, yielding lattice parameters of 3.9237 Å, 4.074 Å and 3.9593 Å, respectively. Relative to Pt, this corresponds to a lateral tensile strain in the closely packed plane of 3.8 % for Pt_3Y and 0.9 % for Pt_3Sc. Measurements performed by Ifan E.L. Stephens.

Samples of Pt_3Y and Pt_3Sc were mounted in an UHV chamber (different from the one described in section 2.1). They were sputter cleaned and the surface region composition was analysed by Auger Electron Spectroscopy (AES), which gave surface region compositions of ∼70 % Pt and ∼30 % Sc for Pt_3Sc and ∼80 % Pt, ∼20 % Y for Pt_3Y. The samples were then moved to an argon flushed fast entry lock where they were covered with a droplet of H_2 saturated millipore water before being transported to the electrochemical cell.

The ORR activity is measured in a rotating disk electrode assembly as described in section 2.2. Figure 4.3 shows cyclic voltammograms of the Pt_3Y and Pt_3Sc samples in an O_2-saturated solution. The onset potential for the ORR is seen to be at around 1.0 V for all three samples. The current is then seen to increase exponentially which is characteristic of kinetic control. The potential range most interesting for fuel cell applications is 0.7 V $\leq U \leq$ 0.95 V. In this range the current approaches the mixed regime, where mass transport plays an increasingly important role. For lower potentials the current reaches its diffusion limited value, $\sim$ 5.8 mA cm^{-2}.

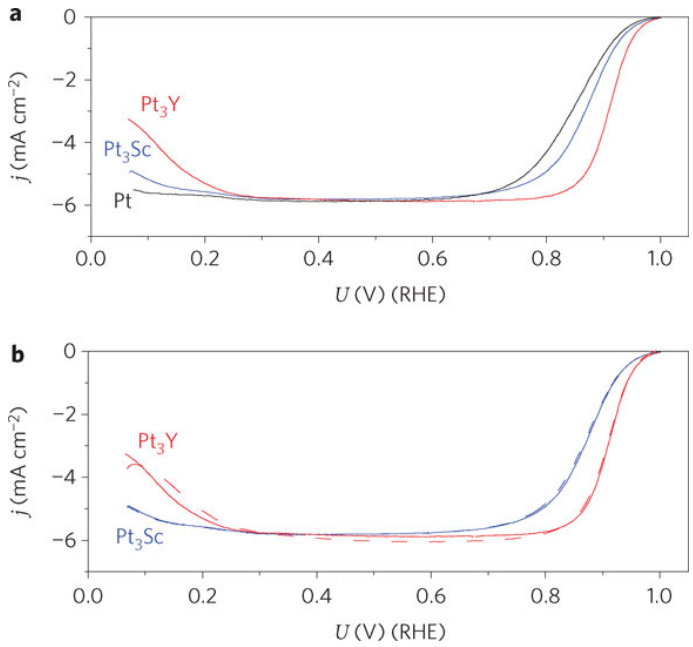

Figure 4.3: Cyclic voltammograms (anodic sweep) of Pt, Pt_3Sc and Pt_3Y in O_2-saturated electrolyte. **a** The first stable sweep. **b** Comparing the first steady cycle (solid lines) and after 90 minutes of cycling (dashed lines). Measurements were taken at 20 mV/s and 1600 rpm in 0.1M $HClO_4$ at $23 \pm 2°C$. Figure reprinted from [16].

The ORR activity of different catalysts can be compared by evaluating the half wave potential, $U_{1/2}$, which is the potential at which the current reaches half its diffusion limited value. The measured activity for polycrystalline platinum shown in Figure 4.3 is in good agreement with litterature [47]. For the Pt_3Sc sample the half wave potential is shifted $\sim$ 20 mV in the positive direction and for the Pt_3Y sample the observed shift is $\sim$ 60 mV also in the positive direction. This confirms the prediction from the screening study that these alloys should have an increased activity compared to platinum. As mentioned earlier the screening study also predicted that theses alloys should have an increased stability compared to Pt_3M alloys (M=Ni, Co, Fe). Figure 4.3b shows the ORR activity of the first steady cycle compared to that after 90 minutes of cycling between 1.0 V and 0.07 V. It is seen that the alloy electrodes are stable under the 90 minutes continued cycling. The rotation of the electrode enhances not only the transport of O_2 but also of contaminents to the surface. Over longer periods of time possible contamination of the electrode by remote amounts of contaminants present in the electrolyte may occur and it is therefore

not possible to investigate the long-term stability in a RDE setup [8]. In order to investigate the long-term stability measurements in membrane electrode assemblies in a fuel cell need to be performed [105, 106].

Figure 4.4a shows the tafel plot of the measured current density corrected for mass transport using eq. (2.13) in order to obtain the true kinetic current density, j_k, of the catalyst, as a function of the potential. The activity is seen to increase in the order Pt < Pt_3Sc < Pt_3Y, which is the same trend as was seen when considering the shift in half wave potential. The tafel slope for Pt and Pt_3Sc are seen to be quite similar whereas Pt_3Y shows an increased tafel slope.

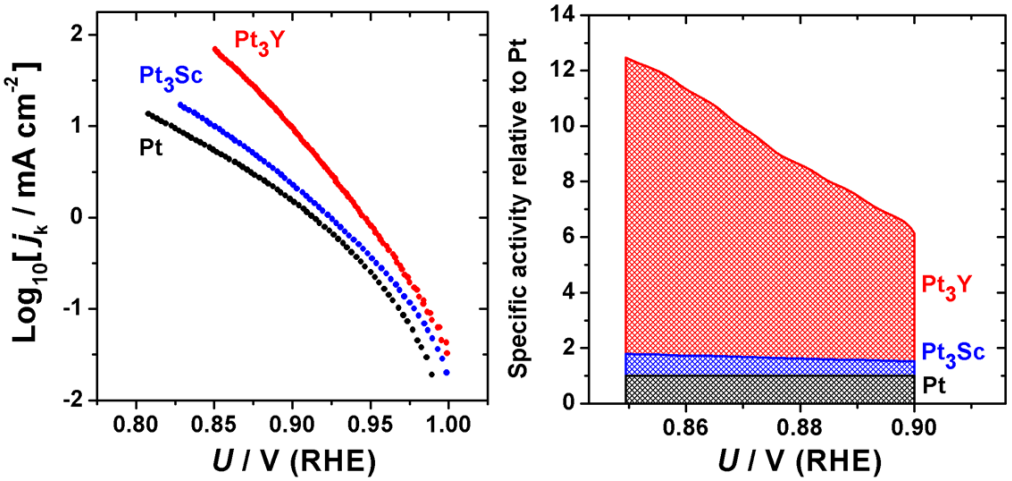

Figure 4.4: a) Tafel plot of showing the ORR activity of Pt, Pt_3Sc and Pt_3Y. b) The ORR activity relative to polycrystalline Pt. Both figures adapted from [16].

On Figure 4.4b the kinetic currents are normalised to those of polycrystalline platinum and plotted as a function of potential. At 0.9 V, Pt_3Sc shows an increase by 50 % in specific activity over Pt, and Pt_3Y shows an increase by a factor of six over Pt. At lower potentials the increase in activity is even higher, due to the increased tafel slope. At 0.87 V, Pt_3Sc shows an activity increase of 80 % over Pt and for Pt_3Y the activity is enhanced by an order of magnitude.

Figure 4.5 shows the volcano plot from Figure 1.8 revisited with added data points for Pt_3Sc and Pt_3Y. As far as known the ORR activity of Pt_3Y is the the highest measured to date under these conditions for any bulk, polycrystalline metallic surface. Only single-crystal $Pt_3Ni(111)$ has a higher activity [26].

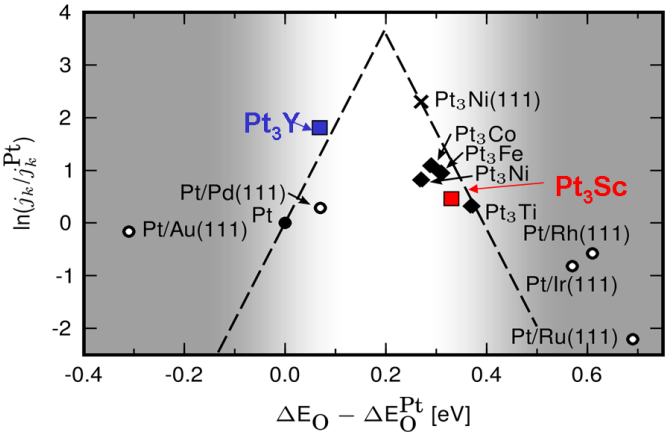

Figure 4.5: Revisited volcano curve for the ORR. This time including the sputtered polycrystalline samples of Pt_3Sc and Pt_3Y. For references to the other data points see Figure 1.8. Figure adapted from [16].

4.3 Other alloys of Pt with early transition metals

Since the original screening study, polycrystalline samples of platinum alloyed with early transition metals have been investigated further at CINF, DTU. Firstly the different stable phases of Pt-Y were considered. The Pt rich stable phases are Pt_5Y, Pt_2Y and PtY (Figure A.1 in the appendix shows the phase diagram of Pt-Y). Bulk polycrystalline samples of these alloys were tested by Stephens et al. [107] using the same experimental procedure as for Pt_3Y and Pt_3Sc. The PtY and Pt_2Y samples were seen to corode upon immersion into the electolyte. For Pt_5Y, however, no sign of corrosion was seen and the measured activity was close to that of Pt_3Y.
For Pt-Sc the only stable phases are seen to be Pt_3Sc, PtSc and $PtSc_2$ (Figure A.2 in the appendix shows the phase diagram of Pt-Sc). Due to the high corrosion observed for Pt_2Y and PtY the Sc rich phases were not pursued further.
Considering the transition metals in the periodic table the elements close to Sc and Y are: Ti, Zr, Hf and La. Pt_3Ti has been reported in [27] to have a slight improvement in ORR activity over Pt. Figure 4.6 ranks the activity of different polycrystalline alloys of Pt and the early transition metals at U=0.9 V. For Pt_3Zr no enhancement in ORR activity was seen and for Pt_3Hf only a small enhancement was seen. XPS analysis showed that the low activity could be related to the formation of subsurface hydroxide or oxide phases and that part of the surface is blocked by these oxide

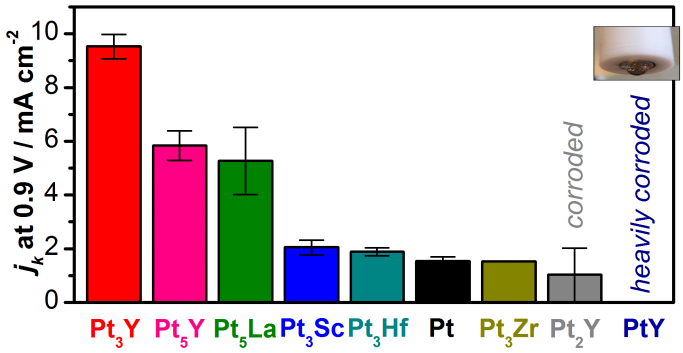

Figure 4.6: Overall ranking of ORR activity for sputter-cleaned polycrystalline alloys of Pt and early transition metals, obtained by measuring the kinetic current density j_k at 0.9 V. The measurements are taken from the anodic sweep of a cyclic voltammogram in O_2-saturated 0.1 M $HClO_4$ at 23 °C and 1600 RPM (same conditions as Figure 4.3). Measurements made by Ifan E.L. Stephens and Alexander S. Bondarenko. Figure reprinted from [108].

compounds [107]. For Pt_5La, however, the activity was only slightly lower than for Pt_5Y [108, 109].

Figure 4.7 shows the ARXPS depth profile of Pt_5Y and Pt_5La after ORR activity measurements. For both samples an initial layer of adventitious contamination is seen followed by a 10-15 Å thick Pt overlayer with a negligible amount of Y and La on the surface. A similar result was also obtained for Pt_3Y.

A relevant question is whether or not Pt-Y catalysts in nanoparticulate form will show a similar increase in ORR activity. Recently mass selected Pt-Y nanoparticles have been produced using a gas aggregation source (described in detail in [98–100]). The measured ORR activity of the produced Pt-Y nanoparticles was seen to be on the order of 2-5 times higher than that for Pt nanoparticles of the same size [110].

4.4 Discussion and conclusion

In the DFT screening study the active site of Pt_3Y was assumed to be the Pt overlayer site having yttrium as a neighbour in the second layer. However, the observed thick Pt overlayer after ORR measurements indicates that the increase in ORR activity cannot be related to the presence of the solute metal in the second layer. The

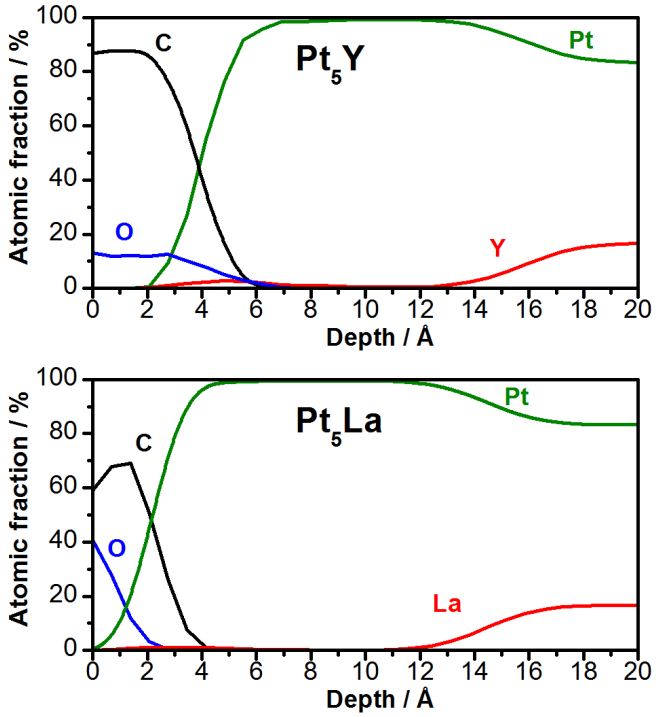

Figure 4.7: ARXPS depth profiles of Pt_5Y and Pt_5La. Measurements made by Lone Bech, Ifan E.L. Stephens and Alexander S. Bondarenko. Figure adapted from [107, 108].

active site is therefore not well understood, motivating the further study of these alloys in the following chapters. The descrepancy in the active site will be further adressed at the end of Chapter 6.

In summary, a DFT screening study identified Pt_3Sc and Pt_3Y as interesting ORR catalysts. The ORR activity of sputter cleaned bulk polycrystalline samples of Pt_3Sc and Pt_3Y was measured in a rotating disk electrode setup in an electrochemical cell. Compared to Pt they showed an increase in ORR activity by a factor of 1.5–1.8 and 6–10, respectively, in the range 0.9–0.87 V.

In parallel to the work described in this thesis, the ORR activity of other Pt bimetallic alloys was investigated. The activity was seen to increase in the order:

$Pt < Pt_3Hf < Pt_3Sc \ll Pt_5La < Pt_5Y < Pt_3Y$.

Chapter 5

UHV studies of polycrystalline Pt alloys

In Chapter 4, clean sputtered polycrystalline samples of Pt_3Sc and Pt_3Y were seen to experience an improved ORR activity over pure platinum [16]. As discussed in the introduction, Markovic and coworkers demonstrated that clean sputtered Pt_3M (M=Ni, Co, Fe, Ti, V) are highly active catalysts for the ORR and vacuum annealing these alloys induces a so called Pt-skin structure which is even more active than the clean sputtered samples [14]. In order to gain more insight on the active site of Pt_3Y, Pt_5Y, Pt_3Sc and Pt_5La ORR catalysts the vacuum annealing of these alloys is investigated. The formation of a Pt overlayer is essential in this respect, since this is the active structure of the catalyst under the ORR conditions in a PEMFC. Is it possible to form Pt overlayers on these alloys by vacuum annealing? If so, will the Pt overlayer be stable after performing ORR measurements? These are some of the key questions addressed in this chapter.

5.1 Pt_3Y

5.1.1 UHV annealing

A polycrystalline sample of Pt_3Y is mounted in the UHV chamber and cleaned by performing sputtering and annealing cycles. Figure 5.1 shows the ISS spectrum

before and after annealing to 1273 K. The clean sputtered sample shows a peak at around 1015 eV corresponding to Y and another peak at around 1120 eV which corresponds to Pt. A small peak at around 500 eV corresponding to oxygen is also seen. After annealing, the spectrum is more or less the same suggesting that a Pt overlayer structure is not formed.

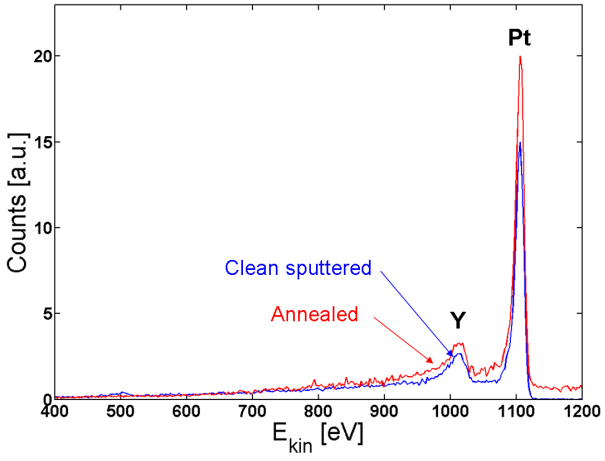

Figure 5.1: ISS spectrum of polycrystalline Pt_3Y before (blue) and after (red) annealing at T=1273 K. No Pt skin is formed.

Table 5.1 shows the concentrations obtained by XPS. After annealing the Pt:Y ratio is seen to be 3 indicating that the surface composition is the same as the bulk. The oxygen signal is seen to be around 14 % indicating that the yttrium is oxidised. Many cycles of sputtering at room temperature, annealing to 1273 K and sputtering

	Pt	Y	C	O	Pt:Y ratio
Pt_3Y clean sputtered	74	15	0	11	4.9
Pt_3Y annealed	64	21	1	14	3

Table 5.1: Concentration of the different elements as obtained by XPS.

at 1273 K were performed but still more or less the same amount of oxygen was seen. The heat of formation of yttrium oxide ($2Y + 1.5O_2 = Y_2O_3$) is ΔH = -1905kJ/mol or corresponding to a gain of 9.9 eV per yttrium atom whereas the Pt_3Y alloy "only" stabilises each yttrium atom by 4 eV [111]. Considering the high affinity of yttrium for oxygen, the more or less constant amount of oxygen seen by XPS could

be a consequence of yttrium oxide formation from some oxygen containing species present in the chamber background, despite the low pressure of $\sim 1 \cdot 10^{-10}$ torr in the UHV chamber.

Even though a Pt overlayer was not formed, the reactivity of the surface was tested by CO TPD. Figure 5.2 shows the CO TPD of the UHV annealed Pt_3Y sample. There is a pronounced initial CO desorption peak at low temperatures. For Pt(111) this peak was much smaller and ascribed to CO desorbing from the W wire holding the sample. In the case of Pt_3Y the peak is larger and it can not be excluded that some of it is due to desorbed CO from the sample itself. One should, however, be careful about analysing features right at the beginning of the TPD, due to the initial temperature ramp not being well defined. The first CO TPD of Pt_3Y (blue graph) shows mainly two features, one intense and narrow peak at around 345 K and another broader peak at around 440 K. In the second CO TPD (red graph), the peak at around 440 K is very reduced. This shows that the first TPD changes the surface, maybe due to CO dissociation induced by Y present at the surface.

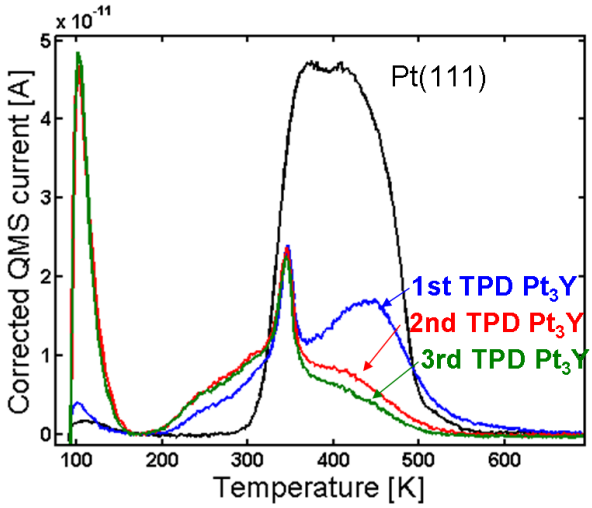

Figure 5.2: CO TPD's of Pt_3Y after annealing to T=1233K (both Pt and Y present in the surface).

5.1.2 Producing a Pt overlayer on polycrystalline Pt_3Y

It was seen that vacuum annealing of the polycrystalline Pt_3Y sample did not result in the formation of a Pt overlayer. Since the formation of a Pt overlayer is essential in order to study the same surface under UHV as in electrochemistry various attempts were made to produce a Pt overlayer on the Pt_3Y sample.

5.1.2.1 Pt overlayer by annealing in 2 mbar CO

Annealing in high pressures of CO was discussed in the introduction (section 1.4) to cause surface segregation in order for CO to be bound as strong as possible. For Pt-Co nanoparticles this was seen to induce surface segregation of Pt [48]. The first method tried was therefore to anneal the sample in 2 mbar CO in order to see if this could pull Pt to the surface. CO was dosed at 2 mbar both at room temperature and while heating to 673K. In both cases both Y and Pt were seen in ISS after the high pressure CO exposure, meaning that no Pt overlayer formation was seen.

5.1.2.2 Pt overlayer by electrolyte exposure

As discussed in Section 1.3 a Pt skeleton structure is formed when immersing the Pt_3Y sample in perchloric acid. The idea described in this section is to initially produce a Pt skeleton surface by exposure to perchloric acid, then remove possible contaminents from the surface and finally slightly anneal the surface to form a smooth Pt overlayer. Markovic and coworkers recently used this approach to produce smooth thick Pt overlayers on Pt-Ni nanoparticles [112].
The annealed sample was isolated in the HPC. The HPC was removed and the surface of the sample was rinsed first with a droplet of 0.1 M $HClO_4$ and then with millipore water. The sample was dried and the HPC was mounted and baked. XPS and ISS spectra of the sample were taken. The ISS spectum showed only a low energy peak corresponding to dirt on the surface. The XPS spectrum showed considerable amounts of carbon and oxygen. The sample was exposed to 10 mbar of hydrogen for 10 min at T=373-673 K. After each exposure, an XPS spectrum was made and still carbon and oxygen was seen. Continuous ISS spectra using helium were taken for 2 hours in order to mildly sputter the contaminents on the surface

of the sample without sputtering the Pt. When Pt was seen in the ISS spectrum the mild sputtering was stopped and an XPS spectrum was made still showing large amounts of carbon and oxygen. Another exposure to 10 mbar hydrogen at T=673 K was made and afterwards XPS and continuous ISS was made again. After sputtering mildly for some time small peaks of both yttrium and platinum appear in ISS. Cleaning the sample after exposure to electrolyte without affecting the sample itself was therefore not possible.

5.1.2.3 Pt overlayer by Pt evaporation

Another way of making a Pt overlayer structure could be by Pt evaporation. A Pt evaporator was constructed by clamping small pieces of 0.5 mm diameter Pt 99.99% purity wire around a 0.38 mm diameter W 99.95% purity wire. The tungsten wire, however, burned over before any Pt evaporation is observed. Two new Pt evaporators were constructed, one was simply a 0.5 mm diameter Pt wire shaped like a coil and the other was constructed by tightly winding a 0.1 mm diameter Pt wire around a 0.25 mm tungsten thread (inspired by [113]).
The potential over the evaporator ("Pt on W") was slowly increased until the W wire was seen to light up. The calibration procedure hereafter was to clean the sample, place it in front of the evaporator for 10 min (sample kept at around 320 K) and thereafter check with ISS how much Pt was evaporated. When U=7.6 V and I=5.5 A the ISS spectrum showed an increase in the Pt signal and a decrease in the Y signal, indicating that Pt had been deposited.
Calibrating the evaporation rate of the Pt evaporator by making ISS before and after deposition proved to be a very difficult task. The main reason being that the evaporator was seen to be unstable and not giving the same evaporation rate when using the same settings.
At one point, approximately a monolayer was estimated by ISS to have been evaporated (no yttrium signal seen in the last ISS spectrum). To investigate the stability of the deposited Pt overlayer ISS was done at every 50 K while heating the sample. Apart from the O signal disappearing at around 520 K, corresponding to CO desorbing from the surface, no change was seen until 670 K. At 720 K a small Y signal was seen and at 770K a larger Y signal was seen. This shows that the Pt overlayer is stable until around 700-750 K.

At another instance the evaporator suddenly changed its resistance resulting in a much higher evaporation rate. Figure 5.3 shows the ISS spectrum before (black graph) and after (blue graph) Pt deposition. Only Pt and O (most likely from CO on the surface) is seen in the spectrum after Pt deposition.

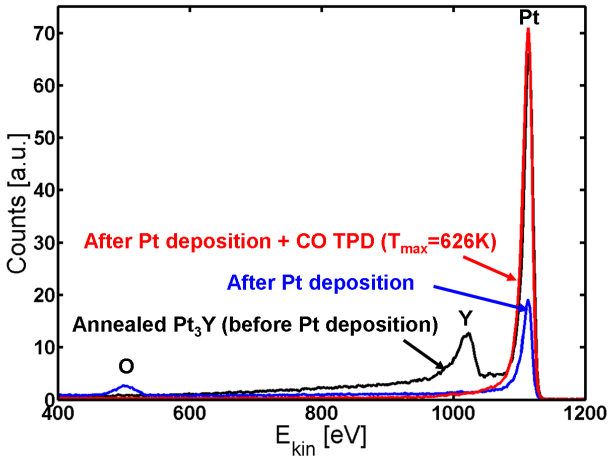

Figure 5.3: ISS of Pt_3Y after "a lot" of Pt had been deposited (blue graph). The red graph shows the ISS spectrum after a CO TPD and the black graph before Pt deposition.

The blue and red graphs in Figure 5.4 are the 1st and 2nd CO TPD of the sample after Pt deposition. The end temperature of the first CO TPD was 626 K whereas the end temperature of the second was 775 K. The first TPD only has a feature at around 500 K, whereas for the second TPD a feature at around 390 K also appears. After the first TPD the ISS spectrum shown in the red graph in Figure 5.3 was obtained. The O signal (probably from CO) that was seen after Pt deposition has gone and only a peak corresponding to Pt is left. Following the second TPD, an XPS spectrum was obtained showing only Pt and small amounts of carbon. No yttrium was seen, meaning that a very thick Pt overlayer had been formed. The sample was then annealed to 1273 K and the CO TPD in green was obtained. It is quite similar to that of annealed Pt_3Y seen in Figure 5.2, however, without the intense peak 345 K. XPS and ISS are also made (data not shown here). Both ISS and XPS shows the same spectra as obtained for the annealed Pt_3Y, showing that the annealing the sample at 1273 K has brought yttrium back to the surface again. Further Pt deposition experiments were performed, however, even though Pt eva-

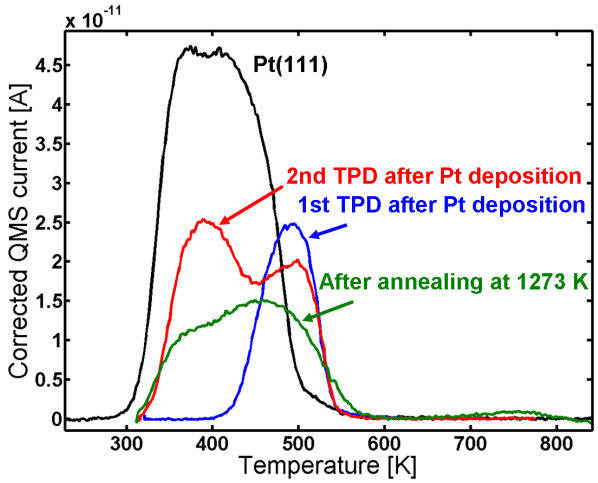

Figure 5.4: CO TPD's of the Pt_3Y sample after deposition of a thick Pt overlayer. Note that all TPD's were started from around 313 K.

poration was observed (by ISS after deposition) it was not possible to produce a full overlayer of Pt. From the Pt-Y phase diagram (see Figure A.1 in the appendix) it is seen that there is a stable more Pt rich Pt-Y phase present, namely Pt_5Y. It was therefore thought that the increase in Pt signal, but still lack of complete overlayer formation could be due to the formation of Pt_5Y.

5.2 Pt_5Y

In section 4.3 it was mentioned that Stephens et al. [107] recently found that polycrystalline Pt_5Y is almost as active as polycrystalline Pt_3Y. Since Pt_5Y is the most Pt rich Pt-Y phase which is still stable, it is thought that it might form a Pt overlayer either by UHV annealing or Pt deposition. This is investigated in the following.

Figure 5.5 shows the ISS spectrum of the sputter cleaned (blue graph) and annealed (red graph) polycrystalline Pt_5Y sample. After sputtering the spectrum shows only peaks corresponding to Y and Pt indicating a clean surface. After annealing both peaks are still present showing that a Pt overlayer is not formed upon annealing to 1273 K.

Figure 5.6 shows the CO TPD of the annealed polycrystalline Pt_5Y sample (with Y

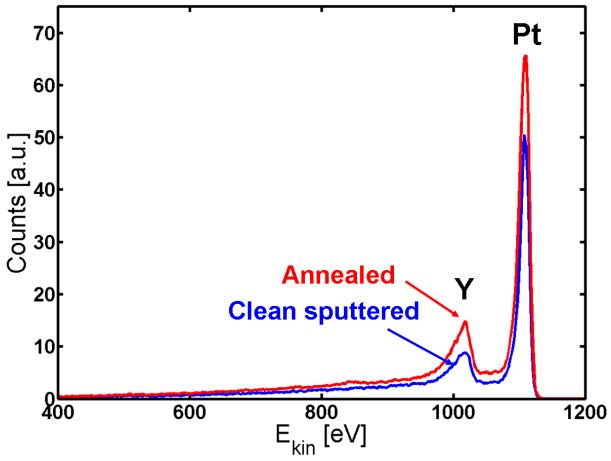

Figure 5.5: ISS spectrum of Pt_5Y after clean sputtering (blue graph) and after annealing to 1273 K (red graph). No Pt skin formed.

in the surface) compared to Pt(111). The CO TPD of UHV annealed Pt_5Y is seen to be very similar to that of UHV annealed Pt_3Y. They both show distinct peaks at around 345 K and a second peak at around 440 K. In the case of Pt_5Y the CO TPD is furthermore seen to be reproducible.

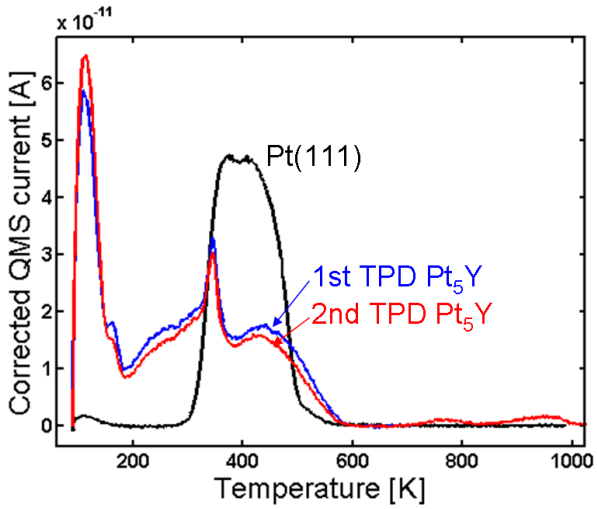

Figure 5.6: CO TPD of Pt_5Y after annealing to 1273 K. The first TPD is shown in blue and the repeated in red. CO TPD of Pt(111) is shown in black.

Pt deposition was also tried for Pt_5Y. It was, however, not possible (due to different

problems with the Pt evaporators) to produce a Pt overlayer structure on Pt_5Y.

5.3 Pt_5La

In Figure 4.6 it was shown that clean sputtered polycrystalline Pt_5La shows an increase in ORR activity on the same order as for Pt_5Y. A sample of Pt_5La was mounted in the UHV chamber in order to investigate if vacuum annealing induces a Pt overlayer. Figure 5.7 shows the ISS spectrum before and after annealing.

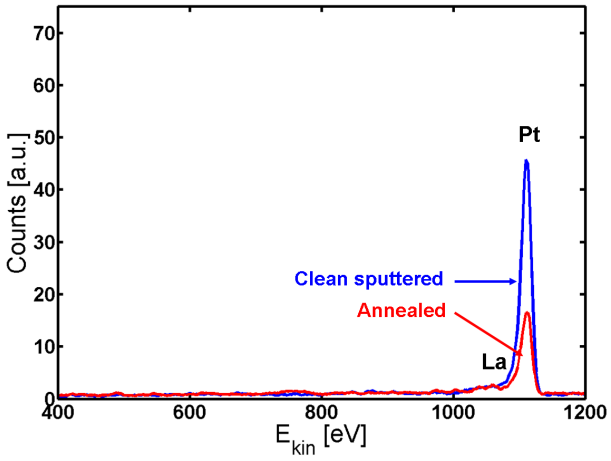

Figure 5.7: ISS spectrum of Pt_5La before and after annealing at T=1173 K. It is challenging to separate the Pt and La peaks.

A clear peak is seen at around 1120 eV which corresponds to Pt. From eq. (2.8) we have that La should appear at around 1090 eV. Looking closely at the ISS spectrum in Figure 5.7 it is possible to see a small peak in this range, however, it is difficult to separate it from the Pt peak at 1120 eV. This problem is illustrated in Figure 2.5 where it is seen that using He^+ as probe ions results in a very small difference in the kinetic energy of the scattered ion from La and Pt. It is also seen from Figure 2.5 that using Ar^+ ions as probe will increase the seperation of the La and Pt peaks, however, this will also increase the sputter damage.
Figure 5.8 shows the ISS spectrum obtained using Ar^+ ions to probe the surface of Pt_5La before and after annealing at 1173 K.
For the clean sputtered sample (blue graph) two peaks are seen, one at around

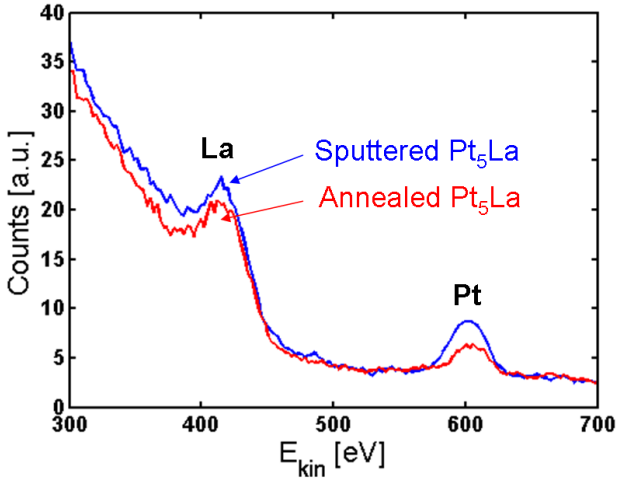

Figure 5.8: ISS spectrum of Pt_5La using Ar^+ ions. Peaks corresponding to Pt and La are seen both before (blue graph) and after (red graph) annealing at T=1173 K.

600 eV corresponding to Pt and one at around 420 eV corresponding to La. After annealing (red graph) both peaks are still seen in the ISS spectrum. This could mean that the Pt overlayer is not formed upon vacuum annealing of Pt_5La. However, due to the high sputter damage of the surface when using Ar^+ ions the fact that both La and Pt are seen could also be due to the Pt overlayer being sputtered away. In order to adress this a Ne gas bottle was ordered and mounted on the ion gun. However, due to time limitations it was not possible to perform these measurements within the framework of this thesis.

The blue graph in Figure 5.9 shows the CO TPD of the annealed Pt_5La sample. It is seen that CO is bound very weak on the surface. A significant lower binding of CO was also found by Raaen and coworkers [73] for the annealed La/Pt(111) system (see introduction). It should, however, be remembered that it is difficult to interpret the features right at the beginning of the TPD, due to the initial temperature ramp not being well defined and possible contribution from CO on the W wire from which the crystal is held. The red graph in Figure 5.9 shows the repeated CO TPD, which is seen to be nearly identical to the first.

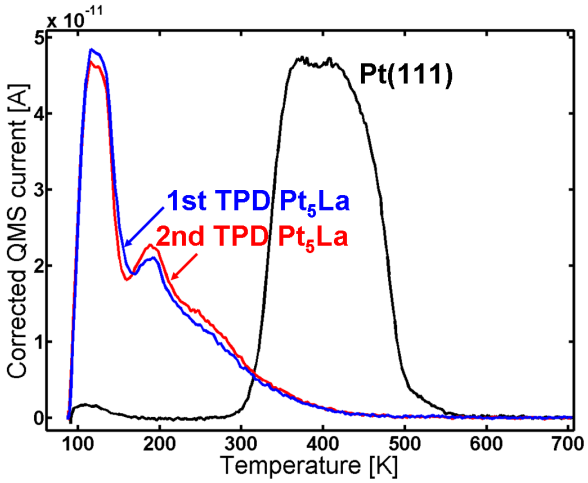

Figure 5.9: CO TPD of Pt_5La after annealing at T=1173 K (1st TPD: blue graph, 2nd TPD: red graph) compared to Pt(111) (black graph).

5.4 Pt_3Sc

A polycrystalline sample of Pt_3Sc is mounted in the UHV chamber and cleaned by performing sputtering and annealing cycles. Figure 5.10 shows the ISS spectrum before and after annealing. Before annealing two peaks are seen in the ISS spectrum, one at around 900 eV which corresponds to Sc and one at around 1120 eV which corresponds to Pt. No other peaks are seen indicating a clean surface containing only Pt and Sc. After annealing the Sc peak at around 900 eV disappears and only the Pt peak is seen. This suggests the formation of a Pt overlayer upon annealing, in line with the results of Markovic and coworkers for Pt_3M (M=Ni, Co, Fe, Ti, V) polycrystalline samples [14]. Table 5.2 shows the concentration of different elements from XPS before and after annealing. After annealing the carbon content on the surface is seen to slightly increase. Many sputtering and annealing cycles were made in order to try and remove the carbon, but without success. The Pt:Sc ratio is seen to be 6.3. A bulk terminated sample of Pt_3Sc should naturally have a Pt:Sc ratio of 3. For the sputtered sample there could be some minor deviation from this value due to preferential sputtering of one of the elements, but not enough to explain the ratio seen by XPS.

The Pt-Sc phase diagram (see Figure A.2 in the appendix) shows that the most Pt rich Pt-Sc phase which is stable is Pt_3Sc. The XRD measurements shown in Figure

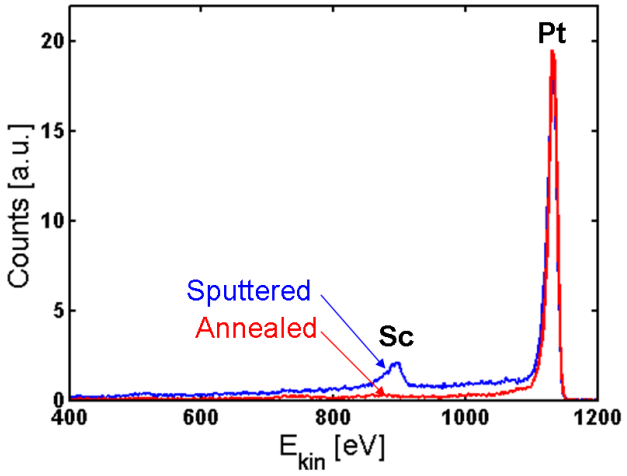

Figure 5.10: ISS spectrum of polycrystalline Pt_3Sc before and after annealing to T=1273 K. A Pt skin is seen to form upon annealing in UHV.

	Pt	Sc	C	O	Pt:Sc ratio
Pt_3Sc clean sputtered	83	13	2	2	6.3
Pt_3Sc annealed	81	13	5	1	6.2

Table 5.2: Concentration of the different elements in the polycrystalline Pt_3Sc sample before and after vacuum annealing as obtained by XPS.

4.2 gives that the bulk of the sample is Pt_3Sc. It is therefore peculiar that the XPS gives a Pt:Sc ratio of around 6.

The reactivity of the Pt overlayer is now probed by CO TPD. The blue graph in Figure 5.11 shows the CO TPD of the annealed Pt_3Sc. The red graph in Figure 5.11 is the repeated CO TPD. The repeated CO TPD is seen to be the same as the first except for the small peak at around 740K which only appears in the first TPD. The black graph in Figure 5.11 is the CO TPD for Pt(111). It is seen that CO is bound weaker than on Pt(111). The amount of CO desorbed from the Pt_3Sc surface (the area under the peak) is 0.56 compared to Pt(111). This difference could be due to a lower saturation coverage of CO on Pt_3Sc compared to Pt(111). It could, however, also be due to some of the sites on Pt_3Sc being blocked by carbon (see XPS data Table 5.2).

Before taking the sample out and measuring the oxygen reduction activity the stability in air is tested, by exposure to 200 mbar oxygen. Figure 5.12 shows the XPS

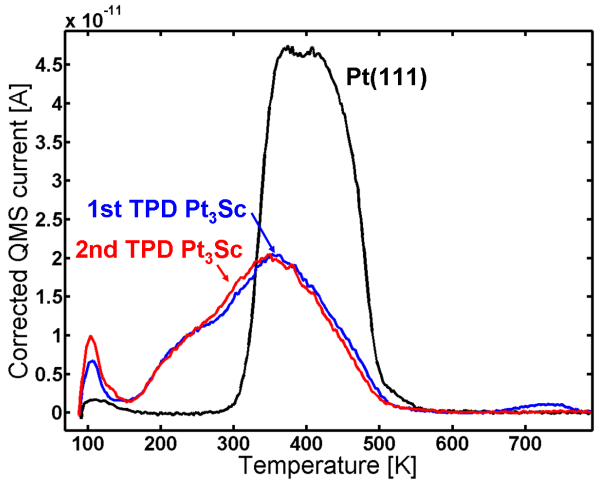

Figure 5.11: The first (blue graph) and second (red graph) CO TPD of Pt_3Sc after annealing at T=1273K. The CO TPD of Pt(111) (black graph) is shown for comparison.

signal from the Sc2p line of the annealed Pt_3Sc before (a) and after (b) exposure to 200 mbar O_2. Before exposure to 200 mbar O_2 the Sc2p peaks can be fitted well to metallic Sc. After exposure to 200 mbar O_2 an additional contribution, corresponding to Sc oxide, is needed to fit the data. By fitting the peaks it is estimated that 14 % of the Sc is in the oxidised state, indicating that the Pt overlayer is not completely hindering the Sc from oxidising.

In order to remove the adsorbed oxygen from the surface, the sample was now exposed to 2 mbar CO for 10 min at 304 K and a CO TPD was performed (not shown here). The CO TPD showed significantly higher binding of CO than the annealed Pt_3Sc, again indicating that the Sc had oxidised.

Having established that UHV annealing of Pt_3Sc to 1273 K gives a Pt overlayer structure the sample was sputtered, annealed and taken out for electrochemical testing. However, before the electrochemical testing, the sample is mounted in another UHV chamber equipped with angle resolved XPS (ARXPS). The purpose of this is to check the electrochemical stability of the sample by measuring the ARXPS depth profile before and after electrochemistry. Figure 5.13 shows the ARXPS depth profile before electrochemistry. Air exposure is seen to result in a layer of adventitious contamination (the carbon and oxygen) on the surface of the sample together with some Sc oxide. The observed formation of Sc oxide upon air exposure is in

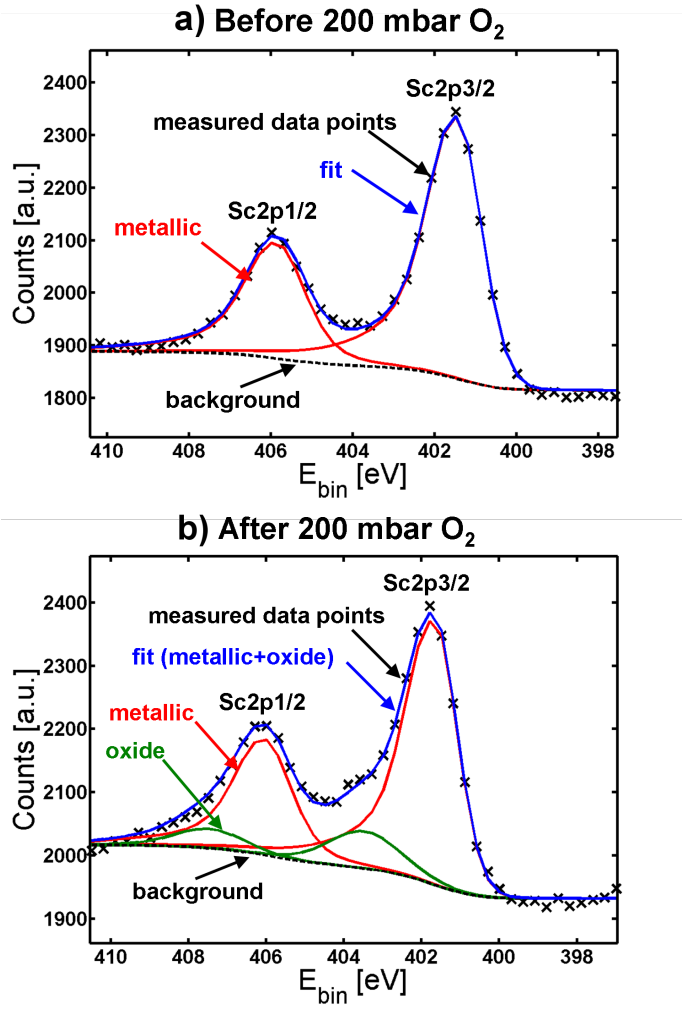

Figure 5.12: XPS spectra of the Sc2p peak of annealed Pt_3Sc (a) before and (b) after exposure to 200 mbar O_2. Fitting the recorded data to metallic (red) and oxidised (green) Sc gives 14 % Sc oxide after 200 mbar O_2. Before exposure to 200 mbar O_2 only metallic Sc was seen.

agreement with the 200 mbar O_2 exposure experiment shown in Figure 5.12) and suggest that the Pt overlayer is not completely stable in air. This is different to the stable Pt overlayers on UHV annealed Pt_3M (M=Ni, Co, Fe, Ti, V) observed by Stamenkovic et al. [14].

Below the Sc oxide follows a region of pure platinum and then the bulk Pt_3Sc structure. A restriction on the fit is that from 20 Å and deeper the Pt:Sc ratio is set to 3, corresponding to Pt_3Sc. Earlier it was, however, seen that both the sputter cleaned and the annealed Pt_3Sc had a Pt:Sc ratio of around 6 (see Table 5.2). This descrep-

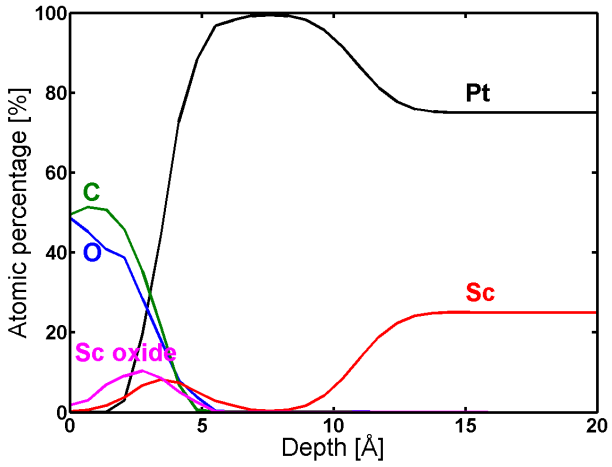

Figure 5.13: ARXPS depth profile of the UHV annealed Pt_3Sc after transferring it in air, but before electrochemistry. The air exposure is seen to produce a layer of adventitious contamination at the surface together with some Sc oxide. Below these a region of pure Pt and then the bulk Pt_3Sc ratio. Measurements performed by Paolo Malacrida.

ancy together with the general uncertainty in the fitting of the ARXPS depth profile means that the ARXPS depth profile should mainly be considered qualitatively. It is therefore also challenging to determine the exact thickness of the Pt overlayer.

5.4.1 Electrochemical measurements

The sample was then taken out and mounted in the rotating disk electrode setup for electrochemical testing. Figure 5.14 shows the oxygen reduction activity on a Tafel plot. The UHV annealed Pt_3Sc sample has a similar activity to that of clean sputtered Pt_3Sc. The Tafel slope, however, is seen to be somewhat different. In order to investigate the stability after electrochemical testing, the sample is again mounted in the ARXPS chamber.

Figure 5.15 shows the ARXPS depth profile after electrochemistry (solid lines) together with the ARXPS depth profile before electrochemistry (dashed lines). The main difference between the two spectra is that the Sc oxide which was at the surface before electrochemistry is not there anymore. This is expected since Sc in the surface is not expected to be stable in perchloric acid. There is also a slight difference

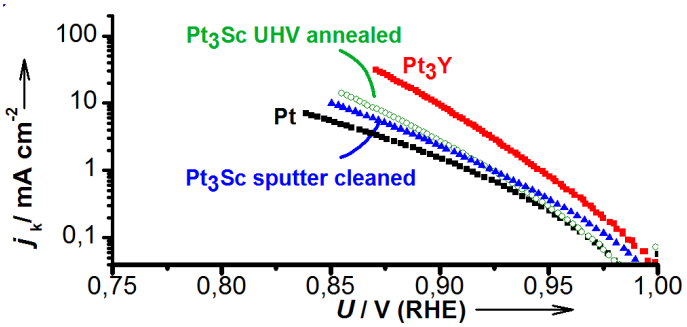

Figure 5.14: Tafel plot of the vacuum annealed polycrystalline Pt_3Sc sample compared with sputter cleaned polycrystalline samples of Pt_3Sc, Pt_3Y and Pt. The temperature was T=23 °C and the scan rate 20 mV/s. Measurements performed by Patricia Hernandez-Fernandez and Ifan Stephens.

in the size of the Pt overlayer, which could indicate that the overlayer is not completely stable. As mentioned before there are considerable uncertainties connected with the ARXPS profile and the results should therefore be considered qualitatively rather than quantitatively. It is therefore not possible to conclude whether or not the increased thickness of the Pt overlayer after electrochemistry is due to Sc oxide segregating to the surface making a thicker overlayer or the inaccuracy of the ARXPS depth profile.

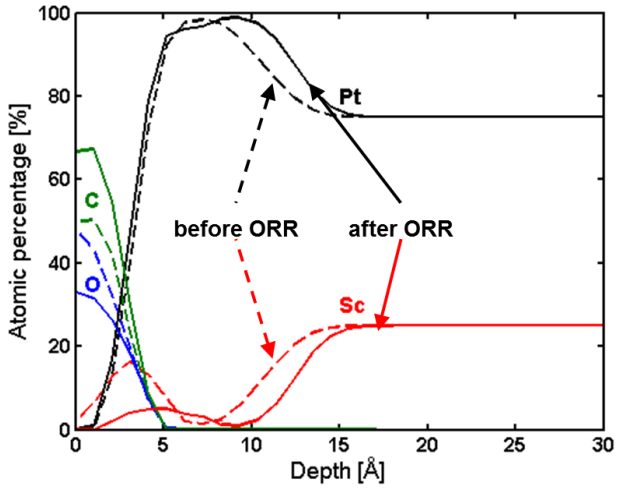

Figure 5.15: ARXPS depth profile of the UHV annealed Pt_3Sc before electrochemistry (dashed lines) and after electrochemistry (solid lines). Measurements performed by Paolo Malacrida.

5.5 Discussion and conclusion

In the previous section polycrystalline samples of Pt_3Sc, Pt_3Y, Pt_5Y and Pt_5La have been investigated in UHV. By annealing the samples in UHV a Pt overlayer was formed on Pt_3Sc, but not for either Pt_3Y, Pt_5Y or Pt_5La.
Table 5.3 shows the calculated energy required to move an X atom from the second layer to the surface layer of a Pt_3X alloy with a 1 ML thick Pt skin. The calculation is made for initial X concentrations of 50 % and 25 % in the second layer. If the energy is negative the Pt overlayer is not stable. It is seen that for Pt_3Ni the Pt overlayer is stable which is in agreement with experiments made by Stamenkovic et al. [26]. As mentioned in the introduction there are different reports on the termination of $Pt_3Ti(111)$ after vacuum annealing. The suggestion by Chen et al. [31] that Pt segregation is enhanced by a slight nonstoichiometry (Pt excess) in the bulk of the crystal is in agreement with the result for Pt_3Ti shown in Table 5.3 where the system with 50 % Ti in the second layer is seen to be unstable whereas the 25 % in the second layer is stable.

Concentration	Pt_3Y	Pt_3Sc	Pt_3Ni	Pt_3Ti
50%	-2.27	-1.24	0.36	-0.74
25%	0.41	0.90	0.75	1.16

Table 5.3: Energy in eV required to move 1 X atom from the sub surface layer to the surface layer of a Pt_3X alloy with a 1 ML thick Pt skin. Calculations were performed for both 50 % and 25 % initial X concentrations in the second layer. Calculations performed by Heine Hansen. Table adapted from [114].

From Table 5.3 it is seen that the system with 50 % concentration of the solute metal in the second layer is not stable for either Pt_3Sc or Pt_3Y, but the system with 25 % concentration of the solute metal in the second layer is. For Pt_3Sc this is in agreement with the experiment (Pt overlayer formed upon annealing in UHV) whereas for Pt_3Y the predicted stable Pt overlayer is not formed. It is, however, worth noting that the energy required for Y (in the 25 % case) to go to the surface is only 0.41 eV. A reason for surface segregation of Pt not occuring could be that in order for Pt to segregate to the surface a slight excess of Pt in the bulk is required, as was observed for $Pt_3Ti(111)$. When depositing a thick layer of Pt on top of Pt_3Y the formed overlayer was, however, still seen not to be stable when annealing to 1273 K.

The surface reactivity of the different polycrystalline alloys was tested in UHV by CO TPD. The main interest of these alloys is, however, for the oxygen reduction reaction, which has oxygen species as intermediates. A relevant question is therefore if it is possible to relate the binding energy of OC* to that of the oxygen species in the oxygen reduction reaction. When considering different metals their OC* and HO* binding energies do not scale [115]. For the Pt overlayers on top of Pt_3M alloys such a relation could, however, be possible.
Figure 5.16 shows the calculated OC*, HO* and HOO* binding energies on three different sites ("0", "1" and "2") of Pt overlayer structures on Pt_3Sc and Pt_3Y with subsurface solute metal concentrations of 25 % and 50 %.

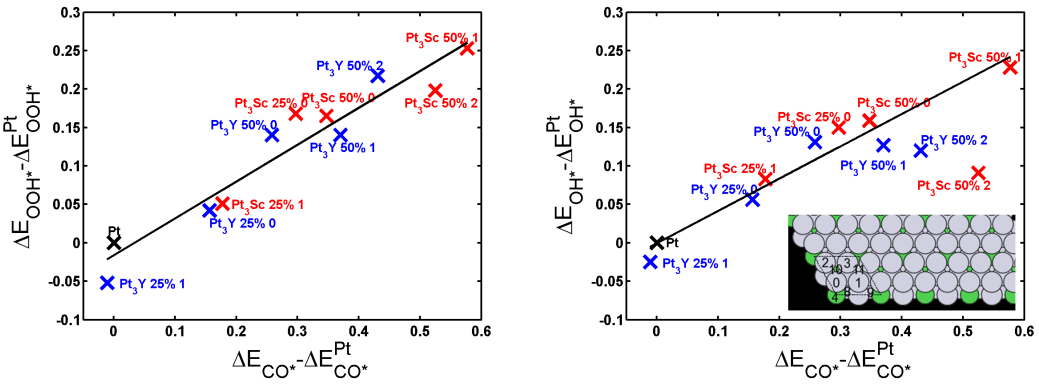

Figure 5.16: Calculated OC*, HO* and HOO* binding energies on various Pt overlayer structures. "Pt_3Y 50% 2" refers to a the site 2 on the inset figure for a Pt_3Y sample with 50 % Y in the second layer. Calculations made by Heine A. Hansen.

Although not perfectly linear a clear trend is seen that a surface which binds OC* weaker will also bind HO* and HOO* weaker. Two datapoints ("Pt_3Y 50% 2" and "Pt_3Sc 50% 2") on the HO* vs. OC* binding energy graph are outliers and it is noted that they are also outliers when comparing the HO* and HOO* binding energies which should scale linearly. A linear fit is made to the data (except the two outliers) giving the following relation:

$$\Delta E_{\text{bin, OH}} = (0.42 \pm 0.04) \cdot \Delta E_{\text{bin, CO}} \tag{5.1}$$

$$\Delta E_{\text{bin, OOH}} = (0.48 \pm 0.05) \cdot \Delta E_{\text{bin, CO}} \tag{5.2}$$

From the volcano plot in Figure 1.6 it is seen that the ideal ORR catalyst should bind oxygen around 0.2 eV weaker than Pt. From the scaling relations between O* and HO* this corresponds to binding HO* 0.1 eV weaker. From eq. 5.1 this is seen to correspond to a weaker binding of OC* by $\frac{0.1\text{eV}}{0.42} = 0.24\text{eV}$. Ruff et al. [116] have plotted the adsorption energy of CO as a function of the desorption temperature CO. They found that there is a linear relation between the two, which can be expressed as:

$$\Delta E_{\text{bin, CO}} \approx 0.0028\frac{\text{eV}}{\text{K}} \cdot \Delta T_{\text{des, CO}} \tag{5.3}$$

From eq. (5.3) we get that a weaker binding of OC* by 0.24 eV corresponds to a lowering in desorption temperature of CO by $\frac{0.24\text{eV}}{0.0028\frac{\text{eV}}{\text{K}}} = 85\text{K}$. There is clearly some uncertainty on this value, but the important point is that a Pt overlayer catalyst should bind CO weaker (on the order of 85 K) in order for it to have optimal bonding of the O species relevant for the oxygen reduction reaction.

For vacuum annealed polycrystalline Pt_3Sc a downshift in CO desorption temperature on the order of 50 K was found. According to the above mentioned relation between the CO desorption temperature and the HO* binding energy this should move Pt_3Sc closer to the top of the ORR volcano. This is in good agreement with the measured increase in ORR activity.

Vacuum annealed polycrystalline samples of both Pt_3Y and Pt_5Y show a distinct peak in the CO TPD corresponding to a CO desorption temperature in the range 50-100 K lower than Pt(111). This shift in the desorption temperature of CO fits well with the estimated shift of around 85 K for materials at the tip of the ORR volcano. It should, however, be emphasised that a Pt skin was not formed on these alloys upon vacuum annealing. Since the yttrium containing surface structure is different from the electrochemically active skeleton surface, it is not given that the observed CO TPD's can be correlated with the measured activity.

Ross and coworkers have also studied the CO TPD spectra of vacuum annealed Pt alloys [117]. The $Pt_3Co(111)$ single crystal formed a Pt overlayer upon UHV annealing [118], whereas $Pt_3Ti(111)$ [29] and $Pt_3Sn(111)$ [119] were found to be bulk terminated. For all three crystals a downshift in CO binding energy on the order of 50 K compared to Pt(111) was seen. This is similar to the shift observed for the UHV annealed polycrystalline samples of Pt_3Sc, Pt_3Y and Pt_5Y.

It is worth mentioning that the observed lower CO binding energy for vacuum an-

nealed Pt_3Sc also could make it interesting for the anode of the PEMFC. The reason for this is that the anode of a PEMFC (where HOR happens) is very sensitive to impurities of CO in the hydrogen feed [120, 121]. A catalysts which is active for the HOR and binds CO weaker than pure platinum will therefore experience less CO poisoning. This is e.g. the principle in the Pt-Ru catalyst for HOR [122].
In summary, polycrystalline alloys of Pt_3Sc, Pt_3Y, Pt_5Y and Pt_5La have been investigated under UHV. For Pt_3Y and Pt_5Y, annealing to 1273 K in UHV did not induce the formation of a Pt overlayer, whereas for Pt_3Sc it did. For Pt_5La it was not possible to determine whether or not a Pt overlayer was formed. The reactivity of the samples was tested by CO TPD, which for Pt_3Sc, Pt_3Y and Pt_5Y showed a downshift in desorption temperature of CO on the order of 50-100 K, whereas for Pt_5La the downshift was on the order of 200 K. The ARXPS depth profile showed the formation of some Sc oxide on the surface upon air exposure. After electrochemical measurements this had gone, but otherwise roughly the same depth profile was obtained. The ORR activity of the UHV annealed Pt_3Sc was comparable to that of sputter cleaned Pt_3Sc.

Chapter 6

Y deposition on Pt(111)

In the previous chapter, surface science studies of bulk polycrystalline alloys were presented. However, in order to learn more about the nature of the active site of the catalyst it would be very interesting to study single crystal surfaces. In Section 1.3 it was discussed that the active sites of the oxygen reduction reaction is believed to mainly be the (111) facet sides. Stamenkovic et al. [26] used a $Pt_3Ni(111)$ single crystal to gain insight into the nature of the earlier observed higher ORR activity of Pt_3Ni catalysts in comparison to Pt.
It was therefore thought to be very interesting to study a $Pt_3Y(111)$ crystal, which was ordered from Mateck in autumn 2009. However, Mateck failed in their attempts to synthesise this crystal. Consequently a different route was pursued, namely depositing Y on top of a Pt(111) single crystal. This procedure has been tried several times before for deposition of other metals on Pt. It was used for Cu on Pt(111) where deposition of Cu (either by evaporation in UHV or using electrochemical underpotential deposition) resulted in the formation of a Cu/Pt(111) near surface alloy [40, 51]. It was also used for preparing the Ni/Pt, Co/Pt, Ce/Pt(111), La/Pt(111) and Tm/Pt(111) systems discussed in the introduction [54, 55, 69–74].

6.1 Y monolayer deposition

Y, Sc and Pt evaporators were mounted on the chamber. The Y evaporator was made by cutting small pieces of Y from a 0.15 mm 99.9 % yttrium foil (supplied

by Goodfellow) and attaching them to a coil shaped 0.25 mm 99.95 % tungsten wire. Due to the difficulties observed earlier in calibrating the Pt evaporators using ISS and XPS a linear drive with a QCM is also mounted in the chamber, enabling deposition rates to be monitored before and after deposition on the sample. The QCM is positioned in the line of sight for both the Pt and the Y evaporator. Figure 6.1 shows a photograph of the evaporators and the QCM.

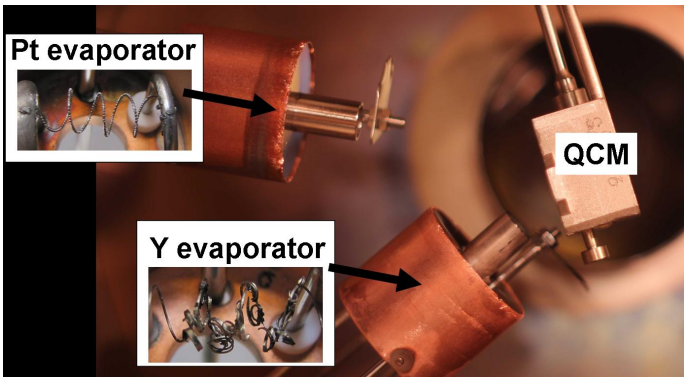

Figure 6.1: Photograph of the yttrium and platinum evaporators together with the QCM. The evaporation rate can be monitored before and after deposition by moving the QCM in front of the evaporator.

Initially small amounts of Y was deposited on the Pt(111) in order to investigate the possible formation of a Pt-Y near surface alloy. The Y evaporation rate was calibrated using a QCM and the rate was measured to be 1 Å per 75 sec. The Pt(111) crystal was sputter cleaned, annealed and then kept at 317 K while evaporating Y on to the crystal for 225 sec corresponding to an evaporated Y thickness of 3 Å. Figure 6.2 shows the ISS spectrum before and after Y evaporation. Both an Y peak and a Pt peak is seen in the ISS spectrum.
Table 6.1 shows the concentrations obtained from XPS. Some C and O is seen and the Y peak is not purely metallic.
The sample was then heated in UHV at a rate of 2 K/s in steps of 50 K and ISS was made for each 50 K. Figure 6.3 shows the Y to "Pt+Y" ratio plotted as a function of the temperature. It is seen that the Y to "Pt+Y" ratio exhibits a rapid decrease, corresponding to the formation of a Pt overlayer, at a temperature of around 800 K. The sample was annealed to a maximum temperature of 1173 K and then cooled to 673 K where detailed XPS spectra were obtained.
Table 6.1 shows that the Pt:Y ratio after annealing is around a factor of 2 larger

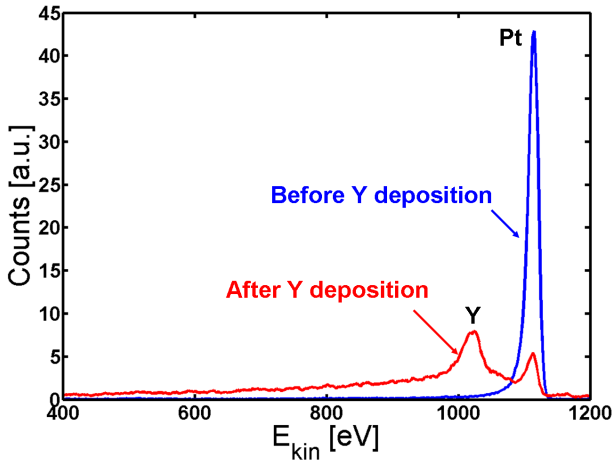

Figure 6.2: ISS spectrum of Pt(111) before (blue) and after (red) deposition of Y. According to the QCM around 3Å of Y is deposited.

	Pt	Y	C	O	Pt:Y ratio
After Y dep.	81	11	4	4	7
After Y dep. and annealing	92	6	1	1	15
After Y dep. annealing and CO TPD	91	8	0	1	11
After Y dep., annealing, CO TPD and O_2 TPD	76	10	0	14	7.6

Table 6.1: Concentration of the different elements as obtained by XPS performed on the 3 Å Y/Pt(111) crystal.

than before annealing. The C and O signals have basically disappeared (they were most probably due to CO which desorbed from the surface during heating of the sample) and the Y peak is seen to correspond to metallic yttrium. The sample was then placed in the LEED position and the LEED screen was moved in to the chamber. Due to an error it was, however, not possible to move the LEED screen completely in to its position in the chamber and the spectrum can therefore only be used qualitatively. Figure 6.4 shows the LEED image. A hexagonal structure similar to that of Pt(111) is seen together with superspots around each spot.
In order to saturate the surface of the sample with CO, the chamber is filled with $2 \cdot 10^{-7}$ torr CO for 45 min while cooling the sample down from 673 K to 90 K using liquid nitrogen. Figure 6.5 shows the CO TPD from this experiment (blue graph) compared with that of a clean Pt(111) (black graph). The CO TPD spectrum consists of three new low temperature peaks located at 275 K, 290 K and 315 K and a

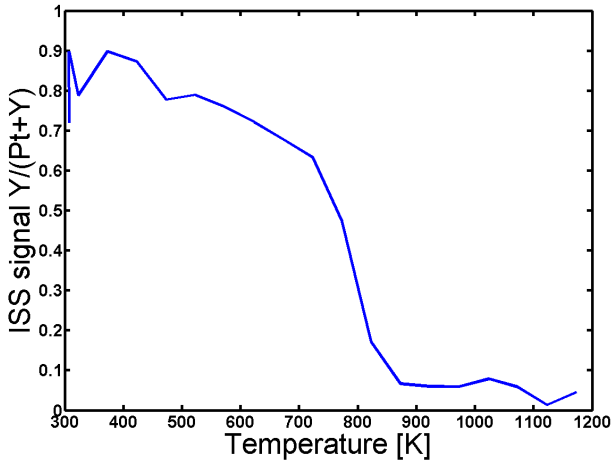

Figure 6.3: Y to "Pt+Y" ratio in the surface as a function of temperature. The ratio is obtained by integrating the Pt and Y peaks in ISS for every 50 K using a linear background. No sensitivity factors are used and the ratio should therefore only be considered qualitatively. The ratio decreases significantly at 800 K corresponding to the formation of a Pt overlayer.

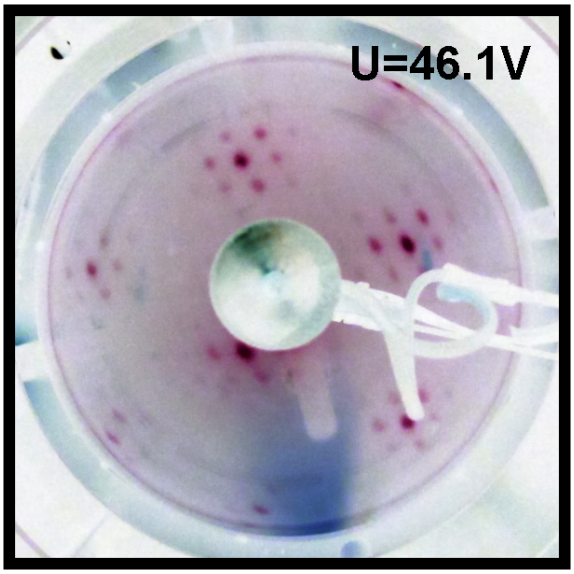

Figure 6.4: Photograph of the LEED pattern observed for ∼3 Å Y/Pt(111) annealed at 1173 K (colors have been inverted). Due to an error it was not possible to move the LEED screen completely in to the chamber. U=46.1 V and T=673 K.

fourth peak at around 400K which is similar in temperature to that of Pt(111). It is seen that most of the CO is bound weaker on this surface than on Pt(111). CO is

dosed again while cooling the sample from 700 K to 90 K. The red graph in Figure 6.5 shows the repeated CO TPD. It is slightly lower in intensity, but otherwise the CO TPD is seen to be reproducible. The total amount of desorbed CO from the Y/Pt(111) sample is ∼30 % greater than for Pt(111).

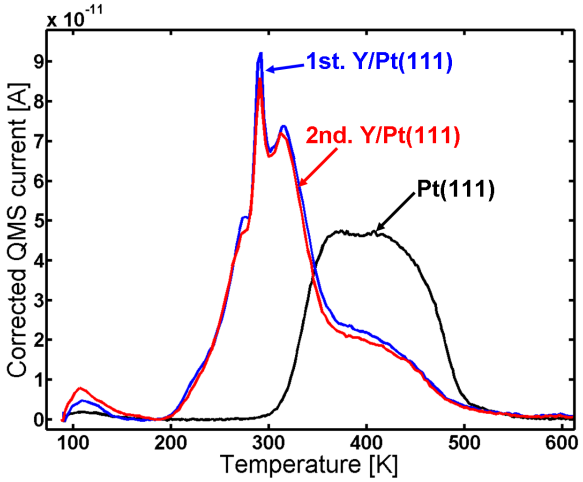

Figure 6.5: CO TPD of the 1173 K annealed Y/Pt(111). The first TPD (blue graph) and second TPD (red graph) compared to the annealed Pt(111) (black graph). Areas: 1st TPD compared to Pt(111): 1.34, 2nd TPD compared to Pt(111): 1.26.

Following the CO TPD measurement, XPS and ISS spectra were measured. The concentrations from XPS are shown in Table 6.1. A slightly higher Y signal is seen, but otherwise the XPS spectrum does not show any difference before and after the CO TPD. Figure 6.6 shows the ISS spectum after annealing to 1173 K (blue) and after CO TPD's (red). An intense Pt peak and a minor Y peak is seen suggesting that the overlayer is stable to the CO TPD.

The CO TPD provides information about the surface reactivity, and as was shown in Section 5.5 it can be related to the oxygen binding energy. A more direct measure of the oxygen binding energy would be to perform an O_2 TPD [123, 124]. The question is, however, if the combination of adsorbed oxygen and heating the sample will cause the formation of yttrium oxide. In order to investigate this an O_2 TPD was now made. Oxygen was dosed on the sample by background dosing at p=$2.0 \cdot 10^{-7}$ torr for 500 s, while cooling the crystal from 773 K to 312 K using pressurised air cooling. Figure 6.7 shows the O_2 TPD of the sample compared to that of Pt(111). It is seen that oxygen binds a bit stronger on the annealed Y/Pt(111) than on the

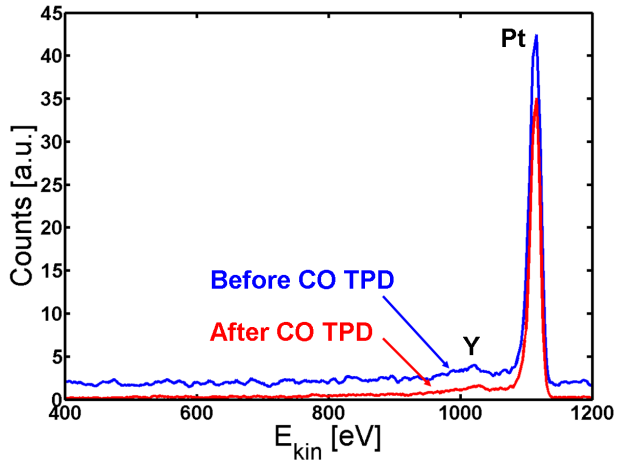

Figure 6.6: ISS spectrum after Y deposition and annealing to 1173 K (blue) and after CO TPD's (red).

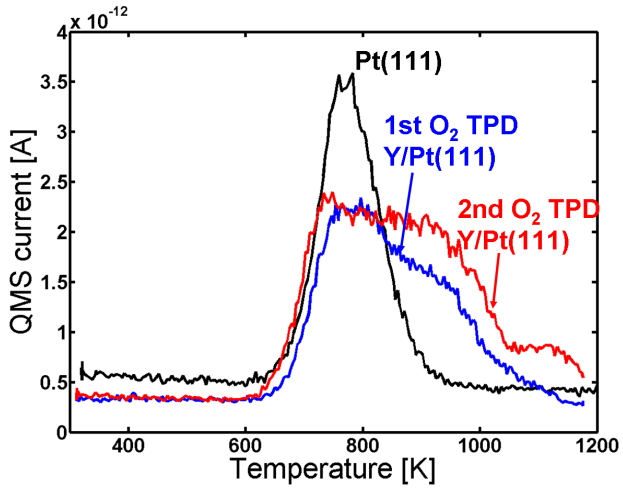

Figure 6.7: Oxygen TPD's (mass/charge = 32). In black the Pt(111) O_2 TPD, in blue the first O_2 TPD of the annealed Y/Pt(111) and in red the second O_2 TPD of the annealed Y/Pt(111).

pure Pt(111). The question is, however, if the Pt overlayer was stable during the oxygen exposure. Figure 6.8 shows the Y3d peak before (a) and after (b) the O_2 TPD. Before the O_2 TPD the Y3d peaks can be fitted to metallic Y, but after the O_2 TPD it is clearly seen that the yttrium is oxidised (see also Table 6.1). Fitting the XPS peaks to metallic and oxide phases gives around 41 % of Y oxide. The ISS

spectrum (not shown here) shows mainly Pt although also some Y is seen, indicating that the surface is still mainly consisting of Pt, but the subsurface yttrium has oxidised.

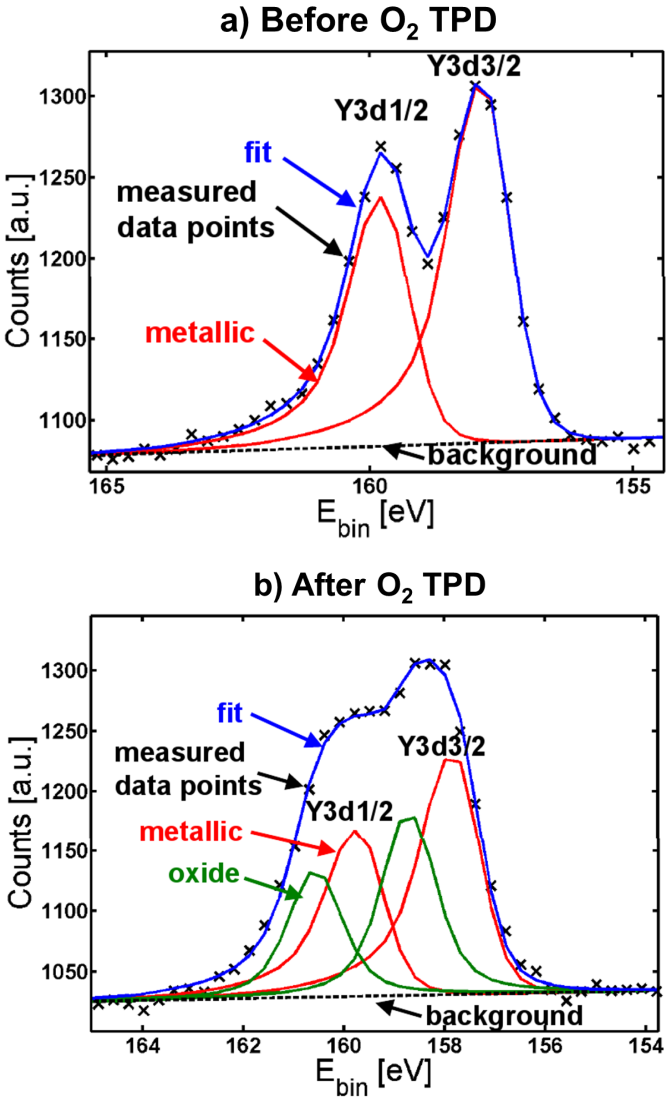

Figure 6.8: XPS spectra of Y3d (a) before and (b) after O_2 TPD. Fitting the recorded data to metallic (red) and oxidised (green) yttrium gives 41 % yttrium oxide. Before O_2 TPD only metallic yttrium was seen.

Figure 6.9 shows the CO TPD spectrum of the sample after the O_2 TPD. The CO TPD is seen to resemble that of pure Pt(111), indicating that the yttrium no longer effects the binding of CO to the Pt surface sites.

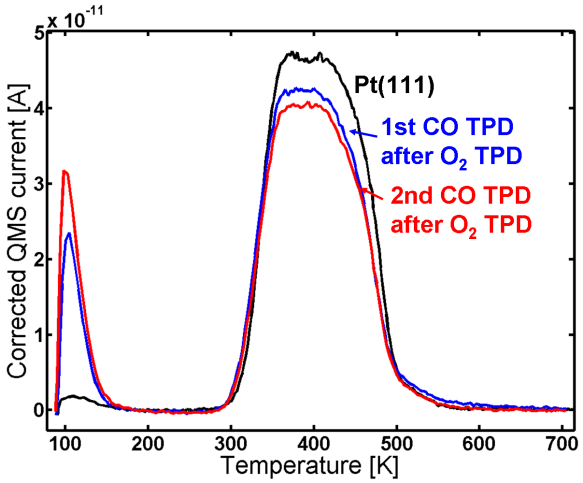

Figure 6.9: CO TPD's. In black the Pt(111), blue: before O_2 TPD, red: first after O_2 TPD, red dashed second after O_2 TPD.

The sample was then cleaned by performing sputtering and annealing cycles until yttrium was no longer seen by XPS.

In the following period several different Y depositions were performed on the annealed Pt(111), the results of which will not be discussed in detail here, however, some general aspects are worth noting. The CO TPD's typically resembled the blue graph shown in Figure 6.5. The error hindering the LEED screen to be positioned properly was corrected and LEED images were aquired. Typically they showed additional spots corresponding to a 1.88×1.88 R30° structure (this structure will be considered in more detail later) along with superspots similar to those seen in Figure 6.4. However, after annealing to 1273 K the ISS spectrum always showed a considerable peak corresponding to yttrium and the XPS spectrum showed the presence of oxygen. This was ascribed to the formation of yttrium oxide on the surface of the sample probably coming from some oxygen containing species present in the chamber background. It was therefore decided to perform future depositions of yttrium at a temperature where the yttrium will go subsurface and be protected by the Pt overlayer. The future sample temperature while evaporating yttrium was chosen to be 1173 K, being well above the 800 K at which, according to Figure 6.3, the Pt overlayer forms. Furthermore, it was decided to aim for a larger amount of deposited yttrium.

6.2 Y multilayer deposition

This section deals with higher amounts of deposited Y. The purpose of the higher deposition is to make a thick Pt_xY alloy region (on the order of 100 monolayers) so that the surface properties would be the same as in the case of a bulk Pt_xY alloy. The Pt(111) sample was cleaned and annealed to 1273 K. The sample temperature was then kept at 1173 K while around 88 Å (measured on the QCM) of Y was deposited on the sample. Figure 6.10 shows the ISS spectrum before (blue graph) and after (red graph) Y evaporation. Only Pt is seen in both spectra.

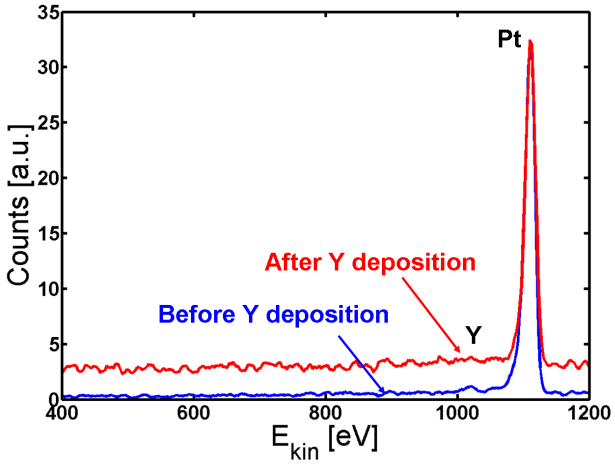

Figure 6.10: ISS spectrum before (blue) and after (red) Y deposition. Only Pt is seen indicating the formation of a Pt skin.

Table 6.2 shows the concentrations obtained by XPS after Y evaporation. A Pt:Y ratio of 4.8 is obtained proving that Y is present in the near surface region. Furthermore the O signal is on the detection limit. The deposition at a higher temperature therefore was seen to hinder the formation of yttrium oxide. Combining the results from ISS and XPS gives that the sample consists of a Pt overlayer on top of some Pt-Y system. Assuming the structure to be a single monolayer of Pt on top of a Pt_xY alloy, x is calculated using eq. (2.5) to be 3.7.
Figure 6.11 shows photographs of the LEED pattern seen before Y deposition (left image) and after Y deposition (right image). The LEED pattern after deposition in seen to consist of a large hexagon together with a smaller hexagon. In some of the LEED images very weak superspots were seen, however, they were too weak to

	After Y dep. at 1173 K	Annealed to 1348 K
Pt	81 %	87 %
Y	17 %	12 %
C	1 %	0 %
O	1 %	1 %
Pt:Y ratio	4.8	7.3
x assuming Pt/Pt$_x$Y	3.7	5.7
x assuming Pt/Pt$_2$Y/Pt/Pt$_x$Y	3.4	6.5

Table 6.2: Concentration of the different elements as obtained by XPS for the 88 Å Y/Pt(111) annealed at 1173 K and 1348 K. The values of x are calculated using eq. (2.5) (with added terms for the Pt/Pt$_2$Y/Pt/Pt$_x$Y system which will be considered later). Pt/Pt$_x$Y refers to a Pt overlayer on top of Pt$_x$Y.

enable analysis of them. The ratio B1/C is measured to be 1.72 ±0.02 (which is close to $\sqrt{3}$) and the angle between B1 and C is measured to be 30°. Combining vectors B1 and B2 can therefore be seen to give vector C, meaning that the larger hexagon can be constructed from the smaller hexagon. The ratio A/B1 is measured to be 1.88 ±0.02 and the angle between A and B1 is measured to be 30°. Relative to the Pt(111) structure, the annealed Y/Pt(111) therefore shows a 1.88×1.88 R30° structure.

Such a structure could corresponds to a 2×2 R30° structure where the lattice is under 6 % compressive strain or a $\sqrt{3} \times \sqrt{3}$ R30° structure where the lattice is under 9 % tensile strain. These possibilities will be considered further in the discussion section.

The blue graph in Figure 6.12 shows the CO TPD spectrum of the sample. It is seen that CO is bound weaker than for Pt(111) with a pronounced peak at around 295 K and a smaller peak at around 275 K. The origin of the sharp peak at around 295 K could be due to strong CO-CO interactions on an ordered CO layer on the surface. At around 295 K some of the CO from this ordered structure desorbs which causes the ordered CO structure to collapse and immediately desorb from the surface. The red graph in Figure 6.12 is the second (repeated) CO TPD of the sample which is made in order to check the reproducibility. It is seen to be almost identical to the first TPD experiment. It is also seen that the CO TPD of 88 Å Y/Pt(111) is similar to the CO TPD of 3 Å Y/Pt(111) shown in Figure 6.5, however, the peak at 295 K is much sharper and the feature corresponding to CO on Pt(111) has disappeared. After the CO TPD, detailed XPS spectra showed the same concentrations of Pt, Y,

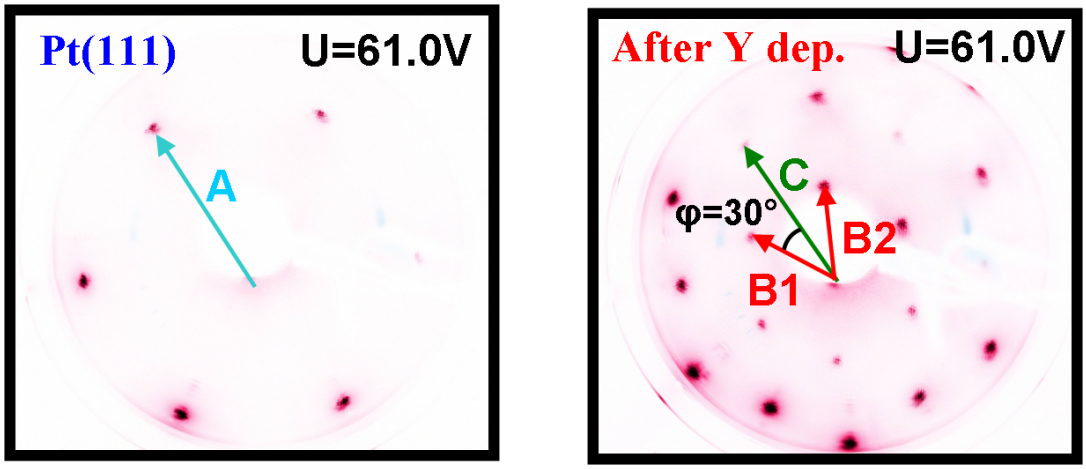

Figure 6.11: Photographs of the observed LEED patterns for Pt(111) (left, T=316 K) and for Y/Pt(111) annealed to 1173 K (right, T=373 K).

C and O as before the CO TPD, indicating that the surface was stable to the CO TPD.

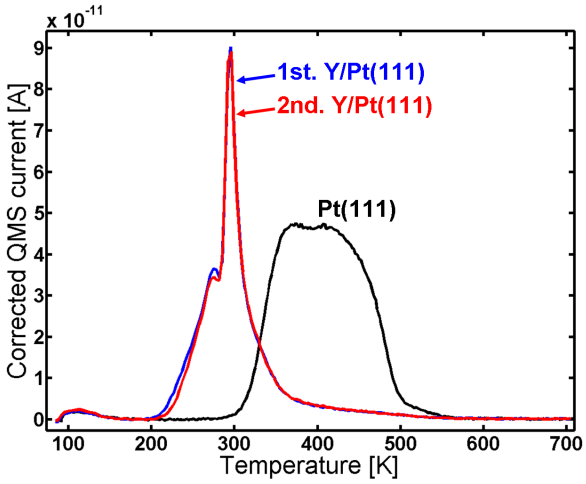

Figure 6.12: CO TPD of the 88 Å Y/Pt(111) sample annealed at 1173 K. The first TPD (blue graph) and second TPD (red graph) compared to the annealed Pt(111) (black graph). Areas: 1st TPD compared to Pt(111): 0.63, 2nd TPD compared to Pt(111): 0.62.

LEED was performed at 90 K after saturating the surface with CO. This was done in order to investigate if it was possible to see the ordering of the adsorbed CO in the LEED spectrum. However, the same LEED pattern as for the non CO covered

surface (see Figure 6.11) was observed. For the annealed Pt(111) crystal without any yttrium deposition and at 310 K there was also seen to be no difference between the spectrum before and after saturating the surface with CO. This could be related to the mobility of CO on the surface, causing a weakening in the LEED pattern [125], however, further measurements are necessary in order to understand this.
The surface stability in oxygen was then tested by dosing 200 mbar O_2 for 10 min at 300 K. After oxygen exposure XPS was made which showed 11 % oxygen on the surface but the yttrium peak did not show any oxide feature. Unexpectedly the ISS did not show any oxygen peak. A TPD was now made to test if the oxygen would desorb or form yttrium oxide. The temperature was ramped linearly with 2 K/s from 304 K to 1173 K. Hardly any oxygen was seen in the TPD, which could indicate the formation of yttrium oxide during the temperature ramp. XPS was made at 1173 K after the TPD and showed 5 % oxygen, and the yttrium 3d peak in XPS showed some oxidised feature indicating that yttrium oxide had formed. In the LEED spectrum extra spots appeared which could also be due to the formation of yttrium oxide. A CO TPD was also performed and it surprisingly showed roughly the same features as before oxygen exposure, however, the area under the TPD was 35 % less.
The sample was then lightly sputtered in order to remove the formed yttrium oxide and then annealed to 1348 K. This annealing temperature was higher than the normally used (1173 K or 1273 K) and the reason was to investigate whether a higher annealing temperature would result in a higher degree of ordering on the surface and cause the very weak superspots in LEED to become brighter.
Figure 6.13 shows the LEED image after annealing to 1348 K. The higher annealing temperature made two sets of hexagonal superspots appear, corresponding to long range ordered structures. The distances B and C indicated in the LEED pattern are measured to be the same as in Figure 6.11. The ratios A/D and A/E in the two superspot patterns are measured to be 10.4 ± 0.5 and 6.4 ± 0.3, respectively. The angle between A and D is 0° and the angle between A and E is 30°. The superspots therefore correspond to 6.4×6.4 R30° and 10.4×10.4 structures, referring to the original Pt(111) spots. Since $6.4 \cdot \sqrt{3} \approx 11.1$, combining vectors from the smaller superspots roughly gives the larger superspots, meaning that the E hexagon could be viewed as a higher order diffraction of D.
The blue graph in Figure 6.14 shows the CO TPD of the sample after annealing to 1348 K. The TPD is seen to have the same features as the one annealed to 1173 K,

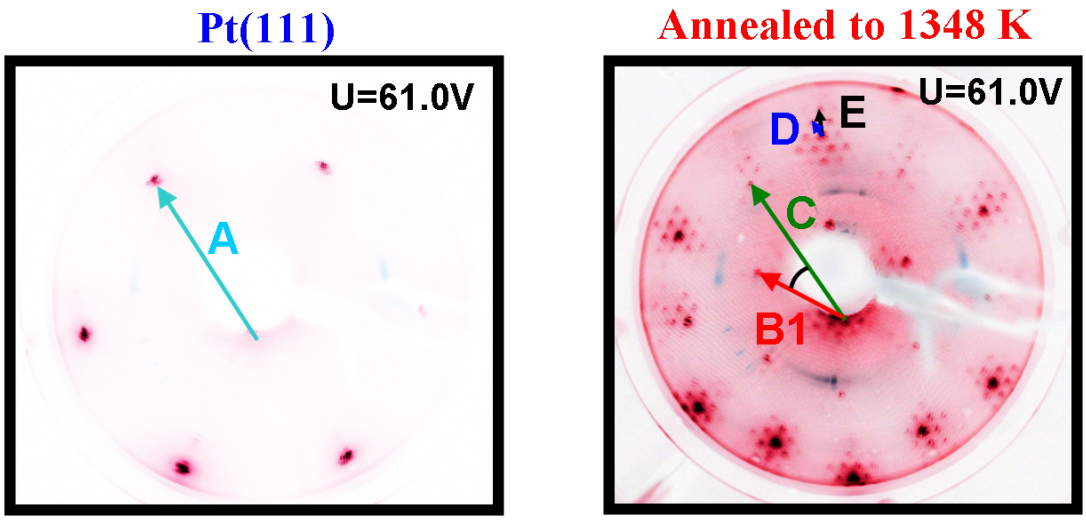

Figure 6.13: Photographs of the observed LEED patterns for Pt(111) (left, T=316 K) and for Y/Pt(111) annealed to 1348 K (right, T=312 K). The increased annealing temperature causes superspots, indicated by D and E, to appear.

however, the very distinct peak at 295 K is seen to be lower in intensity and have a bit broader shoulder to the right of it. The CO TPD was repeated two times and showed perfect reproducibility. Table 6.2 lists the concentrations of Pt, Y, C and O as obtained by XPS after annealing to 1348 K. The higher annealing temperature is seen to have caused an increase in the Pt:Y ratio. Assuming a Pt overlayer on a Pt_xY structure gives x=5.7.

The sample was then taken out of the chamber in order to measure the oxygen reduction activity. However, before mounting the sample in the electrochemical cell an ARXPS depth profile was measured in order to compare the depth profile before and after electrochemistry (same procedure as for the annealed polycrystalline Pt_3Sc sample).

Figure 6.15 shows the ARXPS depth profile before electrochemistry. The ARXPS depth profile shows an initial layer of carbon and some oxygen on the sample together with a small amount of yttrium oxide. Then follows a platinum overlayer structure and then the bulk of the sample was fixed to be Pt_5Y. This ratio of Pt:Y was chosen on the basis of the XPS measurements shown in Table 6.2, together with the fact that Pt_5Y is the most Pt rich stable Pt-Y phase. Qualitatively the ARXPS depth profile is seen to be similar to that obtained from the polycrystalline sample of Pt_3Sc (see Figure 5.13).

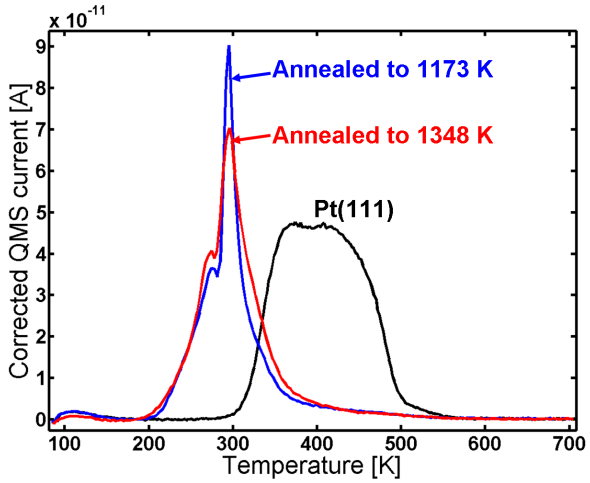

Figure 6.14: CO TPD of the 88 Å Y/Pt(111) after annealing to 1348 K (red graph) compared to the sample annealed to 1173 K (blue graph) and Pt(111) (black graph)

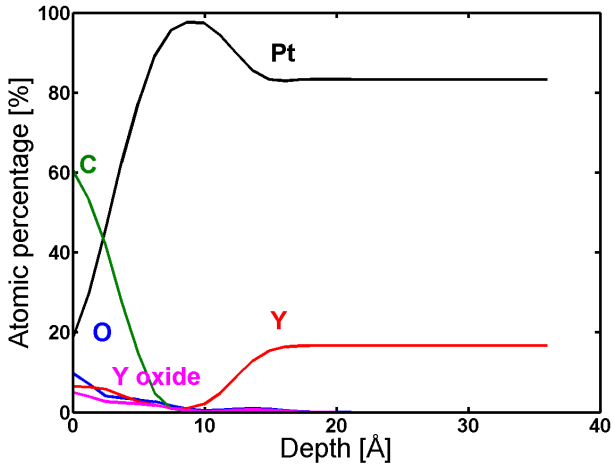

Figure 6.15: ARXPS depth profile of the UHV annealed (1348 K) Y/Pt(111) before ORR activity measurements. Measurements performed by Paolo Malacrida.

The oxygen reduction activity was then measured and Figure 6.16 shows the measured activity on a Tafel plot. The activity of the sample is significantly higher than polycrystalline platinum and close to that of the clean sputtered Pt_3Y.
Figure 6.17 shows the ARXPS depth profile after electrochemistry compared with before. It is seen that after the electrochemical experiment the platinum overlayer has substantially increased meaning that yttrium has leached out from the underly-

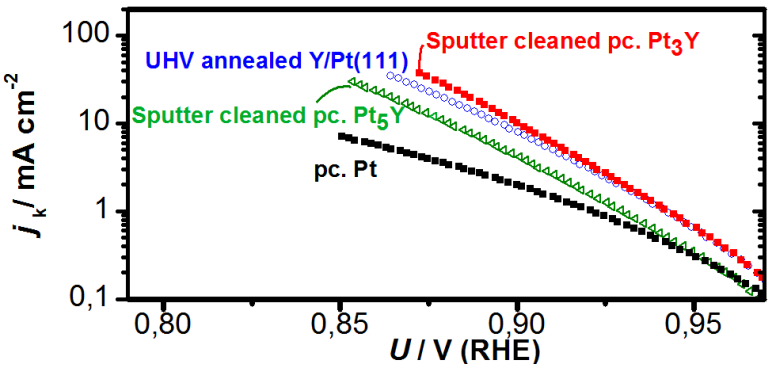

Figure 6.16: Tafel plot of the 1348 K UHV annealed Y/Pt(111) sample compared with the sputter cleaned polycrystalline samples of Pt_3Y, Pt_5Y and Pt. Measurements are done at T=60°C and at a scan rate of 50 mV/s. Measurements performed by Patricia Hernandez-Fernandez and Ifan Stephens.

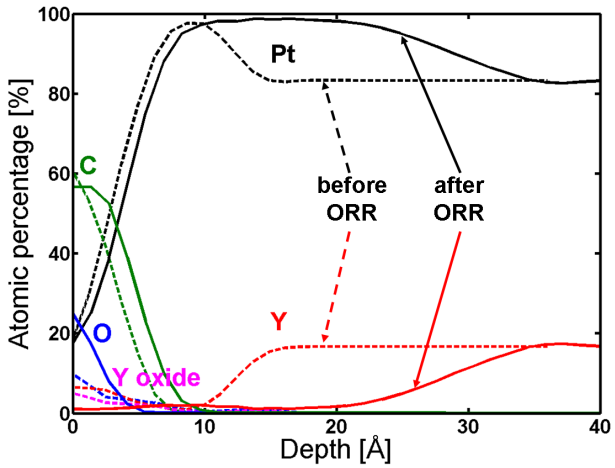

Figure 6.17: ARXPS depth profile of the 1348 K UHV annealed Y/Pt(111) before (dashed lines) and after (solid lines) ORR activity measurements. Measurements performed by Paolo Malacrida.

ing layer. The Pt skin structure prepared in UHV therefore results in a Pt skeleton structure upon immersion in the electrolyte. This is contrary to the result for polycrystalline Pt_3Sc, shown in Figure 5.15, where little change after electrochemical measurements was seen. This also means that the surface studied under UHV conditions is different from the surface relevant for the electrochemical experiments. In order to directly correlate measurements done under UHV with the electrochemical

measurements it is necessary to have a surface which is stable. The sample is therefore again mounted in the UHV chamber in order to investigate the electrochemically active surface. A problem seen from the ARXPS data in Figure 6.17 is, however, that the surface is covered with a layer of adventitious contamination originating from both electrolyte and air exposure. To remove this layer of adventitious contamination without effecting the sample itself is difficult (as was also shown in Section 5.1.2.2 for the polycrystalline Pt_3Y sample after exposure to 0.1 M $HClO_4$), nonetheless, an attempt was made.

The sample was first mildly sputtered by making continous ISS until platinum was seen in the spectrum. Then the CO TPD from 90 K to 700 K, shown in Figure 6.18, was obtained. The first TPD mainly shows CO bound stronger than on Pt(111)

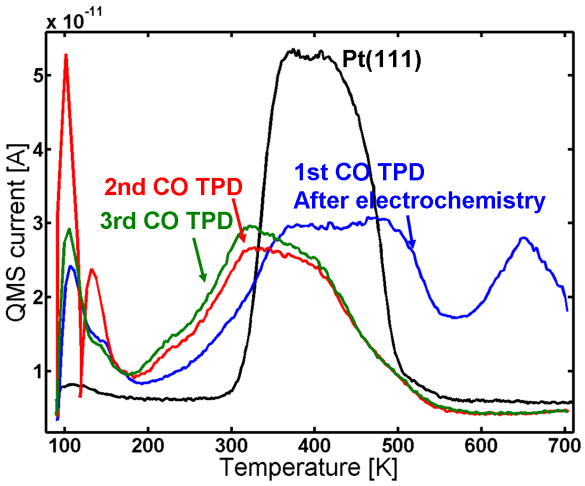

Figure 6.18: CO TPD after electrolyte exposure and mildly sputtering of contaminants by ISS.

whereas the second and third TPD's show some CO which is weaker bound than on Pt(111). LEED was also performed giving a weak hexagonal pattern corresponding to Pt(111). Further cleaning of the sample was attempted by exposure to 7.5 mbar hydrogen for 10 min at 673 K (in order to remove carbon species), 9.5 mbar CO was dosed for 10 min first at 313 K and then at 673 K (in order to remove oxygen species). CO TPD's and O TPD's were made and the sample was again annealed in high pressure of hydrogen. However, at the end also yttrium was seen in the ISS spectrum showing that it was not possible to remove the adventitous contamination from the sample without the sample itself being affected.

6.3 Discussion and conclusion

In the previous section it was shown that when depositing yttrium on Pt(111) at 1173 K a Pt overlayer is formed on top of a Pt_xY structure. The XPS data shown in Table 6.2 indicates a Pt:Y ratio between 3 and 7 underneath the Pt overlayer (depending on the annealing temperature and the assumed structure). Relative to the Pt(111) structure the annealed Y/Pt(111) shows a 1.88×1.88 R30° structure. Considering the XPS data and the Pt-Y phase diagram (see Figure A.1 in the appendix) Pt_3Y and Pt_5Y are considered to be possible candidates to the formed structure of annealed Y/Pt(111). DFT calculations were performed, investigating the stability of different surfaces which could fit with the experimental observations. They will now be considered in the following.
Table 6.3 shows the relative stability of different Pt-Y structures. Common for the different structures is that they all have a Pt overlayer and Pt_3Y in the bulk. The second and third layers are then varied with different stoichiometries of Pt and Y. Since the lattice constant of pure Pt(111) and Pt_3Y(111) are 3.9237 Å and 4.074 Å, respectively, a Pt overlayer in the Pt_3Y structure will be under 3.8 % tensile strain.

	Stability	CO binding energy
Pt/Pt_3Y	(-0.07 ± 0.06) eV	0.04 eV
$Pt/Pt_2Y/Pt/Pt_3Y$	(-0.01 ± 0.06) eV	-0.15 eV
$Pt/Pt_2Y/Pt_3Y$	(0.13 ± 0.06) eV	-0.15 eV
$Pt/PtY/Pt/Pt_3Y$	(0.40 ± 0.06) eV	-0.25 eV
$Pt/PtY/Pt_3Y$	(0.54 ± 0.06) eV	-0.25 eV

Table 6.3: DFT calculations of the stability and CO binding energy relative to Pt of different Pt-Y structures (layers are illustrated in Figure 6.19). In case different adsorption sites exist on the surface the one with the highest CO binding energy is reported. Only the first two layers are considered and the CO coverage is 1/4. Calculations performed by Anders Konge Jepsen [126].

Table 6.3 shows that among the considered structures the most stable one consists of a Pt overlayer on top of Pt_3Y. Assuming that the periodicity of the yttrium atoms would give rise to an observable LEED pattern, this structure would correspond to a 2×2 structure under 3.8 % tensile strain. This is not in agreement with the observed LEED pattern. The second most stable structure has Pt_2Y and pure Pt as second

and third layers, respectively. The Pt_2Y structure corresponds to a $\sqrt{3} \times \sqrt{3}$ R30° structure under 3.8 % tensile strain. As mentioned earlier the observed 1.88×1.88 R30° structure with respect to Pt(111) in LEED could be interpreted as a $\sqrt{3} \times \sqrt{3}$ R30° structure, however, the structure must in that case be under 9 % tensile strain, which is a highly strained structure not in agreement with the 3.8 % tensile strain for Pt_3Y. Table 6.3 also shows that having a PtY layer in the second layer is not very stable neither with or without a pure Pt layer in the third layer.
Figure 6.19 shows the different Pt-Y layers used for the calculations reported in Table 6.3.

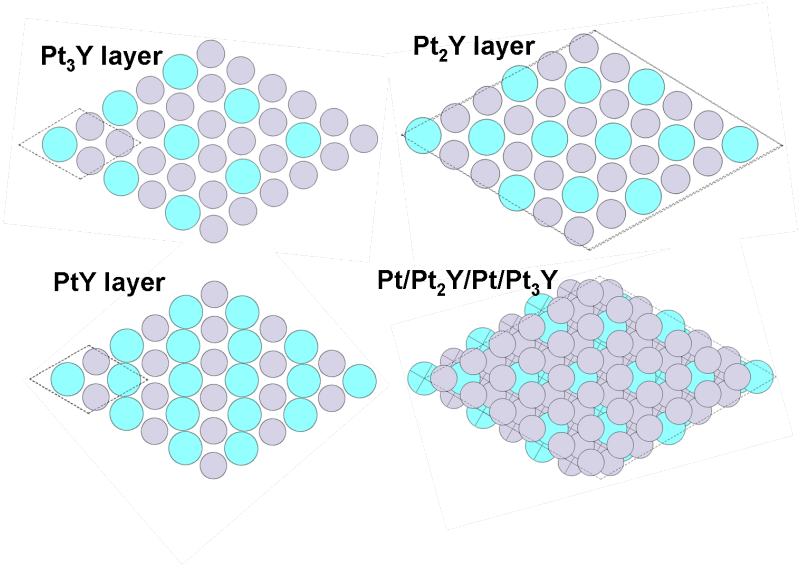

Figure 6.19: Illustration of PtY, Pt_2Y and Pt_3Y layers together with the $Pt/Pt_2Y/Pt/Pt_3Y$ system. Illustration made by Anders Konge Jepsen.

The CO binding energies are also calculated on the structures and listed in Table 6.3. The $Pt/Pt_2Y/Pt/Pt_3Y$ structure is seen to bind CO 0.15 eV weaker than Pt. The distinct peak in the CO TPD seen in Figure 6.14 of the annealed Y/Pt(111) system is seen to be shifted roughly 120 K compared to Pt(111). From eq. (5.3) a lowering in CO desorption temperature of 120 K is seen to correspond to a weaker binding of CO on the order of 0.3 eV.
The only stable more Pt rich Pt-Y phase is Pt_5Y which will be considered in the following. Figure 6.20 shows the structure of $Pt_5Y(111)$. Stephens et al. have measured the XRD spectrum of bulk polycrystalline Pt_5Y and found that it has an fcc unit cell, where each lattice point consists of an Y atom surrounded by 5 Pt atoms

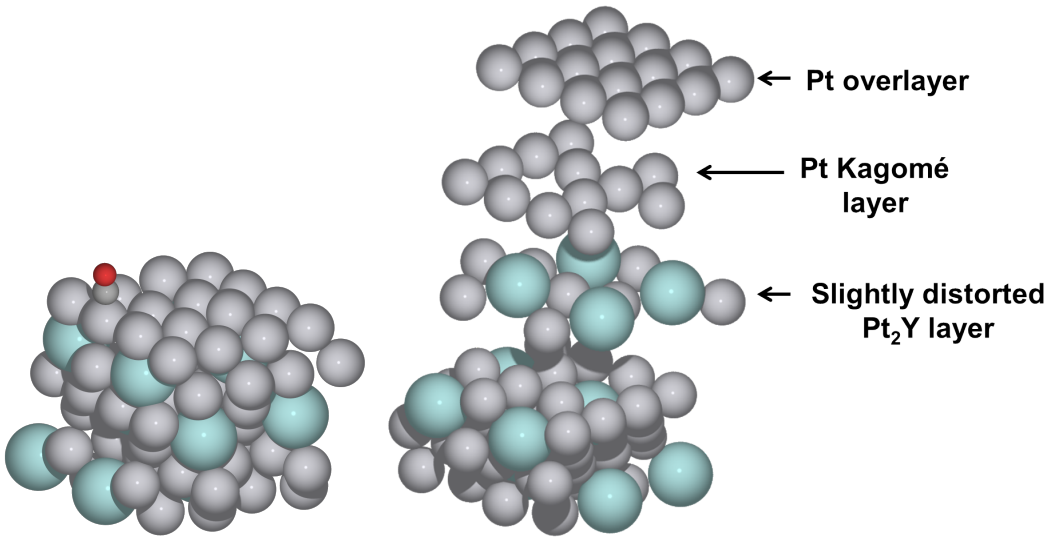

Figure 6.20: Left: structure of Pt_5Y (with an adsorbed CO molecule) as calculated by DFT. Right: "layer by layer" model of Pt_5Y which can be considered constructed from alternating layers of pure Pt Kagomé and slightly distorted Pt_2Y. In both illustrations the Pt_5Y structure is terminated by a Pt overlayer. The CO binding energy on this structure is calculated to be 0.3 eV weaker than on Pt(111). Calculations and illustration made by Ulrik Grønbjerg Andersen [127].

resulting in a lattice parameter of 7.490 Å. The crystal prototype was found to be $AuBe_5$ [107]. Unlike Pt_3Sc and Pt_3Y, the bulk structure of Pt_5Y does not have any closely packed planes. It can be considered formed by alternating layers of pure Pt Kagomé and slightly distorted Pt_2Y, similar to the structure of Pt_5Ce mentioned in the introduction [70]. The vacancies in the Pt Kagomé can be seen to have a 2×2 structure. For the Pt overlayer structure on Pt_5Y, shown in Figure 6.20, two possible adsorption sites of CO exists. Both sites are "on top" sites of Pt, but in one case there are three Pt atoms below the Pt atom binding to CO and in the other case there are two Pt atoms and a vacancy below the Pt atom. The binding energy of CO was calculated to be 0.3 eV weaker than Pt(111) on both sites [127].
If the Pt overlayer is omitted, i.e. the Pt_5Y structure is terminated with the Pt Kagomé net, CO can either bind on top of the vacancy, which binds CO 1.0 eV weaker than Pt, or on top of a Pt atom, which binds CO 0.5 eV weaker than Pt. As mentioned above the shift in CO desorption temperature seen in Figure 6.14 is correlated with a lower CO binding energy of around 0.3 eV, which is in good agreement with the result obtained for the Pt overlayer structure on Pt_5Y.

The Pt overlayer on $Pt_5Y(111)$ and the Pt Kagomé layer are both calculated to be under 5 % compressive strain compared to Pt(111). The structure of the vacancies in the Pt Kagomé layer can be seen to be 2×2 compared to the Pt overlayer. The observed LEED pattern of 1.88×1.88 R30° compared to Pt(111) can be considered a 2×2 R30° structure if the lattice is assumed to be under 6 % compessive strain. Apart from the 30° rotation this structure is seen to match with the structure of the vacancies in the Pt Kagomé. Such a structure was also seen by Tang et al. [69] for thin Ce films on Pt(111) as discussed in the introduction. It is interesting to note that for UHV annealed samples of both Ce, La and Tm on Pt(111) a downshifts in the CO TPD similar to that of UHV annealed Y/Pt(111) is seen.
It is at present not possible to determine with certainty which structure the UHV annealed Y/Pt(111) forms, however, the mentioned Pt_5Y structure appears to be a good candidate.
On a different note, it is worth mentioning that the lower CO binding energy for a Pt overlayer on top of the Pt_xY alloy compared to the polycrystalline Pt_3Y sample where Y was present in the surface also suggests that CO annealing will not produce a Pt overlayer.
When the annealed Y/Pt(111) was exposed to electrolyte, a thicker Pt overlayer was observed. The fact that yttrium is not stable in the second layer can be due to different effects. One is the high driving force for Y dissolution due to the very negative standard reduction potential of Y ($E_0 = -2.372$ V for $Y \Rightarrow Y^{3+}$) [13]. Another is the high affinity of yttrium for oxygen (ΔH = -1905kJ/mol or corresponding to a gain of 9.9 eV per yttrium atom for $2Y + 1.5O_2 = Y_2O_3$) [111] which could favour the formation of subsurface oxygen or segregation of Y, leading to a depletion of yttrium [54–56].
It is interesting to compare the UHV annealed Y/Pt(111) crystal with the UHV annealed Pt_3Sc polycrystal. For Sc the standard reduction potential ($E_0 = -2.077$ V for $Sc \rightarrow Sc^{3+}$) [13] and affinity towards oxygen (ΔH = -1908kJ/mol for $2Sc + 1.5O_2 = Sc_2O_3$) [111] is more or less as high as for Y. The heat of formation of Pt_3Sc, Pt_3Y and Pt_5Y are also more or less the same (see figure 4.1 and [128]). Nevertheless, UHV annealed Pt_3Sc showed little change in the Pt overlayer thickness after ORR measurements, whereas for UHV annealed Y/Pt(111) a thick Pt overlayer was formed. The most striking difference between UHV annealed Pt_3Sc and UHV annealed Y/Pt(111) is the difference in strain. Pt_3Sc is under 0.9 % tensile strain whereas UHV annealed Y/Pt(111) is under 3.8 % tensile strain assuming a Pt_3Y

structure or 5 % compressive strain assuming a Pt_5Y structure. One could hypothesise that this difference in the amount of strain is the reason for the difference in stability of the Pt overlayer. This notion is supported by very recent work by Jepsen and Rossmeisl [126] illustrated in Figure 6.21.

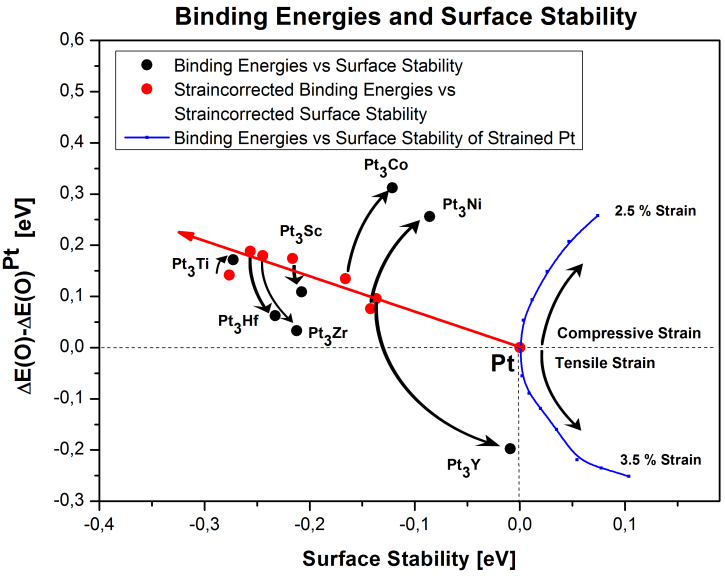

Figure 6.21: DFT calculated correlation between the O binding energy relative to Pt and the stability for different Pt bimetallic alloys. All structures are Pt overlayers on top of Pt_3M alloys, i.e. with 25 % of the solute atom in the second layer. Calculations and figure made by Anders Konge Jepsen [126].

The black dots on Figure 6.21 shows the oxygen binding energy as a function of the Pt overlayer stability for different Pt bimetallic alloys. Pt_3Y is seen to have the least stable Pt overlayer, whereas the Pt overlayer on Pt_3Sc is around 0.2 eV more stable. The 5 % compressed Pt overlayer on Pt_5Y was not considered in the calculations, but from the blue graph in the figure it is seen that a strained Pt overlayer, regardless of whether it is under tensile or compressive strain, will be less stable than a not strained surface. No correlation is seen between the oxygen binding energy and the Pt overlayer stability. When correcting the oxygen binding energy and the Pt overlayer stability for strain effects the red data points are obtained. The variation in the oxygen binding energy of the different Pt bimetallic alloys is then only due to the ligand effect. For the strain corrected values the data is seen to lie close to a

straight line.

The fact that the UHV annealed Y/Pt(111) shows a significant increase in activity compared to Pt(111) although several monolayers have been depleted from yttrium demands further attention. First of all the thick Pt overlayer seen on the ARXPS depth profile could be an artefact of the ARXPS analysis. However, for the Cu/Pt(111) near surface alloy it was possible to resolve a monolayer thick Pt overlayer [40]. Furthermore Stephens et al. [107] also reported a thick Pt overlayer in the case of sputter cleaned bulk polycrystalline samples of Pt_3Y and Pt_5Y. It is therefore likely that the thick Pt overlayer is not an artefact of the ARXPS analysis.

The increase in ORR activity for Pt bimetallic alloys can be ascribed to two orthogonal effects namely the ligand effect and the strain effect. The thick (several monolayers) Pt overlayer makes the ligand effect negligible. Peter Strasser and coworkers found that enhanced ORR activity of a dealloyed Pt-Cu thin film (several monolayers Pt overlayer) is primarily due to the compressive strain in the surface layer [129]. For UHV annealed Y/Pt(111) the LEED structure could correspond to a Pt_5Y structure on which a Pt overlayer will be under 5 % compressive strain. Assuming that the electrochemical active surface is also under compressive strain, the observed increase in ORR activity could be explained as a strain effect. For Pt_3Y, however, the Pt overlayer is under tensile strain which should strengthen the binding of adsorbates such as O^*, HO^* and HOO^* moving further away from the top of the volcano. A possible explanation of the higher ORR activity could in that case be the effect of coverage on the adsorption energy of oxygen. Grabow et al. reported that the shape of the volcano is significantly affected by adsorbate–adsorbate interactions for strong O and CO adsorption energies (left side of the volcano) [130]. Preliminary calculations performed by Ulrik Grønbjerg Andersen have shown that the adsorption energy of the second oxygen atom is much lower than the first, and in fact quite close to the target value [131].

It is at this point relevant to consider the implications this has on nanoparticles of Pt_3Y. The observation that yttrium dissolves from more than a nanometer inside the annealed Y/Pt(111) could lead one to think that Pt_3Y nanoparticles would be completely depleted of yttrium and therefore not show any improvement in ORR activity. This is, however, not necessarily the case. Peter Strasser and coworkers found that more Cu is dissolved in the surface layers of a Pt-Cu thin film compared to Pt-Cu nanoparticles. The reason for this is suggested to be that the surface of the Pt-Cu films becomes rough or porous during the dealloying whereas small

diameter nanoparticles may not support the porous surface [129]. It is therefore not possible to directly transfer information about the thickness of the Pt overlayer for bulk samples to that of nanoparticles.

As mentioned in Section 4.3 Pt-Y nanoparticles do in fact show an increase in ORR activity compared to Pt nanoparticles of the same size and produced under the same conditions. Further measurements are needed in order to understand the origin of their increased activity.

The thick Pt overlayer makes the Pt-Y catalyst similar to the Pt-Cu catalyst investigated by Strasser et al. One of the main differences between the two is the very negative alloying energy of Pt_3Y. This could suggest that the Pt-Y catalyst will show better long term stability in a fuel cell.

In summary, it was shown that Y evaporated on Pt(111) forms a Pt overlayer when annealed above 800 K. The annealed structure was seen to bind CO weaker than Pt(111) with a pronounced peak in the CO TPD at 295 K. When depositing a large amount of yttrium at 1173 K a 1.88×1.88 R30° structure relative to Pt(111) was seen by LEED. The Pt overlayer was relatively stable in air, however, after performing ORR activity measurements in the electrochemical cell a thick Pt overlayer was measured by ARXPS depth profile. The observed LEED pattern could correspond to a 2×2 R30° structure under 6 % compressive strain. This structure is in agreement with a Pt Kagomé layer in Pt_5Y rotated 30° with respect to the bulk Pt(111). The structure in the electrochemical cell and the origin of the higher ORR activity has been discussed, but it is still an open question what the active site for the ORR is for both UHV annealed Y/Pt(111), polycrystalline Pt-Y alloys and Pt-Y nanoparticles. Further investigations are necessary in order to understand these points in more detail.

Chapter 7

Summary and outlook

In this thesis, new materials for the oxygen reduction reaction (ORR) have been investigated.

Initially the changes in the surface morphology of Pt(111) and Pt nanoparticles upon exposure to high pressures of CO was investigated. For sputtered Pt(111) high pressures of CO was seen to enhance the annealing of the defect sites. On Pt nanoparticles, studied in a seperate chamber, a slight roughening was observed when annealing the particles in high pressure of CO. In principle, these effects could be used to tune the catalyst morphology and thereby optimise the catalytic performance.

From a density functional theory (DFT) screening study, catalysts consisting of Pt_3Sc and Pt_3Y were identified as promising candidates for the ORR, expected to both have a high activity and improved stability compared to the already known Pt bimetallic ORR catalysts. Sputter cleaned bulk polycrystalline samples of Pt_3Sc and Pt_3Y showed an enhancement in ORR activity by a factor of 1.5–1.8 and 6–10, respectively, in the range 0.9–0.87 V.

The formation of a Pt overlayer upon annealing in UHV was investigated for bulk polycrystalline alloys of Pt_3Y, Pt_5Y, Pt_5La and Pt_3Sc. Only in the case of Pt_3Sc the formation of a Pt overlayer was found upon UHV annealing. The reactivity of the Pt overlayer on Pt_3Sc was probed by CO TPD, which showed a decreased desorption temperature of CO on the order of 50 K compared to Pt(111). Using DFT calculations it was found that the decrease in CO binding energy could be related to a decrease in OH binding energy bringing the catalyst closer to the top

of the ORR volcano.
The deposition of Y on a Pt(111) crystal was also investigated. When annealing the crystal above 800 K a Pt overlayer was formed on top of a Pt-Y structure. The LEED pattern of the annealed crystal showed a 1.88×1.88 R30° structure compared to Pt(111). This stucture could correspond to a 2×2 R30° structure under 6 % compressive strain, which fits good with the structure of Pt_5Y.
The reactivity of the annealed Y/Pt(111) sample was probed by CO TPD, which showed a very distinct peak at 295 K, corresponding to the breakdown of an ordered structure with strong CO-CO interactions, and a general weaker binding of CO (on the order of 120 K) compared to Pt(111).
The ORR activity of the annealed Y/Pt(111) was measured to be comparable to that of sputter cleaned bulk polycrystalline Pt_3Y. Angle resolved x-ray photoelectron spectroscopy (ARXPS) depth profile before and after the electrochemical measurements showed that the Pt overlayer did not prevent subsurface yttrium from dissolving in the electrolyte creating a thick Pt overlayer. Consequently, the surface characterised in UHV was not identical to the surface tested in the electrochemical cell.

For future experiments on annealed Y/Pt(111) it would be very interesting if the same surface could be studied in UHV and electrochemistry, in particular if a smooth thicker Pt overlayer on top of Pt_3Y could be studied. One way of achieving this could be by evaporating Pt on top of the annealed Y/Pt(111) crystal in order to obtain a thicker Pt overlayer on the sample which could then be stuided in UHV and possibly be stable under the ORR activity measurements. Another approach would be to have an electrochemical cell attached to a UHV chamber enabling transfer between the UHV and the electrochemical cell without exposure to air. Assuming that the electrolyte exposure results in minor or no contamination of the sample this would enable the UHV characterisation of the crystal "post leaching" of yttrium. On the ARXPS chamber, such an electrochemical cell is currently being installed.
In order to investigate the structure of the annealed Y/Pt(111) crystal further, yttrium deposition on Pt(111) is currently being investigated in another UHV chamber which is equipped with a scanning tunneling microscope (STM). Hopefully this can give additional information to the interpretation of the seen LEED structures.
It would also be very interesting to study Sc/Pt(111) and La/Pt(111) in UHV and to test their ORR activity and stability before and after electrochemical measurements.

The fundamental knowledge gained by investigating Pt bimetallic alloys is of key importance in the design of active and stable catalysts for the ORR. A better understanding of the nature of the active site is important both from a scientific and a technological point of view.

Appendix A

Phase diagrams

A.1 Pt-Y phase diagram

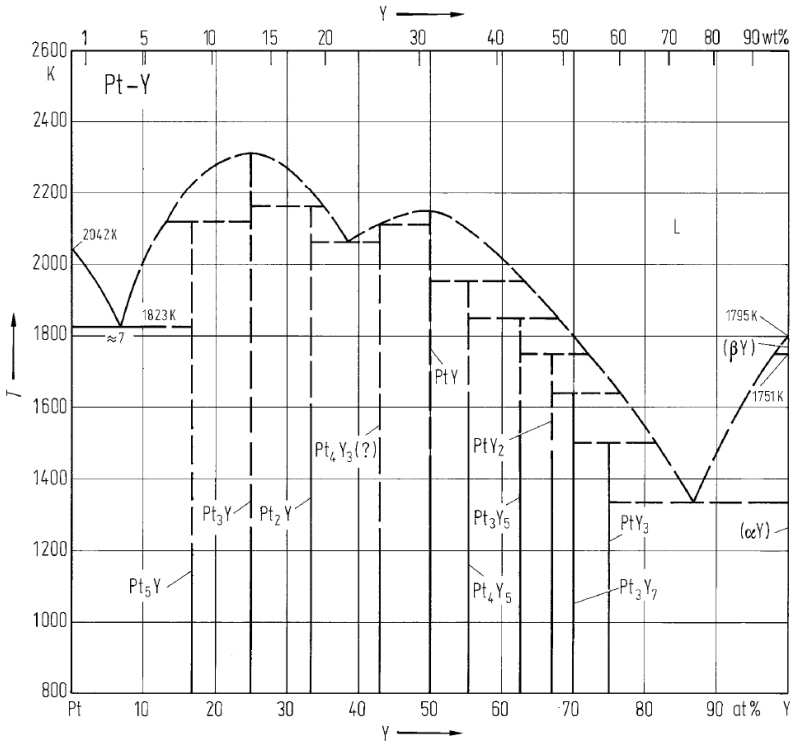

Figure A.1: Pt-Y phase diagram. Reprinted from [132].

A.2 Pt-Sc phase diagram

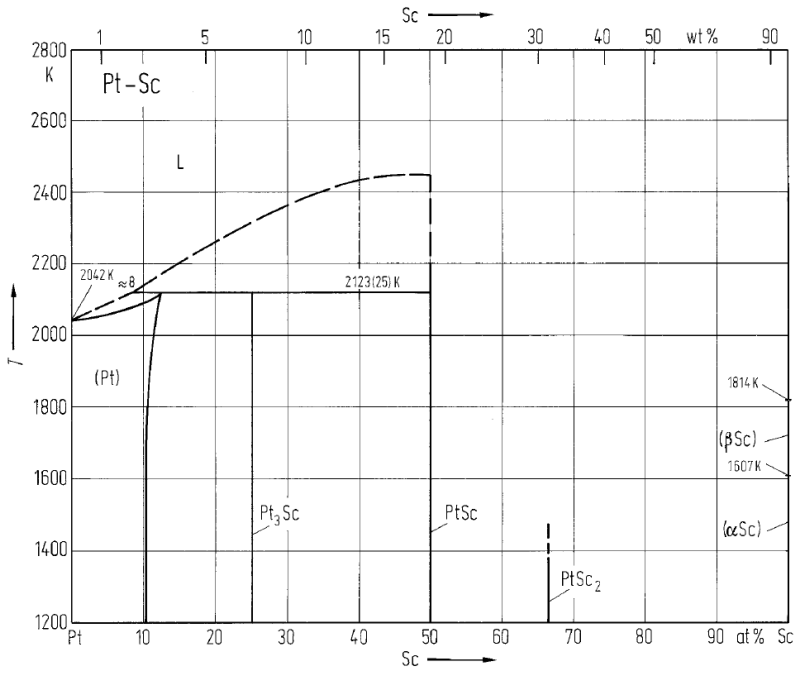

Figure A.2: Pt-Sc phase diagram. Reprinted from [133].

Bibliography

[1] BP Statistical Review of World Energy June 2011. http://www.bp.com.

[2] Nathan Lewis: said at "Ørsted Lecture", given at the Technical University of Denmark 4/12-08.

[3] N. Armaroli and V. Balzani. Towards an electricity-powered world. *Energy & Environmental Science*, 4(9):3193–3222, September 2011.

[4] I. Chorkendorff and J. W. Niemantsverdriet. *Concepts of Modern Catalysis and Kinetics*. Wiley-VCH Verlag Gmbh & Co, 2003.

[5] U. Eberle and R. von Helmolt. Sustainable transportation based on electric vehicle concepts: a brief overview. *Energy & Environmental Science*, 3(6):689–699, June 2010.

[6] H. A. Gasteiger and J. Garche. *Handbook of heterogeneous catalysis, Chapter 13.20.2*. Wiley-VCH, Weinheim, 2008.

[7] http://www1.eere.energy.gov/hydrogenandfuelcells/mypp/pdfs/fuel_cells.pdf U.S. Department of Energy.

[8] H. A. Gasteiger, S. S. Kocha, B. Sompalli, and F. T. Wagner. Activity benchmarks and requirements for Pt, Pt-alloy, and non-Pt oxygen reduction catalysts for PEMFCs. *Applied Catalysis B: Environmental*, 56(1-2):9–35, March 2005.

[9] G. M. Whitesides and G. W. Crabtree. Don't forget long-term fundamental research in energy. *Science*, 315(5813):796–8, February 2007.

[10] H. A. Gasteiger, D. R. Baker, and R. N. Carter. *in Hydrogen Fuel Cells: Fundamentals and Applications.* Wiley-CPH, 2010.

[11] Y. Shao-Horn, W. C. Sheng, S. Chen, P. J. Ferreira, E. F. Holby, and D. Morgan. Instability of supported platinum nanoparticles in low-temperature fuel cells. *Topics In Catalysis*, 46(3-4):285–305, December 2007.

[12] R. Borup, J. Meyers, B. Pivovar, Y. S. Kim, R. Mukundan, N. Garland, D. Myers, M. Wilson, F. Garzon, D. Wood, P. Zelenay, K. More, K. Stroh, T. Zawodzinski, J. Boncella, J. E. McGrath, M. Inaba, K. Miyatake, M. Hori, K. Ota, Z. Ogumi, S. Miyata, A. Nishikata, Z. Siroma, Y. Uchimoto, K. Yasuda, K. I. Kimijima, and N. Iwashita. Scientific aspects of polymer electrolyte fuel cell durability and degradation. *Chemical Reviews*, 107(10):3904–3951, October 2007.

[13] M. Pourbaix. *Atlas of Electrochemical Equilibria in Aqueous Solutions*. National Association of Corrosion Engineers, Houston, Texas, 1974.

[14] V. R. Stamenkovic, B. S. Mun, M. Arenz, K. J. J. Mayrhofer, C. A. Lucas, G. F. Wang, P. N. Ross, and N. M. Markovic. Trends in electrocatalysis on extended and nanoscale Pt-bimetallic alloy surfaces. *Nature Materials*, 6(3):241–247, March 2007.

[15] K. J. J. Mayrhofer, K. Hartl, V. Juhart, and M. Arenz. Degradation of Carbon-Supported Pt Bimetallic Nanoparticles by Surface Segregation. *Journal of the American Chemical Society*, 131(45):16348–16349, November 2009.

[16] J. Greeley, I.E.L. Stephens, A.S. Bondarenko, T.P. Johansson, H.A. Hansen, T.F. Jaramillo, J. Rossmeisl, I. Chorkendorff, and J.K. Nørskov. Alloys of platinum and early transition metals as oxygen reduction electrocatalysts. *Nature chemistry*, 1(7):552–6, October 2009.

[17] J. Rossmeisl, G. S. Karlberg, T. Jaramillo, and J. K. Nørskov. Steady state oxygen reduction and cyclic voltammetry. *Faraday Discuss.*, 140:337–346, 2008.

[18] G. S. Karlberg, J. Rossmeisl, and J. K. Nørskov. Estimations of electric field effects on the oxygen reduction reaction based on the density functional theory. *Physical Chemistry Chemical Physics*, 9(37):5158–5161, 2007.

[19] A Damjanov and V. Brusic. Electrode Kinetics of Oxygen Reduction On Oxide-free Platinum Electrodes. *Electrochimica Acta*, 12(6):615–628, 1967.

[20] A. A. Gewirth and M. S. Thorum. Electroreduction of dioxygen for fuel-cell applications: Materials and challenges. *Inorganic Chemistry*, 49(8):3557–3566, April 2010.

[21] J. K. Nørskov, J. Rossmeisl, A. Logadottir, L. Lindqvist, J. R. Kitchin, T. Bligaard, and H. Jónsson. Origin of the Overpotential for Oxygen Reduction at a Fuel-Cell Cathode. *Journal of Physical Chemistry B*, 108:17886–17892, 2004.

[22] V. Tripkovic, E. Skulason, S. Siahrostami, J. K. Nørskov, and J. Rossmeisl. The oxygen reduction reaction mechanism on Pt(111) from density functional theory calculations. *Electrochimica Acta*, 55(27):7975–7981, November 2010.

[23] M. J. Janik, C. D. Taylor, and M. Neurock. First-Principles Analysis of the Initial Electroreduction Steps of Oxygen over Pt(111). *Journal of the Electrochemical Society*, 156(1):B126–B135, 2009.

[24] J. Rossmeisl, A. Logadottir, and J. K. Nørskov. Electrolysis of water on (oxidized) metal surfaces. *Chemical Physics*, 319(1-3):178–184, December 2005.

[25] V. Stamenkovic, T. J. Schmidt, P. N. Ross, and N. M. Markovic. Surface composition effects in electrocatalysis: Kinetics of oxygen reduction on well-defined Pt_3Ni and Pt_3Co alloy surfaces. *Journal of Physical Chemistry B*, 106(46):11970–11979, November 2002.

[26] V. R. Stamenkovic, B. Fowler, B. S. Mun, G. F. Wang, P. N. Ross, C. A. Lucas, and N. M. Markovic. Improved oxygen reduction activity on $Pt_3Ni(111)$ via increased surface site availability. *Science*, 315(5811):493–497, January 2007.

[27] V. Stamenkovic, B. S. Mun, K. J. J. Mayrhofer, P. N. Ross, N. M. Markovic, J. Rossmeisl, J. Greeley, and J. K. Nørskov. Changing the activity of electrocatalysts for oxygen reduction by tuning the surface electronic structure. *Angewandte Chemie (International ed. in English)*, 45(18):2897–901, April 2006.

[28] L. J. Wan, T. Moriyama, M. Ito, H. Uchida, and M. Watanabe. In situ STM imaging of surface dissolution and rearrangement of a Pt-Fe alloy electrocatalyst in electrolyte solution. *Chemical Communications*, (1):58–59, 2002.

[29] U. Bardi, D. Dahlgren, and P. N. Ross. Structure and Chemisorptive Properties of the Pt_3Ti Surface. *Journal of Catalysis*, 100(1):196–209, July 1986.

[30] Z. Duan, J. Zhong, and G. Wang. Modeling surface segregation phenomena in the (111) surface of ordered Pt_3Ti crystal. *The Journal of chemical physics*, 133(11):114701, September 2010.

[31] W. Chen, Paul J. A. K., A. Barbieri, M. A. Van Hove, S. Cameron, and D. J. Dwyer. Structure Determination of $Pt_3Ti(111)$ By Automated Tensor Leed. *Journal of Physics-condensed Matter*, 5(27):4585–4594, July 1993.

[32] S. Axnanda, K. D. Cummins, T. He, D. W. Goodman, and M. P. Soriaga. Structural, Compositional and Electrochemical Characterization of Pt-Co Oxygen-Reduction Catalysts. *Chemphyschem*, 11(7):1468–1475, May 2010.

[33] J. L. Zhang, M. B. Vukmirovic, Y. Xu, M. Mavrikakis, and R. R. Adzic. Controlling the catalytic activity of platinum-monolayer electrocatalysts for oxygen reduction with different substrates. *Angewandte Chemie-international Edition*, 44(14):2132–2135, 2005.

[34] J.R. Kitchin, J.K. Nørskov, M.A. Barteau, and J.G. Chen. Modification of the surface electronic and chemical properties of Pt(111) by subsurface 3d transition metals. *Journal of Chemical Physics*, 120(21):10240–10246, June 2004.

[35] M. Mavrikakis, B. Hammer, and J.K. Nørskov. Effect of strain on the reactivity of metal surfaces. *Physical Review Letters*, 81(13):2819–2822, September 1998.

[36] M. Lischka, C. Mosch, and A. Gross. Tuning catalytic properties of bimetallic surfaces: Oxygen adsorption on pseudomorphic Pt/Ru overlayers. *Electrochimica Acta*, 52(6):2219–2228, January 2007.

[37] H. E. Hoster, O. B. Alves, and M. T. M. Koper. Tuning Adsorption via Strain and Vertical Ligand Effects. *Chemphyschem*, 11(7):1518–1524, May 2010.

[38] A. Schlapka, M. Lischka, A. Gross, U. Kasberger, and P. Jakob. Surface strain versus substrate interaction in heteroepitaxial metal layers: Pt on Ru(0001). *Physical Review Letters*, 91(1):016101, July 2003.

[39] P. Strasser, S. Koh, T. Anniyev, J. Greeley, K. More, C. F. Yu, Z. C. Liu, S. Kaya, D. Nordlund, H. Ogasawara, M. F. Toney, and A. Nilsson. Lattice-strain control of the activity in dealloyed core-shell fuel cell catalysts. *Nature Chemistry*, 2(6):454–460, June 2010.

[40] I. E. L. Stephens, A. S. Bondarenko, F. J. Perez-Alonso, F. Calle-Vallejo, L. Bech, T. P. Johansson, A. K. Jepsen, R. Frydendal, B. P. Knudsen, J. Rossmeisl, and I. Chorkendorff. Tuning the activity of Pt(111) for oxygen electroreduction by subsurface alloying. *Journal of the American Chemical Society*, 133(14):5485–91, April 2011.

[41] A. Bonakdarpour, K. Stevens, G. D. Vernstrom, R. Atanasoski, A. K. Schmoeckel, M. K. Debe, and J. R. Dahn. Oxygen reduction activity of Pt and Pt-Mn-Co electrocatalysts sputtered on nano-structured thin film support. *Electrochimica Acta*, 53(2):688–694, December 2007.

[42] M. K. Debe, A. K. Schmoeckel, G. D. Vernstrorn, and R. Atanasoski. High voltage stability of nanostructured thin film catalysts for PEM fuel cells. *Journal of Power Sources*, 161(2):1002–1011, October 2006.

[43] S. W. Lee, S. Chen, J. Suntivich, K. Sasaki, R. R. Adzic, and Y. Shao-Horn. Role of Surface Steps of Pt Nanoparticles on the Electrochemical Activity for Oxygen Reduction. *Journal of Physical Chemistry Letters*, 1(9):1316–1320, May 2010.

[44] J. Greeley, J. Rossmeisl, A. Hellman, and J. K. Nørskov. Theoretical trends in particle size effects for the oxygen reduction reaction. *Zeitschrift Fur Physikalische Chemie-international Journal of Research In Physical Chemistry & Chemical Physics*, 221(9-10):1209–1220, 2007.

[45] G.A. Tritsaris, J. Greeley, J. Rossmeisl, and J.K. Nørskov. Atomic-Scale Modeling of Particle Size Effects for the Oxygen Reduction Reaction on Pt. *Catalysis Letters*, 141(7):909–913, July 2011.

[46] K. J. J. Mayrhofer, D. Strmcnik, B. B. Blizanac, V. Stamenkovic, M. Arenz, and N. M. Markovic. Measurement of oxygen reduction activities via the rotating disc electrode method: From Pt model surfaces to carbon-supported

high surface area catalysts. *Electrochimica Acta*, 53(7):3181–3188, February 2008.

[47] U. A. Paulus, A. Wokaun, G. G. Scherer, T. J. Schmidt, V. Stamenkovic, N. M. Markovic, and P. N. Ross. Oxygen reduction on high surface area Pt-based alloy catalysts in comparison to well defined smooth bulk alloy electrodes. *Electrochimica Acta*, 47(22-23):3787–3798, August 2002.

[48] K. J. J. Mayrhofer, V. Juhart, K. Hartl, M. Hanzlik, and M. Arenz. Adsorbate-induced surface segregation for core-shell nanocatalysts. *Angewandte Chemie-international Edition*, 48(19):3529–3531, 2009.

[49] M. Arenz, K. J. J. Mayrhofer, V. Stamenkovic, B. B. Blizanac, T. Tomoyuki, P. N. Ross, and N. M. Markovic. The effect of the particle size on the kinetics of CO electrooxidation on high surface area Pt catalysts. *Journal of the American Chemical Society*, 127(18):6819–6829, May 2005.

[50] Y. Gauthier, M. Schmid, S. Padovani, E. Lundgren, V. Bus, G. Kresse, J. Redinger, and P. Varga. Adsorption sites and ligand effect for CO on an alloy surface: a direct view. *Physical Review Letters*, 87(3):036103, July 2001.

[51] K. J. Andersson, F. Calle-Vallejo, J. Rossmeisl, and I. Chorkendorff. Adsorption-driven surface segregation of the less reactive alloy component. *Journal of the American Chemical Society*, 131(6):2404–2407, February 2009.

[52] D. Friebel, D. J. Miller, D. Nordlund, H. Ogasawara, and A. Nilsson. Degradation of Bimetallic Model Electrocatalysts: An In Situ X-Ray Absorption Spectroscopy Study. *Angewandte Chemie-international Edition*, 50(43):10190–10192, 2011.

[53] L. Vitos, A. V. Ruban, H. L. Skriver, and J. Kollar. The surface energy of metals. *Surface Science*, 411(1-2):186–202, August 1998.

[54] C. A. Menning and J. G. Chen. Regenerating Pt-3d-Pt model electrocatalysts through oxidation-reduction cycles monitored at atmospheric pressure. *Journal of Power Sources*, 195(10):3140–3144, May 2010.

[55] C. A. Menning and J. G. Chen. Theoretical Prediction and Experimental Verification of Stability of Pt-3d-Pt Subsurface Bimetallic Structures: From Single Crystal Surfaces to Polycrystalline Films. *Topics In Catalysis*, 53(5-6):338–347, May 2010.

[56] C. A. Menning and J. G. Chen. Thermodynamics and kinetics of oxygen-induced segregation of 3d metals in Pt-3d-Pt(111) and Pt-3d-Pt(100) bimetallic structures. *Journal of Chemical Physics*, 128(16):164703, April 2008.

[57] B. Fowler, C. A. Lucas, A. Omer, G. Wang, V. R. Stamenkovic, and N. M. Markovic. Segregation and stability at $Pt_3Ni(111)$ surfaces and $Pt_{75}Ni_{25}$ nanoparticles. *Electrochimica Acta*, 53(21):6076–6080, September 2008.

[58] R. Makharia, S. Kocha, P. Yu, M. A. Sweikart, W. Gu, F. Wagner, and H. A. Gasteiger. Durable PEM Fuel Cell Electrode Materials: Requirements and Benchmarking Methodologies. *ECS Transactions*, 1(8):3–18, 2006.

[59] S. Chen, H. A. Gasteiger, K. Hayakawa, T. Tada, and Y. Shao-Horn. Platinum-Alloy Cathode Catalyst Degradation in Proton Exchange Membrane Fuel Cells: Nanometer-Scale Compositional and Morphological Changes. *Journal of the Electrochemical Society*, 157(1):A82–A97, 2010.

[60] G. H. Johannesson, T. Bligaard, A. V. Ruban, H. L. Skriver, K. W. Jacobsen, and J. K. Nørskov. Combined electronic structure and evolutionary search approach to materials design. *Physical Review Letters*, 88(25):255506, June 2002.

[61] S. Dahl, A. Logadottir, R. C. Egeberg, J. H. Larsen, I. Chorkendorff, E. Tornqvist, and J. K. Nørskov. Role of steps in N_2 activation on Ru(0001). *Physical Review Letters*, 83(9):1814–1817, August 1999.

[62] B. L. M. Hendriksen, M. D. Ackermann, R. van Rijn, D. Stoltz, I. Popa, O. Balmes, A. Resta, D. Wermeille, R. Felici, S. Ferrer, and J. W. M. Frenken. The role of steps in surface catalysis and reaction oscillations. *Nature Chemistry*, 2(9):730–734, September 2010.

[63] F. Tao, S. Dag, L. W. Wang, Z. Liu, D. R. Butcher, H. Bluhm, M. Salmeron, and G. A. Somorjai. Break-Up of Stepped Platinum Catalyst Surfaces by High CO Coverage. *Science*, 327(5967):850–853, February 2010.

[64] F. Tao, S. Dag, L. W. Wang, Z. Liu, D. R. Butcher, M. Salmeron, and G. A. Somorjai. Restructuring of hex-Pt(100) under CO Gas Environments: Formation of 2-D Nanoclusters. *Nano Letters*, 9(5):2167–2171, May 2009.

[65] L. A. Kibler, A. Cuesta, M. Kleinert, and D. M. Kolb. In-situ STM characterisation of the surface morphology of platinum single crystal electrodes as a function of their preparation. *Journal of Electroanalytical Chemistry*, 484(1):73–82, April 2000.

[66] L. P. Ford, H. L. Nigg, P. Blowers, and R. I. Masel. The role of step atom density on the binding and reaction of surface species. *Journal of Catalysis*, 179(1):163–170, October 1998.

[67] B. Hammer, O. H. Nielsen, and J. K. Nørskov. Structure sensitivity in adsorption: CO interaction with stepped and reconstructed Pt surfaces. *Catalysis Letters*, 46(1-2):31–35, 1997.

[68] T. Michely and G. Comsa. Temperature dependence of the sputtering morphology of Pt(111). *Surface Science*, 256(3):217–226, October 1991.

[69] J. Tang, J. M. Lawrence, and J. C. Hemminger. Structure and Valence of the Ce/Pt(111) System. *Physical Review B*, 48(20):15342–15352, November 1993.

[70] C. J. Baddeley, A. W. Stephenson, C. Hardacre, M. Tikhov, and R. M. Lambert. Structural and electronic properties of Ce overlayers and low-dimensional Pt-Ce alloys on Pt111. *Physical Review B*, 56(19):12589–12598, November 1997.

[71] B. Vermang, M. Juel, and S. Raaen. CO adsorption on Ce-Pt(111) studied with LEED, XPS, and temperature programmed desorption. *Physical Review B*, 73(3):033407, January 2006.

[72] A. Kildemo, A. Juel, and S. Raaen. Properties of Tm-Pt(111) surface alloys. *Surface Science*, 581(2-3):133–141, May 2005.

[73] A. Ramstad and S. Raaen. Formation of and CO adsorption on an inert La-Pt(111) surface alloy. *Physical Review B*, 59(24):15935–15941, June 1999.

[74] A. Ramstad, S. Raaen, and N. Barrett. Electronic structure of the La-Pt(111) surface alloy. *Surface Science*, 448(2-3):179–186, March 2000.

[75] Essen J. M., C. Becker, and Wandelt K. Pt_xCe_{1-x} Surface Alloys on Pt(111): Structure and Adsorption. *e-Journal of Surface Science and Nanotechnology*, 7:421–428, 2009.

[76] Nana Maria Pii Schumacher. *Nanoscale Modification of Copper for Novel Methanol and Water-Gas Shift Catalysts*. PhD thesis, Center for Individual Nanoparticle Functionality, Department of Physics, Technical University of Denmark, 2007.

[77] I. Chorkendorff. *Surface Physics/Chemistry*. Lecture notes, 2010.

[78] D. P. Woodruff and T. A. Delchar. *Modern Techniques of Surface Science*. Cambridge University Press, 1994.

[79] G. A. Somorjai. *Chemistry in Two Dimensions, Surfaces*. Cornell University Press, Ithaca, 1981.

[80] P. J. Cumpson. Angle-resolved XPS and AES - Depth-resolution limits and a general comparison of properties of depth-profile reconstruction methods. *Journal of Electron Spectroscopy and Related Phenomena*, 73(1):25–52, May 1995.

[81] D. Briggs and M. P. Seah. *Practical Surface Analysis*, volume 1 Auger and X-ray Photoelectron Spectroscopy. John Wiley & Sons Ltd., 1992.

[82] D. Briggs and M. P. Seah. *Practical Surface Analysis*, volume 2 Ion and Neutral Spectroscopy. John Wiley & Sons Ltd., 1992.

[83] H. Niehus and R. Spitzl. Ion Solid Interaction At Low Energies - Principles and Application of Quantitative ISS. *Surface and Interface Analysis*, 17(6):287–307, June 1991.

[84] H. H. Brongersma, M. Draxler, M. de Ridder, and P. Bauer. Surface composition analysis by low-energy ion scattering. *Surface Science Reports*, 62(3):63–109, March 2007.

[85] H. Niehus, W. Heiland, and E. Taglauer. Low-energy ion scattering at surfaces. *Surface Science Reports*, 17(4-5):213–303, 1993.

[86] K. Oura, V. G. Lifshits, A. A. Saranin, A. V. Zotov, and M. Katayama. *Surface Science, An introduction*. Springer-Verlag Berlin Heidelberg, 2003.

[87] J. B. Pendry. *Low Energy Electron Diffraction*. Academic Press, London and New York, 1974.

[88] http://www.fhi-berlin.mpg.de/ rammer/java/LEEDpat1/LEEDpat1.html.

[89] http://www.ap.cityu.edu.hk/personal-website/van-hove.htm.

[90] G. Sauerbrey. Verwendung von schwingquarzen zur wägung dünner schichten und zur mikrowägung. *Zeitschrift für Physik A Hadrons and Nuclei*, 155(2):206–222, 1959.

[91] S. W. Lee, S. Chen, W. Sheng, N. Yabuuchi, Y. T. Kim, T. Mitani, E. Vescovo, and Y. Shao-Horn. Roles of Surface Steps on Pt Nanoparticles in Electro-oxidation of Carbon Monoxide and Methanol. *Journal of the American Chemical Society*, 131(43):15669–15677, 2009. PMID: 19824642.

[92] A. den Dunnen. Master Research Project: "Surface Science Studies of the Reactivity of Pt(111) in Comparison to Nanoparticles", August 2010 – December 2010.

[93] J. Engbæk, O. Lytken, J. H. Nielsen, and I. Chorkendorff. CO dissociation on Ni: The effect of steps and of nickel carbonyl. *Surface Science*, 602(3):733–743, February 2008.

[94] H. Steininger, S. Lehwald, and H. Ibach. On the Adsorption of CO on Pt(111). *Surface Science*, 123(2-3):264–282, 1982.

[95] H. R. Siddiqui, X. Guo, I. Chorkendorff, and J. T. Yates. CO adsorption site exchange between step and terrace sites on Pt(112). *Surface Science*, 191(1-2):L813–L818, November 1987.

[96] M. R. McClellan, J. L. Gland, and F. R. McFeeley. Carbon monoxide adsorption on the kinked Pt(321) surface. *Surface Science*, 112(1-2):63–77, 1981.

[97] J. Xu and J. T. Yates. Terrace width effect on adsorbate vibrations : a comparison of Pt (335) and Pt (112) for chemisorption of CO. *Surface Science*, 327:193–201, 1995.

[98] S. Murphy, C. Strebel, S. B. Vendelbo, C. Conradsen, Y. Tison, K. Nielsen, L. Bech, R. M. Nielsen, M. Johansson, I. Chorkendorff, and J. H. Nielsen. Probing the crossover in CO desorption from single crystal to nanoparticulate Ru model catalysts. *Physical Chemistry Chemical Physics*, 13(21):10333–10341, 2011.

[99] R. M. Nielsen, S. Murphy, C. Strebel, M. Johansson, J. H. Nielsen, and I. Chorkendorff. A comparative STM study of Ru nanoparticles deposited on HOPG by mass-selected gas aggregation versus thermal evaporation. *Surface Science*, 603(24):3420–3430, December 2009.

[100] R. M. Nielsen, S. Murphy, C. Strebel, M. Johansson, I. Chorkendorff, and J. H. Nielsen. The morphology of mass selected ruthenium nanoparticles from a magnetron-sputter gas-aggregation source. *Journal of Nanoparticle Research*, 12(4):1249–1262, May 2010.

[101] S. Horch, H. T. Lorensen, S. Helveg, E. Læaegsgaard, I. Stensgaard, K. W. Jacobsen, J. K. Nørskov, and F. Besenbacher. Enhancement of surface self-diffusion of platinum atoms by adsorbed hydrogen. *Nature*, 398(6723):134–136, March 1999.

[102] A. V. Ruban, H. L. Skriver, and J. K. Nørskov. Crystal-structure contribution to the solid solubility in transition metal alloys. *Physical Review Letters*, 80(6):1240–1243, February 1998.

[103] A.E. Dwight, R.A. Conner, and J.W. Downey. Some AB3 Compounds of Transition Metals. *Acta Crystallographica*, 14(1):75–76, 1961.

[104] Jcpds powder diffraction file 004-0802.

[105] K. C. Neyerlin, R. Srivastava, C. F. Yu, and P. Strasser. Electrochemical activity and stability of dealloyed Pt-Cu and Pt-Cu-Co electrocatalysts for the oxygen reduction reaction (ORR). *Journal of Power Sources*, 186(2):261–267, January 2009.

[106] S. C. Ball, S. L. Hudson, B. R. Theobald, and D. Thompsett. PtCo, a Durable Catalyst for Automotive PEMFC? *ECS Transactions*, 11(1):1267–1278, 2007.

[107] I. E. L. Stephens, A. S. Bondarenko, L. Bech, and I. Chorkendorff. Oxygen electroreduction activity and x-ray photoelectron spectroscopy of alloys of platinum and early transition metals. *ChemCatChem*, 2011 (accepted).

[108] I. E.L. Stephens, A. S. Bondarenko, U. Grønbjerg, J. Rossmeisl, and I. Chorkendorff. Understanding the electrocatalysis of oxygen reduction on platinum and its alloys. *Submitted*, 2012.

[109] J. Greeley, I. E. L. Stephens, A. S. Bondarenko, T. P. Johansson, H. A. Hansen, T. F. Jaramillo, J. Rossmeisl, I. Chorkendorff, and J. K. Nørskov. Patent: WO 2011/006511 A1, Platinum and palladium alloys suitable as fuel cell electrodes, 2011.

[110] C. Strebel, D. McCarthy, A. Nierhoff, and P. Hernandez-Fernandez. Unpublished work, experiments perfomed in 2011 at the Center for Individual Nanoparticle Functionality (CINF), Technical University of Denmark (DTU).

[111] W. M. Haynes, editor. *"Standard thermodynamic properties of chemical substances", p. 5-17 in CRC Handbook of Chemistry and Physics*. CRC Press/-Taylor and Francis, Boca Raton, FL., Internet Version 2012.

[112] C. Wang, M. F. Chi, D. G. Li, D. Strmcnik, D. van der Vliett, G. F. Wang, V. Komanicky, K. C. Chang, A. P. Paulikas, D. Tripkovic, J. Pearson, K. L. More, N. M. Markovic, and V. R. Stamenkovic. Design and Synthesis of Bimetallic Electrocatalyst with Multilayered Pt-Skin Surfaces. *Journal of the American Chemical Society*, 133(36):14396–14403, September 2011.

[113] A. W. Grant, J. H. Larsen, C. A. Perez, S. Lehto, M. Schmal, and C. T. Campbell. Methanol decomposition on Pt/ZnO(0001)-Zn model catalysts. *Journal of Physical Chemistry B*, 105(38):9273–9279, September 2001.

[114] H. A. Hansen. *Density Functional Theory Studies of Electrochemical Processes*. PhD thesis, DTU Physics, 2009.

[115] P. Ferrin, A. Nilekar, J. Greeley, M. Mavrikakis, and J. Rossmeisl. Reactivity descriptors for direct methanol fuel cell anode catalysts. *Surface Science*, 602(21):3424–3431, November 2008.

[116] M. Ruff, N. Takehiro, P. Liu, J. K. Nørskov, and R. J. Behm. Size-specific chemistry on bimetallic surfaces: A combined experimental and theoretical study. *Chemphyschem*, 8(14):2068–2071, October 2007.

[117] P. N. Ross. Trends in the bonding of CO to the surfaces of Pt_3M alloys (M=Ti, Co, and Sn). *J. Vac. Sci. Technol. A*, 10:2546–2550, 1992.

[118] U. Bardi, B. C. Beard, and P. N. Ross. CO Chemisorption on the [111] and [100] Oriented Single Crystal Surfaces of the Alloy $CoPt_3$. *Journal of Catalysis*, 124(1):22–29, July 1990.

[119] A. H. Haner, P. N. Ross, U. Bardi, and A. Atrei. Surface composition determination of Pt-Sn alloys by chemical titration with carbon monoxide. *Journal of Vacuum Science & Technology A-vacuum Surfaces and Films*, 10(4):2718–2722, July 1992.

[120] M. Boaventura, H. Sander, K. A. Friedrich, and A. Mendes. The influence of co on the current density distribution of high temperature polymer electrolyte membrane fuel cells. *Electrochimica Acta*, 56(25):9467–9475, October 2011.

[121] H. F. Oetjen, V. M. Schmidt, U. Stimming, and F. Trila. Performance data of a proton exchange membrane fuel cell using H_2/CO as fuel gas. *Journal of the Electrochemical Society*, 143(12):3838–3842, December 1996.

[122] T. R. Ralph and M. P. Hogarth. Catalysis for Low Temperature Fuel Cells. *Platinum Metals Review*, 46(3):117–135, July 2002.

[123] M. J. T. C. van der Niet, A. den Dunnen, L. B. F. Juurlink, and M. T. M. Koper. The influence of step geometry on the desorption characteristics of O_2, D_2, and H_2O from stepped Pt surfaces. *Journal of Chemical Physics*, 132(17):174705, May 2010.

[124] M. J. T. C. van der Niet, A. den Dunnen, L. B. F. Juurlink, and M. T. M. Koper. A detailed TPD study of H_2O and pre-adsorbed O on the stepped Pt(553) surface. *Physical Chemistry Chemical Physics*, 13(4):1629–1638, 2011.

[125] G. Ertl, M. Neumann, and K. M. Streit. Chemisorption of CO On The Pt(111) Surface. *Surface Science*, 64(2):393–410, 1977.

[126] A. K. Jepsen and J. Rossmeisl. Unpublished work, calculations perfomed january 2012 at the Center for Atomic-scale Materials Design, Technical University of Denmark (DTU).

[127] U. G. Andersen and J. Rossmeisl. Unpublished work, calculations perfomed january 2012 at the Center for Atomic-scale Materials Design, Technical University of Denmark (DTU).

[128] A. Palenzona and S. Cirafici. The Pt-Y (Platinum-Yttrium) system. *Journal of Phase Equilibria*, 11(5):493–497, 1990.

[129] R. Z. Yang, J. Leisch, P. Strasser, and M. F. Toney. Structure of Dealloyed $PtCu_3$ Thin Films and Catalytic Activity for Oxygen Reduction. *Chemistry of Materials*, 22(16):4712–4720, August 2010.

[130] L. C. Grabow, B. Hvolbæk, and J. K. Nørskov. Understanding Trends in Catalytic Activity: The Effect of Adsorbate-Adsorbate Interactions for CO Oxidation Over Transition Metals. *Topics In Catalysis*, 53(5-6):298–310, May 2010.

[131] Ulrik Grønbjerg Andersen. Report: "activity and stability of platinum alloys for oxygen reduction". Catalysis and Sustainable Energy Solutions, course 10331, DTU Physics., June 29th, 2011.

[132] B. Predel. Pt-Y (Platinum-Yttrium). Madelung, O. (ed.). SpringerMaterials - The Landolt-Börnstein Database.

[133] B. Predel. Pt-Sc (Platinum-Scandium). Madelung, O. (ed.). SpringerMaterials - The Landolt-Börnstein Database.

List of included papers

Paper 1:

Alloys of platinum and early transition metals as oxygen reduction electrocatalysts.

J. Greeley, I.E.L. Stephens, A.S. Bondarenko, T.P. Johansson, H.A. Hansen, T.F. Jaramillo, J. Rossmeisl, I. Chorkendorff , and J.K. Nørskov.

Nature chemistry **1** (2009) 552 – 556

Paper 2:

Structural modification of Pt under high pressure CO annealing measured by Temperature Programmed Desorption.

D.N. McCarthy, A. Nierhoff, C.E. Strebel, T.P. Johansson, A. den Dunnen, J.H. Nielsen and I. Chorkendorff.

In preparation, draft included.

Paper 3:

Vacuum annealed polycrystalline Pt_3Sc as an electrocatalyst for oxygen reduction.

T.P. Johansson, E.T. Ulrikkeholm, P. Hernandez-Fernandez, P. Malacrida, A.S. Bondarenko, H.A. Hansen, I.E.L. Stephens, J. Rossmeisl, J.K. Nørskov and I. Chorkendorff.

In preparation, draft included

Paper 4:

Correlating the structure and reactivity for Y/Pt(111).

T.P. Johansson, E.T. Ulrikkeholm, P. Hernandez-Fernandez, P. Malacrida, U.G. Andersen, A.K. Jepsen, I.E.L. Stephens, J. Schiøtz, J. Rossmeisl and I. Chorkendorff.

In preparation, abstract included

Paper 5:

The Pt(111)/Electrolyte Interface under Oxygen Reduction Reaction Conditions: An Electrochemical Impedance Spectroscopy Study.

A.S. Bondarenko, I.E.L. Stephens, H.A. Hansen, F.J. Perez-Alonso, V. Tripkovic, T.P. Johansson, J. Rossmeisl, J.K. Nørskov and I. Chorkendorff.

Langmuir **27(5)** (2011) 2058 – 2066

Paper 6:

Tuning the Activity of Pt(111) for Oxygen Electroreduction by Subsurface Alloying.

I.E.L. Stephens, A.S. Bondarenko, F.J. Perez-Alonso, F. Calle-Vallejo, L. Bech, T.P. Johansson, A.K. Jepsen, R. Frydendal, B.P. Knudsen, J. Rossmeisl and I. Chorkendorff.

J. Am. Chem. Soc. **133(14)** (2011) 5485 – 5491

Patent

Patent:

Platinum and palladium alloys suitable as Fuel Cell electrodes

J.K. Nørskov, J. Greeley, I.E.L. Stephens, A.S. Bondarenko, T.P. Johansson, H.A. Hansen, T.F. Jaramillo, J. Rossmeisl and I. Chorkendorff.

PCT Patent WO2011/006511 A1

ARTICLES
PUBLISHED ONLINE: 23 SEPTEMBER 2009 | DOI: 10.1038/NCHEM.367
nature chemistry

Alloys of platinum and early transition metals as oxygen reduction electrocatalysts

J. Greeley[1†], I. E. L. Stephens[2], A. S. Bondarenko[2], T. P. Johansson[2], H. A. Hansen[1], T. F. Jaramillo[2†], J. Rossmeisl[1], I. Chorkendorff[2] and J. K. Nørskov[1*]

The widespread use of low-temperature polymer electrolyte membrane fuel cells for mobile applications will require significant reductions in the amount of expensive Pt contained within their cathodes, which drive the oxygen reduction reaction (ORR). Although progress has been made in this respect, further reductions through the development of more active and stable electrocatalysts are still necessary. Here we describe a new set of ORR electrocatalysts consisting of Pd or Pt alloyed with early transition metals such as Sc or Y. They were identified using density functional theory calculations as being the most stable Pt- and Pd-based binary alloys with ORR activity likely to be better than Pt. Electrochemical measurements show that the activity of polycrystalline Pt_3Sc and Pt_3Y electrodes is enhanced relative to pure Pt by a factor of 1.5–1.8 and 6–10, respectively, in the range 0.9–0.87 V.

The development of low-temperature polymer electrolyte membrane fuel cells (PEMFCs) is severely hampered by the fact that the oxygen reduction reaction (ORR) is slow, even when using platinum as a catalyst. Platinum is expensive and scarce, and it has been suggested that for PEMFCs to become viable using Pt-based catalysts, these catalysts would need to show stable catalytic activity of at least two to four times that of Pt[1]. Several Pt alloys, including late transition metals such as Ni, Co, Cr and Fe, together with partially dealloyed core-shell catalysts derived from Pt-Cu nanoparticles, are considerably more active than Pt and have been studied intensively[1–11]. In the present paper, we introduce a new set of Pt alloys and intermetallic compounds with promising properties for the ORR.

The ORR is a challenging reaction to catalyse in the sense that the catalyst material must be stable under the extremely corrosive conditions at a fuel cell cathode yet chemically active enough to be able to activate O_2 and noble enough to be able to release the oxygen from the surface in the form of H_2O. O_2 activation typically involves a proton and electron transfer to form adsorbed OOH before the O–O bond is broken[12], hence the catalyst must be able to stabilize OOH moderately. After dissociation, adsorbed O and OH are formed on the catalyst surface, and the catalyst must not bind these species too strongly in order for H_2O desorption to be fast.

We concentrate on metallic ORR catalysts made from alloys or intermetallic compounds (referred to hereafter as alloys). We will limit ourselves to systems that form Pt or Pd overlayers (or 'skins') at the surface. These are the only metallic elements that are stable under the high potentials and acidic conditions of a PEMFC and, at the same time, exhibit surface chemical properties close to optimum for the ORR[12]. The overall goal is to find alloys of the composition Pt_3X or Pd_3X using the following criteria: (1) they should form Pt or Pd overlayers with ORR activity larger than that of Pt, and (2) they should be as stable as possible. Our approach is to first use density functional theory (DFT) calculations to identify interesting candidates and to then test them experimentally[13,14]. Computationally based electrocatalyst discovery is the principal aim of this approach, but more generally and, perhaps, more importantly, this study probes our present understanding of the ORR. In the field of catalysis, there is no stronger evidence for the robustness and accuracy of a theoretical framework than the ability to use that framework to identify new active materials.

Results

Computational screening. Our understanding of ORR activity trends on different metal surfaces is summarized in Fig. 1. Plotting measured activities for a series of different catalysts from a number of different experimental groups as a function of the calculated oxygen adsorption energy results in a simple 'volcano' relationship[6,12]. Fig. 1a shows such a volcano for different Pt overlayers and demonstrates that the oxygen adsorption energy is a good descriptor for the catalytic activity.

The origin of this picture is the following. Density functional calculations of the free energy changes during the ORR (see Fig. 1b for further details) show that on close-packed Pt surfaces two reaction steps can be sluggish, that is, involve a positive change in free energy (ΔG): the first electron and proton transfer to form adsorbed OOH, and the last such transfer to remove OH (or O) from the surface to form water. We will use the values of ΔG for these steps (defined as ΔG_1 and ΔG_2, respectively) as a measure of the rate; the smaller the ΔG, the faster the corresponding reaction step is. The implicit assumption in this analysis is that any additional activation barriers are the same for all systems or that they scale with ΔG in a Brønsted–Evans–Polanyi-type relationship[15]; indeed, there is good evidence that this is a valid assumption[16]. By restricting our calculations to closely packed surfaces, another implicit assumption is that these dominate the activity of polycrystalline Pt and Pt_3X, as well as the surfaces of Pt nanoparticles in fuel cell catalysts. This also appears to be a reasonable conjecture, given that more open surfaces tend to bind O and OH considerably stronger and hence become blocked[17]. Moreover, experimental evidence suggests that the activity enhancement over

[1]Center for Atomic-scale Materials Design, Department of Physics, Building 311, Technical University of Denmark, DK-2800 Lyngby, Denmark, [2]Center for Individual Nanoparticle Functionality, Department of Physics, Building 312, Technical University of Denmark, DK-2800 Lyngby, Denmark; †Present address: Center for Nanoscale Materials, Argonne National Laboratory, Argonne, Illinois 60439 (J.G.), Department of Chemical Engineering, Stanford University, Stanford, California 94305-5025 (T.F.J.). *e-mail: norskov@fysik.dtu.dk

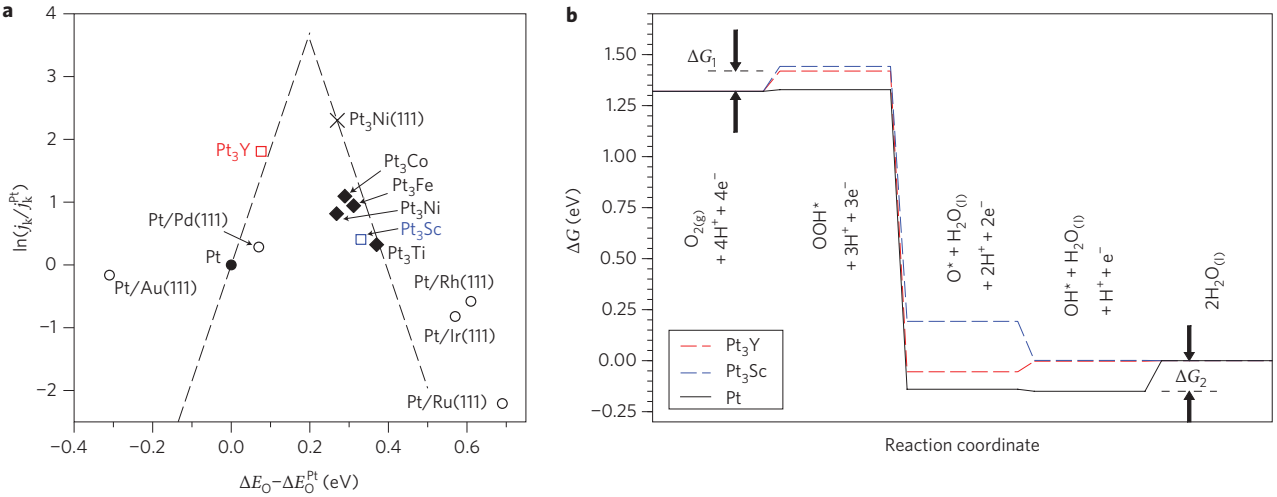

Figure 1 | Volcano plots and free-energy diagrams for the oxygen reduction reaction on Pt-based transition metal alloys. a, Measured kinetic current density as reported in the literature for a range of alloy electrocatalysts with Pt 'skins' plotted as a function of the calculated oxygen adsorption energy, ΔE_O. All data are shown relative to Pt. This removes many of the systematic variations in conditions of the different experiments. The sources of the experimental data are marked by: circles[34] (Pt monolayers supported on single-crystal metal electrodes), diamonds[6] (polycrystalline alloys annealed in ultrahigh vacuum before immersion in the electrochemical cell) and crosses[2] (bulk $Pt_3Ni(111)$ alloys annealed in ultrahigh vacuum before immersion). The dashed lines are the theoretical predictions from refs 12,35. We have also included data points for the Pt_3Y (red) and Pt_3Sc (blue) catalysts studied in the present work. **b**, Calculated free energy diagram for the oxygen reduction reaction at 0.9 V with respect to the reversible hydrogen electrode (RHE) under standard conditions for Pt(111) (solid line) and for Pt overlayers on the $Pt_3Sc(111)$ and $Pt_3Y(111)$ surfaces (dashed). The free energy changes for the formation of OOH (ΔG_1) and the removal of OH (ΔG_2) are indicated. In each case a water bilayer as well as electric field effects (see ref. 36) are included.

Pt observed on extended surfaces of Pt_3X alloys is reproduced qualitatively on nanoparticulate Pt_3X alloy surfaces[4,7,18].

On a given surface, the magnitudes of ΔG_1 and ΔG_2 (and thus the rate of the ORR) are related to the stability of adsorbed OOH, OH and O. Forming a Pt 'skin' on top of a Pt_3X compound is one way to modify the electronic structure of the Pt surface to tune the stability of these critical intermediates. The stabilities of the OOH and OH (and O) intermediates, in turn, scale roughly with the stability of adsorbed O (ΔE_O); hence, this parameter is particularly useful for characterizing both ΔG_1 and ΔG_2[19,20]. If ΔE_O becomes increasingly positive, adsorbed OOH is destabilized, resulting in a larger ΔG_1. Simultaneously, however, ΔG_2 decreases because it becomes easier to break the Pt–OH (and Pt–O) bonds. These opposing effects give rise to the volcano observed in Fig. 1a.

Figure 1a shows both experimental activity data as well as a dashed line indicating predicted activity based on our DFT model. Both the experimental data and the model strongly suggest that a surface that binds O 0.0–0.4 eV more weakly than Pt(111) should exhibit an ORR activity better than Pt, with the optimum at a binding energy of roughly 0.2 eV weaker than that of Pt. We note that, although all of the computational results in the figure are obtained on perfect, close-packed single crystal surfaces, the experimental data are taken from a mixture of single crystal, vacuum-annealed polycrystalline and Ar-sputtered polycrystalline surfaces. The resulting structural differences do introduce deviations from our single-crystal models, implying modest changes in ORR activity[21], but the differences do not substantially alter the trends described above.

In addition to looking for active skin-type Pt_3X or Pd_3X compounds for the ORR, we also searched for such alloys that are stable using a database developed from DFT calculations[22,23]. In Fig. 2, we show the calculated oxygen adsorption energy on the skins, ΔE_O relative to Pt, as a function of the calculated heat of formation of the bulk alloys, $\Delta E_{alloy} = E(\text{alloy}) - E(\text{constituents})$, where E is the total energy of the alloy and the constituents in metallic form, for a range of alloys.

One pathway to Pt or Pd skin formation is for Pt/Pd in the second layer of the close-packed (111) surface to exchange with X in the first layer; the concentration of X in the second layer then increases from the stoichiometric 25% to 50%[18]. Alternatively, a Pt skin may be formed simply by dissolution of X from the first layer, after which the remaining Pt atoms reaggregate to partially heal the surface. This latter process, which would be more likely to result in a stoichiometric (~25%) concentration of X in the layer below the Pt surface, is, in principle, possible for all of the alloys included in Fig. 2 because they have a standard potential for stripping, U_{strip}, which is more negative than, or approximately equal to, the oxide or hydroxide formation potential, U_{ox}. Whether the concentration of X in the second layer is stoichiometric or higher depends on the system and the method by which it is formed.

We have calculated the O adsorption energy for both 25 and 50% X in the second layer for a number of the systems considered. The systems with 50% X in the second layer will only have surface Pt/Pd atoms with X neighbours, whereas systems with only 25% X in the second layer have two inequivalent types of Pt atoms—those with X neighbours in the second layer and those without. Both types will in principle contribute to the activity, but in cases like Pt_3Y, those surface Pt atoms coordinated to purely Pt neighbours in the second layer will bind O too strongly and will be blocked. Only the less reactive sites with second-layer Y neighbours will be active (full details of the computational methods can be found in the Supplementary Information). These sites are approximately equivalent to the active surface sites on the second-layer systems with 50% X. We therefore concentrate in the following analysis on these systems (red points in Fig. 2).

It is clear from Fig. 2 that, of the alloys with ΔE_O values in the optimal range, Pt_3Y and Pt_3Sc stand out as the most stable. In fact, these are the most stable of all the face-centred cubic alloys in a database that consists of more than 60,000 compounds[22]. The common feature of these alloys is that they combine Pt or Pd and an early transition metal. The high stability of these compounds in the bulk can therefore be understood in terms of metal–metal d bonds that are approximately half filled (each of the two elements in the bond contribute half of nine d electrons for Pt or Pd plus one from X). This means that the bonding states are filled and the antibonding states are empty[24].

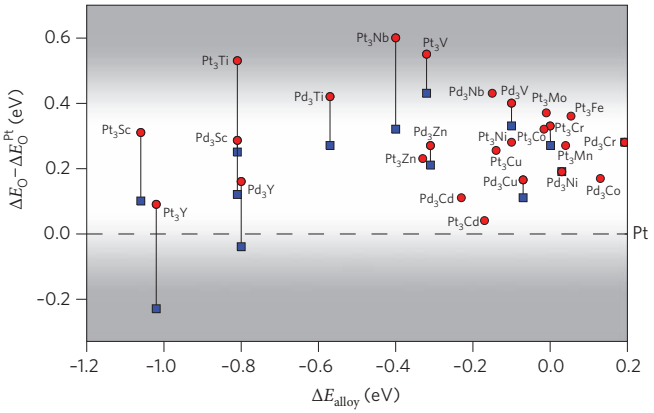

Figure 2 | Output of computational screening procedure, showing the oxygen binding energy, relative to that of Pt, on a Pt or Pd skin surface, as a function of alloying energy. ΔE_{alloy} is the calculated energy of formation of the indicated elements from the appropriate bulk elemental precursors, specified on a per atom basis. For some systems we include results for the cases where there are 50% (circles) and 25% (squares) of the alloying element in the second layer. The range of interesting oxygen adsorption energies where the ORR activity should be higher than that of Pt, according to the model, is highlighted with a greyscale gradient representing the edges of the range to recognize limitations on the accuracy of DFT calculations.

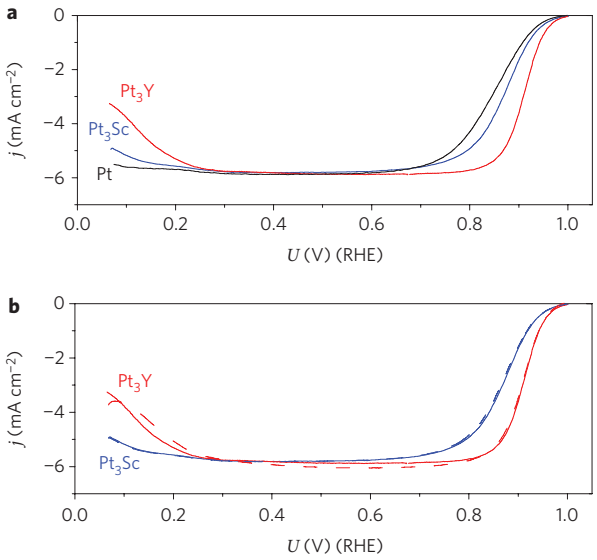

Figure 3 | Anodic sweeps of cyclic voltammograms of Pt, Pt_3Sc and Pt_3Y in O_2-saturated electrolyte. a, The first stable sweep. **b**, A comparison of the first steady cycle (solid lines) and after 90 minutes of cycling (dashed lines), for Pt_3Y and Pt_3Sc only, under the same conditions as **a**. Measurements were taken at 20 mV s^{-1} and 1,600 rpm in 0.1 M $HClO_4$ at 23 ± 2 °C.

We note that the favourable bulk heat of formation of Pt_3Y and Pt_3Sc is still not sufficient to make these alloys thermodynamically stable against oxidation or dissolution under the conditions of a cathode in a PEMFC. It is, however, expected to affect the kinetic stability of these compounds. Transport of Y or Sc atoms from the interior of the alloy to the surface, where they may eventually dissolve or oxidize, will involve an energy barrier determined in part by the heat of formation of the compound.

Experimental results. In the following, we report an experimental characterization of the two most promising (active and stable) compounds described above, Pt_3Y and Pt_3Sc. The alloys were prepared in bulk, polycrystalline form. To pre-condition the surfaces for electrochemical testing, they were sputter-cleaned and analysed under ultrahigh vacuum conditions, without vacuum annealing (full details of the experimental methods can be found in the Supplementary Information). The catalysts' electrochemical activity was measured using a rotating disc electrode assembly. These procedures were similar to those used by Markovic and co-workers in their investigations of other polycrystalline bimetallic Pt alloys[25].

The activity of the catalysts for the ORR was measured by carrying out cyclic voltammograms in an O_2-saturated solution, shown in Fig. 3a. The onset for each electrode starts at ~1 V, and there is an initial exponential increase in the current, characteristic of kinetic control. At lower potentials (~0.7 V < U < ~0.95 V), the current approaches the mixed regime, where mass transport plays an increasingly important role. This potential range is the most interesting for fuel cell applications. At still lower potentials, the current reaches its diffusion-limited value, ~5.8 mA cm^{-2}. In the mixed regime, the ORR activity of different catalysts can be compared by evaluating the half wave potential, $U_{1/2}$ (that is, the potential at which the current reaches half its diffusion-limited value). The ORR activity reported for polycrystalline Pt in this work corresponds well to data reported in the literature[7]. The Pt_3Sc shows a positive shift in $U_{1/2}$ of ~20 mV relative to Pt, whereas the Pt_3Y shows a positive shift of ~60 mV. These data show that both Pt_3Y and Pt_3Sc exhibit significant activity improvements over Pt, in line with our theoretical predictions.

Discussion

Modern PEMFCs have been designed for efficient delivery of reactive gases, thus mass transport effects are only of secondary importance; electrochemical kinetics are the primary cause of inefficiency[1]. In Fig. 4a, the measured current density is corrected for mass transport to obtain the true kinetic current density, j_k, of the catalyst, as a function of the potential, U. The same catalyst ranking is found as that determined by the half wave potential: activity increases in the following order: Pt < Pt_3Sc < Pt_3Y.

In Fig. 4b, the activity enhancement of Pt_3Sc and Pt_3Y over Pt is plotted as a function of potential. At 0.9 V, Pt_3Sc shows a 50% increase in specific activity over Pt, and Pt_3Y shows an improvement by a factor of six. At 0.87 V, Pt_3Sc shows an 80% increase in activity whereas the activity of Pt_3Y is enhanced by an order of magnitude. Owing to the steep gradient (or Tafel slope) of the polarization curve for Pt_3Y, the activity improvement over Pt should be even more pronounced at potentials below 0.87 V. To the best of our knowledge, the Pt_3Y electrode shows the highest ORR activity measured under these conditions for any bulk, polycrystalline metallic surface. The activity of our Pt_3Y sample is closer to that of single-crystal $Pt_3Ni(111)$[2] than to polycrystalline Pt_3Ni, which is not quite as active[7].

The alloy electrodes are stable under continued cycling, as shown in Fig. 3b. Long-term stability will, however, need to be investigated in membrane electrode assemblies in a fuel cell[26,27].

By combining the experimental activity data from Fig. 4a with the theoretically derived ΔE_O from Fig. 2, we have added the Pt_3Y and Pt_3Sc data points onto the volcano plot shown in Fig. 1a. Clearly, the new data follow the general trends very well. This result indicates that our model, describing trends in the ORR activity of alloys, has true predictive power. In Fig. 1b, we have also included more detailed calculations for the two alloy surfaces. It can be seen that the calculations support the notion that the free energy changes of the rate-limiting steps for Pt_3Y and Pt_3Sc are more favourable than the corresponding changes for Pt.

It is highly desirable to find ORR catalysts that are not only more active than Pt but also free from precious metals. The model discussed in the present work suggests two avenues. One is to find

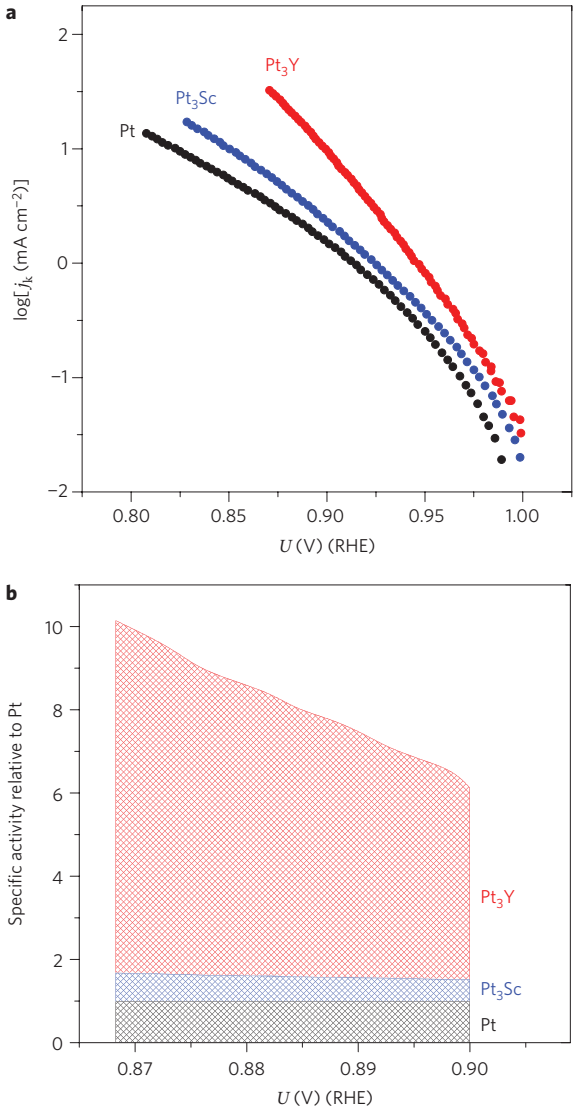

Figure 4 | Activity increase of Pt_3Y and Pt_3Sc versus Pt for the oxygen reduction reaction. a, Specific activity as a function of the electrode potential, *U*, for Pt, Pt_3Sc and Pt_3Y, expressed as a kinetic current density, j_k. **b**, Activity enhancement relative to Pt (j_k/j_k^{Pt}), from data shown in **a** and plotted on a linear scale. All data were extracted from the voltammograms shown in Fig. 3a.

alloys of non-precious metals with surface bonds to oxygen in the right range (0.0 to 0.4 eV weaker than Pt). The problem is that such alloys are usually not stable under polymer electrolyte fuel cell conditions[28]. A more radical approach is to find ways of avoiding the constraints of the volcano relationship in Fig. 1a. The volcano is the result of specific scaling relations between the stability of O, OH and OOH. If the structure of the active site is changed relative to the close-packed surfaces of metal alloys considered in the present paper, new scaling relations result and new volcanoes can arise. Rutile oxides have, for instance, been found to have a different volcano[29] and some rutile oxides show ORR activity[30]. The enzymes cytochrome *c* oxidases and multicopper oxidases, which catalyse the ORR with very high specific rates[31], represent interesting structures, and the recently reported iron-based catalysts[32] may represent another such interesting class of materials. However, for the time being the kinetic current densities of the Pt alloys are considerably higher owing to the high density of active sites[33], and our model offers a reliable path to the discovery of such alloys with useful properties.

Received 2 July 2009; accepted 12 August 2009; published online 23 September 2009

References

1. Gasteiger, H. A., Kocha, S. S., Somappli, B. & Wagner, F. T. Activity benchmarks and requirements for Pt, Pt-alloy, and non-Pt oxygen reduction catalysts for PEMFCs. *Appl. Catal. B-Environ.* **56,** 9–35 (2005).
2. Stamenkovic, V. *et al.* Improved oxygen reduction activity on $Pt_3Ni(111)$ via increased surface site availability. *Science* **315,** 493–497 (2007).
3. Koh, S. & Strasser, P. Electrocatalysis on bimetallic surfaces: modifying catalytic reactivity for oxygen reduction by voltammetric surface dealloying. *J. Amer. Chem. Soc.* **129,** 12624–12625 (2007).
4. Chen, S. *et al.* Origin of oxygen reduction reaction activity on "Pt_3Co" nanoparticles: atomically resolved chemical compositions and structures. *J. Phys. Chem. C* **113,** 1109–1125 (2009).
5. Wakisaka, W., Suzuki, H., Mitsui, S., Uchida, H. & Watanabe, M. Increased oxygen coverage at Pt-Fe alloy cathode for the enhanced oxygen reduction reaction studied by EC-XPS. *J. Phys. Chem. C* **112,** 2750–2755 (2008).
6. Stamenkovic, V. *et al.* Changing the activity of electrocatalysts for oxygen reduction by tuning the surface electronic structure. *Angew. Chem. Int. Ed.* **45,** 2897–2901 (2006).
7. Paulus, U. A. *et al.* Oxygen reduction on high surface area Pt-based alloy catalysts in comparison to well defined smooth bulk alloy electrodes. *Electrochim. Acta* **47,** 3787–3798 (2002).
8. Paulus, U. A. *et al.* Oxygen reduction on Carbon-Supported Pt-Ni and Pt-Co Alloy Catalysts. *J. Phys. Chem. B* **106,** 4181–4191 (2002).
9. Mayrhofer, K. J. J., Juhart, V., Hartl, K., Hanzlik, M. & Arenz, M. Adsorbate-induced surface segregation for core–shell nanocatalysts. *Angew. Chem. Int. Ed.* **48,** 3529–3531 (2009).
10. Koh, S., Leisch, J., Toney, M. F. & Strasser, P. Structure–activity–stability relationships of Pt–Co alloy electrocatalysts in gas-diffusion electrode layers. *J. Phys. Chem. C* **111,** 3744–3752 (2007).
11. Koh, S., Toney, M. F. & Strasser, P. Activity–stability relationships of ordered and disordered alloy phases of Pt_3Co electrocatalysts for the oxygen reduction reaction (ORR). *Electrochim. Acta* **52,** 2765–2774 (2007).
12. Nørskov, J. K. *et al.* Origin of the overpotential for oxygen reduction at a fuel cell cathode. *J. Phys. Chem. B* **108,** 17886–17892 (2004).
13. Nørskov, J. K, Bligaard, T., Rossmeisl, J. & Christensen, C. H. Towards the computational design of solid catalysts. *Nature Chem.* **1,** 37–46 (2009).
14. Strasser, P., Fan, Q., Devenney, M. & Weinberg, W. H. High throughput experimental and theoretical screening of materials—a comparative study of search strategies for new fuel cell anode catalysts. *J. Phys. Chem B* **107,** 11013–11021 (2003).
15. Skulason, E. *et al.* Density functional theory calculations for the hydrogen evolution reaction in an electrochemical double layer on the Pt(111) electrode. *Phys. Chem. Chem. Phys.* **9,** 3241–3250 (2007).
16. Janik, M. J., Taylor, C. D. & Neurock, M. First-principles analysis of the initial electroreduction steps of oxygen over Pt(111). *J. Electrochem. Soc.* **156,** B126–B135 (2009).
17. Greeley, J., Rossmeisl, J., Hellman, A. & Nørskov, J. K. Theoretical trends in particle size effects for the oxygen reduction reaction. *Z. Phys. Chem.* **221,** 1209–1220 (2007).
18. Stamenkovic, V. R. *et al.* Trends in electrocatalysis on extended and nanoscale Pt-bimetallic alloy surfaces. *Nature Mater.* **6,** 241–247 (2007).
19. Rossmeisl, J., Logadottir, A. & Nørskov, J. K. Electrolysis of water on (oxidized) metal surfaces. *Chem. Phys.* **319,** 178–184 (2005).
20. Abild-Pedersen, F. *et al.* Scaling properties of adsorption energies for hydrogen-containing molecules on transition-metal surfaces. *Phys. Rev. Lett.* **99,** 016105 (2007).
21. Stamenkovic, V. R., Mun, B. S., Mayrhofer, K. J. & Ross, P. N., Markovic, N. M. Effect of surface composition on electronic structure, stability, and electrocatalytic properties of Pt-transition metal alloys: Pt-skin versus Pt-skeleton surfaces. *J. Am. Chem. Soc.* **128,** 8813–8819 (2006).
22. Johannesson G. H. *et al.* Combined electronic structure and evolutionary search approach to materials design. *Phys. Rev. Lett.* **88,** 255506 (2002).
23. Bligaard, T. *et al.* Pareto-optimal alloys. *Appl. Phys. Lett.* **83,** 4527–4529 (2003).
24. Ruban, A. V., Skriver, H. L. & Nørskov, J. K. Crystal-structure contribution to the solid solubility in transition metal alloys. *Phys. Rev. Lett.* **80,** 1240 (1998).
25. Stamenkovic, V. R., Schmidt, T. J., Ross, P. N. & Markovic, N. M. Surface composition effects in electrocatalysis: kinetics of oxygen reduction on well-defined Pt_3Ni and Pt_3Co alloy surfaces *J. Phys. Chem. B* **106,** 11970–11979 (2002).
26. Neyerlin, K. C., Srivastava, R., Yu, C. & Strasser, P. Electrochemical activity and stability of dealloyed Pt–Cu and Pt-Cu-Co electrocatalysts for the oxygen reduction reaction (ORR). *J. Power Sources* **186,** 261–267 (2009).
27. Ball, S. C., Hudson, S. L., Theobald, B. R. C. & Thompsett, D. PtCo, a durable catalyst for automotive proton electrolyte membrane fuel cells? *ECS Transactions* **11,** 1267–1278 (2007).

28. Greeley, J. & Nørskov, J. K. Combinatorial density functional theory-based screening of surface alloys for the oxygen reduction reaction. *J. Phys. Chem. C* **113,** 4932–4939 (2009).
29. Rossmeisl, J., Qu, Z.-W., Zhu, H., Kroes, G.-J. & Nørskov, J. K. Electrolysis of water on oxide surfaces. *J. Electroanal. Chem.* **607,** 83–89 (2007).
30. Takasu, Y., Yoshinaga, N. & Sugimoto, W. Oxygen reduction behavior of RuO_2/Ti, IrO_2/Ti and IrM (M: Ru, Mo, W, V) O_x/Ti binary oxide electrodes in a sulfuric acid solution. *Electrochem. Commun.* **10,** 668–672 (2008).
31. Mano, N., Soukharev, V. & Heller, A. A laccase-wiring redox hydrogel for efficient catalysis of O_2 electroreduction. *J. Phys. Chem. B* **110,** 11180–11187 (2006).
32. Lefèvre, M., Proietti, E., Jaouen, F. & Dodelet, J.-P. Iron-based catalysts with improved oxygen reduction activity in polymer electrolyte fuel cells. *Science* **324,** 71–74 (2009).
33. Gasteiger, H. A. & Markovic, N. M. Just a dream—or future reality? *Science* **324,** 48 (2009).
34. Zhang, J. L, Vukmirovic, M. B., Xu, Y., Mavrikakis, M. & Adzic, R. R. Controlling the catalytic activity of platinum-monolayer electrocatalysts for oxygen reduction with different substrates. *Angew. Chem. Int. Ed.* **44,** 2132–2135 (2005).
35. Rossmeisl, J., Karlberg, G. S., Jaramillo, T. F. & Nørskov, J. K. Steady state oxygen reduction and cyclic voltammetry. *Faraday Discuss.* **140,** 337–346 (2008).
36. Karlberg, G. S., Rossmeisl, J. & Nørskov, J. K. Estimations of electric field effects on the oxygen reduction reaction based on the density functional theory. *Phys. Chem. Chem. Phys.* **9,** 5158–5161 (2007).

Acknowledgements

J.G. and T.F.J. are both recipients of H. C. Ørsted Postdoctoral Fellowships from the Technical University of Denmark. Funding by the Danish Council for Technology and Innovation's FTP program and by the Danish Strategic Research Council's HyCycle program is gratefully acknowledged. The Center for Atomic-scale Materials Design is supported by the Lundbeck Foundation. The Center for Individual Nanoparticle Functionality is supported by the Danish National Research Foundation.

Author contributions

J.G., H.A.H., J.R. and J.K.N. contributed to the computational work in this paper. I.E.L.S., A.S.B., T.P.J., T.F.J., and I.C. contributed to the experimental work.

Additional information

Supplementary information accompanies this paper at www.nature.com/naturechemistry. The authors declare competing financial interests: details accompany the full-text HTML version of the paper at www.nature.com/naturechemistry. Reprints and permission information is available online at http://npg.nature.com/reprintsandpermissions/. Correspondence and requests for materials should be addressed to J.K.N.

Structural modification of Pt under high pressure CO annealing measured by Temperature Programmed Desorption

D. N. McCarthy,[1] C.E. Strebel,[1] T.P. Johansson,[1] A. den Dunnen,[1] A. Nierhoff,[1] J.H. Nielsen,[1] and Ib Chorkendorff[1]

[1] *Center for Individual Nanoparticle Functionality, Department of Physics, Technical University of Denmark, 2800 Kgs. Lyngby, Denmark**

Abstract

Using temperature programmed desorption experiments, we have studied the adsorption of CO on both Platinum (Pt) single crystals, and mass-selected Pt nanoparticles in the size range of 2nm to 10nm, for CO dosing pressures in 10-7mbar and mbar ranges. From low pressure CO adsorption experiments on the Pt(111) crystal, we establish a clear link between the degree of pre-sputtering of the surface prior to CO adsorption, and the amount of CO bound at high temperature. It was found that the rougher, or more defect rich, the surface, the greater the amount of tightly bound CO. The result is consistent with literature results from stepped single crystals that have found high temperature desorption features of CO due to the presence of step and kink sites on the crystal facets. For the nanoparticles, a study of the dependence of the CO desorption profile with particle size revealed an increase in tightly bound CO as the nanoparticle size was decreased, consistent with the expectation for more under-coordinated sites at smaller particle sizes. Thus, for both systems there is a clear relation between surface roughness or coordination, and the temperature of the CO desorption. Investigation of these structural features was then made for mbar CO dosing pressures. Intriguingly, from these experiments it was observed that elevated CO pressures enhanced the annealing of the Pt(111) surface, but on the otherhand, caused an apparent roughening of the nanoparticles.

PACS numbers:

INTRODUCTION

The structural modification of nanoscale systems due to adsorbate-surface interactions can be observed via a number of spectroscopic techniques: electron microscopy [1, 2], scanning tunneling microscopy in both gaseous and liquid environments [3–5], and also through techniques such as XRD [6]. The modification of surfaces due to environmental conditions is important for applications such as catalysis, where reaction rates can be strongly influenced by surface structure [7, 8], for instance in the formation of steps that could aid bond dissociation. With the advent of atom-sensitive techniques that operate nearer to reaction conditions (e.g. high pressure XPS, Environmental-TEM), the richness of the surface dynamics during reactions can be observed. Surface dynamics are interesting in many respects, but in particular to heterogeneous catalysis, where catalysts have traditionally been considered to play essentially a spectator role in reactions. Modern studies now reveal the dynamics of particle surfaces; changes to oxidation state, surface roughness, and surface elemental composition of alloy materials, have all been observed. These types of changes are all relevant to catalytic activity - a recent example reported by Hendriksen and coworkers [6] (for an earlier review see [9]) where spontaneous oscillations in CO oxidation rates of a Pd crystal were related to rapid oscialltory changes of the oxidation state and surface roughness of the crystal surface. Further investigations into different material systems are then warranted.

In this report we present investigations into Pt crystals and nanoparticles. Platinum is a highly studied catalyst material due to its noble bonding characteristics, which makes it a suitable (albeit expensive) material for catalytic reactions that involve reactive gases such as oxygen, where the use of less noble metals could be complicated by processes such as oxidation. Currently, there is significant interest in Pt (and it's alloys) in electrochemical environments, due to their high activity for reactions such as oxygen reduction and methanol oxidation, where the noble properties of Pt are especially important for it's high activity, and it's long term stability in typically acidic environments. Pt catalysts are also important in gas phase reactions such as in the oxidation of soot and hydrocarbons in exhaust systems. Knowledge of the modifications of Pt surfaces undergo due to gas composition and temperature is clearly important for understanding the performance of Pt as a catalyst, both in terms of it's activity, but also with regards to it's long term stability against processes such as sintering, or dissolution. Advances to our understanding of environmentally induced

changes to a catalyst could help lead to fundamental advances in catalyst design, leading to their implementation of environmentally friendly fuel cell technologies.

In contrast to the expensive spectroscopic techniques such as E-TEM, HP-XPS (which typically requires synchrotron facilities), a comparatively simple way to probe surface structure is to use gas adsorption, combined with temperature programmed desorption. Changes to surface structure, in particular changes to the coordination of the surface atoms, should be apparent in the desorption profile due to the coordination dependent binding energies of gas molecules [10]. The adsorption of CO on Pt has been studied thoroughly in past decades, for various surface terminations of the Pt single crystal. For low index surface orientations, adsorbate structures of CO have been studied with high precision using techniques such as Scanning Tunneling Microscopy, Low Energy Electron Diffraction (LEED), temperature programmed desorption (TPD), and Electron Energy Loss (EELS). From the annealed Pt(111) crystal surface, Steininger et al [11] observed the desorption of CO over a broad temperature range, from 300K to 500K. From LEED experiments, a variety of different CO adsorbate structures were observed, depending on the CO coverage. In order to investigate the CO desorption temperatures of less coordinated atoms, McClellan et al [12] performed similar CO adsorption experiments on the Pt(321) surface (essentially a (111) surface with monatomic steps every three atoms). From these experiments the desorption of CO was observed in two distinct temperature ranges: from 300 to 500K, and from 500 to 600K. The two desorption features were respectively attributed to CO bound on fullly coordinated Pt terrace atoms, and to undercoordinated Pt atoms at steps and kinks. Thus it is possible to distinguish desorption sites using TPD.

The main objective of the present work is to investigate the structural changes induced by CO absorption on both a roughened Pt(111) single crystal and nanoparticulate samples. Our work is motivated by STM experiments which have shown reconstructions of Pt surfaces in CO atmospheres [3, 4, 13], for CO pressures ranging from high vacuum to near atmospheric pressure. In those experiments, the reconstruction of the Pt surface due to CO coverages has been variously argued to result from entropic considerations for Pt(110) surfaces, or strain effects in vicinal Pt(111) surface. Strain is certainly an important consideration for nanoparticles, and it is therefore interesting to consider the effect of CO on nanoparticles of different sizes, and at different pressures/temperatures. Using TPD experiments, we demonstrate the similarity between the desorption features of CO from roughened single

crystals and nanoparticles, linking the undercoordinated sites of the two systems. We then perform comparative experiments at 10mbar, and different temperatures, and discover modifications to the desorption spectra for the two systems, which are interpreted as an annealing out of the single crystal, versus a roughening of the nanoparticles. An apparent size dependence to the roughening of the nanoparticles suggests some strain dependence.

EXPERIMENT

The experimental results described in this report were performed in two separate UHV systems. Experiments on Pt nanoparticles were performed in a multichamber ultrahigh vacuum (UHV) system (Omicron, Multiscan Lab) with a base pressure in the low 10^{-11} mbar region. This system is equipped with facilities for combined scanning tunneling microscopy (STM) and scanning electron microscopy (SEM), as well as Auger electron spectroscopy (AES), Ion scattering spectroscopy (ISS) and temperature programmed desorption (TPD) measurements. A second UHV system with a base pressure below 10^{-10} mbar was used for the Pt(111) experiments. This chamber is equipped with facilities for TPD, ISS, and X-ray photoelectron spectroscopy (XPS). Both vacuum systems are equipped with high pressure cells into which samples can be transferred and dosed at pressures up to 1bar. The high pressure cells are attached directly to the main vacuum chambers, and have dedicated pumping and gas dosing lines, which allows for sample transfer and dosing without exposure of the samples to outside contamination.

The nanoparticle production and analysis setup

Mass-selected nanoparticles were deposited from an inert-gas aggregation source (Mantis Deposition Ltd.), which is described in detail elsewhere [14–16]. Briefly, a flux of Pt atoms is produced in a source chamber by magnetron sputtering of a 99.9 percent purity Pt target (Williams Advanced Materials Inc.). Sputtered atoms are then condensed into nanoparticles using cooled Ar or He atoms, and carried from the source chamber through an exit nozzle into a flight tube. As a significant fraction of the nanoparticles produced using this method are singly ionized, within the flight tube is a quadrupole mass filter which is used to filter the nanoparticle beam according to a particular mass/charge ratio. The nanoparticles

exiting the quadrupole are then focused via electrostatic lenses onto SiO_2 wafers mounted in Omicron VT sample holders in the main vacuum chamber. For these experiments the nanoparticles are deposited in the soft-landing regime (i.e. they have a kinetic energy of ≤ 0.1eV/atom).

An interesting aspect of this work is the choice of substrate, which in this case is a 100nm thick SiO_2 layer grown via wet chemistry on a 300μm thick Si(111) wafers. The wafer design will be described more fully in a future publication, but certain important details should be mentioned. Firstly, the wafer has a sandwich type structure, with the 100nm thick SiO_2 on the topside, supported by the Si(111) wafer, which has on the backside a Platinum resistance-temperature device (RTD) lithographically integrated to allow for accurate temperature measurements. During the temperature programmed desorption experiments, the Si wafers were heated resistively by passing DC current through the Si wafer, with the wafer temperature monitored by measuring the resistance of the RTD, and comparing with externally calibrated temperature/resistance curves. Note that the TD was electrically isolated from the Si wafer itself via a 100nm thick Silicon Nitride layer. The wafers were designed and produced at DTU-Nanotech.

To ensure the cleanliness of the samples prior to the CO adsorption experiments, after insertion into UHV the entire manipulator head (including sample holder and sample) were degassed at 600°C for 12hrs. The Si-wafers were then annealed to 500°C based on the RTD calibration, and then exposed to 10^{-6}mbar O_2 for 30mins, to oxidize any hydrocarbons that might be present on the SiO2 surface. After the oxidation, samples were cooled to room temperature (typically 45 minutes) before the nanoparticles were deposited onto the surface. Ion Scattering Spectroscopy (ISS) was used to confirm the cleanliness of the as cleaned SiO2 surface, and of the surface directly after the deposition of Pt nanoparticles. The ISS spectra were recorded using 980 eV He^+ ions produced by a differentially pumped electron impact ion source (ISE 100, Omicron Nanotechnology). The reflected ions were detected at a 147° scattering angle with a hemispherical energy analyser.

Temperature programmed desorption experiments were performed in the preparation chamber of the UHV system. The samples were dosed with isotopically labeled CO30 molecules, 12C18O (CIL, 2per 16O), to distinguish from the background CO28. The CO30 was dosed through a leak valve until a chamber pressure of 10^{-7} mbar was attained, for a dosing time of 10 min, corresponding to an exposure of 60 Langmuir, sufficient to saturate

the surface. After dosing was completed, the chamber was evacuated, then the sample temperature was ramped at a rate of 1 K/s in UHV and the CO desorption from the substrate was analysed using a differentially pumped Balzers QMA 125 quadrupole mass spectrometer. The spectrometer was equipped with an oxygen-free high conductivity (OFHC) copper sniffer tip with a 1 mm diameter aperture, positioned within 0.5 mm of the sample surface. This arrangement allows the local gas composition above the sample surface to be measured with negligible contribution from the sample holder or surroundings. The temperature ramp of the TPD was controlled via a Labview script that limited the power supply heating the Si-wafer via based on the resistance measured across the RTD.

Single Crystal

For the single crystal experiments, performed in the second vacuum system, we used a 5mm diameter Pt(111) single crystal supplied by MaTecK. The crystal has three through holes drilled parallel to the surface (111) plane. A 0.38mm tungsten wire used for heating is looped through two of these holes, while a K-type thermocouple is secured into the third hole to allow for measurement of the crystal temperature. The back ends of the tungsten loop are screwed onto a cryostat, which could be air cooled to 300K, or to 80K using liquid nitrogen. A PID algorithm linking the power supply to the tungsten wire, and the thermocouple allowed for constant temperature.

The Pt(111) single crystal was cleaned by sputtering with 1.2 keV Ar ions, with the crystal temperature maintained at 1273 K. After sputtering, the crystal was annealed for a further minute at 1273 K. The cleanliness of the crystal was verified by ISS, and XPS, as well as oxygen titration experiments. In order to roughen the Pt crystal surface, the crystal was sputtered with Ar ions at various temperatures between 88 K and 673 K. In these experiments, the crystal was sputtered under the same conditions as for the cleaning procedure, however with the crystal temperature kept constant, and with no post sputter annealing treatment. It was observed that after the sputtering, a 1min anneal of the crystal to 1273 K could return the crystal surface to the state seen for the as annealed crystal, as determined by XPS, and CO desorption experiments. Therefore the sputtering process does not contaminate the surface.

In the TPD experiments, CO28 was dosed by background dosing at $2 * 10^{-7}$ mbar for

500 seconds while cooling the crystal down from the temperature at which it was sputtered. When air cooling was used the crystal did not cool down sufficiently fast and dosing CO for an extra 500 seconds was needed till the sample reached a temperature of 313 K. The total CO dose was on the order of 100 L, more than sufficient to saturate the surface with CO.

For HPC CO experiments, the sample was sputtered at 373 K or 573 K in the UHV chamber. CO was dosed by background dosing at $2 * 10^{-7}$ mbar for 500 seconds while cooling down the crystal. The sample was taken down to the HPC (while still dosing CO) and the HPC was sealed off from the UHV chamber. CO was subsequently dosed at a pressure of 2 mbar or 11 mbar while heating up the sample to the same temperature as where the sample was sputtered at (373 K or 573 K) and kept at that temperature for 10 minutes. After 10 minutes the sample was cooled down while still dosing CO for 500 seconds. After pumping out the HPC, the sample was moved back to the UHV chamber for analysis.

Mbar range CO experiments

For CO dosing pressures in the mbar range, an important consideration is the potential for Ni-carbonyls present in the gas to react on the Pt surface, and deposit Ni. In order to minimise the potential for Ni contamination, the CO28 gas was passed through an active carbon filter, and secondly through a liquid nitirogen cold trap. In addition to the gas cleaning procedures, the gas lines leading from the filters to the high pressure cell are made from copper, rather than stainless steel, and the high pressure cells are constructed from Ni free steel. After the high pressure experiments, the lack of any Ni contamination in both the nanoparticle and single crystal systems was verified by ISS, or XPS, respectively.

RESULTS

Structural features for low pressure CO dosing

In Fig. 1 we show the CO TPD spectra from the Pt(111) single crystal, prepared with different degrees of sputtering: annealed at 1200K, sputtered at 373K, sputtered at 573K, and sputtered at 673K. In the figure, the ion signals from the desorbing CO have been normalised to their maximum signal height to enhance the sputter dependent desorption features of each spectra. From the purely annealed crystal, the CO desorption spectra is a

single broad feature spanning from 300K to 500K, consistent with results by Steininger [11]. In comparison, for sputtered crystal surfaces a second desorption feature appears in the spectra between 500K and 550K. It is clear from the figure that the lower the sputtering temperature, and therefore the rougher the surface [17], the more significant the shoulder at high temperature. This trend is consistent with the expectation for undercoordinated Pt atoms present on the rougher/sputtered surface to provide stronger adsorption sites for CO molecules [10], which should be apparent as a shift in CO desorption to higher temperatures. To summarise, the rougher the surface, the higher the proportion of strongly bound CO.

A second, less obvious feature of the CO desorption spectra from the single crystal is the narrowing of the low temperature desorption feature for increased surface roughness, and a slight shifting of the peak position of the main desoprtion feature to higher temperatures; compare the low temperature peak positions for the crystal when sputter annealed at 373K (T_{peak} ~400K), versus that of the crystal sputter annealed at 573K (T_{peak} ~390K). As both these peak temperatures are encompassed by the broad desorption feature from the purely annealed crystal, the narrowing and shifting with lower sputter temperatures suggests a disruption of the ordering of CO on the terraced surface regions. The narrowing of the peak, and shift to higher temperatures is reminiscent of the desorption feature observed by Steininger for low coverage doses e.g. 30% coverage of the CO monolayer, as well as the comparatively narrow low temperature desorption features observed on the stepped Pt(112) [18] and Pt(321) surfaces [12]. Besenbacher cov dependence?.

In Fig. 2 we present TPD spectra taken from the single crystal, both after annealing and after room temperature sputtering, and compare these with the TPD spectra of ~ 11nm Pt nanoparticles supported on SiO2. As the samples were prepared in different vacuum systems, the CO dosing and TPD procedures were made as similar as possible. In the case of the single crystal, CO was dosed at 10-7mbar for 10 mins, directly after annealing or sputtering of the crystal. The CO TPD's were then performed at a heating rate of 1K/s. For the nanoparticle sample, CO was dosed immediately after the particle deposition was completed (depositions typically take 10minutes from start to finish), at 10-7mbar for 10 minutes, before performing the temperature ramp at 1K/s. Again the spectra have been normalised to their respective maxima to better compare the shapes of the desorption spectra. The desorption spectra taken from the single crystal are similar to those shown in Fig. 1, consistent with the minor change in ramp rate. More noteworthy is the desorption profile from the 11nm particles: here

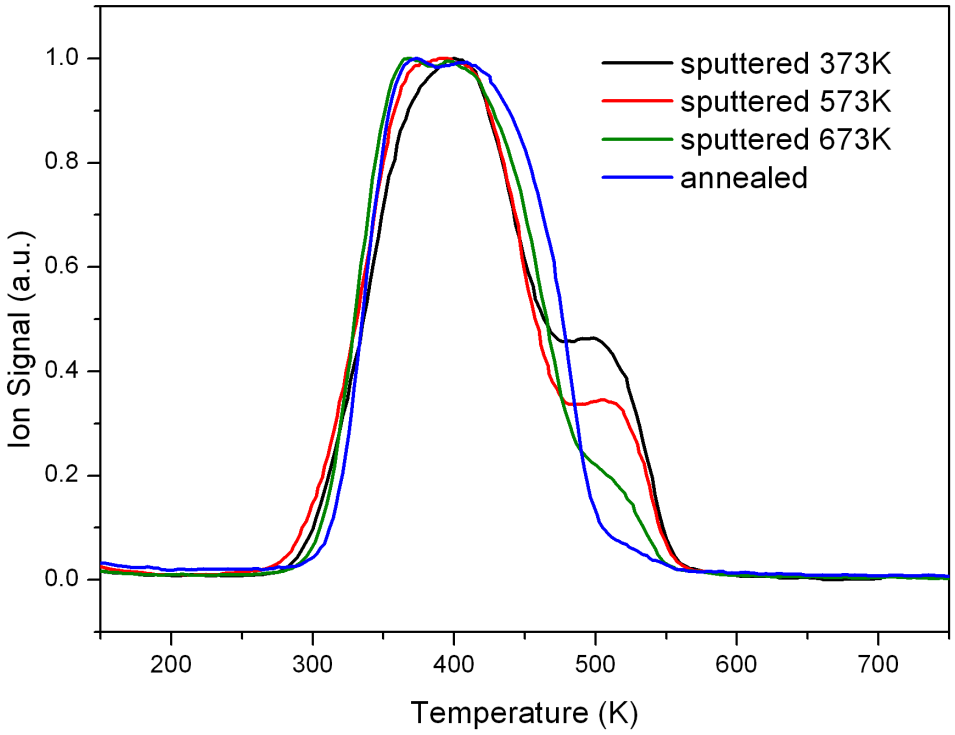

FIG. 1: CO TPD spectra from the Pt(111) crystal after different preparations. Ramp rates of 2K/s.

the CO desorption kicks off at essentially the same temperature as the SC (though slightly later than both SC spectra), then forms a comparatively narrow main feature centred at 390K, followed by a shoulder at high temperature that extends to 575K. For comparison, in the TPD spectra of the sputtered SC the CO is fully desorbed by 540∼550K.

In Fig. 3 we show TPD spectra from three different samples, where the nanoparticles of the individual samples were produced by optimising the source conditions for 3nm, 6nm, and 11nm. The ion signals have been normalised to the maximum signal height to make apparent the different desorption profiles for each system. From Fig. 3 we can see that as the mean nanoparticle size is reduced from 11nm to 3nm, the high temperature feature in the CO desorption spectra becomes more prominent. The trend is consistent with the idea of smaller nanoparticles having a higher proportion of undercoordinated sites. In addition to the increased amount of CO bound at undercoordinated sites, for smaller particles, there

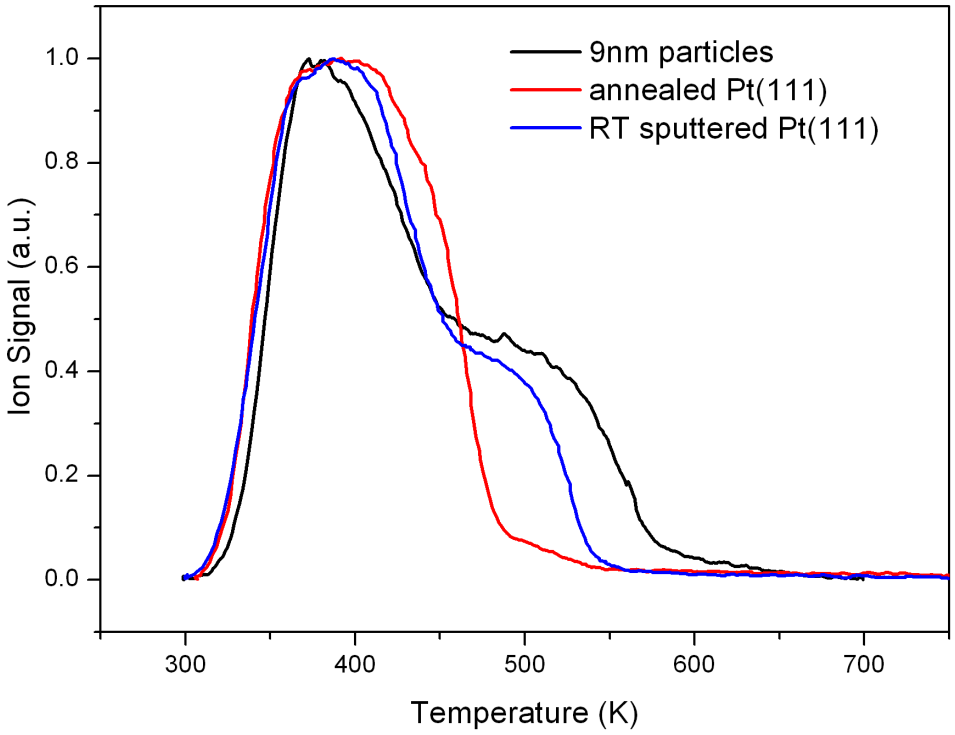

FIG. 2: Comparison of CO TPD spectra from the annealed Pt(111) crystal, a sputtered, and 9nm/SiO_2 nanoparticles. Each of the samples was dosed at room temperature, in a background CO pressure of 10-7mbar for ten minutes, and the ramp rate of each TPD was 1K/s.

is a minor shift towards higher initial desorption temperatures for the CO. A size dependent binding energy has been observed for oxygen atoms on small Pt particles [19]. However an opposite effect has been observed for Pt aggregates grown by a diffusion aggregation process on HOPG, in this case the later desorption temperature postulated to occur due to core level shifts in the Pt nanostructures [20]. Note that these TPDs were taken from freshly deposited (unannealed) particles, and are expected to have some roughness from the aggregation process i.e. the particles are not perfect Wulff shapes. Consecutive TPDs were taken which showed no major changes, except for a reduction of the shoulder feature, consistent with our expectation for some minor annealing of the particles due to the TPD, that should reduce some of the initial roughness.

Figures 1, 2, 3 demonstrate that the temperature dependence of the CO desorption is

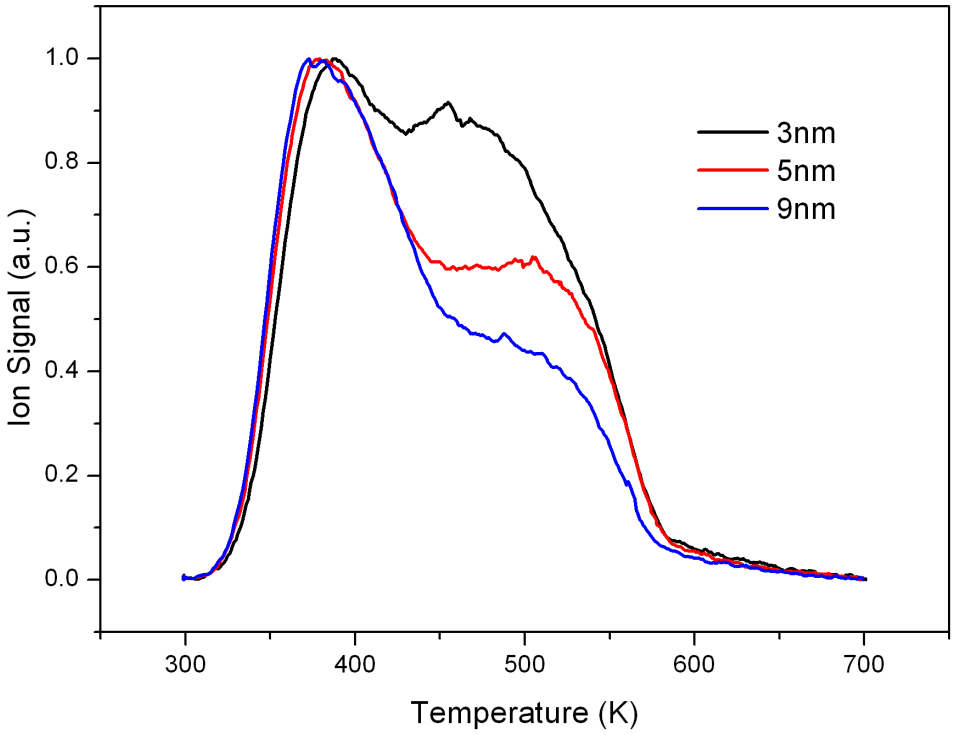

FIG. 3: CO TPD spectra from Pt nanoparticles produced using source conditions and filtering for 3nm, 6nm, and 11nm particles, deposited onto SiO2 supports. The ramp rate was 1K/s.

closely linked to the coordination of the exposed Pt atoms, and that CO TPDs is a useful probe of surface structure.

Structural features for high pressure CO dosing and annealing

Having established the use of CO TPDs as a way to probe the surface structure of Pt, in the next set of experiments we investigate the effects of higher CO pressures on the structure of the different Pt systems. In Fig. 4 we show CO desorption spectra from crystals sputtered at 373K, then maintained at this temperature in 10mbar CO. We also show the same experiments from a sample sputtered at 573K, then maintained at this temperature in 10mbar CO. Each high pressure spectra is compared against spectra taken from the sputtered crystals after annealing in vacuum for 10mins at the same temperature. It can be

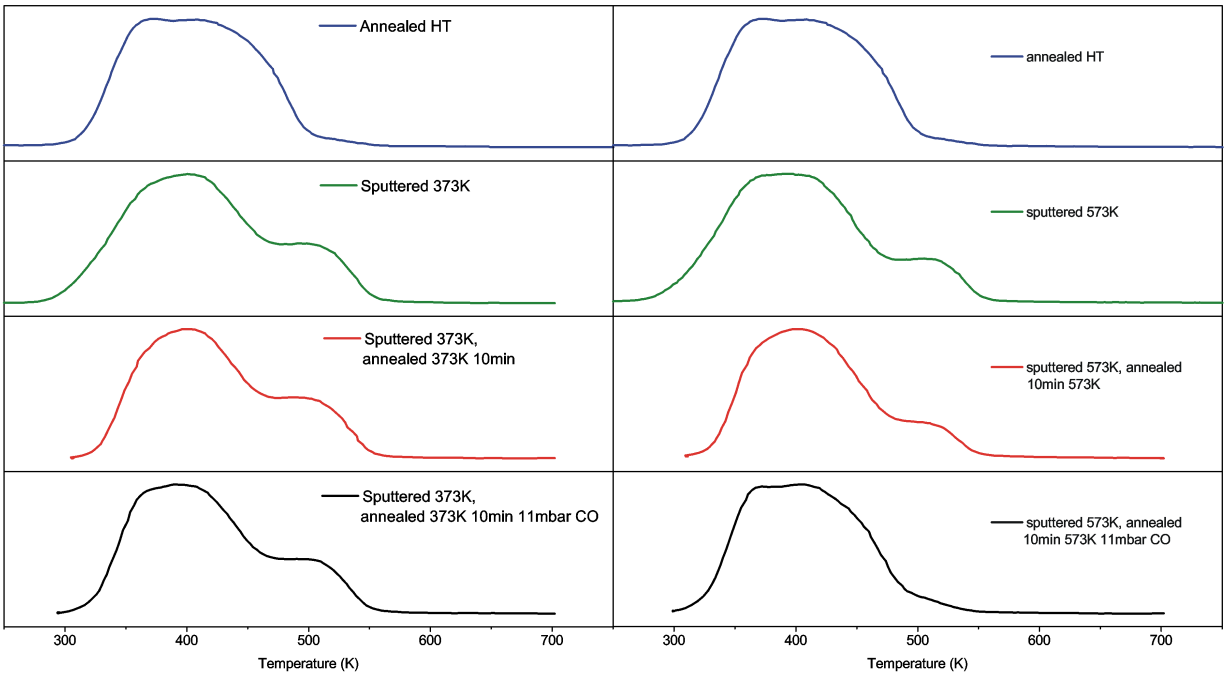

FIG. 4: CO TPD spectra from (a) the annealed Pt(111) crystal, sputtered at 373K, sputtered then annealed for 10min at 373K, and sputtered at 373K with a 10min anneal in 10mbar CO. (b) The annealed Pt(111) crystal, sputtered at 573K, sputtered then annealed for 10min at 573K, and sputtered at 573K with a 10min anneal in 10mbar CO. The ramp rate of each TPD was 2K/s.

seen from the Fig. 4 (a) that at 373K the presence of 10mbar CO has virtually no affect on the desorption spectra, while from Fig. 4 (b) for the crystal at 573K the presence of 10mbar CO produces a large annealing effect. Note that we have also observed the same annealing effect when the crystal was exposed to 2mbar CO, at 573K. It is apparent from the results that CO has the effect of aiding the diffusion of underlying Pt atoms, beyond the effect of the temperature alone.

To extend this work to the nanoparticle system, similar experiments were performed for the Pt/SiO2 samples, for 3nm, 6nm, and 11nm particles. In each case, the samples had first been treated to two prior CO30 dosing/TPD cycles, so that the particles had already been through two temperature ramps, and thus should have attained a stable structure. Afterwards, the samples were inserted into the high pressure cell, where they were annealed at 573K in ∼5 mbar of CO28. After ten minutes of annealing, the samples were cooled in CO at the dosing pressure until a temperature of 303K was reached, at which point the CO

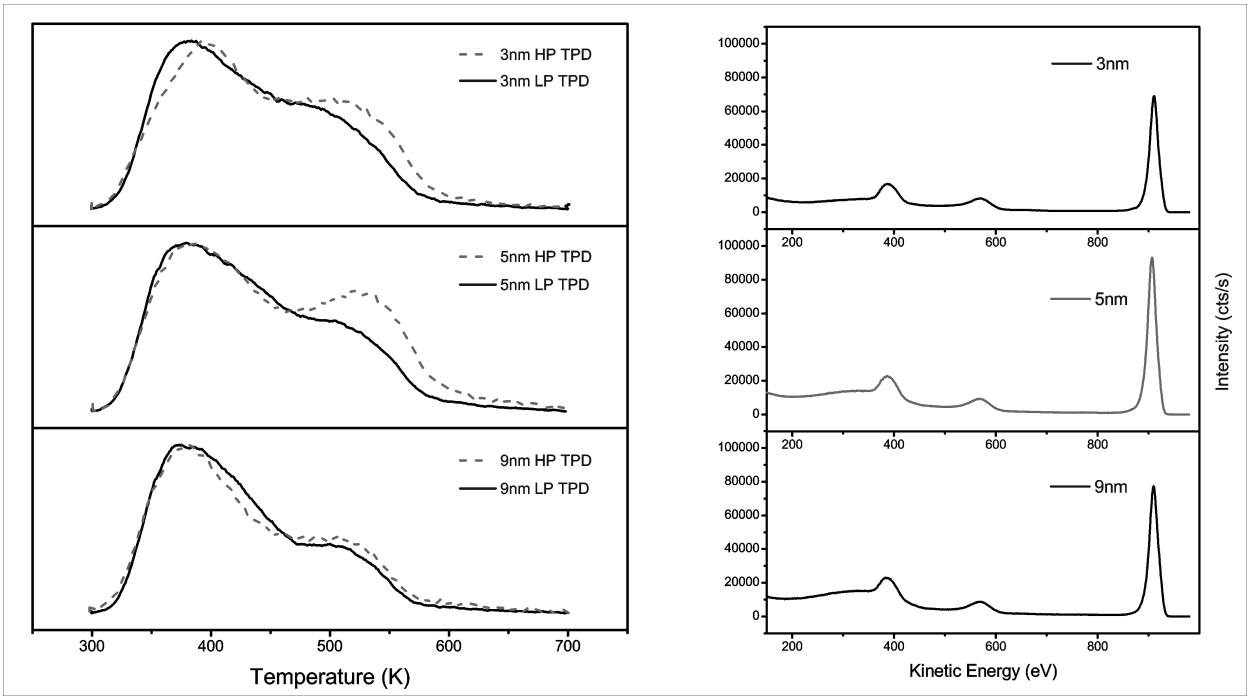

FIG. 5: CO TPDs from nanoparticle samples for particles of 3nm, 5nm, and 9nm. The full line is the signal measured for the second CO30 TPD where P=10-7mbar. The dashed line is the signal measured after subsequent annealing of the samples at 573K in 5mbar CO.

in the cell was evacuated, the samples then transferred to the main vacuum chamber, and the TPD performed. The TPDs from each sample are shown in Fig. 5, where the full line is from the second CO30 TPD, and the dashed line is from the subsequent HP TPD.

Beginning with the TPDs of the 3nm particles, after annealing in CO there is a slight shift of the low temperature desorption feature, but the main difference is the more prominent high temperature shoulder, which doesn't decay fully until well past 550K. For the 6nm particles, the low temperature desorption feature is very similar for the low and high pressure dosings, however the high temperature feature of the high pressure sample is much more prominent, actually forming a separate peak.The increased prominence of the high temperature feature was observed for three different 6nm samples, prepared under similar conditions. For the 11nm particles, there are no significant differences in the desorption spectra for low or high pressure dosings.

Along with the TPD spectra we also include ISS spectra taken from the samples after the HP experiments. We show the ISS spectra because of the possibility of Ni-carbonyls being

deposited on the particle surface during the high temperature dosing, unless the appropriate cleaning procedures are followed. From the ISS spectra of these three samples, we observe only the expected Oxygen, Silicon, and Platinum peaks. We should say that when the correct cleaning procedure was not followed, a clear feature in the ISS spectra was observed at , which we assigned to Ni. Hence we are confident that the features seen in the TPD spectra of Fig. 5 are a consequence of changes to the Pt particles, and not due to contamination of the sample.

DISCUSSION

Low Pressure Dosing Experiments

From the roughened single crystal, the additional desorption feature between 500K and 550K is consistent with results from stepped single Pt crystals, such as the Pt(112) surface, where a desorption feature is observed between 500 and 550K [18], assigned to CO bound solely at Pt(100) step-edges. For the nanoparticle samples, where the desorption does not fully decay until $\sim$ 575K, the desorption temperature is consistent with CO desorption from the kinked Pt(321) surface [12]. We would expect that the Pt nanoparticles have a number of severely undercoordinated atoms at facet edges and vertices, similar to the coordination of atoms on the Pt(321) surface, where the steps consist of a kink site for every step site.

Mbar Pressure Annealing Experiments

The annealing out of the single crystal under high CO pressures can be understood in terms of the greater binding energies of CO molecules to the undercoordinated Pt atoms at the sputter induced defects. It is already known that CO can cause a breaking of Pt-Pt bonds on the surface of a metal crystal [10, 13], as the increased binding energy of CO to undercoordinated Pt atoms is on the order of the strength of the intermetallic bonds i.e. the difference in intermetallic bonds of a 5-fold coordinated Pt atom compared with six-fold coordinated atom is similar to the additional bond energy of CO to a five-fold coordinated rather than to a six fold coordinated atoms. Even though it only leads to minor enthalpy changes, CO can actively increases the proportion of undercoordinated Pt atoms is considered to be driven by the higher entropy of the roughened surface. These previous

observations have found that CO molecules can cause the rearrangement of Pt atoms at a step edge in order to accommodate more CO, however our observations show that an additional consequence of the CO-Pt binding is a reduced diffusion barrier for the Pt atoms, as signalled by Fig. 4, seen in annealing of crystal to a state of low surface roughness. From Fig. 4, where the adsorption of 11mbar CO at 373K is presented, it was observed that there was very little difference to the high temperature feature in the TPDs of the sample annealed in 11mbar CO, to the sample dosed at 10-7mbar. This suggests that little additional CO is adsorbed on the surface due to the higher pressure, which might be expected if the step edges were roughened in high CO pressures to accommodate more CO, however this interpretation could be hidden if there was a combination of annealing and roughening processes, in which case the presence of a high temperature CO desorption feature would depend on which of the annealing or roughening processes was more dominant.

The benefits of annealing in CO has been observed before in other systems, for instance Kibler et al [21] have studied the effects of cooling flame annealed Pt single crystals in gases such as Hydrogen, Carbon Monoxide, and air, and demonstrated the different surface morphologies that can result under the different gas conditions. In these experiments, there was noticeable reduction in the surface roughness, and a higher degree of surface ordering, when the crystals were cooled in reducing environments, however as the experiments were performed under gas mixtures it is difficult to isolate the active component. In electrochemical environments, the sweeping of the cell potential in a CO saturated electrolyte has been shown to induce surface structure changes on Pt electrodes [5], suggesting enhanced mobility of Pt atoms when bonded to CO, though with EC potential sweeps there is also the effect of Pt oxidation to consider.

CONCLUSIONS

We have demonstrated the use of temperature programmed desorption as a structure sensitive probe, that can establish the presence of undercoordinated Pt atoms on single crystals and nanoparticles. By applying this technique to two model systems, Pt single crystals and gas aggregated nanoparticles, we have found good agreement between the desorption characteristics of the roughened single crystal, and the undercoordinated sites that predominate on nanoparticles. The high temperature desorption features of the nanoparticles were con-

sistent with both the roughened single crystal, and literature results from vicinal Pt crystal surfaces.

In our high pressure CO experiments on the single crystal, the presence of CO was found to be beneficial for annealing a rough crystal surface. This phenomenon is considered to be due to CO induced weakening of the intermetallic bonds of undercoordinated surface Pt atoms, allowing more mobillity of these atoms, which leads to a faster relaxation of the surface to a thermodynamically favourable configuration, which in the case of the Pt(111) single crystal is perfectly smooth surface. This result contrasts with literature results from the vicinal Pt(557) system [4], where mbar CO pressures induce a roughening of the stepped crystal surface. From the nanoparticles of 3nm and 6nm sizes, there was a clear increase in the proportion of CO bound at high temperature when dosed at 5mbar. Especially for the 6nm particles, the high temperature desorption feature became very prominent, which we interpret as an increase in the particle roughness. The increased CO adsorption was not so apparent for the 11nm particles, which tentatively suggests some size dependence to the roughening, which could be consistent with different single crystal experiments where roughening is observed for the strained Pt(557) system, but not for the Pt(332) [4], or the sputtered Pt(111) crystal of this work.

Outlook: use of tpd to monitor roughness under reaction conditions. extend to higher CO pressures

References

* Electronic address: ibchork@fysik.dtu.dk

[1] P. Hansen, J. Wagner, S. Helveg, J. Rostrup-Nielsen, B. Clausen, and H. Topsoe, SCIENCE **295**, 2053 (2002).

[2] P. C. K. Vesborg, I. Chorkendorff, I. Knudsen, O. Balmes, J. Nerlov, A. M. Molenbroek, B. S. Clausen, and S. Helveg, JOURNAL OF CATALYSIS **262**, 65 (2009).

[3] F. Tao, S. Dag, L.-W. Wang, Z. Liu, D. R. Butcher, M. Salmeron, and G. A. Somorjai, NANO LETTERS **9**, 2167 (2009).

[4] F. Tao, S. Dag, L.-W. Wang, Z. Liu, D. R. Butcher, H. Bluhm, M. Salmeron, and G. A. Somorjai, SCIENCE **327**, 850 (2010).

[5] D. S. Strmcnik, D. V. Tripkovic, D. van der Vliet, K.-C. Chang, V. Komanicky, H. You, G. Karapetrov, J. Greeley, V. R. Stamenkovic, and N. M. Markovic, JOURNAL OF THE AMERICAN CHEMICAL SOCIETY **130**, 15332 (2008).

[6] B. L. M. Hendriksen, M. D. Ackermann, R. van Rijn, D. Stoltz, I. Popa, O. Balmes, A. Resta, D. Wermeille, R. Felici, S. Ferrer, et al., NATURE CHEMISTRY **2**, 730 (2010).

[7] S. Dahl, A. Logadottir, R. Egeberg, J. Larsen, I. Chorkendorff, E. Tornqvist, and J. Norskov, PHYSICAL REVIEW LETTERS **83**, 1814 (1999).

[8] M. P. Andersson, E. Abild-Pedersen, I. N. Remediakis, T. Bligaard, G. Jones, J. Engbwk, O. Lytken, S. Horch, J. H. Nielsen, J. Sehested, et al., JOURNAL OF CATALYSIS **255**, 6 (2008).

[9] R. Imbihl and G. Ertl, CHEMICAL REVIEWS **95**, 697 (1995), ISSN 0009-2665.

[10] P. Thostrup, E. Christoffersen, H. Lorensen, K. Jacobsen, F. Besenbacher, and J. Norskov, PHYSICAL REVIEW LETTERS **87** (2001).

[11] H. Steininger, S. Lehwald, and H. Ibach, Surface Science **123**, 264 (1982).

[12] M. McClellan, J. Gland, and F. McFeeley, Surface Science **112**, 63 (1981).

[13] P. Thostrup, E. Vestergaard, T. An, E. Laegsgaard, and F. Besenbacher, JOURNAL OF CHEMICAL PHYSICS **118**, 3724 (2003).

[14] R. M. Nielsen, S. Murphy, C. Strebel, M. Johansson, J. H. Nielsen, and I. Chorkendorff,

SURFACE SCIENCE **603**, 3420 (2009).

[15] R. M. Nielsen, S. Murphy, C. Strebel, M. Johansson, I. Chorkendorff, and J. H. Nielsen, JOURNAL OF NANOPARTICLE RESEARCH **12**, 1249 (2010).

[16] S. Murphy, C. Strebel, S. B. Vendelbo, C. Conradsen, Y. Tison, K. Nielsen, L. Bech, R. M. Nielsen, M. Johansson, I. Chorkendorff, et al., PHYSICAL CHEMISTRY CHEMICAL PHYSICS **13**, 10333 (2011).

[17] T. Michely and G. Comsa, Surface Science **256**, 217 (1991), ISSN 0039-6028.

[18] H. R. Siddiqui, X. Guo, I. Chorkendorff, and J. Yates, Surface Science **191**, L813 (1987).

[19] L. K. Ono, B. Yuan, H. Heinrich, and B. R. Cuenya, JOURNAL OF PHYSICAL CHEMISTRY C **114**, 22119 (2010).

[20] A. Julukian, T. Fadnes, S. Raaen, and M. Balci, JOURNAL OF APPLIED PHYSICS **109**, 123502 (2011).

[21] L. Kibler, A. Cuesta, M. Kleinert, and D. Kolb, JOURNAL OF ELECTROANALYTICAL CHEMISTRY **484**, 73 (2000).

Vacuum annealed polycrystalline Pt_3Sc as an electrocatalyst for oxygen reduction.

T.P. Johansson[a], E.T. Ulrikkeholm[a], P. Hernandez-Fernandez[a], P. Malacrida[a], A.S. Bondarenko[c], H.A. Hansen[d], I.E.L. Stephens[a], J. Rossmeisl[b], J.K. Nørskov[d], I. Chorkendorff[a]

[a] *Center for Individual Nanoparticle Functionality, Department of Physics, Building 312, Technical University of Denmark, DK-2800 Lyngby, Denmark*
[b] *Center for Atomic-scale Materials Design, Department of Physics, Building 311, Technical University of Denmark, DK-2800 Lyngby, Denmark*
[c] *Center for Electrochemical Sciences, Ruhr-Universitat Bochum, Universitatsstrasse 150 NC 4/73, D-44780 Bochum, Germany*
[d] *SUNCAT Center for Interface Science and Catalysis, Department of Chemical Engineering, Stanford University, Stanford, CA, USA*

Abstract

In order for low temperature polymer electrolyte membrane fuel cells to become economically viable Pt catalyst loading must be significantly reduced. The cathode of the polymer electrolyte membrane fuel cell, where oxygen reduction takes place, is responsible for the main loss and developing new materials for this reaction is essential in order to increase the overall effeciency of the fuel cell. Herein we study the effect of ultra high vacuum annealing on the structure and activity of polycrystalline Pt_3Sc. Upon annealing in ultra high vacuum a Pt overlayer is formed on the polycrystalline Pt_3Sc. The reactivity of the overlayer is probed by temperature programmed desorption of CO which shows a decrease on the order of 50 K in the CO desorption temperature with respect to Pt(111). Using density functional theory calculations the downshift in CO desorption temperature was shown to be correlated with a weaker binding of oxygen species. Exposing the annealed Pt_3Sc sample to 200 mbar O_2 at room temperature results in ~ 14 % Sc oxide. Electrochemical testing of the oxygen reduction activity shows the same activity as for sputter cleaned Pt_3Sc.

Keywords: CO, TPD, Pt_3Sc, Pt, ORR, ISS, ARXPS, DFT

1. Introduction

The main losses in a low temperature polymer electrolyte membrane fuel cell (PEMFC) is due to the slow kinetics of the oxygen reduction reaction (ORR), even when Pt is used as a catalyst.[1] The activity of Pt can be increased by alloying it with transition metals such as Y, Sc, La, Ni, Co, Cr, Fe and Cu. The solute metal of these alloys is not stable in the surface upon immersion in the acidic electrolyte and the active catalysts therefore consists of platinum overlayers on top of platinum alloys.
Markovic and coworkers have intensively studied bulk polycrystalline platinum bimetallic alloys, Pt_3M (M=Ni, Co, Fe, Ti, V). They reported two different ways of producing the active Pt overlayer on these alloys. When the surface of the bulk polycrystalline platinum alloy is prepared by clean sputtering followed by immersion into acidic electrolyte a so called platinum skeleton structure is obtained. The platinum skeleton surfaces are not very well defined, but are reported to have 100 % platinum in the first layer and a minimum of 75 % platinum from the second layer and down [2]. In the case of ultra high vacuum (UHV) annealing the platinum overlayer is formed by Pt diffusion to the surface. Markovic and coworkers [2] reports that the platinum overlayer formation occurs by platinum atoms from the second layer exchanging place with the solute atoms in the surface layer leading to a structure with 100 % platinum in the first layer, 50 % platinum in the second layer and (roughly) 75 % platinum in the following layers.
The ORR activity of the recently discovered Pt_3Sc and Pt_3Y alloys was measured after clean sputtering, corresponding to a Pt skeleton overlayer [3].
In this article we present results from UHV annealed polycrystalline Pt_3Sc.

2. Methods

The main instrument used during this study was an Ultra High Vacuum (UHV) chamber with a base pressure of $1 \cdot 10^{-10}$ torr. A High Pressure Cell (HPC) is attached to the main chamber and can be isolated from it by a lock which utilises a Cu gasket. In the main chamber ion scattering spectroscopy (ISS) and x-ray photoelectron spectroscopy (XPS) can be performed. The chamber is also equipped with a quadropole mass spectrometer (QMS). The Pt_3Sc polycrystalline sample is 5 mm in diameter and 3 mm thick and was supplied by MaTecK, GmbH, Germany. The sample is mounted by hanging it in a hairpin shaped 0.38 mm diameter tungsten wire and the temperature

of the sample is measured by a thermocouple (type K2). The sample is resistively heated by sending current through the tungsten wire from which it hangs. Cooling of the sample is achieved by pumping pressurised air or liquid nitrogen into the hollow manipulator.
The polycrystalline Pt_3Sc sample was cleaned by performing cycles of Ar^+ sputtering at room temperature and annealing to 1273 K.

3. Results

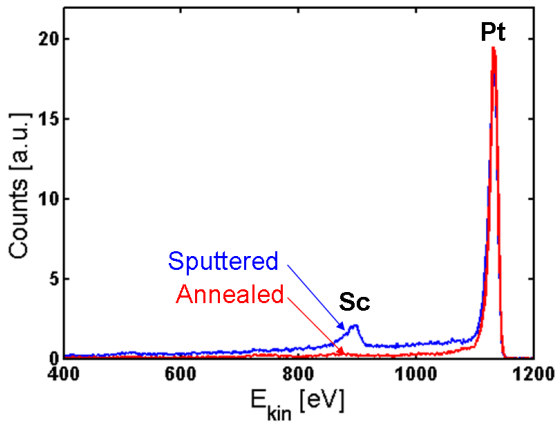

Figure 1: ISS spectrum of polycrystalline Pt_3Sc before and after annealing to T=1273 K. A Pt skin is seen to form upon annealing in UHV.

Figure 1 shows the ISS spectrum before and after annealing. Before annealing two peaks are seen in the ISS spectrum, one at around 900 eV which corresponds to Sc and one at around 1120 eV which corresponds to Pt. No other peaks are seen indicating a clean surface containing only Pt and Sc. After annealing the Sc peak at around 900 eV disappears and only the Pt peak is seen. This suggests the formation of a Pt overlayer upon annealing, in line with the results of Markovic and coworkers for Pt_3M (M=Ni, Co, Fe, Ti, V) polycrystalline samples [2].
Table 1 shows the concentration of different elements from XPS before and after annealing. After annealing the carbon content on the surface is seen to slightly increase. Many sputtering and annealing cycles were made in order to remove the carbon, but no change in the XPS spectrum was observed.

	Pt	Sc	C	O	Pt:Sc ratio
Pt_3Sc clean sputtered	83	13	2	2	6.3
Pt_3Sc annealed	81	13	5	1	6.2

Table 1: Concentration of the different elements in the polycrystalline Pt_3Sc sample before and after vacuum annealing as obtained by XPS.

The Pt:Sc ratio is seen to be 6.3. A bulk terminated sample of Pt_3Sc should naturally have a Pt:Sc ratio of 3. For the sputtered sample there could be some minor deviation from this value due to preferential sputtering of one of the elements, but not enough to explain the ratio seen by XPS.
The Pt-Sc phase diagram (see [4]) shows that the most Pt rich Pt-Sc phase which is stable is Pt_3Sc. XRD measurements on the sample, reported in [5] gives that the bulk of the sample is Pt_3Sc. It is therefore peculiar that the XPS gives a Pt:Sc ratio of around 6.

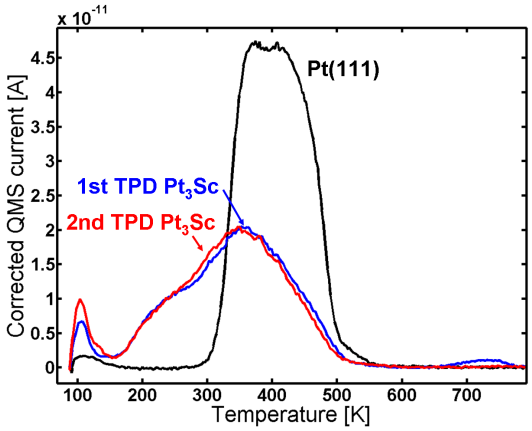

Figure 2: The first (blue graph) and second (red graph) CO TPD of Pt_3Sc after annealing at T=1273K. The CO TPD of Pt(111) (black graph) is shown for comparison.

The reactivity of the Pt overlayer is now probed by CO TPD. The blue graph in figure 2 shows the CO TPD of the annealed Pt_3Sc. The red graph in figure 2 is the repeated CO TPD. The repeated CO TPD is seen to be the same as the first except for the small peak at around 740 K which only appears

in the first TPD. The black graph in figure 2 is the CO TPD for Pt(111). It is seen that CO is bound weaker than on Pt(111). The amount of CO desorbed from the Pt_3Sc surface (the area under the peak) is 0.56 compared to Pt(111). This difference could be due to a lower saturation coverage of CO on Pt_3Sc compared to Pt(111). It could, however, also be due to some of the sites on Pt_3Sc being blocked by carbon (see XPS data table 1).
Before taking the sample out and measure the oxygen reduction activity the stability in air is tested. Figure 3 shows the XPS signal from the Sc2p line of the annealed Pt_3Sc before and after exposure to 200 mbar oxygen. By fitting the peaks it is estimated that 14 % of the Sc is in the oxidised state, indicating that the Pt overlayer is not completely hindering the Sc from oxidising.

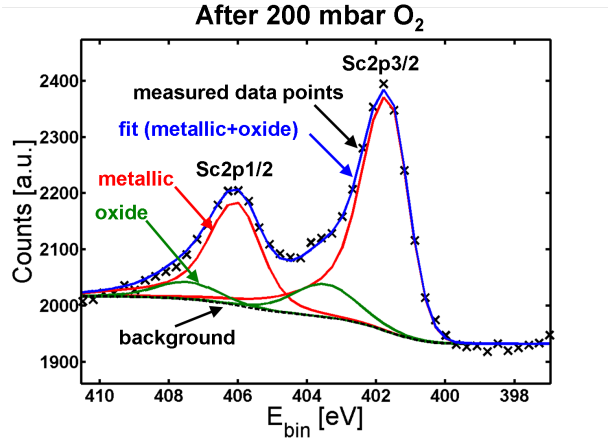

Figure 3: XPS: Sc2p peak of annealed Pt_3Sc after exposure to 200 mbar O_2. Fitting the recorded data to metallic (red) and oxidised (blue) Sc gives 14 % Sc oxide. Before exposure to 200 mbar only metallic Sc was seen.

In order to remove the adsorbed oxygen from the surface, the sample was now exposed to 2 mbar CO for 10 min at 304 K and a CO TPD was made. The CO TPD showed significantly higher binding of CO than the annealed Pt_3Sc, again indicating that the Sc has oxidised.
Having established that UHV annealing of Pt_3Sc to 1273 K gives a Pt overlayer structure the sample was sputtered, annealed and taken out for electrochemical testing. However, before the electrochemical testing, the sample is mounted in another UHV chamber equipped with angle resolved XPS (ARXPS). The purpose of this is to check the electrochemical stability of the

sample by measuring the ARXPS depth profile spectrum before and after electrochemistry. The ARXPS depth profile spectrum before electrochemistry is seen in figure 4. The spectrum shows that air exposure resulted in a

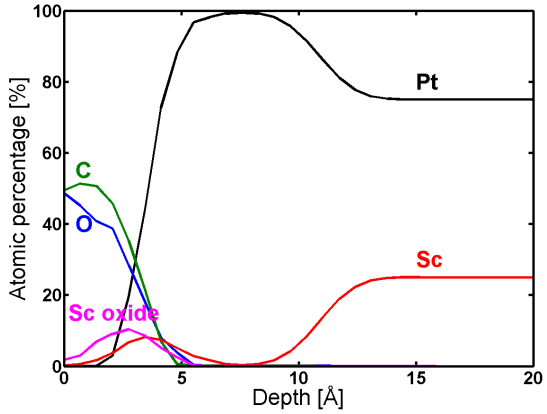

Figure 4: ARXPS depth profile of the UHV annealed Pt_3Sc before electrochemistry.

layer of adventitious contamination (the carbon and oxygen) on the surface of the sample together with some Sc oxide (in agreement with the 200 mbar O_2 exposure experiment shown in figure 3). Then follows a region of pure platinum and then the bulk Pt_3Sc structure. A restriction on the fit is that from 20 Åand deeper the Pt:Sc ratio is set to 3, corresponding to Pt_3Sc. Earlier it was however seen that both the sputter cleaned and the annealed Pt_3Sc had a Pt:Sc ratio of around 6 (see table 1). This descrepancy together with the general uncertainty in the fitting of the ARXPS depth profile should mainly be considered qualitatively. It is therefore also challenging to determine the exact thickness of the Pt overlayer.

3.1. Electrochemical measurements

The sample was then taken out and mounted in a rotating disk electrode setup for electrochemical testing. Figure 5 shows the oxygen reduction activity on a Tafel plot. The UHV annealed Pt_3Sc sample has a similar activity to that of clean sputtered Pt_3Sc. The Tafel slope, however, is seen to be somewhat different. In order to investigate the stability after electrochemical testing, the sample is again mounted in the ARXPS chamber.

Figure 6 shows the ARXPS depth profile after electrochemistry (solid lines)

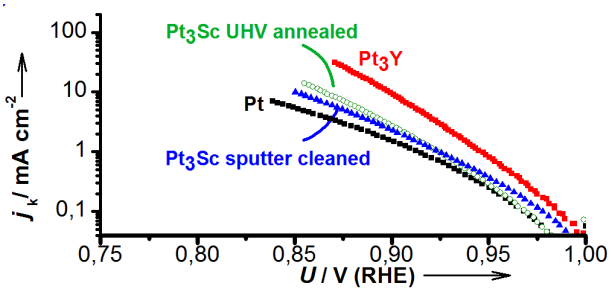

Figure 5: Tafel plot of the vacuum annealed polycrystalline Pt_3Sc sample compared with sputter cleaned polycrystalline samples of Pt_3Sc, Pt_3Y and Pt. The temperature was T=23 °C and the scan rate 20 mV/s.

together with the ARXPS depth profile before electrochemistry (dashed lines). The main difference between the two spectra is that the Sc oxide which was at the surface before electrochemistry is not there anymore. This is expected since Sc in the surface is not expected to be stable in perchloric acid. There is also a slight difference in the size of the Pt overlayer, which could indicate that the overlayer is not completely stable. As mentioned before there are considerable uncertainties connected with the ARXPS profile and the results should therefore be considered qualitatively rather than quantitatively. It is therefore not possible to conclude whether or not the increased thickness of the Pt overlayer after electrochemistry is due Sc oxide segregation to the surface making a thicker overlayer or the inaccuracy of the ARXPS depth profile.

4. Discussion

Table 2 shows the calculated energy required to move an X atom from the second layer to the surface layer of a Pt_3X alloy with a 1 ML thick Pt skin. The calculation is made for initial X concentrations of 50 % and 25 % in the second layer. If the energy is negative the Pt overlayer is not stable. It is seen that for Pt_3Ni the Pt overlayer is stable which is in agreement with experiments made by Stamenkovic et al [6]. There are different reports on the termination of $Pt_3Ti(111)$ after vacuum annealing. [7, 8, 9] The suggestion by Chen et al [8] that Pt segregation is enhanced by a slight nonstoichiometry

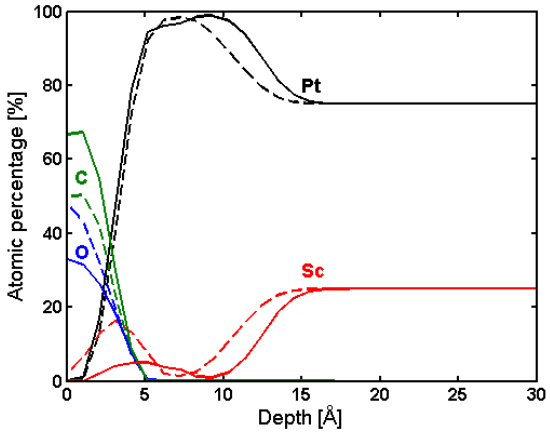

Figure 6: ARXPS depth profile of the UHV annealed Pt_3Sc before electrochemistry (dashed lines) and after electrochemistry (solid lines).

Concentration	Pt_3Y	Pt_3Sc	Pt_3Ni	Pt_3Ti
50%	-2.27	-1.24	0.36	-0.74
25%	0.41	0.90	0.75	1.16

Table 2: Energy in eV required to move 1 X atom from the sub surface layer to the surface layer of a Pt_3X alloy with a 1 ML thick Pt skin. Calculations are made for both 50 % and 25 % initial X concentrations in the second layer.

(Pt excess) in the bulk of the crystal is in agreement with the result for Pt_3Ti shown in table 2 where the system with 50 % Ti in the second layer is seen to be unstable whereas the 25 % in the second layer is stable.
From Table 2 it is seen that the system with 50 % concentration of the solute metal in the second layer is not stable for either Pt_3Sc or Pt_3Y, but the system with 25 % concentration of the solute metal in the second layer is. For Pt_3Sc this is in agreement with the ISS data showing that a Pt overlayer is formed upon annealing in UHV.
The surface reactivity of the different polycrystalline alloys was tested in UHV by CO TPD. The main interest of these alloys is however for the oxygen reduction reaction, which has oxygen species as intermediates. A relevant question is therefore if it is possible to relate the binding energy of OC^* to that of the oxygen species in the oxygen reduction reaction. When considering

different metals their OC* and HO* binding energies do not scale [10]. For the Pt overlayers on top of Pt_3M alloys such a relation could however be possible. Figure 7 shows the calculated OC*, HO* and HOO* binding energies on three

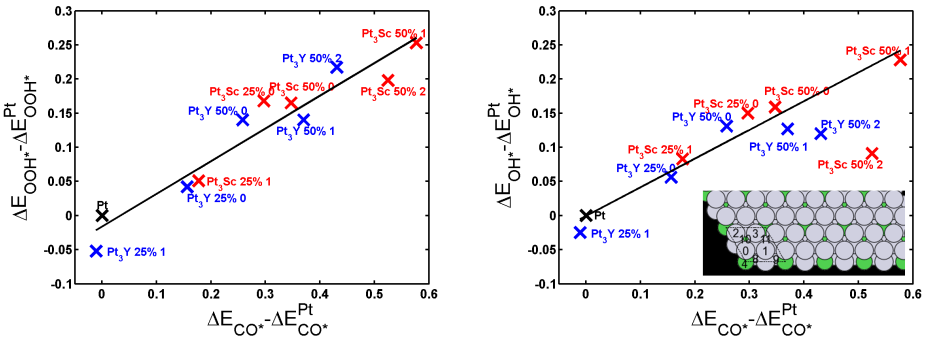

Figure 7: Calculated OC*, HO* and HOO* binding energies on various Pt overlayer structures. "Pt_3Y 50% 2" refers to a the site 2 on the inset figure for a Pt_3Y sample with 50 % Y in the second layer.

different sites ("0", "1" and "2") of Pt overlayer structures on Pt_3Sc and Pt_3Y with subsurface solute metal concentrations of 25 % and 50 %. Although not perfectly linear a clear trend is seen that a surface which binds OC* weaker will also bind HO* and HOO* weaker. Two datapoints ("Pt_3Y 50% 2" and "Pt_3Sc 50% 2") on the HO* vs. OC* binding energy graph are outliers and it is noted that they are also outliers when comparing the HO* and HOO* binding energies which should scale linearly. A linear fit is made to the data (except the two outliers) giving the following relation:

$$\Delta E_{\text{bin, OH}} = (0.42 \pm 0.04) \cdot \Delta E_{\text{bin, CO}} \quad (1)$$

$$\Delta E_{\text{bin, OOH}} = (0.48 \pm 0.05) \cdot \Delta E_{\text{bin, CO}} \quad (2)$$

The ideal ORR catalyst should bind oxygen around 0.2 eV weaker than Pt [3]. From the scaling relations between O* and HO* this corresponds to binding HO* 0.1 eV weaker. From eq. 1 this is seen to correspond to a weaker binding of OC* by $\frac{0.1\text{eV}}{0.42} = 0.24\text{eV}$. Ruff et al [11] have plotted the adsorption energy of CO as a function of the desorption temperature CO. They found that there is a linear relation between the two, which can be

expressed as:

$$\Delta E_{\text{bin, CO}} = 0.0028 \frac{\text{eV}}{\text{K}} \cdot \Delta T_{\text{des, CO}} \tag{3}$$

From eq. (3) we get that a weaker binding of OC* by 0.24 eV corresponds to a lowering in desorption temperature of CO by $\frac{0.24\text{eV}}{0.0028\frac{\text{eV}}{\text{K}}} = 85\text{K}$. There is clearly some uncertainty on this value, but the important point is that a Pt overlayer catalyst should bind CO weaker (on the order of 85 K) in order for it to have optimal bonding of the O species relevant for the oxygen reduction reaction.
For vacuum annealed polycrystalline Pt_3Sc a downshift in CO desorption temperature on the order of 50 K was found. According to the above mentioned relation between the CO desorption temperature and the HO* binding energy this should move Pt_3Sc closer to the top of the ORR volcano. This is in good agreement with the measured increase in ORR activity.
Ross and co-workers have also studied the CO TPD spectra of vacuum annealed Pt alloys [12]. The $Pt_3Co(111)$ single crystal formed a Pt overlayer upon UHV annealing [13], whereas $Pt_3Ti(111)$ [7] and $Pt_3Sn(111)$ [14] were found to be bulk terminated. For all three crystal a downshift in CO binding energy on the order of 50 K compared to Pt(111) was seen. This is similar to the shift observed for the UHV annealed polycrystalline sample of Pt_3Sc. It is also worth mentioning that the observed lower CO binding energy for vacuum annealed Pt_3Sc also makes it interesting for the anode of the PEMFC. The reason for this is that the anode of a PEMFC (where HOR happens) is very sensitive to impurities of CO in the hydrogen feed [15, 16]. A catalysts which is active for the HOR and binds CO weaker than pure platinum will therefore experience less CO poisoning.

5. Summary

In summary, polycrystalline Pt_3Sc has been investigated under UHV. The formation of a Pt overlayer was seen upon annealing to 1273 K in UHV. The reactivity of the samples was tested by CO TPD, which showed a downshift in desorption temperature of CO on the order of 50 K. Using DFT calculations the downshift in CO desorption temperature was shown to be correlated with a weaker binding of oxygen species. The ARXPS depth profile showed the formation of some Sc oxide on the surface upon air exposure. After electrochemical measurements this had gone, but otherwise roughly the same

depth profile was obtained. The ORR activity of the UHV annealed Pt_3Sc was comparable to that of sputter cleaned Pt_3Sc, reported in [3].

References

[1] H. A. Gasteiger, S. S. Kocha, B. Sompalli, F. T. Wagner, Activity benchmarks and requirements for Pt, Pt-alloy, and non-Pt oxygen reduction catalysts for PEMFCs, Applied Catalysis B: Environmental 56 (1-2) (2005) 9–35. doi:10.1016/j.apcatb.2004.06.021.
URL http://linkinghub.elsevier.com/retrieve/pii/S0926337304004941

[2] V. R. Stamenkovic, B. S. Mun, M. Arenz, K. J. J. Mayrhofer, C. A. Lucas, G. F. Wang, P. N. Ross, N. M. Markovic, Trends in electrocatalysis on extended and nanoscale Pt-bimetallic alloy surfaces, Nature Materials 6 (3) (2007) 241–247. doi:10.1038/nmat1840.

[3] J. Greeley, I. Stephens, A. Bondarenko, T. Johansson, H. Hansen, T. Jaramillo, J. Rossmeisl, I. Chorkendorff, J. Nørskov, Alloys of platinum and early transition metals as oxygen reduction electrocatalysts., Nature chemistry 1 (7) (2009) 552–6. doi:10.1038/nchem.367.
URL http://www.ncbi.nlm.nih.gov/pubmed/21378936

[4] Pt-sc (platinum-scandium). madelung, o. (ed.). springermaterials - the landolt-brnstein database.

[5] I. E. L. Stephens, A. S. Bondarenko, L. Bech, I. Chorkendorff, Oxygen electroreduction activity and x-ray photoelectron spectroscopy of alloys of platinum and early transition metals, ChemCatChem.

[6] V. R. Stamenkovic, B. Fowler, B. S. Mun, G. F. Wang, P. N. Ross, C. A. Lucas, N. M. Markovic, Improved oxygen reduction activity on Pt3Ni(111) via increased surface site availability, Science 315 (5811) (2007) 493–497. doi:10.1126/science.1135941.

[7] U. Bardi, D. Dahlgren, P. N. Ross, Structure and Chemisorptive Properties of the Pt3Ti Surface, Journal of Catalysis 100 (1) (1986) 196–209. doi:10.1016/0021-9517(86)90085-0.

[8] W. Chen, P. J. A. K., A. Barbieri, M. A. Van Hove, S. Cameron, D. J. Dwyer, Structure Determination of Pt3Ti(111) By Automated Tensor

Leed, Journal of Physics-condensed Matter 5 (27) (1993) 4585–4594. doi:10.1088/0953-8984/5/27/003.

[9] Z. Duan, J. Zhong, G. Wang, Modeling surface segregation phenomena in the (111) surface of ordered Pt3Ti crystal., The Journal of chemical physics 133 (11) (2010) 114701. doi:10.1063/1.3490792.
URL http://www.ncbi.nlm.nih.gov/pubmed/20866148

[10] P. Ferrin, A. Nilekar, J. Greeley, M. Mavrikakis, J. Rossmeisl, Reactivity descriptors for direct methanol fuel cell anode catalysts, Surface Science 602 (21) (2008) 3424–3431. doi:10.1016/j.susc.2008.08.011.
URL http://linkinghub.elsevier.com/retrieve/pii/S0039602808005426

[11] M. Ruff, N. Takehiro, P. Liu, J. K. Nørskov, R. J. Behm, Size-specific chemistry on bimetallic surfaces: A combined experimental and theoretical study, Chemphyschem 8 (14) (2007) 2068–2071. doi:10.1002/cphc.200700070.

[12] P. N. Ross, Trends in the bonding of CO to the surfaces of Pt3M alloys., J. Vac. Sci. Technol. A 10 (1992) 2546–2550.

[13] U. Bardi, B. C. Beard, P. N. Ross, CO Chemisorption on the [111] and [100] Oriented Single Crystal Surfaces of the Alloy CoPt3., Journal of Catalysis 124 (1) (1990) 22–29. doi:10.1016/0021-9517(90)90100-X.

[14] A. H. Haner, P. N. Ross, U. Bardi, A. Atrei, Surface composition determination of pt-sn alloys by chemical titration with carbon monoxide, Journal of Vacuum Science & Technology A-vacuum Surfaces and Films 10 (4) (1992) 2718–2722. doi:10.1116/1.577964.

[15] M. Boaventura, H. Sander, K. A. Friedrich, A. Mendes, The influence of co on the current density distribution of high temperature polymer electrolyte membrane fuel cells, Electrochimica Acta 56 (25) (2011) 9467–9475. doi:10.1016/j.electacta.2011.08.039.

[16] H. F. Oetjen, V. M. Schmidt, U. Stimming, F. Trila, Performance data of a proton exchange membrane fuel cell using H2/CO as fuel gas, Journal of the Electrochemical Society 143 (12) (1996) 3838–3842. doi:10.1149/1.1837305.

Correlating the structure and reactivity for Y/Pt(111).

T.P. Johansson[a], E.T. Ulrikkeholm[a], P. Hernandez-Fernandez[a], P. Malacrida[a], U.G. Andersen[b], A.K. Jepsen[b], I.E.L. Stephens[a], J Schiøtz[b], J. Rossmeisl[b], I. Chorkendorff[a]

[a] *Center for Individual Nanoparticle Functionality, Department of Physics, Building 312, Technical University of Denmark, DK-2800 Lyngby, Denmark*
[b] *Center for Atomic-scale Materials Design, Department of Physics, Building 311, Technical University of Denmark, DK-2800 Lyngby, Denmark*

Abstract

The fundamental knowledge gained by investigating model catalysts is of key importance in the design of active and stable catalysts for the oxygen reduction reaction.
We have studied the deposition of Y on a Pt(111) crystal under ultra high vacuum (UHV) conditions. A Pt overlayer is formed upon annealing the crystal above 800 K. The annealed structure is seen to bind CO weaker than Pt(111) with a pronounced peak in the CO TPD at 295 K. When depositing a large amount of yttrium at 1173 K a 1.88×1.88 R30° structure relative to Pt(111) is seen by LEED. The observed LEED pattern could correspond to a 2×2 R30° structure under 6 % compressive strain. This structure is in agreement with the structure of the vacancies in a Pt Kagomé layer in Pt_5Y which is rotated 30° with respect to the bulk of the Pt(111).
The Pt overlayer is relatively stable in air, however, after performing ORR activity measurements in the electrochemical cell a thick Pt overlayer is measured by ARXPS depth profile. The activity for the oxygen reduction reaction (ORR) was measured to be similar to that of polycrystalline Pt_3Y.

Keywords: CO, TPD, Y, Pt(111), ORR, ISS, ARXPS, DFT, LEED, Pt Kagomé, Pt_5Y

JACS
JOURNAL OF THE AMERICAN CHEMICAL SOCIETY

ARTICLE

pubs.acs.org/JACS

Tuning the Activity of Pt(111) for Oxygen Electroreduction by Subsurface Alloying

Ifan E. L. Stephens,[†] Alexander S. Bondarenko,[†,§] Francisco J. Perez-Alonso,[†] Federico Calle-Vallejo,[‡] Lone Bech,[†] Tobias P. Johansson,[†] Anders K. Jepsen,[†] Rasmus Frydendal,[†] Brian P. Knudsen,[†] Jan Rossmeisl,[‡] and Ib Chorkendorff[†,*]

[†]Center for Individual Nanoparticle Functionality, Department of Physics, Building 312, Technical University of Denmark, DK-2800 Lyngby, Denmark

[‡]Center for Atomic-scale Materials Design, Department of Physics, Building 311, Technical University of Denmark, DK-2800 Lyngby, Denmark

[§]Center for Electrochemical Sciences, Ruhr-Universität Bochum, Universitätsstrasse 150 NC 4/73, D-44780 Bochum, Germany

Supporting Information

ABSTRACT: To enable the development of low temperature fuel cells, significant improvements are required to the efficiency of the Pt electrocatalysts at the cathode, where oxygen reduction takes place. Herein, we study the effect of subsurface solute metals on the reactivity of Pt, using a Cu/Pt(111) near-surface alloy. Our investigations incorporate electrochemical measurements, ultrahigh vacuum experiments, and density functional theory. Changes to the OH binding energy, ΔE_{OH}, were monitored in situ and adjusted continuously through the subsurface Cu coverage. The incorporation of submonolayer quantities of Cu into Pt(111) resulted in an 8-fold improvement in oxygen reduction activity. The most optimal catalyst for oxygen reduction has an $\Delta E_{OH} \approx 0.1$ eV weaker than that of pure Pt, validating earlier theoretical predictions.

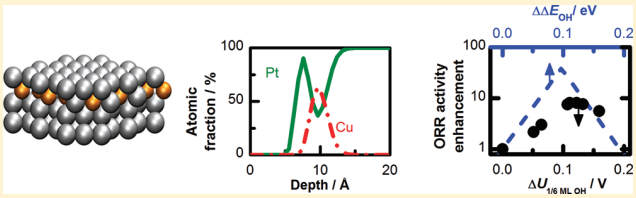

INTRODUCTION

The widespread deployment of electric vehicles would reduce our dependence on fossil fuels and decrease our emissions of greenhouse gases. Polymer electrolyte membrane fuel cells (PEMFCs) are an attractive source of power for such vehicles.[1,2] However, at present, PEMFCs are prohibitively expensive. Further technological advances are needed to decrease the cost and improve the efficiency of the Pt catalysts at the cathode, where the oxygen reduction reaction (ORR) takes place:

$$O_2 + 4H^+ + 4e^- \rightarrow 2H_2O \quad (1)$$

Such breakthroughs would require (a) the replacement of Pt with active and abundant alternatives, or (b) improving the activity of Pt, for instance by alloying it with other metals.[2−4]

To meet this key challenge, a framework was developed to describe and *predict* the overall trends in ORR activity, using density functional theory (DFT) calculations.[5−8] There are at least two to three adsorbed intermediates in the ORR, OH*, OOH*, and O* (where * denotes an adsorbed species). To catalyze the reaction, the binding to all these intermediates needs to be optimized.

On the Pt nanoparticles which catalyze oxygen reduction in PEMFCs, it is widely believed that the active sites are located upon the terraces, in particular the (111) facets.[9,10] More undercoordinated sites bind the intermediates too strongly and would tend to get poisoned. On (111) facets, the overpotential is either due to the hydrogenation of oxygen:[7,8,11]

$$O_2 + H^+ + e^- + * \rightarrow OOH* \quad (2)$$

or the electroreduction of OH* to form water:

$$OH* + H^+ + e^- \rightarrow H_2O + * \quad (3)$$

On Pt(111), the overpotential needed for OH* electrodesorption is marginally higher than that of OOH* formation, which means that step (3) is potential determining.[6,8] It follows that a catalyst which binds to OH* more weakly than Pt(111) would result in a decrease in the overpotential required for OH* reduction. However, it turns out that a surface that binds to OH* more weakly would also bind to OOH* more weakly, in which case OOH* formation, (2), would become potential determining. This is because the stability of O*, OH*, and OOH* all scale linearly.[12,13] Therefore, knowledge of the OH adsorption energy, ΔE_{OH} allows us to describe ΔE_{OOH} and ΔE_O. This is essentially a modern day version of the "Sabatier principle", which states that the most active catalyst for a given reaction should not bind too strongly or too weakly to the reaction intermediates.[14] There are numerous other examples in the recent literature where this principle, corroborated by

Received: December 28, 2010
Published: March 18, 2011

electronic structure theory, has led to the development of quantitative models that describe important trends in gas phase heterogeneous catalysis and electrocatalysis.[5,7,15−22] According to a simple "Sabatier analysis", the most optimal metal catalyst for the ORR has an OH adsorption energy, ΔE_{OH}, ≈ 0.1 eV weaker than Pt(111).[5]

Several strategies have been employed to improve the ORR activity of Pt. These include (a) the utilization of bulk alloys such as Pt_xY, Pt_xSc, Pt_xCo, Pt_xNi, and Pt_xFe;[3,7,23−28] (b) dealloyed $PtCu_x$,[29−31] and (c) the "Pt monolayer" approach, whereby monolayer quantities of Pt are deposited onto a core composed of another, less expensive metal.[32−34] All of these catalysts have a surface overlayer composed entirely of Pt. DFT calculations support the notion that the Pt surface atoms on these catalysts exhibit mildly weaker binding to O* or OH* than pure Pt.[7,29] Indeed, the discovery of Pt_3Y and Pt_3Sc as stable and active catalysts for the ORR was a direct output of the theoretical model, demonstrating its practical application.[7]

Thus far, it has not been possible to probe the descriptor, ΔE_{OH}, experimentally on a number of different surfaces with the same crystal orientation. However, Markovic and co-workers demonstrated that it was possible to estimate the d-band center, ex-situ on a series of polycrystalline Pt_3M alloys, where M = Ni, Co, Fe, Ti, V, using ultraviolet photoemission spectroscopy.[23] The d-band center is a general measure of surface reactivity.[35] A volcano relationship was demonstrated between the d-band center and ORR activity, thus supporting the theoretical model.

On a given crystal facet, the binding of Pt to OH*, OOH*, or O* can be adjusted by two different effects: ligand effects and strain effects.[35−37] Ligand effects occur when the electronic structure of the atoms sitting at the active sites are modified by neighboring atoms of a dissimilar atomic number.[38] For catalysts with a Pt overlayer, ligand effects will be more pronounced when the solute atoms are in the second layer; they are already negligible when the solute atoms are embedded in the fourth atomic layer.[39,40]

Strain effects occur when the catalyst is strained parallel to its surface.[29,39,41] The lattice parameter at the surface will tend toward that of the bulk. Therefore, a change in the bulk composition will result in a corresponding change in the interatomic Pt−Pt distance at the surface. Compressive lattice strain weakens the binding of the Pt surface atoms to adsorbed intermediates, whereas tensile strain will have the opposite effect.

On Pt monolayer catalysts, ligand and strain effects are inseparable.[32−34] This is also the case for bulk Pt alloy catalysts such as Pt_3Y, Pt_3Ni, and Pt_3Co. Their surfaces should always be strained, as their bulk lattice parameters are dissimilar to Pt.[7,42,43] However, the most active forms of Pt_3Co and Pt_3Ni are those with an enrichment of the solute in the subsurface region, suggesting that ligand effects are also important for these catalysts.[25,27]

Strasser and co-workers demonstrated that the high ORR activity of dealloyed $PtCu_x$ could be attributed entirely to strain effects.[29,31] Ex-situ analysis suggested that the catalysts have a thick Pt skin and a Cu-rich core. The smaller lattice parameter of Cu, with respect to Pt, effects a lateral strain to the Pt surface atoms. This, in turn, weakens the binding of the Pt surface atoms to OH*, OOH*, and O*, resulting in a 4−6 fold enhancement in activity over pure Pt.[29] Their study confirmed that bulk lattice strain can be used as a tool to control the ORR activity of Pt. On the contrary, equivalent evidence to demonstrate the role of subsurface alloying has remained elusive.

In the current investigation, we study *near-surface alloys* (NSAs) of Cu/Pt(111). NSAs have unique catalytic properties, distinct from bulk alloys.[21,38,44−47] In a NSA, the solute atoms are only located in the subsurface region, as shown in Figure 1a. Therefore, in a Pt-based NSA, both the surface and the bulk are essentially composed of pure Pt. NSAs have been the focus of several fundamental surface science investigations, conducted under ultrahigh vacuum (UHV) conditions.[21,45−48] To the best of our knowledge, they have not previously been studied for continuous catalytic reactions (i.e., involving turnover) under ambient conditions.

As noted above, there are several reports in the literature where similar, albeit distinct structures have been tested for the ORR. These include (a) well-defined Pt overlayer structures on single crystal substrates, including segregated skin structures and monolayer core−shell structures,[24,32,33] and (b) bulk Pt−Cu alloys in the form of nanoparticles or polycrystalline extended surfaces, where there is always a significant Cu content in the catalyst bulk.[29−31,49] The commonality between these earlier studies is that they were all concerning structures whose core was not composed of pure Pt. This indicates that their activity could at least be partially attributable to bulk lattice strain. Using the Cu/Pt(111) NSA, we aim to elucidate how the catalytic activity of a well-defined single crystal Pt surface can be tuned by the presence of subsurface metals, in the absence of bulk lattice strain.

Our attention was particularly drawn to the Cu/Pt(111) NSA by an investigation by Besenbacher and co-workers.[46] Their DFT calculations suggested that OH* was significantly destabilized on its surface, relative to Pt(111). In the light of the above discussion, this led us to believe that it could have favorable activity for the ORR.

EXPERIMENTAL SECTION

Our experiments capitalize upon the detailed knowledge of the Cu/Pt(111) NSA gained from earlier surface science investigations.[46−48] To prepare and characterize the Cu/Pt(111) NSA in situ, we designed and built a custom setup (further details can be found in the Supporting Information). Briefly, to prepare the desired NSA, up to 1 ML of Cu was electrodeposited onto a Pt(111) single crystal.[50] It was annealed in Ar and H_2 at 400 °C, using an induction heater attached to the cell. On the basis of the earlier studies of this system, the crystal surface should retain its (111) orientation upon the incorporation of subsurface Cu.[46,47] Once the crystal was annealed, the electrode was then characterized in the same cell, using cyclic voltammetry (CV) in 0.1 M $HClO_4$. To measure the ORR activity, the crystal was transferred to a separate cell with a rotating ring disk electrode (RRDE) assembly. The surface structures were independently verified ex-situ, under UHV conditions, using angle resolved X-ray photoelectron spectroscopy (AR-XPS). DFT calculations were used to provide a microscopic interpretation of our experimental results. Full details of the experimental and theoretical methods can be found in the Supporting Information.

RESULTS

Nondestructive depth profiles of the Cu/Pt(111) NSA were obtained using AR-XPS, as shown in the right-hand side of Figure 1. A profile of a Cu/Pt(111) NSA is compared with a pseudomorphic Cu-overlayer on Pt(111)[51,52] and a Cu/Pt(111) surface alloy (SA), where the first layer consists of both Cu and Pt.[47,53] These data should be interpreted qualitatively rather than quantitatively, due to inherent uncertainties in the XPS measurements and the fitting procedures. Nonetheless, the profiles match

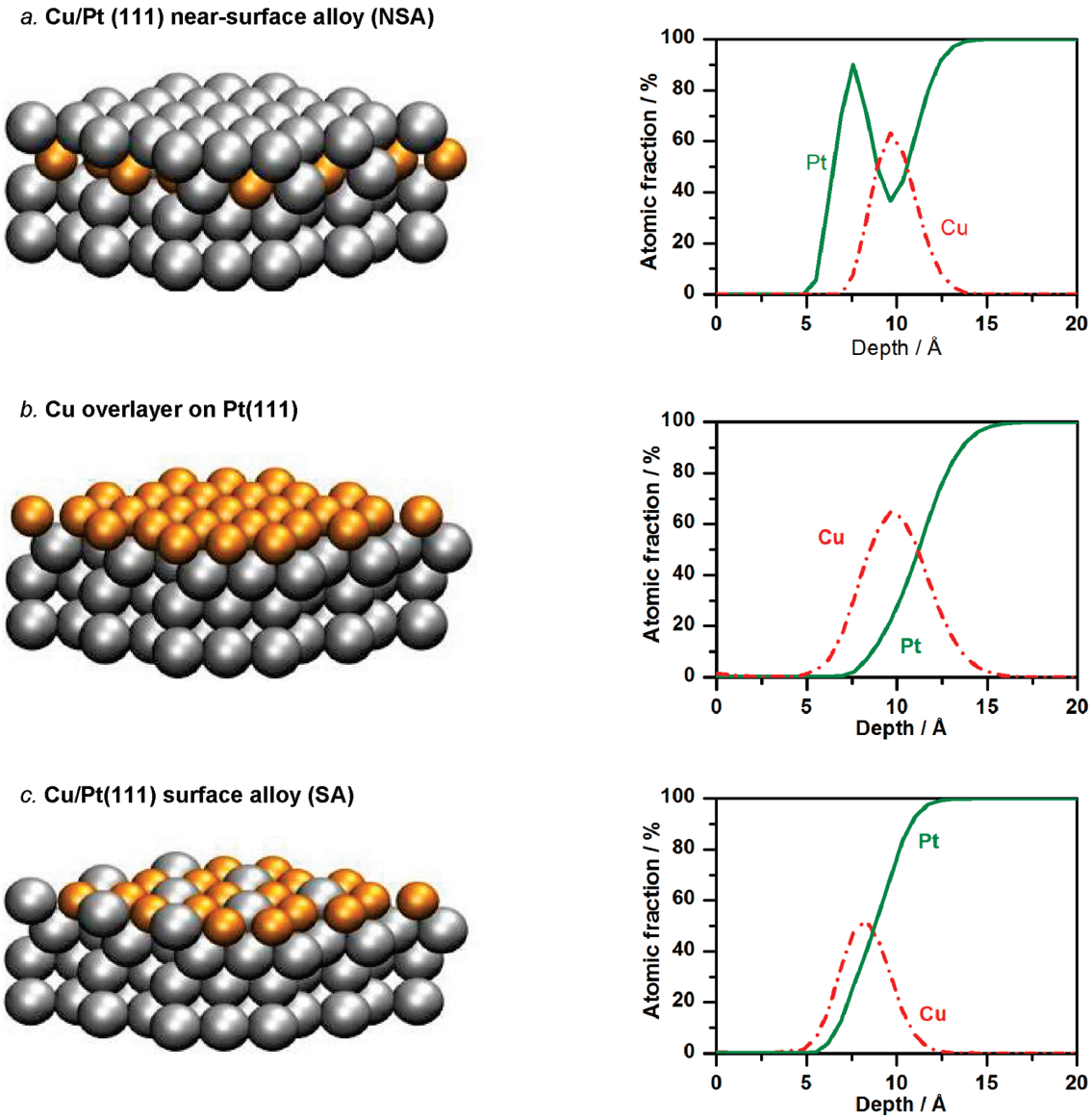

Figure 1. Schematic illustrations (left) and AR-XPS nondestructive depth profiles (right), of (a) the Cu/Pt(111) NSA, with 0.45 ML Cu initially deposited, in comparison to (b) the Cu overlayer on Pt(111), with 1 ML Cu initially deposited and (c) the Cu/Pt(111) surface alloy, with 1 ML Cu initially deposited. In panel a the Cu/Pt NSA had been exposed to ~90 min cycling between 0 and 1 V at 60 °C in O_2-saturated 0.1 M $HClO_4$. The outermost ~5 Å comprised C and O, presumably accumulated from airborne contamination during the transfer from the electrochemical cell, through the laboratory atmosphere to the UHV chamber. The C and O traces have been omitted for clarity.

closely with our expectations, shown in the left-hand side of Figure 1, formed on the basis of previous surface science studies.[46,47,51−53] Moreover, they provide a clear indication that the desired structures are formed.

To quantify the amount of Cu in the near-surface region, in Figure 2 we compare the Cu:Pt intensity ratio, as determined by XPS, for different Cu/Pt(111) NSA samples. The dashed line models the intensity ratio for the case where the amount of Cu initially deposited is equal to the amount of Cu in the second layer. When less than 0.5 ML Cu was initially deposited, there appears to be a 1:1 correspondence between the amount of Cu initially deposited and the final subsurface Cu coverage in the NSA. However, when more than 0.5 ML Cu is initially deposited, the data suggest that some of the Cu is lost from the near-surface region, most likely into the bulk of the crystal. Our observations are consistent with those of Knudsen et al.[46] Their DFT calculations suggested that Cu was stabilized in the second layer of the Cu/Pt(111) NSA, in comparison to deeper layers. On the basis of their XPS results, they estimated that the coverage of Cu in the second layer was 40%, when 1 ML Cu had been deposited initially.

The CVs taken in N_2-saturated 0.1 M $HClO_4$, shown in Figure 3 provide further evidence for the formation of a Pt-skin on the NSA. In the case of the Cu overlayer, there is a sharp anodic peak at ~0.75 V, where Cu dissolves irreversibly into the solution as Cu^{2+}.[52] In the case of the Cu/Pt(111) SA, the Cu dissolution peak is shifted to more anodic potentials, and centered around ~0.85 V. The higher potential required to strip

dx.doi.org/10.1021/ja111690g |J. Am. Chem. Soc. 2011, 133, 5485–5491

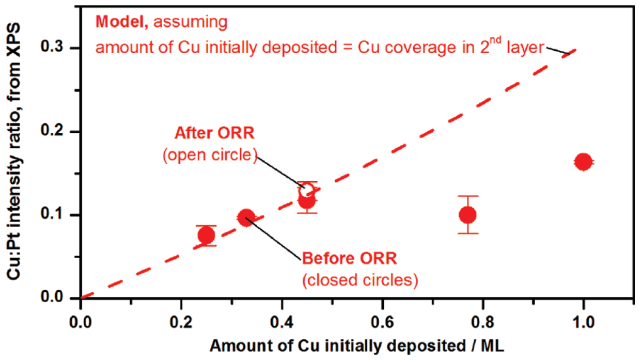

Figure 2. Cu:Pt intensity ratio, from XPS, for the different NSA structures. The analysis was based on the Pt_{4f} and Cu_{2p} photoelectrons emitted at four different angles between 20° and 35° to the sample normal. The Cu:Pt intensity ratio is corrected for the excitation cross section, the mean free path, and the analyzer transmission (full details can be found in the Supporting Information). The error bars show the standard deviations from the data taken at different angles. The dashed line shows the modeled ratio, assuming that the amount of Cu initially deposited (as determined coulometrically), is equal to the subsurface Cu coverage, and that all the Cu is confined to the second layer. The open circle represents the Cu/Pt NSA sample with 0.45 ML Cu initially deposited, after exposure to ~90 min cycling between 0 and 1 V at 60 °C in O_2-saturated 0.1 M $HClO_4$, (the corresponding depth profile is shown in Figure 1a).

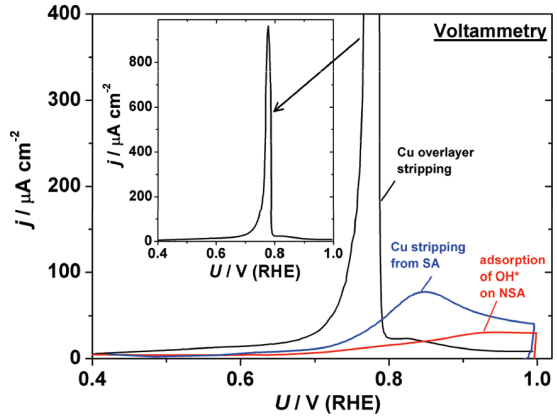

Figure 3. Cyclic voltammograms of the structures shown in Figure 1, in N_2-saturated 0.1 M $HClO_4$, at room temperature, in the absence of Cu^{2+} in solution, $dU/dt = 50$ mV s^{-1}, anodic portion only; in each case 1 ML was deposited initially.

the Cu from the SA suggests that the Cu is stabilized, relative to the overlayer.[54,55] The Cu electro-oxidation features are absent from subsequent cycles; presumably this is because the Cu^{2+} has diffused into the solution. On the contrary, the NSA does not show any features which would suggest that Cu is stripped from the surface. Instead, there is a reversible oxidation feature, unchanged with cycling. This is likely to be due to OH* electrosorption, that is, the reverse of reaction 3.

Cyclic voltammetry in N_2-saturated solution was also used to probe the strength of the interaction of the Cu/Pt(111) NSA with H* and OH*, in situ. Typical CVs of the NSAs with 0−1 ML Cu initially deposited are shown in Figure 4a (a complete set of CVs is shown in the Supporting Information). The shifts in the H* and OH* adsorption peaks show that the presence of Cu in the subsurface destabilizes these adsorbates. Similar features were observed on $Pt_3Ni(111)$ and Pt overlayers on Ru(0001).[24,37] However, the novel feature of the Cu/Pt NSA (and presumably all NSA structures) is the ability to *continuously* adjust the interaction with H* and OH* through the subsurface solute concentration.

The ORR activity was measured for the different NSA surfaces, using CV, as shown in Figure 4b. The activity of Pt(111) reported here compares well with the literature.[24] For each of the catalysts, the current initially shows an exponential increase as the potential is lowered, due to decreasing activation barriers. At higher current densities, the flux of O_2 consumed by the ORR is greater than that which can be sustained by diffusion to the surface. This causes a depletion of O_2 at the electrode, until the current saturates at its diffusion limited value, ~ 6 mA cm^{-2}. The decrease in current below ~0.4 V reflects a change in the reaction pathway, from the complete 4 electron reduction of O_2 to H_2O, to the 2 electron pathway to H_2O_2 (evidence for this is provided in the Supporting Information). In the region of mixed kinetic-diffusion control, between $0.8 < U < 1.0$ V (RHE), there is a pronounced positive shift of up to ~45 mV for the NSAs in comparison with Pt(111), revealing the significantly higher ORR activity of the NSAs.

The ORR activity of the Cu/Pt(111) NSA is stable during the course of the experiment. This observation is consistent with the XPS data shown in Figure 2. The NSA with 0.45 ML Cu initially deposited was analyzed using XPS before and after 90 min of the ORR activity measurement. Within the limits of experimental accuracy, the Cu/Pt ratio remained unchanged.

Over extended time periods, we anticipate that the Cu in the NSA would dissolve into the solution. According to our DFT calculations, the dissolution of the Cu would be thermodynamically favored at potentials above ~0.47 V (as described in more detail in the Supporting Information). We note, in passing, that even the dissolution of bulk Pt is thermodynamically favored above ~1 V.[56] The stability of the Cu in the NSA would be dependent upon the integrity of the Pt overlayer. Once the Cu reaches the surface, it will dissolve easily at high potentials, as shown in the voltammogram of the surface alloy in Figure 3. The kinetics and time scale required for Cu dissolution are challenging to predict. We anticipate that dissolution could either be initiated by OH* or O* induced segregation of Cu to the surface,[57,58] or otherwise due to the dissolution of Pt at steps and other defects.[59] Notably, the data shown in Figure 4 of the Supporting Information show that upon cycling the Cu/Pt(111) NSA to 1.25 V, irreversible changes occur to its voltammogram, suggesting that Cu dissolution may be taking place under these conditions.

DISCUSSION

The overall relationship between the amount of Cu deposited and ORR activity can be deduced from Figure 5a. It is clear that the ORR activity is highly sensitive to the presence of subsurface Cu. Our results confirm that it is possible to optimize the activity of a Pt(111) surface by varying the concentration of Cu in the subsurface region. The curve forms a "volcano", with a broad maximum at ~0.5 ML Cu, representing an 8-fold increase in activity over Pt(111) at 0.9 V. This enhancement is close to the highest recorded to date, that of $Pt_3Ni(111)$.[24]

dx.doi.org/10.1021/ja111690g |J. Am. Chem. Soc. 2011, 133, 5485–5491

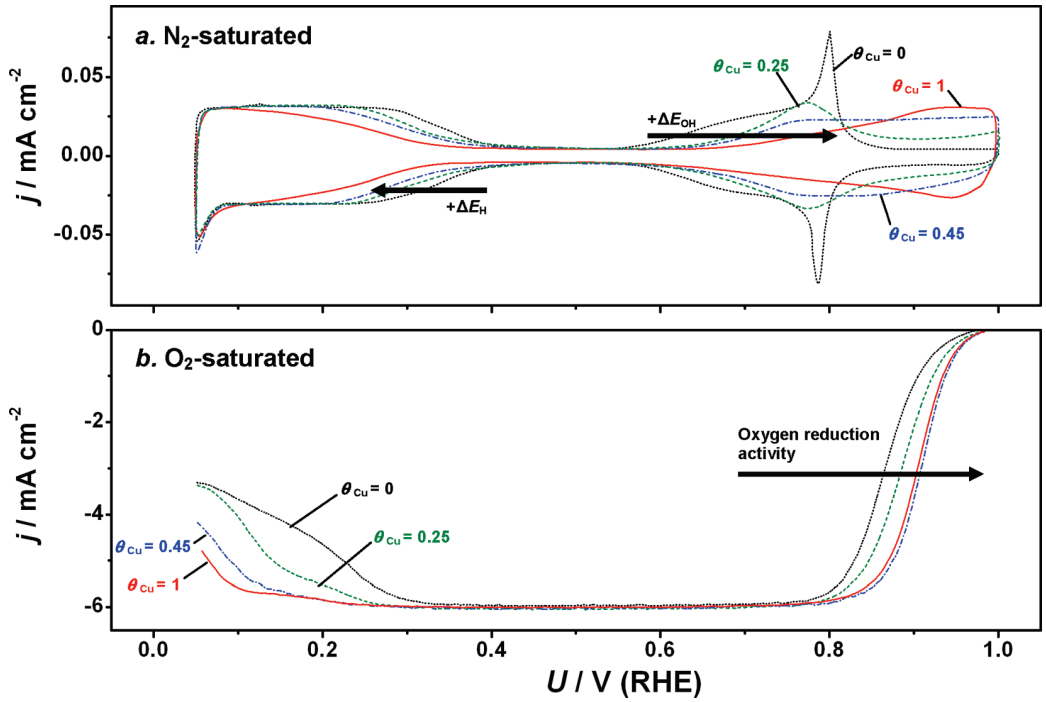

Figure 4. Electrochemical characterization of Cu/Pt(111) NSAs, in comparison with Pt(111), using cyclic voltammetry in 0.1 M $HClO_4$, at dU/dt = 50 mV s^{-1} (a) in N_2-saturated electrolyte; (b) RRDE-voltammograms (anodic scans only) in O_2-saturated electrolyte, taken at 1600 rpm, 60 °C. θ_{Cu} denotes the amount of Cu initially deposited, in monolayers (determined coulometrically, as described in the Supporting Information).

To understand our data in a broader context, it is perhaps more meaningful to relate the activity enhancement to a more universal descriptor, such as the OH binding energy, ΔE_{OH}. Changes to ΔE_{OH}, relative to Pt, that is, $\Delta\Delta E_{OH} = \Delta E_{OH} - \Delta E_{OH}^{Pt}$, can be monitored in situ, through the base voltammograms in N_2, shown in Figure 3a. The shift in potential required to reach $^1/_6$ML coverage of OH*, $\Delta U_{1/6ML\,OH}$, corresponds to the median value of $\Delta\Delta E_{OH}$. On a completely homogeneous Cu/Pt(111) NSA, $\Delta U_{1/6\ ML\ OH} = \Delta\Delta E_{\ OH}$.[6,24]

On Figure 5b, $\Delta U_{1/6ML\,OH}$ is plotted (in black) as a function of the initial amount of Cu electrodeposited onto the crystal. Evidently, $\Delta U_{1/6ML\,OH}$ increases with the Cu content. This trend is reflected in the theoretical plot of $\Delta\Delta E_{OH}$ versus the Cu coverage in the second layer, also shown (in blue) in Figure 5b. Up to ~0.5 ML Cu, the agreement between experiment and theory is good. However, at higher coverages, the large shift in $\Delta\Delta E_{OH}$ that is predicted by DFT is not replicated through $\Delta U_{1/6ML\,OH}$. This is analogous to the trend conveyed by the XPS data shown in Figure 2 and described earlier. Together, these data suggest that it is not possible to obtain a high Cu coverage in the subsurface layer.

It is difficult to ascertain conclusively whether the destabilization of OH* in the NSA arises solely from ligand effects or strain effects. The DFT calculations implicitly assume that the structure is unstrained. The data shown in Figure 5b suggest that the calculations model the experiments well. On that basis, the observed modifications to the binding of the Pt surface could be entirely due to the ligand effect. Even so, there is experimental evidence to suggest that subsurface Cu could introduce some compressive strain to a Pt(111) surface.[48]

Combining the data from Figure 5a and Figure 5b allows us to plot the activity enhancement of the NSA as a function of $\Delta U_{1/6ML\,OH}$, as shown in Figure 5c. The dashed blue line represents the earlier theoretical prediction, based on a simple Sabatier analysis.[5,6] There is a clear maximum in activity for the surface that binds OH* ≈ 0.1 eV weaker than Pt(111), in agreement with earlier theoretical predictions.[5]

We note, from Figure 5c, that the peak activity enhancement from our experiments is around a factor of ~5 lower than that at the peak of the theoretical volcano. This discrepancy could be attributed to kinetic parameters which were not taken into account by the Sabatier analysis.[6] Moreover, it seems likely that the subsurface Cu concentration across the crystal is not uniform. Consequently, $\Delta U_{1/6ML\,OH}$ may not correspond exactly to the $\Delta\Delta E_{OH}$ of the active sites. The most active sites, with the value of $\Delta\Delta E_{OH}$ being closest to the optimum, will dominate the ORR. Nevertheless, a clear trend persists between theory and experiment, as evidenced by the volcano shown in Figure 5c.

The current study complements Strasser and co-workers' investigations of the effect of bulk lattice strain on ORR activity, using dealloyed $PtCu_x$.[29,31] In comparison to dealloyed $PtCu_x$, the Cu/Pt(111) NSAs exhibited slightly higher activity enhancements over pure Pt and also a clear maximum in activity as a function of Cu concentration. It seems that the peak of the volcano can be reached more easily when the solute metal is present in the subsurface. This supports the notion that an important goal in ORR catalysis is the preparation of stable Pt alloy nanoparticles with a high subsurface concentration of the solute component.[25] Moreover, from the data shown in Figure 3, it appears that subsurface Cu is more stable in the NSA than in dealloyed $PtCu_x$.[29,31] One could speculate that our annealing procedure stabilized the solute in the subsurface region, analogous to the observations made for bulk Pt alloys.[60]

dx.doi.org/10.1021/ja111690g | J. Am. Chem. Soc. 2011, 133, 5485–5491

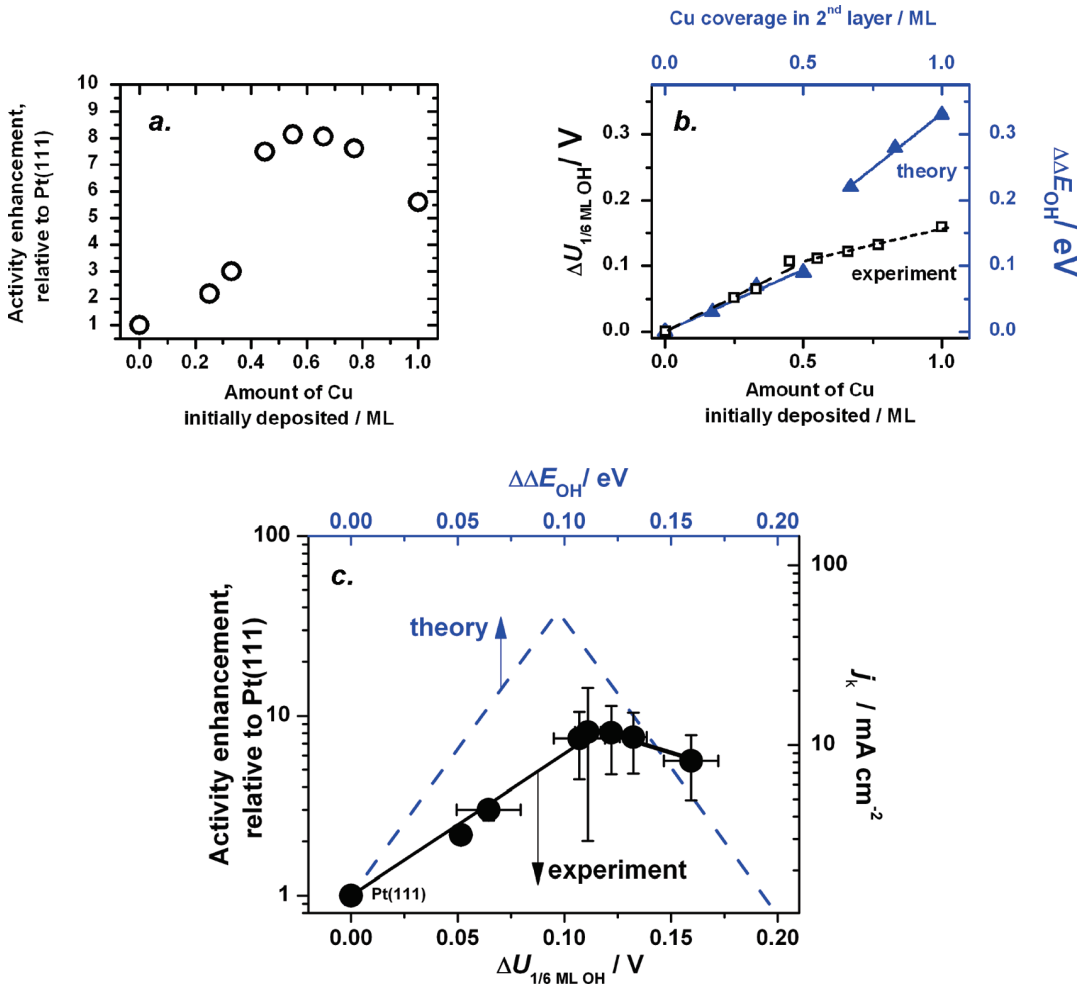

Figure 5. (a) Activity enhancement, relative to Pt(111) at $U = 0.9$ V as a function of the amount of Cu initially deposited, that is $j_{k,NSA}/j_{k,Pt(111)}$, where $j_{k,NSA}$ is the kinetic current density of the Cu/Pt(111) NSA and $j_{k,Pt(111)}$ is the kinetic current density of Pt(111). (b) Experimental and theoretical weakening of OH binding, as a function of Cu content; the linear trendlines were produced using a least-squares fit. (c) Activity enhancement, relative to Pt(111) and kinetic current density, j_k at $U = 0.9$ V versus RHE as a function of $\Delta U_{1/6ML\,OH}$ and $\Delta\Delta E_{OH}$. The circular data points represent experimental data, produced by combining data from *a* and *b*. The data points shown are the mean values, taken from 30 independent measurements, distributed across the entire composition range. The error bars show the standard deviation. The dashed blue line represents earlier theoretical predictions, based upon a simple model using a Sabatier analysis.[5,6] The volcano here is plotted as a function of $\Delta\Delta E_{OH}$ instead of the oxygen adsorption energy, $\Delta\Delta E_O$; the two binding energies, relative to Pt (111), are related by the function $\Delta\Delta E_{OH} \approx 0.5\Delta\Delta E_O$.[13]

CONCLUSION

We have demonstrated that the presence of subsurface 3d metals can weaken the binding of a Pt surface to OH*. This corroborates previous theoretical studies of NSAs.[38,46] We make use of this phenomenon to engineer an ~8-fold enhancement in ORR activity over Pt(111).

We have also shown that it is possible to (a) monitor in situ the binding energy of a simple adsorbate, in this case OH*, on a single crystal surface, (b) tune this binding energy continuously, and (c) use this binding energy as an experimental descriptor for the activity of the surface for a catalytic reaction. We confirm the theoretical prediction that only a slight weakening of the descriptor, ΔE_{OH}, by ~0.1 eV, relative to Pt(111), will lead to optimal activity for the oxygen reduction reaction. To the best of our knowledge, this is the first time that the Sabatier principle has been demonstrated in situ for a continuous catalytic reaction on a well-defined single crystal surface. There is good reason to believe that this principle will continue to be used for the design of yet more active (and ideally abundant) catalysts to meet our future energy requirements.

ASSOCIATED CONTENT

Supporting Information. Full details of the experiments and calculations including the results of additional electrochemical experiments and the raw AR-XPS data. This material is available free of charge via the Internet at http://pubs.acs.org.

AUTHOR INFORMATION

Corresponding Author
ibchork@fysik.dtu.dk

ACKNOWLEDGMENT

Funding by the Danish Strategic Research Council's (DSRC) HyCycle program and SERC project (Grant No. 2104-06-0011)

as well as the Spanish Government's, "Programa Nacional de Movilidad de Recursos Humanos del PN de I+D+I 2008-2011" is gratefully acknowledged. A.S.B. acknowledges additional financial support from the European Union and the MWIFT-NRW (Hightech.NRW competition). The Center for Atomic-scale Materials Design is supported by the Lundbeck Foundation. The Center for Individual Nanoparticle Functionality is supported by the Danish National Research Foundation.

REFERENCES

(1) Eberle, U.; von Helmolt, R. *Energy Environ. Sci.* **2010**, *3*, 689.
(2) Wagner, F. T.; Lakshmanan, B.; Mathias, M. F. *J. Phys. Chem. Lett.* **2010**, *1*, 2204.
(3) Gasteiger, H. A.; Kocha, S. S.; Sompalli, B.; Wagner, F. T. *Appl. Catal., B* **2005**, *56*, 9.
(4) Gasteiger, H. A.; Markovic, N. M. *Science* **2009**, *324*, 48.
(5) Nørskov, J. K.; Rossmeisl, J.; Logadottir, A.; Lindqvist, L.; Kitchin, J. R.; Bligaard, T.; Jonsson, H. *J. Phys. Chem. B* **2004**, *108*, 17886.
(6) Rossmeisl, J.; Karlberg, G. S.; Jaramillo, T.; Nørskov, J. K. *Faraday Discuss.* **2008**, *140*, 337.
(7) Greeley, J.; Stephens, I. E. L.; Bondarenko, A. S.; Johansson, T. P.; Hansen, H. A.; Jaramillo, T. F.; Rossmeisl, J.; Chorkendorff, I.; Nørskov, J. K. *Nat. Chem.* **2009**, *1*, 552.
(8) Tripkovic, V.; Skúlason, E.; Siahrostami, S.; Nørskov, J. K.; Rossmeisl, J. *Electrochim. Acta* **2010**, *55*, 7975.
(9) Greeley, J.; Rossmeisl, J.; Hellman, A.; Nørskov, J. K. *Z. Phys. Chem., Int. J. Res. Phys. Chem. Chem. Phys.* **2007**, *221*, 1209.
(10) Lee, S. W.; Chen, S.; Suntivich, J.; Sasaki, K.; Adzic, R. R.; Shao-Horn, Y. *J. Phys. Chem. Lett.* **2010**, *1*, 1316.
(11) Janik, M. J.; Taylor, C. D.; Neurock, M. *J. Electrochem. Soc.* **2009**, *156*, B126.
(12) Abild-Pedersen, F.; Greeley, J.; Studt, F.; Rossmeisl, J.; Munter, T. R.; Moses, P. G.; Skulason, E.; Bligaard, T.; Nørskov, J. K. *Phys. Rev. Lett.* **2007**, *99*, 016105.
(13) Rossmeisl, J.; Logadottir, A.; Nørskov, J. K. *Chem. Phys.* **2005**, *319*, 178.
(14) Sabatier, P. *Ber. Der Deutsch. Chem. Ges.* **1911**, *44*, 1984.
(15) Logadottir, A.; Rod, T. H.; Nørskov, J. K.; Hammer, B.; Dahl, S.; Jacobsen, C. J. H. *J. Catal.* **2001**, *197*, 229.
(16) Bligaard, T.; Nørskov, J. K.; Dahl, S.; Matthiesen, J.; Christensen, C. H.; Sehested, J. *J. Catal.* **2004**, *224*, 206.
(17) Nørskov, J. K.; Bligaard, T.; Logadottir, A.; Kitchin, J. R.; Chen, J. G.; Pandelov, S.; Stimming, U. *J. Electrochem. Soc.* **2005**, *152*, J23.
(18) Ferrin, P.; Nilekar, A. U.; Greeley, J.; Mavrikakis, M.; Rossmeisl, J. *Surf. Sci.* **2008**, *602*, 3424.
(19) Grabow, L. C.; Mavrikakis, M. *Angew. Chem., Int. Ed.* **2008**, *47*, 7390.
(20) Nørskov, J. K.; Bligaard, T.; Rossmeisl, J.; Christensen, C. H. *Nat. Chem.* **2009**, *1*, 37.
(21) Hansgen, D. A.; Vlachos, D. G.; Chen, J. G. G. *Nat. Chem.* **2010**, *2*, 484.
(22) Neurock, M. *Ind. Eng. Chem. Res.* **2010**, *49*, 10183.
(23) Stamenkovic, V.; Mun, B. S.; Mayrhofer, K. J. J.; Ross, P. N.; Markovic, N. M.; Rossmeisl, J.; Greeley, J.; Nørskov, J. K. *Angew. Chem., Int. Ed.* **2006**, *45*, 2897.
(24) Stamenkovic, V. R.; Fowler, B.; Mun, B. S.; Wang, G. F.; Ross, P. N.; Lucas, C. A.; Markovic, N. M. *Science* **2007**, *315*, 493.
(25) Stamenkovic, V. R.; Mun, B. S.; Arenz, M.; Mayrhofer, K. J. J.; Lucas, C. A.; Wang, G. F.; Ross, P. N.; Markovic, N. M. *Nat. Mater.* **2007**, *6*, 241.
(26) Toda, T.; Igarashi, H.; Uchida, H.; Watanabe, M. *J. Electrochem. Soc.* **1999**, *146*, 3750.
(27) Mayrhofer, K. J. J.; Juhart, V.; Hartl, K.; Hanzlik, M.; Arenz, M. *Angew. Chem., Int. Ed.* **2009**, *48*, 3529.
(28) Chen, S.; Ferreira, P. J.; Sheng, W. C.; Yabuuchi, N.; Allard, L. F.; Shao-Horn, Y. *J. Am. Chem. Soc.* **2008**, *130*, 13818.
(29) Strasser, P.; Koh, S.; Anniyev, T.; Greeley, J.; More, K.; Yu, C. F.; Liu, Z. C.; Kaya, S.; Nordlund, D.; Ogasawara, H.; Toney, M. F.; Nilsson, A. *Nat. Chem.* **2010**, *2*, 454.
(30) Koh, S.; Strasser, P. *J. Am. Chem. Soc.* **2007**, *129*, 12624.
(31) Yang, R.; Leisch, J.; Strasser, P.; Toney, M. F. *Chem. Mater.* **2010**, *22*, 4712.
(32) Zhang, J. L.; Vukmirovic, M. B.; Xu, Y.; Mavrikakis, M.; Adzic, R. R. *Angew. Chem., Int. Ed.* **2005**, *44*, 2132.
(33) Zhou, W. P.; Yang, X. F.; Vukmirovic, M. B.; Koel, B. E.; Jiao, J.; Peng, G. W.; Mavrikakis, M.; Adzic, R. R. *J. Am. Chem. Soc.* **2009**, *131*, 12755.
(34) Adzic, R. R.; Zhang, J.; Sasaki, K.; Vukmirovic, M. B.; Shao, M.; Wang, J. X.; Nilekar, A. U.; Mavrikakis, M.; Valerio, J. A.; Uribe, F. *Top. Catal.* **2007**, *46*, 249.
(35) Bligaard, T.; Nørskov, J. K. *Electrochim. Acta* **2007**, *52*, 5512.
(36) Kitchin, J. R.; Nørskov, J. K.; Barteau, M. A.; Chen, J. G. *Phys. Rev. Lett.* **2004**, *93*, 156801.
(37) Hoster, H. E.; Alves, O. B.; Koper, M. T. M. *ChemPhysChem* **2010**, *11*, 1518.
(38) Kitchin, J. R.; Nørskov, J. K.; Barteau, M. A.; Chen, J. G. *J. Chem. Phys.* **2004**, *120*, 10240.
(39) Schlapka, A.; Lischka, M.; Gross, A.; Kasberger, U.; Jakob, P. *Phys. Rev. Lett.* **2003**, *91*, 016101.
(40) Lischka, M.; Mosch, C.; Gross, A. *Electrochim. Acta* **2007**, *52*, 2219.
(41) Mavrikakis, M.; Hammer, B.; Nørskov, J. K. *Phys. Rev. Lett.* **1998**, *81*, 2819.
(42) Bardi, U.; Beard, B. C.; Ross, P. N. *J. Catal.* **1990**, *124*, 22.
(43) Fowler, B.; Lucas, C. A.; Omer, A.; Wang, G.; Stamenkovic, V. R.; Markovic, N. M. *Electrochim. Acta* **2008**, *53*, 6076.
(44) Greeley, J.; Mavrikakis, M. *Nat. Mater.* **2004**, *3*, 810.
(45) Menning, C. A.; Chen, J. G. *Top. Catal.* **2010**, *53*, 338.
(46) Knudsen, J.; Nilekar, A. U.; Vang, R. T.; Schnadt, J.; Kunkes, E. L.; Dumesic, J. A.; Mavrikakis, M.; Besenbacher, F. *J. Am. Chem. Soc.* **2007**, *129*, 6485.
(47) Andersson, K. J.; Calle-Vallejo, F.; Rossmeisl, J.; Chorkendorff, L. *J. Am. Chem. Soc.* **2009**, *131*, 2404.
(48) Tsay, J. S.; Mangen, T.; Linden, R. J.; Wandelt, K. *Surf. Sci.* **2001**, *482*, 866.
(49) Sarkar, A.; Manthiram, A. *J. Phys. Chem. C* **2010**, *114*, 4725.
(50) Herrero, E.; Buller, L. J.; Abruna, H. D. *Chem. Rev.* **2001**, *101*, 1897.
(51) Leung, L. W. H.; Gregg, T. W.; Goodman, D. W. *Langmuir* **1991**, *7*, 3205.
(52) Markovic, N.; Ross, P. N. *Langmuir* **1993**, *9*, 580.
(53) Andersson, K. J.; Chorkendorff, I. *Surf. Sci.* **2010**, *604*, 1733.
(54) Strasser, P.; Koh, S.; Greeley, J. *Phys. Chem. Chem. Phys.* **2008**, *10*, 3670.
(55) Greeley, J.; Nørskov, J. K. *Electrochim. Acta* **2007**, *52*, 5829.
(56) Pourbaix, M. *Atlas of Electrochemical Equilibria in Aqueous Solutions*; 2nd ed.; National Association of Corrosion Engineers: Houston, TX, 1974.
(57) Abrams, B. L.; Vesborg, P. C. K.; Bonde, J. L.; Jaramillo, T. F.; Chorkendorff, I. *J. Electrochem. Soc.* **2009**, *156*, B273.
(58) Mayrhofer, K. J. J.; Hartl, K.; Juhart, V.; Arenz, M. *J. Am. Chem. Soc.* **2009**, *131*, 16348.
(59) Jinnouchi, R.; Toyoda, E.; Hatanaka, T.; Morimoto, Y. *J. Phys. Chem. C* **2010**, *114*, 17557.
(60) Stamenkovic, V. R.; Mun, B. S.; Mayrhofer, K. J. J.; Ross, P. N.; Markovic, N. M. *J. Am. Chem. Soc.* **2006**, *128*, 8813.

Langmuir
Article
pubs.acs.org/Langmuir

The Pt(111)/Electrolyte Interface under Oxygen Reduction Reaction Conditions: An Electrochemical Impedance Spectroscopy Study

Alexander S. Bondarenko,*[,†,§] Ifan E. L. Stephens,[†] Heine A. Hansen,[‡,∥] Francisco J. Pérez-Alonso,[†] Vladimir Tripkovic,[‡] Tobias P. Johansson,[†] Jan Rossmeisl,[‡] Jens K. Nørskov,[‡] and Ib Chorkendorff[†]

[†]*Center for Individual Nanoparticle Functionality, Department of Physics, Building 312, Technical University of Denmark, DK-2800 Lyngby, Denmark, and* [‡]*Center for Atomic-scale Materials Design, Department of Physics, Building 311, Technical University of Denmark, DK-2800 Lyngby, Denmark.* [§]*Present address: Center for Electrochemical Sciences, Ruhr-Universität Bochum, Universitätsstr. 150 NC 4/73, D-44780 Bochum, Germany.* [∥] *Present address: Department of Materials Science and Engineering, Northwestern University, Evanston, Illinois 60208, United States*

Received October 21, 2010. Revised Manuscript Received December 9, 2010

The Pt(111)/electrolyte interface has been characterized during the oxygen reduction reaction (ORR) in 0.1 M $HClO_4$ using electrochemical impedance spectroscopy. The surface was studied within the potential region where adsorption of OH* and O* species occur without significant place exchange between the adsorbate and Pt surface atoms (0.45−1.15 V vs RHE). An equivalent electric circuit is proposed to model the Pt(111)/electrolyte interface under ORR conditions within the selected potential window. This equivalent circuit reflects three processes with different time constants, which occur simultaneously during the ORR at Pt(111). Density functional theory (DFT) calculations were used to correlate and interpret the results of the measurements. The calculations indicate that the coadsorption of ClO_4* and Cl* with OH* is unlikely. Our analysis suggests that the two-dimensional (2D) structures formed in O_2-free solution are also formed under ORR conditions.

1. Introduction

The oxygen reduction reaction (ORR) on Pt has been studied for decades by both experimentalists and theoreticians,[1−8] particularly upon the (111) facet in acidic solutions. This is not only because of its fundamental importance as a model system, but also for technological reasons: the (111) surface is believed to constitute the active facet of the Pt nanoparticles which catalyze the ORR in polymer electrolyte membrane fuel cells.[1,9]

In the absence of O_2, the electrosorption of oxygenated species such as OH* and O* can be studied more easily than in the presence of O_2, where they constitute reaction intermediates. Consequently, a large body of work has been devoted to the initial stages of Pt electro-oxidation in the absence of O_2.[10−25] These studies have utilized a number of different techniques, including electrochemical methods such as dc voltammetry and electrochemical impedance spectroscopy (EIS). The interpretation of these processes has been aided through the use of ab initio calculations. We recently used density functional theory (DFT) to elucidate the potential dependent stability of different OH* and O* adsorbate structures on Pt (111).[22] Figure 1 shows the most stable adsorbates: (a) 1/3 monolayer (ML) OH* with H_2O (stable between ∼0.78 and ∼0.85 V vs RHE), (b) 1/4ML O* (between ∼0.85 and ∼1.0 V), and (c) 1/3ML O* (between ∼1.0 and ∼1.13 V).

In O_2-free solution, the electrosorption of OH* and O* shows distinct voltammetric peaks, as shown in section 3. However, the 1/4ML O* and 1/3ML O* phases are not clearly distinguishable in situ, even with the use of infrared spectroscopy,[26] small-angle X-ray scattering,[27] or scanning tunneling microscopy.

Under oxygen reduction reaction conditions, it becomes even more difficult to detect and distinguish these different adsorbate structures using electrochemical methods. This is because the

*To whom correspondence should be addressed. E-mail: aliaksandr.bandarenka@rub.de. Telephone: +49 234-32 29432.

(1) Nørskov, J. K.; Rossmeisl, J.; Logadottir, A.; Lindqvist, L.; Kitchin, J. R.; Bligaard, T.; Jonsson, H. *J. Phys. Chem. B* **2004**, *108*, 17886–17892.
(2) Wang, J. X.; Zhang, J.; Adzic, R. R. *J. Phys Chem. A* **2007**, *111*, 12702–12710.
(3) Rossmeisl, J.; Karlberg, G. S.; Jaramillo, T. F.; Nørskov, J. K. *Faraday Discuss.* **2008**, *140*, 337–346.
(4) Janik, M. J.; Taylor, C. D.; Neurock, M. *J. Electrochem. Soc.* **2009**, *156*, B126–B135.
(5) Markovic, N. M.; Adzic, R. R.; Cahan, B. D.; Yeager, E. B. *J. Electroanal. Chem.* **1994**, *377*, 249–259.
(6) Sepa, D. B.; Vojnovic, M. V.; Damjanovic, A *Electrochim. Acta* **1981**, *26*, 781–793.
(7) Tripkovic, V.; Skúlason, E.; Siahrostami, S.; Nørskov, J. K.; Rossmeisl, J. *Electrochim. Acta* **2010**, *55*, 7975−7981.
(8) Greeley, J.; Stephens, I. E. L.; Bondarenko, A. S.; Johansson, T. P.; Hansen, H. A.; Jaramillo, T. F.; Rossmeisl, J.; Chorkendorff, I.; Nørskov, J. K. *Nat. Chem.* **2009**, *1*, 552–556.
(9) Greeley, J.; Rossmeisl, J.; Hellman, A; Nørskov, J. K. *Z. Phys. Chem.* **2007**, *221*, 1209–1220.
(10) Clavilier, J.; Rodes, A.; El Achi, K.; Zamakhchari, M. A. *J. Chim. Phys.* **1991**, *88*, 1291–1337.
(11) Berna, A.; Climent, V.; Feliu, J. M. *Electrochem. Commun.* **2007**, *9*, 2789–2794.
(12) Wakisaka, M.; Suzuki, H.; Mitsui, S.; Uchida, H.; Watanabe, M. *Langmuir* **2009**, *25*, 1897–1900.
(13) Markovic, N. M.; Ross, P. N., Jr. *Surf. Sci. Rep.* **2002**, *45*, 117–229.
(14) Angerstein-Kozlowska, H.; Conway, B. E.; Sharp, W. B. A. *J. Electroanal. Chem.* **1973**, *43*, 9–36.
(15) Koper, M. T. M.; Lukkien, J. K. *J. Electroanal. Chem.* **2000**, *485*, 161–165.
(16) Koper, M. T. M. *Faraday Discuss.* **2008**, *140*, 11–24.
(17) Garcia-Araez, N.; Climent, V.; Herrero, E.; Feliu, J. M.; Lipkowski, J. *Electrochim. Acta* **2006**, *51*, 3787–3793.
(18) Jerkiewicz, G.; Vatankhah, G; Lessard, J.; Soriaga, M. P.; Park, Y. S. *Electrochim. Acta* **2004**, *49*, 1451–1459.
(19) Rai, V.; Aryanpour, M.; Pitsch, H. *J. Phys Chem. C* **2008**, *112*, 9760–9768.
(20) Mostany, J.; Herrero, E.; Feliu, J. M.; Lipowski, J. *J. Electroanal. Chem.* **2003**, *558*, 19–24.
(21) Rossmeisl, J.; Nørskov, J. K.; Taylor, C. D.; Janik, M. J.; Neurock, M. *J. Phys. Chem. B* **2006**, *110*, 21833–21839.
(22) Hansen, H. A.; Rossmeisl, J.; Nørskov, J. K. *Phys. Chem. Chem. Phys.* **2008**, *10*, 3722–3730.
(23) Sibert, E.; Faure, R.; Durand, R. *J. Electroanal. Chem.* **2001**, *515*, 71–81.
(24) Tian, F.; Jinnuochi, R.; Anderson, A. B. *J. Phys. Chem. C* **2009**, *113*, 17484–17492.
(25) Schouten, K. J. P.; van der Niet, M. J. T. C.; Koper, M. T. M. *Phys. Chem. Chem. Phys.* **2010**, *12*, 15217–15224.
(26) Iwasita, T.; Xia, X. *J. Electroanal. Chem.* **1996**, *411*, 95–102.

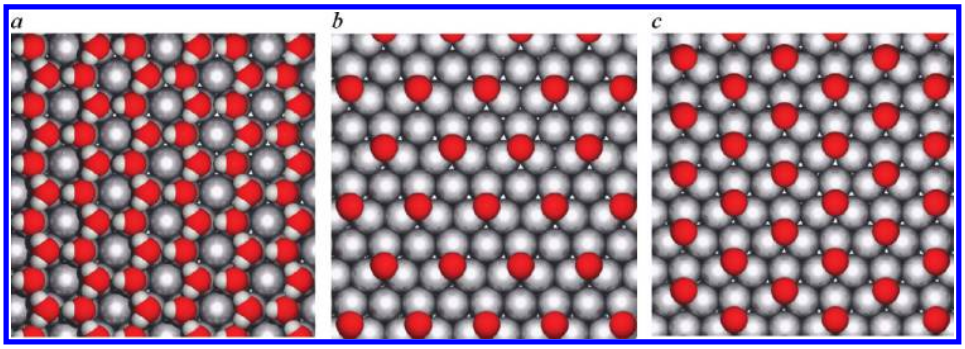

Figure 1. Theoretically stable surface structures on Pt(111) at pH = 1: (a) 1/3ML OH* with water, (b) 1/4ML O*, (c) 1/3ML O* (top view).

electrochemical response associated with the transient electrosorption of these intermediates is obscured by the continuous Faradaic currents due to oxygen reduction, and the influence of mass transport.

Ex situ techniques are able to probe the adsorbates formed in electrochemical environments. For instance, Watanabe and coworkers have recently used X-ray photoelectron spectroscopy (XPS) to monitor the formation of oxygenated adsorbed species on Pt(111), polycrystalline Pt, and Pt alloys in HF electrolytes.[12,28] However, obtaining such information in situ remains a key challenge in the field of electrochemistry.[29] In particular, In situ experimental evidence for the formation of the predicted by DFT O* structures shown in Figure 1b and c under ORR conditions is important. These intermediates could affect the activity and durability of Pt catalysts in the potential range between ~0.85 and ~1.0 V, which is critical for fuel cell applications.

EIS is a sensitive electrochemical technique for the in situ investigation of the solid/liquid interface, which enables the resolution of simultaneous processes.[30] With respect to the oxidation of Pt in acidic solution, three EIS studies are of particular pertinence to the current study: (a) the work of Itagaki et al., whereby a physical model is proposed for the impedance of the ORR on Pt;[31] (b) Ragoisha et al.'s study,[32] investigating the oxidation of polycrystalline Pt; and (c) Sibert et al.'s investigation of the oxidation of Pt(111) up to 0.8 V.[23] More advanced stages of Pt oxidation, such as the adsorption of O*, were not included within the scope of previous investigations of Pt single crystals. Moreover, to the best of our knowledge, there is no EIS study in the literature which compares the state of the Pt(111)/electrolyte interface in the absence and the presence of O_2.

Potentiodynamic EIS provides a routine procedure to decompose the integral ac response acquired *within a potential scan* into constituents related to simultaneous processes occurring at the nonstationary interface.[33−39]

Although potentiodynamic EIS cannot be used to identify exact surface structures a priori, it will be shown in this work that in combination with DFT it can provide more detailed information about two-dimensional (2D) phase formation at the electrode surface.

In this work, we use potentiodynamic EIS to compare the state of the Pt(111)/electrolyte interface in the presence and the absence of O_2 in 0.1 M $HClO_4$. The potential window incorporates the range where adsorption of OH* and O* species occur without significant place exchange between the adsorbate and Pt surface atoms (0.45−1.15 V vs RHE).[12] Importantly, this is also the potential window of interest for fuel cell applications.

2. Experimental Section

Two types of single crystals were used in this work: (a) a small bead-type Pt(111) crystal (oriented to $<0.05°$) obtained from Prof. Juan Feliu (University of Alicante, Spain) prepared according to ref 40; (b) a larger Pt(111) single crystal (diameter 1 cm, oriented to $<0.1°$, obtained from Mateck, Julich, Germany) which was used for the majority of the measurements. The smaller bead-type crystal was used as a benchmark to ensure cleanliness of the experimental setup. However, the majority of the measurements were performed on the larger crystal in order (a) to improve reproducibility of the annealing procedure (the temperature was controlled with a K-type (Ni/Cr+Ni/Al) thermocouple attached to the back side of the crystal) and (b) to increase the signal-to-noise ratio in EIS measurements.

Before each experiment, the bead-type single crystal was flame annealed for 1 min and cooled in a H_2 (5%) + Ar atmosphere. For the larger crystal, a special cell was designed, similar to that reported in ref 41. The cell allows controllable annealing of Pt(111) single crystals in a desired atmosphere using an induction heater. Before each experiment, the larger single crystal Pt(111) was annealed at 850 ± 20 °C in a H_2 (5%) + Ar atmosphere for 2−6 min, followed by annealing in a CO (0.1%) + Ar atmosphere for 2 min at 850 ± 20 °C. In order to minimize contamination during the course of the relatively slow impedance measurements, the crystal was always manipulated without exposure to air. Therefore, it was always kept in a controlled atmosphere, minimizing random contamination from the laboratory environment. A hanging meniscus configuration was used for the electrochemical characterization of the Pt(111) surface.

Before each experiment, the cell was cleaned in a piranha solution consisting of a mixture of 96% H_2SO_4 and 30% H_2O_2 (3:1) for 24 h, followed by multiple heating/rinsing with Millipore water to remove sulfates. Swagelok stainless steel tubes were used

(27) Lucas, C. A.; Cormack, M.; Gallagher, M. E.; Brownrigg, A.; Thompson, P.; Fowler, B.; Gründer, Y.; Roy, J.; Stamenkovic, V.; Markovic, N. M. *Faraday Discuss.* **2008**, *140*, 41–58.
(28) Wakisaka, W.; Suzuki, H.; Mitsui, S.; Uchida, H.; Watanabe, M. *J. Phys. Chem. C* **2008**, *112*, 2750–2755.
(29) Gewirth, A. A.; Thorum, M. S. *Inorg. Chem.* **2010**, *49*, 3557–3566.
(30) Lasia, A. In *Modern Aspects of Electrochemistry*; Conway, B. E., Bockris, J., White, R., Eds.; Kluwer Academic/Plenum Publishers: New York, 1999; Vol. *32*, pp 143−248.
(31) Itagaki, M.; Hasegava, H.; Watanabe, K.; Hachiya, T. *J. Electroanal. Chem.* **2003**, *557*, 59–73.
(32) Ragoisha, G. A.; Osipovich, N. P.; Bondarenko, A. S.; Zhang, J.; Kocha, S.; Iiyama, A. *J. Solid State Electrochem.* **2010**, *14*, 531–542.
(33) van Ingelgem, Y.; Tourwe, E.; Blajiev, O.; Pintelon, R.; Hubin, A. *Electroanalysis* **2009**, *21*, 730–739.
(34) Pettit, C. M.; Goonetilleke, P. C.; Sulyma, C. M.; Roy, D. *Anal. Chem.* **2006**, *78*, 3723–3729.
(35) Ragoisha, G. A.; Bondarenko, A. S. *Electrochim. Acta* **2005**, *50*, 1553.
(36) Ragoisha, G. A.; Bondarenko, A. S. *Electrochem. Commun.* **2003**, *5*, 392–395.
(37) Schiewe, J.; Hazi, J.; Vicente-Beckett, V. A.; Bond, A. M. *J. Electroanal. Chem.* **1998**, *451*, 129.
(38) Popkirov, G. S. *Electrochim. Acta* **1996**, *41*, 1023.
(39) Chang, B. Y.; Park, S. M. *Annu. Rev. Anal. Chem.* **2010**, *3*, 207.
(40) Clavilier, J.; Armand, D.; Sun, S. G.; Petit, M. *J. Electroanal. Chem.* **1986**, *205*, 267.
(41) Komanicky, V.; Chang, K. C.; Menzel, A.; Markovic, N. M.; You, H.; Wang, X.; Myers, D. *J. Electrochem. Soc.* **2006**, *153*, B446–B451.

to supply O_2, Ar, Ar/H_2, and Ar/CO gas mixtures into the cell. Plastic tubing was avoided to minimize outgassing of organic contamination. Each experiment was conducted in 0.1 M $HClO_4$ (Merck, Suprapur) in ultrapure water (Millipore Synergy Pak UV, > 18.2 MΩ cm, 22 ± 2 °C).

A Pt wire (GoodFellow) counter electrode of high surface area was used. A Hg/Hg_2SO_4 electrode (Schott, kept in a separate compartment and separated from the working solution with a porous ZrO_2-ceramic insert) was used as a reference, although all potentials are referred to the reversible hydrogen electrode (RHE) scale. A Biologic Instruments SP-150 potentiostat was used to control the measurements. To minimize artifacts in EIS measurements at high frequencies caused by the potentiostat, a shunt with the capacitance connected between the reference and counter electrode was used. The value of the capacitance was empirically selected in a series of calibration experiments.

In the EIS experiments, the potential was scanned stepwise, similar to the measurements described in refs 33−38 and 42, always from 0.45 to 1.15 V RHE. The ac frequency range was from 30 kHz to 10 Hz. Lower frequencies were avoided in order to keep a reasonable potential scan rate and minimize unwanted reconstruction or contamination during the course of the measurement. In order to verify the equivalent circuit, selected EIS spectra were also recorded in a wider frequency range, from 30 kHz to 0.5 Hz. The EIS spectra analysis including Kramers−Kronig tests was performed with the EIS Spectrum Analyzer software.[43] The quality of the fitting and modeling was controlled by the root-mean-square deviation and individual parameter uncertainties; for example, parameter uncertainties for the constant phase element (CPE) describing the double electric layer ($Z_{CPE} = C_{DL}^{-1}(j\omega)^{-n}$) were below 0.9% in case of exponent n and below 2.5% in case of C'_{DL}. Parameter values which were found to exhibit exceptionally high calculated uncertainties were removed from the corresponding plots.

Following the EIS experiments, base voltammograms were taken in O_2-free solution to ensure the cleanliness of the surface. The general shape of the voltammograms remained the same, without any additional peaks. After around 10 cycles, only small deviations were observable from the initial voltammograms.

3. Results and Discussion

3.1. Base Voltammetry in the Absence of O_2. Typical voltammograms of Pt(111) crystals used in this work in a solution of 0.1 M $HClO_4$ (Merck, Suprapur) in Millipore water are shown in Figure 2. Three different regions are distinguishable in the voltammogram shown in Figure 2. These are associated with hydrogen underpotential deposition (H*), the adsorption of OH*, and the adsorption of O*.[10]

The height and sharpness of the "butterfly" peaks at around 0.8 V RHE are often correlated with the quality of the Pt(111) crystal and the cleanliness of the system.[11] The voltammetric peaks exhibited by the larger crystal were slightly less pronounced than those of the bead-type crystal (Figure 2). We speculate that this could be due to the improved alignment of the bead-type crystal. The voltammograms were stable upon prolonged cycling in the range 0.05−1.0 V RHE for up to 2 h.

Figure 3 shows the DFT-calculated boundaries of the different adsorbate structures of Pt(111), in comparison to the voltammetric charge from the cyclic voltammogram. It is commonly held that the reversible, "butterfly" peak in Figure 2, centered at around 0.8 V, is entirely due to OH adsorption.[11] It is also believed that the peak starting at 1.05 V is due to O* adsorption.[13] The plateau between 0.85 and 1.05 V is considered to be a characteristic of well ordered,

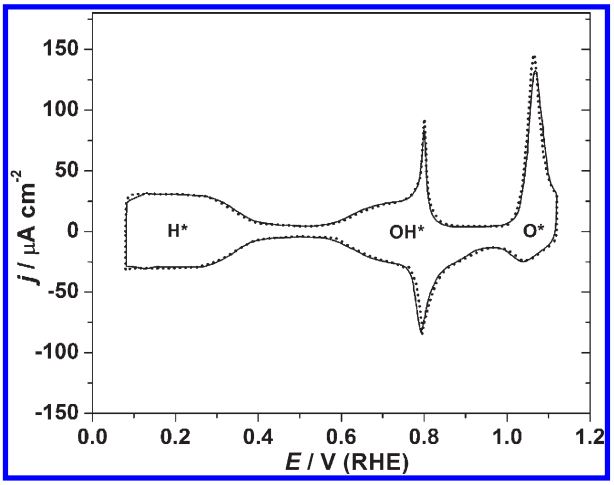

Figure 2. Examples of cyclic voltammograms of bead-type (dotted line) and large, 1 cm diameter (solid line) Pt(111) crystals ($dE/dt = 50$ mV/s).

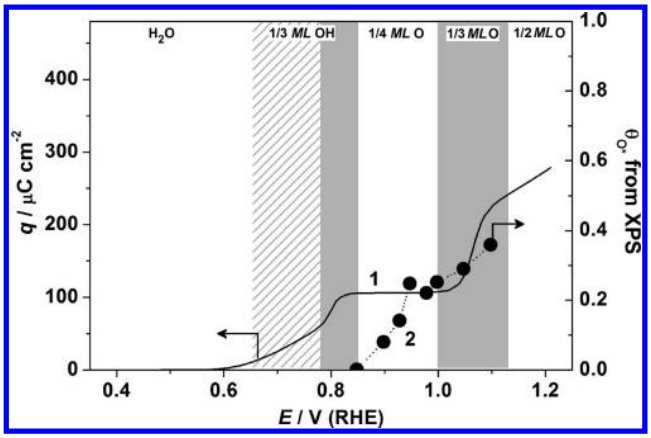

Figure 3. (curve 1) Anodic charge obtained by integrating the voltammogram of a Pt(111) single crystal, starting from 0.5 V RHE and (curve 2) XPS-measured oxygen O* coverage as reported in ref 12. Gray and white regions correspond to the DFT-calculated stability regions for the OH*/O* adsorbate phases as denoted in the figure. The lower boundary of the hatched region corresponds to a coverage of 0.05 ML OH*, assuming a Langmuir adsorption isotherm.[3]

high quality crystals in $HClO_4$.[10] Upon more stepped crystals, there is a significant current in this potential region. We speculate that the plateau could be representative of a kinetic barrier due to the transition between the 1/3ML OH* and 1/4ML O* phase. The highly reversible nature of the 1/3ML OH* electrosorption feature (see Figure 2) indicates that the structure is at thermodynamic equilibrium. Attaining OH* coverages in excess of 1/3ML OH* appears unlikely; DFT calculations show that, at this coverage, the structure shows a local minimum in free energy.[7] This stabilization is provided by the hydrogen bonded network with the icelike water bilayer. The inherent stability of this phase could also be the cause of the sharp peak at ~0.8 V, characteristic of a disorder−order phase transition.[15] In contrast, the asymmetry of the peak on Figure 2 starting at ~1.05 V shows that it is an irreversible, or slow, process. The formation of O* species should occur first at steps and defects, as their stability is enhanced at these sites, relative to the (111) surface.[44] We speculate that above ~0.85 V, these steps

(42) Blajiev, O. L.; Breugelmans, T.; Pintelon, R.; Terryn, H.; Hubin, A. *Electrochim. Acta* **2008**, *53*, 7451–7459.

(43) Bondarenko, A. S.; Ragoisha., G. A. In *Progress in Chemometrics Research*; Pomerantsev, A. L., Ed.; Nova Science Publishers: New York, 2005; pp 89−102 (the program is available online at http://www.abc.chemistry.bsu.by/vi/analyser/).

(44) Abild-Pedersen, F.; Greeley, J.; Studt, F.; Rossmeisl, J.; Munter, T. R.; Moses, P. G.; Sk'ulason, E.; Bligaard, T; Nørskov, J. K. *Phys. Rev. Lett.* **2007**, *99* (1), 016105.

could act as "nucleation centers" for the more thermodynamically stable 1/4ML O* structure upon the terraces.

On the other hand, integrating the voltammetric charge, as shown in Figure 3, yields a different picture. In principle, at each phase boundary, the experimentally determined charge should correspond to the theoretical value. For instance, the complete 1/3ML OH* structure should give a charge equal to 80 μC cm^{-2}, whereas the complete 1/4ML O* structure should give a charge equal to 120 μC cm^{-2}. Consequently, at the boundary between the two coexisiting phases, at 0.85 V, the experimentally determined charge of ~107 μC cm^{-2} seems reasonable. However, this analysis is inconsistent with the hypothesis that the plateau corresponds to a complete 1/3ML OH* structure, which would only require 80 μC cm^{-2}. Moreover, if adsorbed O* had already started to form at around 0.85 V, the coverage of this species should continue to increase within the 1/4 ML O* region. Evidently, there are some discrepancies between the theoretical model and the voltammetric data.

3.2. DFT Calculations Concerning Cl* and ClO_4* Coadsorption. Some authors have proposed that anions such as Cl^- and ClO_4^- are coadsorbed with OH* species on Pt(111) in $HClO_4$ solutions.[45] Anion coadsorption would complicate the interfacial phenomena observed, and could account for the discrepancies noted in the preceding section. We explore this possibility by employing DFT to calculate the adsorption energies of Cl* and ClO_4* in the presence and absence of OH* adsorbates (full details can be found in Appendix A).

We noted above that there is a 27 μC cm^{-2} mismatch between the theoretical charge for 1/3ML OH* and the plateau observed from 0.85 to 1.05 V in Figure 3. This could be accounted for by the coadsorption of 1/3ML OH* with 1/9ML of the adsorbates, Cl* or ClO_4* (assuming one electron for each electrosorption process). Consequently, such a structure was modeled by placing the adsorbed Cl* or ClO_4* species in the center of the hexagonal ring formed by H_2O and OH* species (see Figure 1a) in a 3 × 3 unit cell. This particular water structure of alternating OH and H_2O arranged in a honeycomb pattern was found to be the most stable water structure in UHV experiments when the Pt(111) surface was precovered with oxygen[46] Moreover, it was also predicted theoretically to be the most stable water phase at the potentials of interest for the ORR (0.8−0.9 V).[3,7]

The free energy levels of Cl^- and ClO_4^- in the solution and on the bare platinum surface are illustrated in Figure 4. As a reference for Cl* and ClO_4*, we used Cl_2(g) and H_2O(l). The free energy levels of the ionic species in solution have been taken from the standard electrochemical tables.[47] All the free energy levels have been corrected for pH and ion concentrations.

In our calculated structure, it was not possible to adsorb the ClO_4^- anion in the presence of 1/3ML OH*: once the model was relaxed, this species desorbed spontaneously (see Figure 5). Moreover, the addition of an extra water layer did not stabilize the adsorbate either. On the other hand, on a bare surface, ClO_4* adsorption becomes stable at potentials higher than 1.09 V, where the surface is already oxidized.

As seen from Figure 4, it also seems unlikely that Cl^- could adsorb or coadsorb in the potential region of interest, at pH = 1 and assuming a Cl^- concentration of 10^{-7} M. In the presence of the 1/3 ML OH*, the adsorption of Cl^- only becomes negative in free energy at electrode potentials above 1.82 V (not shown). On a bare surface, the coadsorption of Cl^- only becomes negative in free energy above 1.15 V. It should be noted that the Cl^- concentration that we assume, 10^{-7} M, is an upper bound to the actual concentration in 0.1 M $HClO_4$. There is no consensus in the literature, with estimates ranging from 10^{-10} to 10^{-7} M.[11,45] At lower concentrations, the formation of adsorbed Cl* would be even more unlikely. Illustrations of Cl* and ClO_4* adsorbed on Pt(111) surface without and in the presence of the water bilayer are shown in Figure 5.

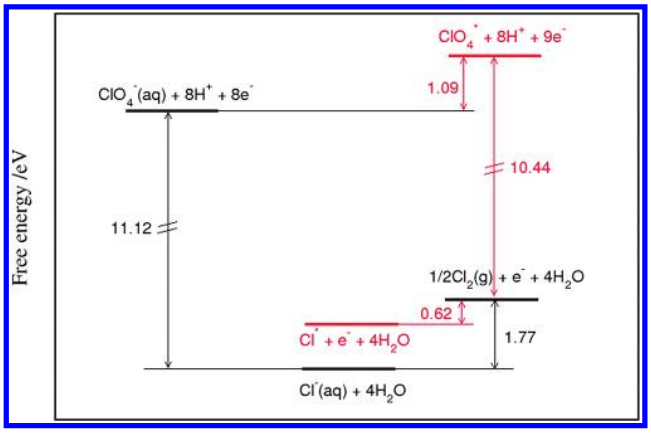

Figure 4. Free energy diagram for Cl^- and ClO_4^- adsorption on a free Pt(111) surface at the assumed experimental conditions (standard conditions, pH = 1, E = 0 V, RHE) and ionic species concentrations ($c(ClO_4^-)$ = 0.1 M, $c(Cl^-) = 10^{-7}$ M). The free energy levels calculated with DFT and the ones taken from electrochemical tables are denoted with red and black, respectively.

In summary, our calculations suggest that Cl* and ClO_4* species are unlikely to be adsorbed on a bare Pt(111) or coadsorbed with OH*. This concurs with earlier experimental observations made by Feliu and co-workers of these phenomena.[11] Nevertheless, more complex interactions with anions cannot be excluded.

3.3. Adsorption of O* at Pt(111) in the Absence of O_2. Evidence for the formation of the 1/4ML O* phase is provided by the ex situ XPS measurements of Wakisaka et al. of the adsorbate structures formed on Pt (111) in HF solutions.[12] Their XPS-determined O* coverage is also shown in Figure 3. There seems to be a reasonable agreement between their measurements and the DFT predicted phase boundaries. Adsorbed O* is first detected at around 0.85 V and continues to increase to ~0.25 ML, at the boundary between 1/4ML O* and 1/3ML O* phases.

Evidently, the increase in O adsorption within this window was not detected by our voltammetric measurements. However, the disparity between the data from the current study and those of Wakisaka et al. could be related to differences in experimental methodology. For instance, they employed a HF based electrolyte, whereas for the current study a $HClO_4$ based electrolyte was employed. On the other hand, it might simply be the case that 1/4ML O* phase formation is too slow to be detected within the time frame required to take a cyclic voltammogram (CV). Voltammograms are normally recorded under very dynamic conditions (high potential scan rates) to obtain a well resolved dc response. However, high scan rates may be inappropriate to detect slow 2D surface ordering, especially in the case of the less reversible formation of O* from OH*. At much lower scan rates (below or close to 1 mV/s), ac impedance measurements become a viable alternative to cyclic voltammetry.

3.4. EIS Measurements in the Presence and the Absence of O_2. The EIS analysis involved finding a physical model and identifying its parameters by fitting the spectrum to an equivalent

(45) Tripkovic, D. V.; Strmcnik, D.; van der Vliet, D.; Stamenkovic, V.; Markovic, N. M. *Faraday Discuss.* **2008**, *140*, 25–40.
(46) Clay, C.; Haq, S.; Hodgson, A. *Phys. Rev. Lett.* **2004**, *92*, 46102.
(47) Bard, A. J. *Encyclopedia of Electrochemistry of the Elements*; Marcel Dekker Inc.: New York, 2002.

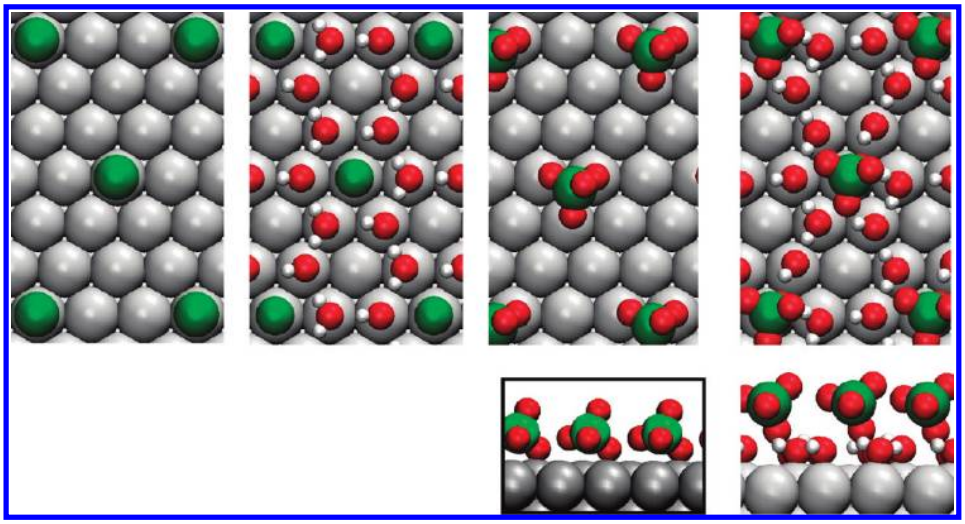

Figure 5. Illustrations of the preferred binding sites for Cl* (top view) and ClO_4* (top and side view) on Pt(111) with and without coadsorbed water. Their coverage corresponds to 1/9 ML. Gray, red, white, and green balls stand for platinum, oxygen, hydrogen, and chlorine atoms, respectively.

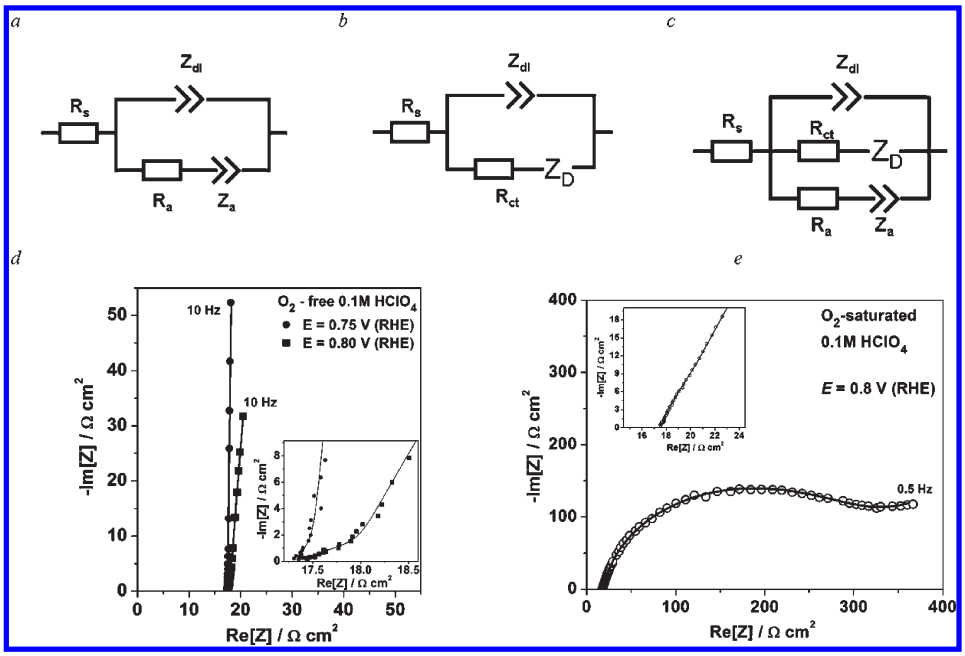

Figure 6. (a–c) Equivalent circuits for: (a) Pt surface oxidation, (b) ORR, and (c) ORR in the presence of Pt surface oxidation. (d,e) Examples of EIS spectra of the Pt(111) electrode in O_2-free and O_2-saturated 0.1 M $HClO_4$. Frequency ranges: (d) 30 kHz to 10 Hz (dE/dt = 0.3 mV/s) and (*e*) 30 kHz to 0.5 Hz. Solid lines represent fitting to the equivalent circuits shown in (a) (for the O_2-free $HClO_4$) and (c) (for the O_2-saturated $HClO_4$). Z_{dl}, impedance of the double layer expressed in terms of constant phase element (see Appendix); R_{ct} and R_a, resistances associated with ORR and Pt oxidation; R_s, electrolyte resistance; Z_a and Z_D, additional impedances depending on system reversibility and the reaction mechanism (see text).

electric circuit (EEC). Recently, several equivalent circuits have been proposed to model OH*/O* adsorption on Pt,[23,48,32] as shown in Figure 6a. The contribution from adsorption was modeled by a series combination of an adsorption resistance R_a and a constant phase element $Z_a = Q_a^{-1}(j\omega)^{-n}$, where j is an imaginary unit, ω is the angular frequency, and the exponent n varies between 0.5 and 1. When $n = 1$, the CPE transforms to the adsorption capacitance C_a.[23]

Itagaki et al. developed an equivalent circuit (Figure 6b) for the ORR.[31] This model includes the contribution of diffusion and constituents originating from the multistage nature of the ORR. In the simplest case, this impedance can be represented by the diffusional Warburg impedance as $Z_D = A_w(j\omega)^{-0.5}$, where A_w is the diffusional Warburg coefficient.

By assuming that the adsorption/desorption of *OH at Pt(111) is reversible within a certain potential range, we propose a new equivalent circuit, shown in Figure 6c. This EEC assumes that the time constant corresponding to the reversible adsorption/desorption of *OH at Pt(111) is considerably faster than the time constant corresponding to the continuous Faradaic current of the ORR. However, the processes are evidently coupled.

Such distinct time constants could possibly be due to differences in the prefactors of the rate equations for the different

(48) Pajkossy, T.; Kolb, D. M. *Electrochim. Acta* **2001**, *46*, 3063–3071.

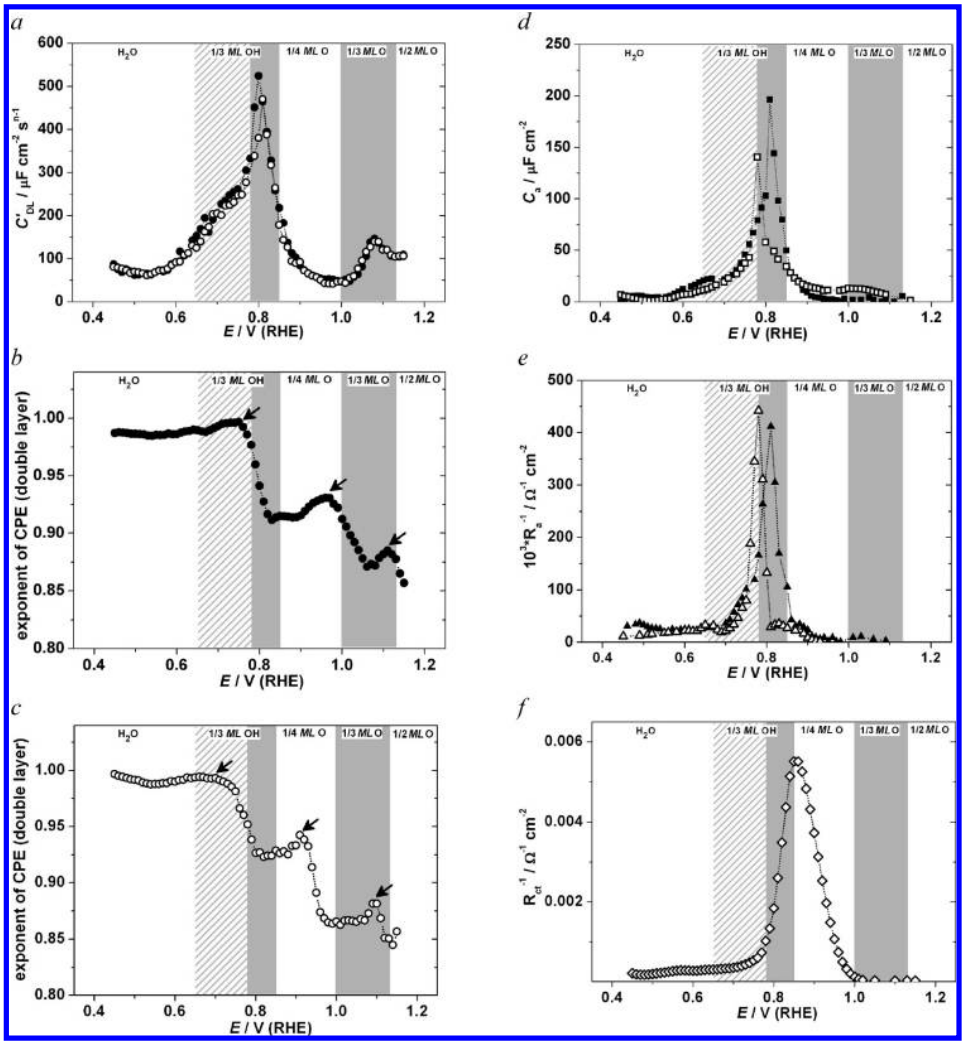

Figure 7. Dependences of the equivalent circuit parameters on potential (anodic scan, $dE/dt = 0.3$ mV/s) for a Pt(111) electrode in O_2-free (bold symbols ●, ■, ▲) and O_2-saturated (open symbols ○, □, △, ◇) 0.1 M $HClO_4$.

processes. The reaction mechanism for the ORR can be simplified as[3]

$$O_2 \rightarrow {}^*OOH \rightarrow {}^*O \rightarrow {}^*OH \leftrightarrow H_2O$$

The prefactor for the rate of the ORR needs to incorporate both gas phase O_2 adsorption and proton transfers. On the contrary, the rate of the final step, OH* adsorption, only includes the prefactor for a single proton transfer and will be larger.[3] Consequently, it seems intuitive that OH* adsorption and desorption should have a much faster time constant than the overall ORR current.

Figure 6d and e show examples of EIS spectra of Pt(111) in O_2-free and O_2-saturated 0.1 M $HClO_4$ taken at different potentials and frequency ranges. EIS spectra of Pt(111) in O_2-free 0.1 M $HClO_4$ fit well (Figure 6d) to the equivalent circuit shown in Figure 6a, while spectra obtained for ORR at the Pt(111) (Figure 6e) fit well to the equivalent circuit shown in Figure 6c. The exponents of the CPEs describing adsorption (Z_a) were found to be close to 1 within whole potential ranges. Therefore, we replaced them with capacitances C_a. The Warburg impedance, arising from diffusion, only contributed significantly at frequencies close to 0.5 Hz; therefore, it was omitted from further analysis of data recorded between 30 kHz and 10 Hz. Issues related to the impedance of the double layer Z_{dl} are discussed in Appendix B.

Figure 7 shows the typical examples of dependences of the equivalent circuit parameters on the potential for Pt(111) in O_2-free and O_2-saturated $HClO_4$. Each point in these dependences is a result of impedance spectra fitting to the corresponding equivalent circuit (shown in Figure 6a for O_2-free and Figure 6c for O_2-saturated $HClO_4$). To be objective, the parameters calculated in the case of the O_2-free $HClO_4$ were not used while fitting the data for O_2-saturated $HClO_4$; that is, both fitting procedures were independent of each other.

In O_2-free $HClO_4$, the dependences of $C'_{DL}(E)$ (parameter which is proportional to the double layer capacitance; see Appendix B) show complex structures (Figure 7a). The C'_{DL} peak value at ~0.8 V corresponds well to that measured using EIS in ref 23 for 0.5 M $HClO_4$ and obtained by Garcia-Araez et al. in ref 17 using Frumkin's thermodynamic method. It is likely that high C'_{DL} values between ~0.6 V < E < ~0.85 V arise because EIS cannot resolve fast OH adsorption as a separate process. Therefore, the C'_{DL} within this potential window can be considered as a sum of contributions from double layer charging and OH adsorption.

The width and positions of the peaks of $C'_{DL}(E)$ in O_2-free $HClO_4$ (Figure 7a) seem to coincide with the domains of stability calculated by DFT. These are (a) the peak at ~0.8 V and the 1/3ML OH* region and (b) the peak at ~1.13 V and the 1/3ML O*

region. Within the stability range of 1/4ML O*, only a poorly resolved shoulder is seen at 0.9 V.

Analysis of the dependences of the CPE exponent, $n(E)$, shown in Figure 7b,c can provide more insight to the interfacial processes (see Appendix B for a fuller explanation of $n(E)$). The exponent n is very close to 1 in the potential region between 0.45 and 0.75 V in the O_2-free electrolyte (Figure 7b). This quite ideal behavior could intuitively be expected for the double layer of a smooth single crystal electrode. However, $n(E)$ steeply decreases (Figure 7b) within the potential region where the sharp "butterfly" peak is observed in the CV (Figure 2) and also in $C'_{DL}(E)$ at around 0.8 V RHE.

The peak in the CVs of Pt(111) in perchloric acid at around 0.8 V RHE is often attributed to the phase disorder/order transition in the OH* layer.[15] The fast decline in n as a result of the 2D phase transition in the OH* adsorbate layer is consistent with those results obtained for Au single crystals,[49] where 2D phase transitions in adsorbate layers also lead to a decrease in n.

Notably, $n(E)$ changes only slightly between 0.8 V RHE and 0.95 V RHE (Figure 7b). Between around 0.95 V RHE and 1.05 V RHE, $n(E)$ once again steeply decreases. The third wave in $n(E)$ starts at around 1.1 V RHE where its value decreases down to 0.85 at 1.15 V RHE (onsets of all the waves are marked with arrows in Figure 7b). Independent XPS results taken from ref 12 (shown in Figure 3) and our DFT calculations both suggest that the $n(E)$ changes could correspond to phase transitions where the ordered 1/3ML OH*, 1/4ML O*, and 1/3ML O* phases are formed. All onsets of the $n(E)$ waves are located close (within ~50 mV) to the phase boundaries. One can notice that in this particular case the slight increase in n(E) correlates with the expected increased disorder near the phase transition.

The dependences of the adsorption capacitance $C_a(E)$ (Figure 7d) and inverse adsorption resistance $R_a^{-1}(E)$ (Figure 7e) show sharp maxima at potentials close to the "butterfly" spike in the CV at around 0.8 V RHE (compare Figures 2 and 7d,e). The C_a peak values are close to those reported in ref 23 for Pt(111) in 0.5 M $HClO_4$. $R_a^{-1}(E)$ peaks (Figure 7e) correlate with the corresponding $C_a(E)$ peaks shown in Figure 7d.

C_a can be expressed as $C_a = -q_a(d\theta/dE)$, where q_a is the total charge to form the complete adlayer and θ is the surface coverage. The integration of $C_a(E)$ dependences related to both O_2-free and O_2-saturated electrolytes gives q_a around 20 μC/cm^2. This is close to the mismatch noted above between the theoretical value for 1/3ML OH* adsorption (80 μC/cm^2) and the plateau between 0.85 and 1.05 V (107 μC/cm^2) in Figure 3. Given that our DFT calculations suggest that only one type of OH* can be adsorbed within the potential window of interest,[3,7,22] the origin of this slower adsorption process is unknown.

Formal integration of the charge of $C_a(E)$ plus $C'_{DL}(E)$ between 0.45 and 0.9 V gives a good agreement between the total charge value determined by EIS and CV, confirming general reversibility of adsorption in this potential range. Conversely, above 0.9 V, the integrated $C_a(E) + C'_{DL}(E)$ charge is lower than the value determined from the CV. This is due to the increased irreversibility of the adsorption processes above 0.9 V. The $C_a(E)$ determined by EIS is generally more sensitive to reversible adsorption. Nevertheless, the irreversible O* formation is still observable through the $C'_{DL}(E)$.

In the presence of O_2, it is striking how similar all the EIS parameters are to those taken in O_2-free $HClO_4$. *The implication of this is that the 2D adsorbate structures formed in the presence of O_2 correspond closely to those formed in the absence of O_2.*

There is a slight negative shift in the plots in Figure 7a−e for the peaks observed in the presence of O_2, relative to those in O_2-free solution. For example, comparison of Figure 7b and c reveals shifts of around 50 and 10 mV for 1/3ML OH* and 1/4ML O* adsorption, respectively. Likewise, Figure 7d and e shows negative shifts for the maxima in $C_a(E)$ and $R_a^{-1}(E)$ when the solution is saturated with O_2. This negative shift can be understood by taking into account the effect of molecular O_2 on the equilibrium coverage of OH*. In O_2-free solution, the coverage of OH* or O* is controlled entirely by the equilibrium between adsorbed O*, OH*, protons, electrons, and water. However, under ORR conditions, the equilibrium is shifted somewhat because it now needs to incorporate molecular oxygen.[3] Consequently, a slightly more negative electrode potential (i.e., increased chemical potential of electrons) is required to obtain a given coverage of OH* or O* and to offset the shift in the equilibrium.

Finally, Figure 7f shows the inverse charge transfer resistance of the oxygen reduction reaction as a function of the electrode potential, $R_{ct}^{-1}(E)$. R_{ct}^{-1} can be expressed in terms of the dc current i related to the ORR as[30]

$$R_{ct}^{-1} = -\frac{\partial i_{ORR}}{\partial E}$$

Under pure kinetic control, R_{ct}^{-1} should show a Tafel-like exponential increase as the potential is decreased. However, due to the increased influence of mass transport at lower potentials, the $R_{ct}^{-1}(E)$ curve peaks at ~0.86 V. Incidentally, this value is very close to the measured "half-wave potential" for Pt(111) using a rotating disk electrode (~0.864 V RHE).[50] In principle, the apparent kinetic rate constant[51] for oxygen reduction could be determined by correcting for the surface concentration of O_2. On the other hand, such a correction would require improved resolution of the Warburg impedance. This was not possible within the narrow frequency range chosen for the present study (see Experimental Section).

4. Summary

In summary, potentiodynamic EIS together with DFT calculations appears to be an efficient tool for the characterization of the Pt(111)/electrolyte interface, especially in the presence of Faradaic reactions. EIS measurements correspond well with our DFT calculations and with recently published experimental data. Physically meaningful equivalent circuits were chosen in lieu of formal EIS modeling. Although the work aimed to separate all of the reactions occurring at the interface, only processes occurring at three separate time constants could be resolved. These were (a) the continuous Faradaic process of oxygen reduction, (b) a slow electrosorption process, and (c) a fast electrosorption process, convoluted with double layer charging. Both (b) and (c) are likely to be due to the adsorption of OH* from water, which in the presence of O_2 is an ORR intermediate. However, it is unclear why (b) and (c) should constitute two separate processes.

Impedance spectroscopy measurements provide evidence for the formation of three separate adsorbate structures at the Pt(111)/$HClO_4$ interface, as predicted by DFT calculations. These structures also appear to be formed in the presence of O_2, albeit at slightly more negative potentials. In particular, the exponent of the CPE seems to be useful as a probe of 2D phase transitions in the adsorbate layer. To the best of our knowledge, this is the first

(49) Neves, R. S.; De Robertis, E.; Motheo, A. J. *Electrochim. Acta* **2006**, *51*, 1215–1224.

(50) Kuzume, A.; Herrero, E.; Feliu, J. M. *J. Electroanal. Chem.* **2007**, *599*, 333–343.

(51) Kerner, Z.; Pajkossy, T. *Electrochim. Acta* **2002**, *47*, 2055–2063.

time that this has been observed for a Pt single crystal in the presence of a continuous Faradaic reaction.

Importantly, in situ EIS measurements (also under ORR conditions) suggest that a slow formation of the O* structure is possible at Pt(111) between 0.85 and 1.0 V (RHE). We note that no features are observed within this region using cyclic voltammetry, presumably because of the relatively high scan rates that this technique requires. The formation of the O* structure concurs with the ex situ XPS measurements performed recently by Wakisaka et al.[12] Both of these works, ex situ and in situ, confirm earlier theoretical predictions of the presence of the O* structure. The binding of this adsorbate species is critical for fuel cell electrocatalysis. Optimal ORR activity requires that the interaction between the Pt surface and O* should be slightly weakened, for instance, by alloying.[8]

There is a disparity in charge of $\sim 27\ \mu C\ cm^{-2}$ between that required to form 1/3ML OH* and the structure which results in the plateau in charge between 0.85 and 1.05 V. Our DFT calculations suggest that this extra charge does not originate from the coadsorption of ClO_4* and Cl* with OH*. Notably, the total charge required for the slow adsorption process detected by EIS came to $\sim 20\ \mu C\ cm^{-2}$. These two unaccountable features could be symptomatic of the same phenomenon and thus merit further investigation.

A combination of DFT calculations and potentiodynamic EIS provides new opportunities for detailed in situ characterization of the electrochemical interface.

Acknowledgment. We thank Professor Juan Feliu from University of Alicante (Spain) for providing a high-quality Pt(111) single crystal. We are also thankful to Dr. Thomas Jaramillo for his suggestions for this manuscript. We gratefully acknowledge funding from the Danish Strategic Research Council's HyCycle program, the Danish Council for Technology and Innovation's FTP program, and the Spanish Government Ministry of Education's "Programa Nacional de Movilidad de Recursos Humanos del Plan Nacional de I-D+I 2008-2011". The Center for Individual Nanoparticle Functionality is supported by the Danish National Research Foundation. The Center for Atomic-Scale Materials Design is supported by the Lundbeck Foundation.

Appendix A: DFT Calculation Details

All the electronic structure calculations were carried out using density functional theory, with the RPBE functional chosen to treat exchange and correlation.[52] The optimized Pt RPBE lattice constant of 4.02 Å was used to model the Pt(111) electrode. The Pt(111) electrode was represented by periodically repeated three layer slabs. The surface dimension of the unit cell was (3×3), and the irreducible Brillouin zone was sampled by the $(4 \times 4 \times 1)$ Monkhorst−Pack k-point sampling grid.[53] We used at least 10 Å of vacuum which was enough to ensure convergence of the total energies. Symmetry was applied to further reduce the number of k-points. The dipole correction was used in all cases to decouple the electrostatic interaction between the periodically repeated slabs. The Kohn−Sham equations were solved using a plane wave basis set with a plane wave and density cutoff of 26 Ry. Ionic cores were described with Vanderbilt ultrasoft pseudopotentials.[54] A Fermi smearing of 0.1 eV was used, and all the total energies were extrapolated to an electronic temperature of 0 K. The two bottom layers of the slab were fixed in their bulk positions, while the top layer together with adsorbates was allowed to relax until the sum of the absolute forces on atoms was less than 0.01 eV $Å^{-1}$. All calculations were performed using the Dacapo software package[55] integrated with the ASE simulation environment.[56]

The adsorption energies of Cl^- and ClO_4^- are referenced to the Cl_2(g) and H_2O(l) and calculated as

$$\Delta G(\mathrm{Cl}) = E(\mathrm{Cl}^*) - E() - 1/2E(\mathrm{Cl_2}) + \Delta\mathrm{ZPE} - T\Delta S \quad (1.1)$$

$$\Delta G(\mathrm{ClO_4}) = E(\mathrm{ClO_4}^*) - E() - 1/2E(\mathrm{Cl_2}) - 4E(\mathrm{H_2O}) + 4E(\mathrm{H_2}) + \Delta\mathrm{ZPE} - T\Delta S \quad (1.2)$$

where $E()$ is the energy of a metal slab and ΔZPE and $T\Delta S$ are the zero point energy and entropy corrections, respectively.

Since the true reference states should be Cl^- and ClO_4^- in aqueous solution, we used the standard electrode potentials[47] to relate the gas phase energy of chlorine to the solution energy levels of the investigated ionic species.

$$\mathrm{Cl^-(aq)} \rightarrow \frac{1}{2}\mathrm{Cl_2(g)} + e^- \qquad E^\theta = 1.36\ \mathrm{V} \quad (1.3)$$

$$\mathrm{ClO_4^-(aq)} + 8\mathrm{H^+(aq)} + 8\mathrm{e^-} \rightarrow \mathrm{Cl^-(aq)} + 4\mathrm{H_2O(1)} \qquad E^\theta = 1.35\ \mathrm{V} \quad (1.4)$$

Appendix B: Note on the Double Layer Capacitance and the Constant Phase Element

A key parameter that can be determined from EIS is the double layer capacitance, C_{DL}. It is a function of the apparent dielectric constant, ε_w, of the inner H_2O layer and the apparent double layer thickness, d_{DL}. Surface H_2O molecule reorientation causes ε_w to vary,[57] while specific adsorption of ions or new 2D phase formation affects both ε_w and d_{DL}, resulting in extrema in C_{DL} dependences on the electrode potential. Consequently, C_{DL} can elucidate adsorption processes at the electrochemical interface (see, e.g., refs 58 and 59) that are difficult to detect using other in situ techniques.

However, fitting of our EIS spectra shows that the double layer exhibits so-called "frequency dispersion"[30] in a wide range of electrode potentials. This is commonly observed for solid electrodes and means that the measured capacitance values depend on the frequency used. To describe this frequency dispersion, a constant phase element CPE is used instead of a pure capacitance:[60]

$$Z_{\mathrm{dl}} = {C'_{\mathrm{dl}}}^{-1}(j\omega)^{-n}$$

where C'_{DL} is the pre-exponential parameter of the CPE, which is proportional to the double layer capacitance of pure capacitive electrodes, and exponent n is the parameter with values $1 \geq n \geq 0.5$ which is directly related to the dispersive behavior.

(52) Hammer, B.; Hansen, L. B.; Nørskov, J. K. *Phys. Rev. B* **1999**, *59*, 7413.
(53) Monkhorst, H. J.; Pack, J. D. *Phys. Rev. B* **1976**, *13*, 5188.
(54) Vanderbilt, D. *Phys. Rev. B* **1990**, *41*, 7892.
(55) *Dacapo pseudopotential code*; Center for Atomic Scale Materiale Design (CAMD), Technical University of Denmark: Lyngby; https://wiki.fysik.dtu.dk/dacapo.
(56) *Atomic Simulation Environment* (*ASE*); Center for Atomic Scale Materiale Design (CAMD), Technical University of Denmark: Lyngby; https/wiki.fysik.dtu.dk/ase.
(57) Kolb, D. *Angew. Chem., Int. Ed.* **2001**, *40*, 1162–1181.
(58) Pajkossy, T.; Kolb., D. M. *Electrochem. Commun.* **2003**, *5*, 283–285.
(59) Bondarenko, A. S.; Ragoisha, G. A.; Osipovich, N. P.; Streltsov., E. A. *Electrochem. Commun.* **2005**, *7*, 631–636.
(60) Pajkossy, T. *J. Electroanal. Chem.* **1994**, *364*, 111–125.

The CPE cannot be represented by any finite number of elements such as R, C, and L.[30]

Several theories have been proposed to explain the frequency dispersion of the double layer capacitance[30] including (1) the roughness effect, (2) effects of fractal nature, which assume self-similarity of the electrode surface on scaling, and (3) distortion of the double layer by Faradaic reactions at the interface. Unfortunately, none of these theories can explain the complete variety of experimental observations reported in the literature.

During the last two decades, this frequency dispersion has also been investigated using well-defined single crystal surfaces.[49,61−63] The main findings obtained using gold single crystals as the model objects are as follows: (1) C'_{DL} and n are strongly dependent on the electrode potential, and when $n = 1$, the interface presents pure capacitive behavior $C'_{DL} = C_{DL}$. (2) There is a strong relationship between the capacitance dispersion and the phase transition processes which takes place at the interface, namely, the reconstruction of the electrode surface, adsorption, and phase transitions in the ordered adsorbed layers. (3) Values of n can sometimes be *significantly lower than 1 if ordering in the adsorbate layer occurs*. (4) In potential ranges where none of the above-mentioned processes take place, the interface presents almost pure capacitive behavior.

Somewhat counterintuitively, there are some reports which show that rough electrodes can exhibit lower capacitance dispersion[60] than smooth ones. Consequently, in some cases, one might expect lower capacitance dispersion using polycrystalline electrodes rather than single crystal surfaces. In summary, the dependences of both C'_{DL} and n on the electrode potential contain valuable information about the interface and can be used as a sensitive probe to monitor the surface condition.

(61) Pajkossy, T. *Solid State Ionics* **1997**, *94*, 123–129.
(62) Motheo, A. J.; Santos, J. R., Jr.; Sadkowski, A.; Hamelin, A. *J. Electroanal. Chem.* **1995**, *397*, 331–334.
(63) Sadkowski, A.; Motheo, A. J.; Neves, R. S. *J. Electroanal. Chem.* **1998**, *455*, 107–119.